UNIVERSITY OF CALIFORNIA,
IRVINE

Noise Reduction and Flow Characteristics in Asymmetric Dual-Stream Jets

THESIS

submitted in partial satisfaction of the requirements
for the degree of

MASTER OF SCIENCE

in Mechanical and Aerospace Engineering

by

Rebecca Suzanne Shupe

Thesis Committee:
Professor Dimitri Papamoschou, Chair
Professor William A. Sirignano
Professor Feng Liu

2007

The thesis of Rebecca Suzanne Shupe is approved:

William A. Sinigramo

Committee Chair

University of California, Irvine
2007

DEDICATION

To my family,

Mom, Dad, Bobby, David, and Grandfather,

thank you for always believing in me.

Especially, to my grandmother, who inspired my love for flight.

> "We're from your Flock, Jonathan. We are your brothers." The words were strong and calm. "We've come to take you higher, to take you home."
>
> "Home I have none. Flock I have none. I am Outcast. And we fly now at the peak of the Great Mountain Wind. Beyond a few hundred feet, I can lift this old body no higher."
>
> "But you can, Jonathan. For you have learned. One school is finished, and the time has come for another to begin."
>
> As it had shined across him all his life, so understanding lighted that moment for Jonathan Seagull. They were right. He *could* fly higher, and it *wa*s time to go home.
>
> He gave one last long look across the sky, across that magnificent silver land where he had learned so much.
>
> "I'm ready," he said at last.
>
> And Jonathan Livingston Seagull rose with the two starbright gulls to disappear into a perfect dark sky.
>
> — Richard Bach

TABLE OF CONTENTS

List of Figures

LIST OF TABLES

LIST OF SYMBOLS

Roman

a_{2D} = two-dimensional lift curve slope

a = speed of sound

A = amplitude modulation function

$\hat{A}$ = Fourier transform of amplitude modulation function

B = wedge base

c = chord length of vane

C_L = coefficient of lift (vane) or sideforce (wedge)

D = nozzle exit diameter

F = thrust

G = mean velocity radial gradient parameter

H = annular gap width (fan duct exit height)

k = turbulent kinetic energy, wavenumber

K = total kinetic energy

L = deflector lift or sideforce

l = side length of wedge

M = Mach number

p = pressure

q = dynamic pressure

r = shear layer velocity ratio

s = shear layer density ratio

S = wedge wetted area

U = jet exit velocity

$\underset{\sim}{u}$ = total velocity vector in jet plume

$\underset{\sim}{u}'$ = fluctuating velocity vector in jet plume

$\underset{\sim}{\bar{u}}$ = mean velocity vector in jet plume

u = mean axial velocity component in jet plume

u' = fluctuating axial velocity component in jet plume

v' = fluctuating vertical velocity component in jet plume

W = wedge-shaped deflector

w' = fluctuating horizontal velocity component in jet plume

w = average vane span

x = axial position with respect to fan exit

Greek

α = vane angle of attack, wedge half angle

γ = specific heat ratio

δ = shear layer thickness

δ' = shear layer growth rate

ε = deflector turning effort

η = similarity parameter, instability wave

θ = polar angle relative to jet axis

ρ = density

τ = shear stress

ϕ = azimuth angle relative to downward vertical

ω = vorticity

Subscripts

a = ambient stream condition

c = convective

f = fan

GSC = generalized secondary core

p = primary (core) stream, potential core

le = leading edge of vane

s = secondary (bypass) stream

sym = symmetric

te = trailing edge of vane

∞ = ambient stream condition

0 = total (stagnation), fixed axial location

1 = fast moving stream

2 = slow moving stream

ACKNOWLEDGEMENTS

I wish to express my profound respect for and appreciation of my research advisor, Professor Dimitri Papamoschou. His expertise and physical intuition proved invaluable to this research effort. Through his dedication and demanding expectations, he has left a positive impact on my professional life. He is a genuinely kind and caring individual, and I am indebted to him for his helpful advice, encouragement, and friendship.

I am thankful to Dr. Khairul Zaman for his guidance and mentorship in fluid mechanics, and also for his help in conducting the crossed hot-wire measurements. I would like to express my thanks to Dr. Jim DeBonis for his expertise in computational fluid dynamics and grid generation, and for his time spent in obtaining the complementary solutions to the experimental investigation.

I would like to extend my thanks to Dr. Stanley Birch for suggesting to me that I should test a pylon very early on, and for his kind and encouraging words. I would like to thank Professor Dennis McLaughlin for his mentorship in Aeroacoustics. Special thanks are due to Professor Robert Liebeck for encouragement and guidance well beyond the call of duty. Thanks to M. Leroy Spearman for many kind words and for sharing his enthusiasm with me about aeronautics.

In addition, I am extremely thankful to all of the engineering professors and students who made life at UCI a unique experience. Their friendship and camaraderie provide energy and a competitive spirit that can inspire innovation in engineering. I am especially thankful to my committee members, Professors Feng Liu and William A. Sirignano, for their insight and special care with respect to reading my thesis.

Funding for this research effort from NASA Glenn Research Center, Grant NAG-3-2345, monitored by Dr. Khairul B. Zaman and Dr. James Bridges, and the NASA Graduate Student Researchers Program (GSRP) Fellowship, are gratefully acknowledged. The Mechanical and Aerospace Engineering Departmental Fellowship, sponsored by the Graduate Assistance in Areas of National Need (GAANN) program, is also gratefully acknowledged.

ABSTRACT OF THE THESIS

Noise Reduction and Flow Characteristics in Asymmetric Dual-Stream Jets

by Rebecca Suzanne Shupe

Master of Science in Mechanical and Aerospace Engineering

University of California, Irvine 2007

Professor Dimitri Papamoschou, Chair

THIS research effort is motivated by the advent of asymmetric nozzle concepts for directional suppression of jet noise from turbofan engines. The specific method addressed is the fan flow deflection (FFD) technique, whereby aerodynamic devices deflect downward the fan stream of the turbofan exhaust and thus create an asymmetry in the plume of the jet exiting an otherwise coaxial nozzle. The asymmetry reduces jet noise emissions in downward and sideward directions affecting airport communities. Flow field and acoustic measurements were conducted to understand what flow quantities are affected by the departure from symmetry and how their changes impact noise emission. The experiments were complemented by computations that included the effect of forward flight. It is found that FFD reduces the radial gradients of mean velocity, the turbulent kinetic energy, and the Reynolds stress on the underside of the jet. A preliminary correlation between downward velocity gradient and downward sound emission indicates that velocity gradient reduction is an important ingredient for noise suppression using FFD. Further, a correlation between the maximum radial gradient of the axial velocity component and peak turbulent kinetic energy was obtained.

In an additional related aspect of this work, the effect of baseline nozzle geometry on efficacy of methods that create jet asymmetry was studied. A phenomenological investigation between nozzles with parallel exit flow lines and converging exit flow lines was conducted. Jets with uniformly reduced radial gradients below the centerplane were found to be acoustically superior to jet plumes with focused or narrow gradient reduction.

Chapter 1

Introduction

1.1. Motivation

Today, a primary goal of the National Aeronautics and Space Administration's (NASA) Aeronautics Research Mission Directorate (AMRD) is the advancement of aviation technology that will enable the United States to maintain a distinctly preeminent role in industry. Aircraft noise emissions reduction has become a driving factor for competitive aircraft design, as political and environmental laws have become more firm. Additionally, takeoff noise reduction is a key challenge for developing future supersonic jetliners. After careful planning and testing, successful implementation of innovative jet noise reduction concepts in commercial turbofan engines and military aircraft engines may be achieved for reduction of jet noise at both supersonic and subsonic jet exhaust configurations.

The essence of this work arises from the need to improve the current understanding of turbulent mixing noise and noise suppression in asymmetric dual-stream jets. The closure problem of turbulence necessarily places limitations on noise predictions in jets using computational methods. Solutions for high Reynolds number jets using Direct Numerical

Simulations (DNS) will not be feasible in the foreseeable future. Computational methods such as Large Eddy Simulation (LES) and Reynolds Averaged Navier-Stokes (RANS) use models that are promising, but as of yet cannot be relied upon for accurately predicting noise emissions of dual-stream jets. As a consequence, applications involving turbulent flows remain heavily reliant on empirical data for predictions. The work herein is a first step in the aim to develop an empirical relation between key mean flow field parameters and reduction in peak overall sound pressure level (OASPL). This correlation is expected to improve computational predictions that will assist in the design of quiet aircraft engine nozzle configurations.

1.2. The Turbofan Engine

The turbofan engine is the most efficient propulsion system for aircraft traveling at high subsonic cruise speeds. Most commercial aircraft travel at a cruise Mach number of M = 0.85 (564 mph, 35,000 ft altitude) so the turbofan engine is widely used. The General Electric GE90 model, which is currently the world's most powerful engine and is used on the Boeing 777 airliner, is shown in Fig. 1.1. New composite material technologies have been incorporated into the design of this engine adding to its improved efficiency and power capabilities from previous models. The fan blades are made from composite material, carbon-fiber reinforced epoxy, and the engineering process was designed to make the material fibers completely free of defect, including wrinkles or voids.

A turbofan engine has all of the same internal components as a turbojet engine, but it is surrounded by a bypass duct. Figure 1.2 shows the main components. During subsonic

flight, the inlet section of the turbofan engine is designed to decrease the velocity of the air that is brought into the engine. A fan accelerates the air through the fan duct. The ratio of the mass of air that is routed through the bypass duct to the mass of air that is routed through the core during a fixed time period is called the bypass ratio. With increased bypass ratio, the engine becomes quieter and more efficient. Tradeoffs are drag due to an increased cross-sectional area and increased weight. A compressor increases the pressure of the air before it enters the combustion chamber. The air that passes through the core is mixed with fuel, and chemical energy is converted to useful work after the air-fuel mixture undergoes combustion in the burner. As the extremely hot gases leave the combustion chamber, they expand through the turbine, causing the shaft to spin. The fan and compressor are powered by the turbine shaft. The primary (core) jet exhaust is characterized by very high speeds and temperatures, while the secondary (bypass) stream has much lower speeds and is much cooler.

Turbofan engine noise consists of jet noise, fan noise, and core noise. Jet noise, the focus of this study, is dominant during takeoff and climb when high thrust is required. The fan noise component of engine noise is dominant on a landing approach when thrust is reduced. Other noise sources are rotary machinery internal to the core engine and pressure and temperature fluctuations inside the combustor. These sources lumped together with fan noise that is propagated internally to the core engine, are referred to as core noise. Figure 1.3 shows tone-corrected perceived noise level for jet noise relative to other aircraft noise sources on takeoff and on landing. To date, the two primary developments that have entered into service on commercial airliners to aid in reduction of engine noise are acoustic linings for engine nacelles and increased bypass ratio engines,

and the leading technology for jet noise reduction, currently under research and development, is chevron mixers, discussed in the next section.

1.3. Previous Works

Several emerging technologies for jet noise reduction in turbofan engines have demonstrated potential for improving the noise metric in air-breathing jet propulsion systems. Chevrons were recently tested as part of Boeing's Quiet Technology Demonstrator 2 (QTD 2) program for jet noise reduction. This test program was a collaborative effort between Boeing, General Electric, and NASA, among others, to validate new technologies for noise emissions reduction that will be used on next generation aircraft, Ref. 18. Chevrons on the core and fan nozzles were integrated with the GE90 engine and flight tests were conducted. Peak sound pressure level (SPL) measured on the ground during flyover was reduced by 2dB without increasing noise at higher frequencies. In a separate study, Ref. 19, five chevron and tab mixer configurations, for example Fig. 1.4, reduced jet noise by at least 2.5dB with no more than 0.5% thrust loss, with respect to the baseline nozzle. Both chevrons and tabs were more effective when placed on the core nozzle. Chevrons on the fan nozzle had the tendency to reduce thrust loss when used with core chevrons or tabs, while tabs on the fan nozzle had the tendency to increase thrust loss.

Integration of noise reduction technologies can be successful in achieving both noise reduction and enhancing engine performance. One elegant example of an integrative design concept is the bluebell nozzle, which includes chevrons and corrugations. A bluebell nozzle design has been shown to achieve a 4dB acoustic benefit with 1% thrust

augmentation at supersonic exhaust conditions when compared to its round converging-diverging baseline counterpart, Ref. 20.

As opposed to the traditional wing-mounted engine configuration, below the wing, a straight-forward noise reduction solution is an over-the-wing-mounted engine configuration. This results in a wing-shielding effect, inhibiting transmission of some of the engine noise to the ground. Tests conducted in the 1970's showed a 3dB reduction, with respect to the traditional configuration, even though the wing chord length was not large enough to cover the entire engine. A large aircraft would have the greatest potential in making use of a wing-shielding benefit because its longer chord would shield more of the noise sources. However, regions of intense turbulent mixing and noise production in the jet plume occur at about 5 fan diameters downstream of the fan exit plane for a bypass ratio 5 turbofan engine. It follows that a chord length of more than 12 m would be required to shield the dominant noise sources of the jet for a turbofan engine with a 2.4 m fan exit diameter. The Boeing 777 uses a mean aerodynamic chord length of 6.6 m.

The offset-stream concept addressed in this work uses a thick stream of low-speed air to virtually shield the noise sources in both flyover and sideline directions. Offset-stream jets, Refs.1-17, have shown significant potential for noise attenuation at both subsonic and supersonic exhaust conditions, on the order of 5dB reduction in peak overall sound pressure level (OASPL). The success of offset-stream technology for jet noise suppression was first demonstrated using an eccentric dual-stream jet configuration at the University of California, Irvine, Refs.1-3. In an eccentric configuration, the axis of the primary (inner) nozzle is offset with respect to the axis of the secondary (outer) nozzle. Significant noise reduction occurs in the direction of the thickened low-speed flow region

on the underside of the core jet, and also in the sideline directions. Figure 1.6 shows SPL reduction observed at UCI in the eccentric nozzle configuration with respect to a single and a coaxial jet. This noise reduction trend was confirmed in a larger facility at NASA Glenn Research Center, Ref. 3. In view of the drastic redesign of the engine nacelle that would be needed, an alternative technique was developed, called Fan Flow Deflection (FFD). The idea is to deflect the secondary airstream in the downward and sideward directions using airfoil-shaped vanes or wedge-shaped deflectors placed in the secondary flow path. Figure 1.5 shows the concept.

Two types of deflectors have been investigated so far: airfoil-shaped vanes, Refs. 4-13, mounted at various azimuth angles, and wedge-shaped deflectors, Refs. 14-17, mounted at the top of the nozzle. Both devices can be internal or external to the fan duct. Studies have shown that wedge-shaped deflectors, installed on a nozzle with convergent streamlines, have the potential to reduce jet mixing noise significantly, particularly in the direction of peak emission, for a range of azimuth angles without crossover at high polar angles, Fig. 1.7.

Recent works have predicted the aerodynamic performance of both vane, Ref. 16, and wedge-type deflectors (private communication Vance Dippold III). The thrust loss has been predicted to be on the order of 0.1%. An experimental investigation at the University of California, Irvine, measured the coefficient of pressure of the wedge-shaped deflector placed externally to the fan duct, Ref. 17. The unique aerodynamics of this configuration make it favorable to minimal thrust loss when it is deployed for noise suppression.

1.4. Program Objectives

At the University of California, Irvine, the jet aeroacoustics research group aims to study the flow field of asymmetric dual-stream jets, and its relation to noise suppression resulting from that symmetry. Novel concepts developed at the University of California, Irvine have demonstrated noise reduction of peak OASPL in the downward and sideline directions, across all frequencies in the downward direction. Consequently, it is desirable to correlate the noise suppression resulting from these methods with the asymmetry in the flow field characteristics of the dual-stream jets. The specific flow field characteristics are reduced velocity gradients, Reynolds stresses, and peak turbulent kinetic energy.

The objectives addressed in this thesis entail the assessment of mean and turbulent flow field characteristics that impact noise radiated to the far-field, and the development of an empirical model correlating asymmetry in the flow field with noise suppression. This model would enhance predictions for the design of acoustically superior engine nozzle configurations. The primary tools of the investigation, discussed in detail in subsequent chapters, encompass microphone noise measurements, mean and fluctuating velocity field surveys, and computational simulations. Central to this research effort is the analysis of the asymmetric dual-stream jet flow field characteristics including velocity gradients and inflectional layers, Reynolds stresses, and turbulent kinetic energy.

The main objectives and results of this research effort are outlined as follows:

- Understand the effect of the baseline nozzle shape on the mean flow characteristics of the jet and on the efficacy of fan flow deflectors (FFD) to suppress noise. This research effort was conducted at the University of California Irvine, and is the topic of Chapter 5.

- Obtain a preliminary correlation between radial velocity gradient and OASPL reduction, in the strictly downward direction, Chapter 5.
- Examine both the mean and turbulent flow fields of the nonaxisymmetric jets produced by wedge-shaped deflectors. This research effort was conducted at the NASA Glenn Research Center, and is the topic of Chapter 6.
- Obtain a correlation between reduction in maximum radial gradient of the axial velocity component and maximum turbulent kinetic energy, Chapter 6.
- Obtain computational flow field predictions using the Shear Stress Transport (SST) turbulence model, and Wind-US, a Reynolds-Averaged Navier-Stokes (RANS) solver. This research effort was conducted at the NASA Glenn Research Center, and is the topic of Chapter 7.

These steps help illustrate the link between the mean flow field and noise suppression in the asymmetric dual-stream jets. Developing a clear picture of the nature of the flow field characteristics will facilitate the ultimate goal of obtaining empirical relationships between far-field sound emissions reduction and altered flow field parameters in the jet plume with respect to the baseline jet. This will be important for designing an optimized system for noise reduction on the turbofan engine.

Figure 1.1. General Electric GE90 high bypass turbofan engine.
Source: http://academic.csuohio.edu/cact/jet engine.png

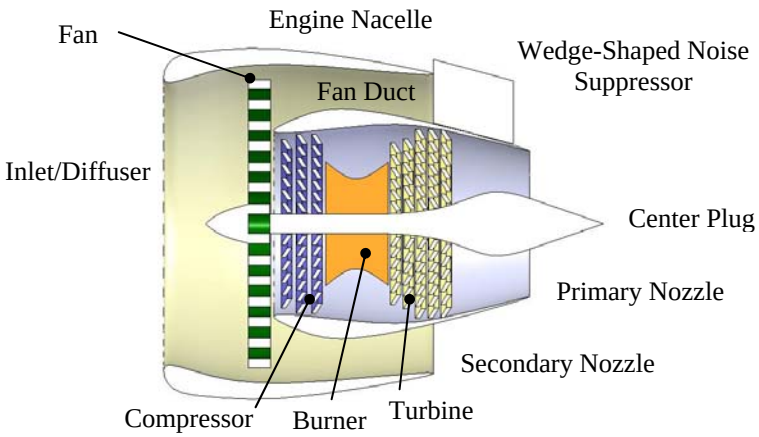

Figure 1.2. Illustration showing main components of a turbofan engine.

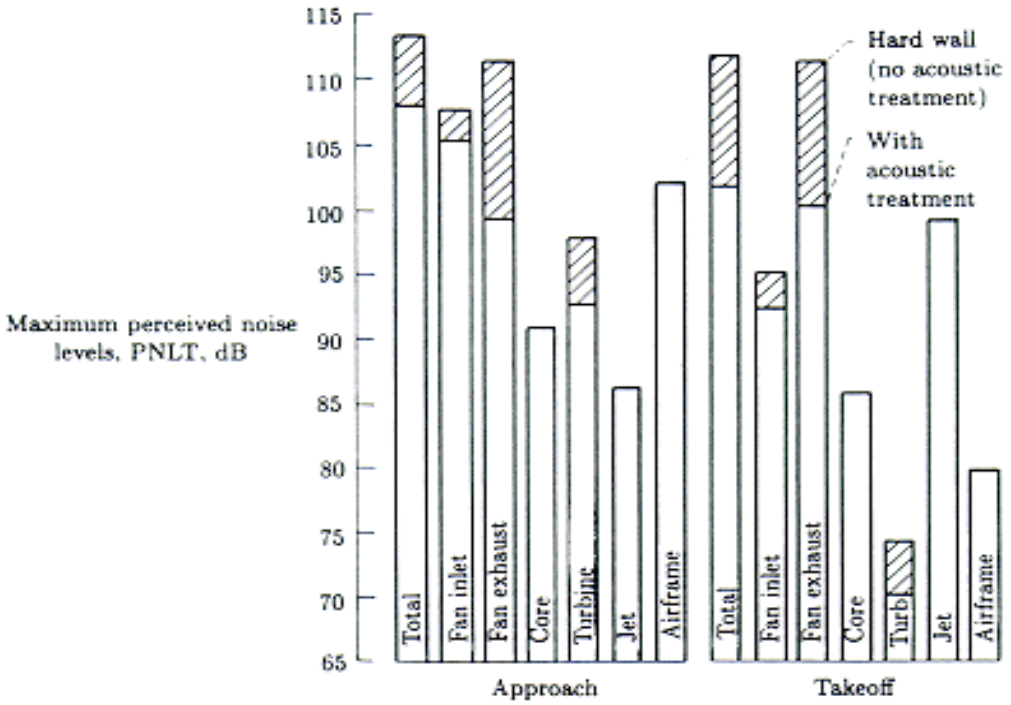

Figure 1.3. Bar graph distinctly showing relative components of aircraft noise for approach and takeoff. (From Ref. 79, Session I.1 Fig. 5)

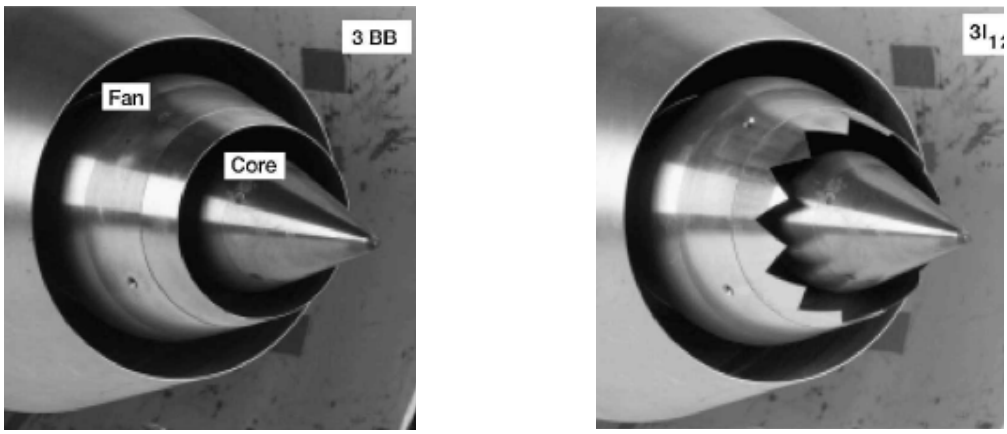

a) **b)**

Figure 1.4. Bypass ratio 5 a) baseline nozzle and b) with chevrons for mixing enhancement on primary (core) nozzle. (Ref.19, Figs. 3 and 6).

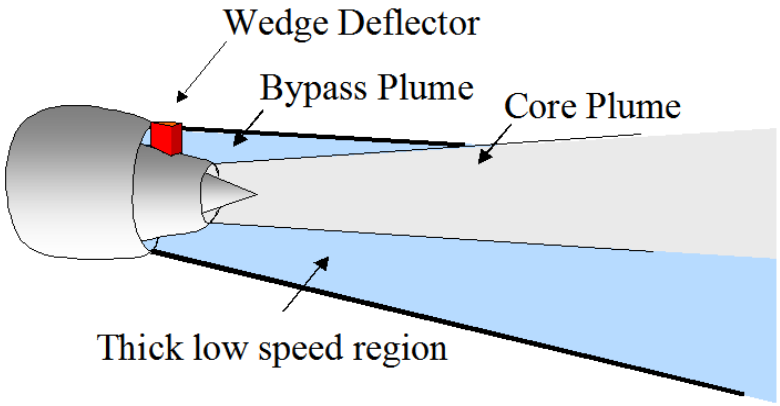

Figure 1.5. General concept of fan flow deflection (FFD). Mean velocity gradients are reduced on underside of jet.

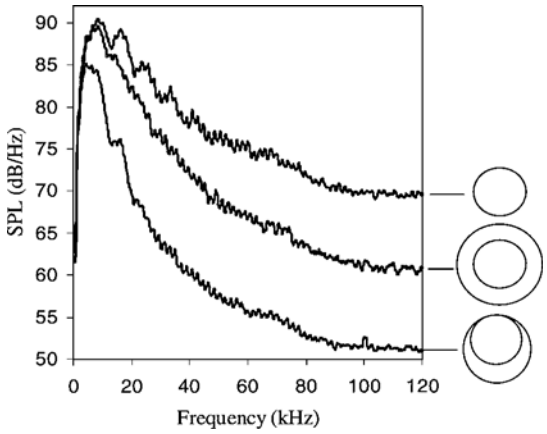

Figure 1.6. SPL reduction of a coaxial jet and eccentric jet with respect to a single jet. (From Ref. 8, Fig.1).

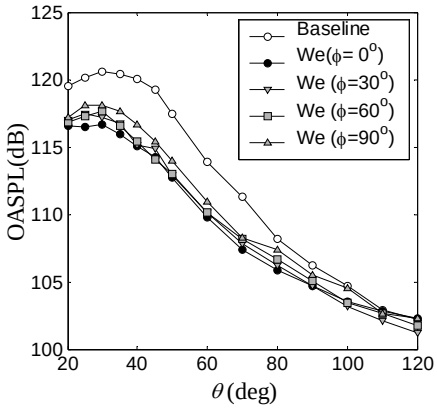

Figure 1.7. A wedge-shaped deflector achieves reduction with respect to a baseline jet with bypass ratio of 5. OASPL measured at several azimuthal and polar angles. (From Ref. 17, Fig.3).

Chapter 2

Background

The focus of this work is on improving the current understanding of the physical mechanism responsible for noise suppression in asymmetric subsonic and supersonic dual-stream jet configurations. The jets under discussion here are referred to as asymmetric because they have offset primary and secondary streams. The primary and secondary streams represent the core and bypass exhausts, respectively, of turbofan engines. Offset-stream nozzles include eccentric configurations and arrangements with deflection of the fan stream. These configurations alter the mean flow field of the jet plume, concentrating the low-speed fan flow underneath the core stream, thus reducing downward and sideward noise emissions with respect to the baseline coaxial jet.

2.1. Physical Elements of the Coaxial Jet

In this section, a literature review is provided, outlining some of the basic physical elements of axisymmetric coaxial dual-stream jets as they are relevant to jet noise emissions. In the initial region of the jet, a primary shear layer and a secondary shear layer exist, Fig. 2.1. The primary and secondary shear layers are formed between the

primary and secondary potential cores and between the secondary core and the ambient fluid surrounding the jet, respectively. In the potential cores, the fluid is irrotational, and the velocity is nearly uniform and equal to the nozzle exit velocities. The shear layers work to mix the two core streams of fluid. Because of the difference in velocity between the two streams, rotational motion is induced and turbulent eddies are formed in the shear layers. At the end of the secondary core, the primary and secondary shear layers merge, marking the beginning of the intermediate region of the jet, in Fig. 2.1. This is a very important noise generation region because the primary jet is left exposed to the ambient, and a single shear layer forms with a much higher velocity gradient than either of the two shear layers in the initial region. The merging of the two shear layers makes it a complex region to analyze. Analysis of the inflectional layers of the mean velocity is one way of studying this complex region. The significance of the inflectional loci will be discussed later in this chapter. Far downstream is the fully-developed region of the jet, characterized by large turbulent eddies that span the entire plume. This region of the jet is self-similar, and is characteristic of a single round jet, with Gaussian-like profiles, which collapse onto one another when nondimensionalized properly. References 33-36 present a wealth of experimental data from single and coaxial turbulent jets, both subsonic and supersonic.

The primary and secondary axisymmetric shear layers, in the initial region of the jet, are closely approximated by the turbulent planar shear layer, Fig. 2.2. Therefore, empirical relations for the growth rate of the turbulent planar shear layer provide good estimates for growth rates and potential core lengths in round jets. These are presented in the following sections for the axisymmetric dual-stream jets. The spatial growth rate of a

shear layer is, sometimes referred to as a spreading rate, is the change in thickness with position from a virtual origin, and it is constant for a fully developed, turbulent planar shear layer:

$$\delta' = \frac{d\delta}{dx} = const. \tag{2.1}$$

The growth rate will depend on the definition of thickness that is used. In the literature, three common definitions include the pitot thickness, vorticity thickness, and the visual thickness. One can predict the maximum radial gradient of the axial component of the mean velocity, using the definition of the vorticity thickness. In the next section, the convective Mach number is introduced. The convective Mach number of turbulent eddies in the jet shear layer adjacent to the ambient has a direct impact on the noise emissions of a dual-stream jet.

2.1.1 Convective Mach Number

The convective Mach number is best described as the Mach number felt by a disturbance (instability wave or turbulent eddy) as it convects downstream in the shear layer. The Mach number of the shear layer disturbance with respect to surrounding fluid is important for consideration of Mach wave emissions. It is measured in a frame of reference moving with the constant phase speed of the disturbance U_c. The definition is as follows:

$$M_{c1} = \frac{U_1 - U_c}{a_1}, \qquad M_{c2} = \frac{U_c - U_2}{a_2} \tag{2.2}$$

where the subscript 1 makes reference to the fast moving freestream and the subscript 2 makes reference to the slow moving freestream, Fig. 2.2.

The so-called “symmetric” convective Mach number was first determined by Bogdanoff, Ref. 21, and later by Papamoschou and Roshko, Refs. 22-23, by assuming that the flow is brought to rest isentropically at a stagnation point between the large-scale turbulent structures in the shear layer. There must be equality of pressure to maintain a stable stagnation point, and the total pressures in the convective frame are assumed to be equal on either side of the shear layer.

$$p_{01c} = p_{02c}$$

$$p_1\left(1+\frac{\gamma_1-1}{2}M_{c1}{}^2\right)^{\frac{\gamma_1}{\gamma_1-1}} = p_2\left(1+\frac{\gamma_2-1}{2}M_{c2}{}^2\right)^{\frac{\gamma_2}{\gamma_2-1}}$$

For $\gamma_1 = \gamma_2$, it follows that $M_{c1} = M_{c2}$, since the static pressure is balanced on either side of the shear layer. The Mach number of either stream, called the symmetric convective Mach number is

$$M_{csym} = \frac{U_1 - U_2}{a_1 + a_2} \tag{2.3}$$

At high compressibility, the convective Mach number cannot be assumed symmetric due to entropy generation.

The convective Mach number is very important for noise emissions considerations, because it is an indicator of the amount of energy that can be radiated to the acoustic far-field. An analytical treatment is provided in Ref. 4 that yields insight into the physics relevant to noise emissions reduction and it is summarized here. Using a parallel flow approximation, the solution to the Rayleigh equation yields disturbances that amplify for wavenumbers below a neutral value and decay for wavenumbers above the neutral value. The growth or decay is exponential. Accounting for non-parallel, spatially-growing

mean flow, an initially-amplifying disturbance will saturate and decay with axial distance. This can be expressed as a wave-packet $\eta(x,t)$ with amplitude modulation function $A(x)$ of arbitrary units in length, Fig. 2.3. To simplify the analysis, a disturbance with wave number of unity is considered. The disturbance is expressed as follows

$$\eta(x,t) = \hat{A}(x)e^{i(x-U_c t)} \tag{2.4}$$

where U_c is the convective speed of the instability wave. Assuming the Fourier transform exists for the amplitude modulation function, $A(x)$, it can be written as a continuous spectrum of cosines and sines by taking the inverse Fourier transform

$$A(x) = \frac{1}{2\pi}\int_{-\infty}^{\infty} \hat{A}(k)e^{ikx}dk \tag{2.5}$$

The wave packet can be expressed in Fourier space as

$$\eta(x,t) = \frac{1}{2\pi}\int_{-\infty}^{\infty} \hat{A}(k)e^{i[(k+1)x-U_c t]}dk$$

and equivalently,

$$\eta(x,t) = \frac{1}{2\pi}\int_{-\infty}^{\infty} \hat{A}(k-1)e^{ik\left[x-\frac{U_c}{k}t\right]}dk \tag{2.6}$$

Since this result can be thought of as a continuous spectrum of waves with individual phase-amplitudes $\hat{A}(k\text{-}1)/2\pi$, dimensionless phase-speeds U_c/k, and dimensionless phase-Mach numbers (recall a disturbance with a wavenumber of unity is assumed) $m_c = U_c/ka = M_c/k$, it follows that Mach wave emissions occur for the portion of the spectrum with phase-speed greater than the speed of sound, Fig. 2.4. One can see that even if M_c is subsonic there is a portion of the spectrum with supersonic phase-Mach numbers. By reducing M_c, less energy will be radiated to the far-field as noise. Refer to Liepmann and Roshko, Ref. 77, for a treatment of small perturbation theory and flow past a wave-

shaped wall. With this in mind, an aeroacoustician can reduce the convective speed of the turbulent eddies in the dominant noise source region, near the end of the primary potential core in a dual-stream jet, thereby reducing acoustic radiation to the far-field.

2.1.2 Density vs. Compressibility Effects

Before the growth rate of a compressible turbulent shear layer had been shown to correlate well with the convective Mach number, it was well known that the spreading rate of the axisymmetric shear layer in a compressible jet was much less than that in an incompressible jet. However, the difference had been popularly attributed to density effects. The experiments by Brown and Roshko, Ref. 24, showed that the effect of density on the growth rate for an incompressible shear layer was much smaller than that which was observed in the compressible case. Growth rate reduction of only about 20% was observed for large density differences. This could not explain the 80% reduction of growth rate observed in compressible shear layers, Fig. 2.5.

Papamoschou and Roshko, Refs. 22 - 23, showed that the convective Mach number could be used to isolate the effect of compressibility on shear layer growth rate from the effect of density and velocity difference. Using this parameter, and normalizing by the corresponding incompressible value, the growth rate data collapsed onto a single curve, Fig. 2.6. Thus, it was shown that the convective Mach number could universally correlate the growth rate data of the compressible turbulent shear layer nondimensionalized by its incompressible counterpart. With increasing compressibility, the growth rate decreases significantly. Past a convective Mach number of about 1.0, the growth rate does not continue to decrease, but levels off to a constant value, about 20% of the corresponding

incompressible value. The same general trend has been observed in several instability analyses, Refs. 25 - 32.

The data presented in Fig. 2.6 suggest the relation between shear layer growth rate and convective Mach number could be given by

$$\delta'(r,s,M_c) = \delta'_{inc}(r,s) \cdot f(M_c) \tag{2.7}$$

where the relation for the incompressible growth rate is

$$\delta'_{inc}(r,s) = C\frac{(1-r)(1+\sqrt{s})}{1+r\sqrt{s}} \tag{2.8}$$

and is due to Brown and Roshko, Ref. 24. C is a constant that depends on the definition of growth rate that is used. Using C = 0.16 for the vorticity thickness growth rate constant, Eqs. 2.8 and 2.9 provide an accurate estimate of the maximum radial gradient of the axial component of the mean velocity for the incompressible coaxial jet shear layers presented in this work. The vorticity thickness

$$\delta_\omega = \frac{1}{\Delta U} \cdot \left(\partial U \big/ \partial y_{\max} \right), \tag{2.9}$$

is defined as the maximum velocity gradient divided by the difference in velocities of the two streams. C = 0.14 is used for the growth rate of the pitot thickness, which has been defined as the width of the pitot pressure profile from 5% to 95% of the difference in the freestream values, Refs.22-23. The velocity and density ratios are defined as $r = U_2/U_1$ and $s = \rho_2/\rho_1$ respectively, where the subscript 1 refers to the fast moving stream and the subscript 2 refers to the slow moving stream.

A good curve fit to the data, suggested by Murakami and Papamoschou, Ref. 8, is

$$f(M_c) = 0.23 + 0.77e^{-3.5M_c^2} \tag{2.10}$$

also shown in Fig. 2.6. The fit provides an empirical estimate of good quality for the shear layer thickness growth rate as a function of the symmetric convective Mach number in Eq. 2.3. In the next section it is used to estimate the potential core lengths of a coaxial jet.

2.1.3 Mean Flow Model for Compressible Dual-Stream Jets

The convective Mach number is an important compressibility effect parameter, and is useful for developing empirical models for mean flow in compressible jets. In the work by Murakami and Papamoschou, Ref. 8, an empirical model is developed that enables accurate prediction of the primary and secondary potential core lengths in dual-stream compressible jets.

For a single jet, the potential core length scales with the inverse of the growth rate.

$$L_p = D \cdot \left(\frac{d\delta}{dx} \right)^{-1} \tag{2.11}$$

The limits of a single jet and an infinitely coflowing jet are considered, see Fig.2.7, and the primary potential core length of the coaxial jet with finite annular gap thickness is considered to lie within the two limits.

Making use of Eq. 2.10, empirical models for the potential core lengths of the single jet and of the coflowing jet are formed.

$$\frac{L_{\text{p single}}}{D} = \frac{1}{\delta'_{\text{single}}} = \left\{ 0.14(1+\sqrt{s}) \left[0.23 + 0.77 e^{-3.5 M_c^2} \right] \right\}^{-1}$$

$$\frac{L_{\text{p coflowing}}}{D} = \frac{1}{\delta'_{coflowing}} = \left\{ 0.14 \frac{(1-r)(1+\sqrt{s})}{(1+r\sqrt{s})} \left[0.23 + 0.77 e^{-3.5 M_c^2} \right] \right\}$$

A model is developed for L_p in the coaxial jet based on the limiting cases.

$$L_p = L_{\text{single}} + f\left(\beta \frac{L_s}{L_{\text{coflowing}}}\right)\left(L_{\text{coflowing}} - L_{\text{single}}\right)$$

The physical expectation is that f approaches the limits $f(0) \to 0$ and $f(\beta) \to 1$ asymptotically. This is satisfied by using a hyperbolic tangent profile for *f*.

$$\frac{L_p}{L_{\text{single}}} = 1 + \tanh\left(\beta \frac{L_s}{L_{\text{coflowing}}}\right)\left(\frac{L_{\text{coflowing}} - L_{\text{single}}}{L_{\text{single}}}\right) \tag{2.12}$$

In Eq. 2.12, β = 2.8, and the length of the secondary potential core L_s is taken to be proportional to the inverse of the average of the inner and outer shear layer growth rates, resulting in the following expression for L_s/D_p.

$$\frac{L_s}{D_p} = \alpha \frac{H}{D_p}\left(\frac{L_{\text{coflowing}} / D_p}{\delta'_s \, L_{\text{coflowing}} / D_p + 1}\right) \tag{2.13}$$

The constant of proportionality in Eq. 2.13 is α = 2.8, and δ'_s is found using Eq. 2.10. The empirical model outlined above results in very accurate predictions of the primary and secondary core lengths when compared with experimental data, within 5% for the secondary core and 8% for the primary core. The model enables one to make an estimate of the volume of the noise source regions in an axisymmetric dual-stream jet, given the operating conditions: the velocity ratio *r*, the density ratio *s*, the annular gap width *H*, and the symmetric convective Mach number M_c, for the shear layers developing between the primary and secondary streams and also between the secondary and ambient streams.

2.2 Asymmetric Dual-Stream Jets

The working principle of the Fan Flow Deflection (FFD) method is reduction of the convective Mach number of turbulent eddies that generate intense downward and

sideward sound radiation. In a coaxial separate-flow turbofan engine, this is achieved by tilting in the general downward direction, by a few degrees, the secondary (bypass) plume relative to the primary (core) plume. Tilting of the secondary stream is possible by means of fixed or variable deflectors installed near the exit of the fan duct. Figure 1.5 depicts the general concept. The wedge increases the volume of low speed flow between the end of the generalized secondary core and the end of the primary potential core. This can be thought of as effectively increasing the annular gap thickness on the underside of the jet to target the dominant noise source region.

Mean flow surveys have shown that the misalignment of the two flows results in reduction of the mean velocity gradients on the underside of the high-speed primary flow, especially in the region near the end of the primary potential core which contains the dominant noise sources. In addition to the reduction of mean velocity gradients at the end of the primary potential core, an elongated generalized secondary core (GSC) on the underside of the high-speed primary jet has been noted, Fig. 2.8. The secondary core reduces the convective Mach number of the primary eddies, thus hindering their ability to generate sound that travels to the downward acoustic far field.

One can estimate the distributions of convective Mach numbers of primary and secondary eddies. One of the challenging aspects here is determining the velocity along the inflection point defining the lower edge of the primary shear layer, $u_s(x)$. See Fig. 2.8. Measurements were performed by Papamoschou, Ref. 7. The following definitions

$$M_{cp} = \frac{U_{cp}(x) - u_s(x)}{a_s(x)}, \qquad M_{cs} = \frac{U_{cs}(x) - U_\infty}{a_\infty} \tag{2.14}$$

were used together with the Crocco-Busemann relation, to plot the convective Mach number distributions of the primary and secondary eddies. A more balanced distribution

between the convective Mach numbers of the primary and secondary eddies (i.e., the average of both primary and secondary eddy convective Mach numbers was lower for the duration of their existence) was achieved using deflectors placed in the secondary flow than by using eccentric nozzles. Analysis of experimental data collected from mean flow surveys in the asymmetric dual-stream jets showed that by displacing some of the slow moving fluid of the secondary stream from above the primary jet to the sides and underneath the primary jet, the GSC was elongated underneath the jet and the primary potential core was shortened. So, the longer the GSC, the more effective the asymmetric configuration is in reducing the convective Mach number of the eddies in the primary shear layer, and hence, in reducing noise emissions.

Figure 2.8 shows the important flow-field parameters as described in Ref. 7. The length of the generalized secondary core (GSC) is determined by the loop formed between the loci of inflection points of the transverse mean velocity profiles. Past the end of the GSC, only one inflection point remains, and it persists into the far-field of the jet. After the end of the GSC, the maximum gradient of the mean velocity profile exists along this locus of inflection points, i_1. As we shall see, the maximum radial gradient of the mean velocity is an important parameter for noise considerations. For a coaxial jet, the length of the GSC is approximately the same as the length of the secondary potential core. For an asymmetric jet, the GSC underneath the primary jet is elongated and above the primary jet it is shortened with respect to the coaxial jet.

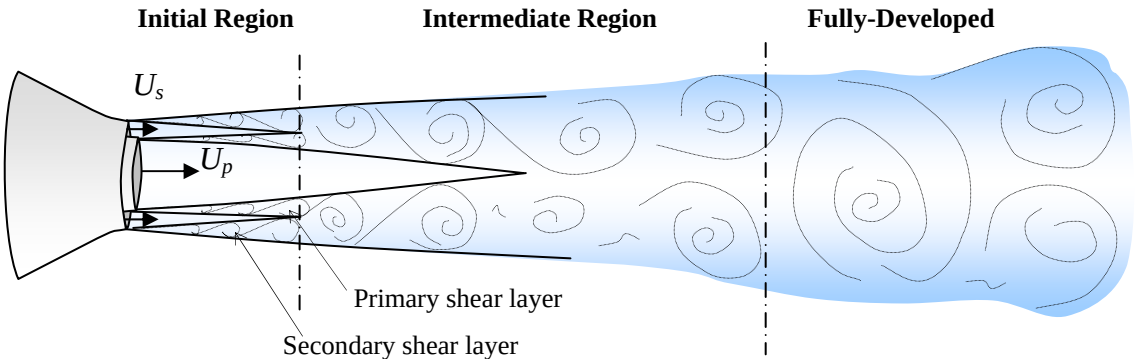

Figure 2.1. Illustration of primary potential core and secondary potential core in a dual-stream jet.

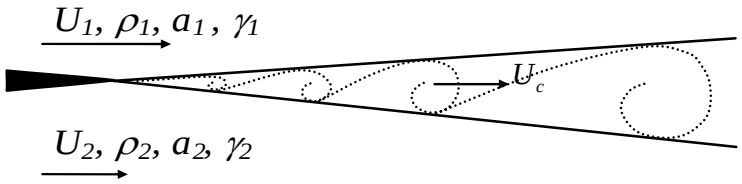

Figure 2.2. The compressible turbulent shear layer formed between two gases.

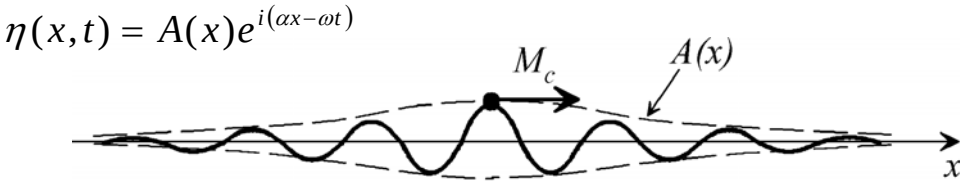

Figure 2.3. The Mach number as measured in the frame of reference of the disturbance is called the convective Mach number. The growth-decay nature of the disturbance (wave-packet) is described by an amplitude modulation function *A(x)*. (From Ref. 4, Fig.1)

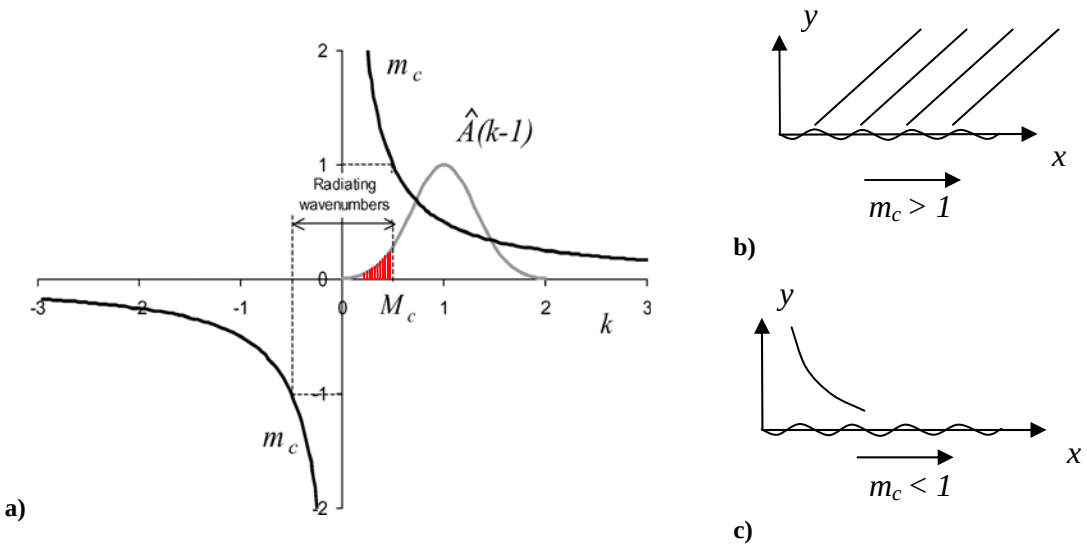

Figure 2.4. a) Illustrates the idea that there exists a spectrum of phase-speeds (From Ref. 4, Fig. 1) b) Those that convect supersonically will have solutions that radiate c) while those that convect subsonically decay.

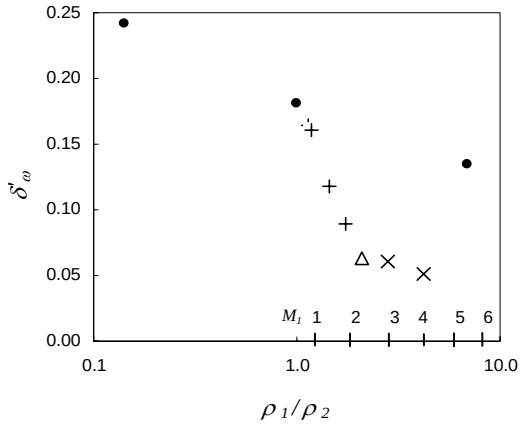

Figure 2.5. Solid circles – growth rate data for incompressible shear layer by Brown and Roshko. Other symbols – growth rate data for compressible shear layers for several investigators as compiled by Brown and Roshko. Maximum vorticity growth rate is used. (From Ref. 24, Fig. 15).

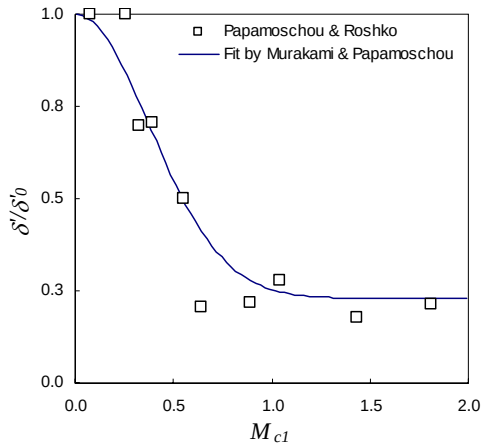

Figure 2.6. Pitot thickness growth rate data vs. convective Mach number (From Ref. 21, Fig. 5.3) and curve fit suggested by Murakami & Papamoschou (From Ref. 8).

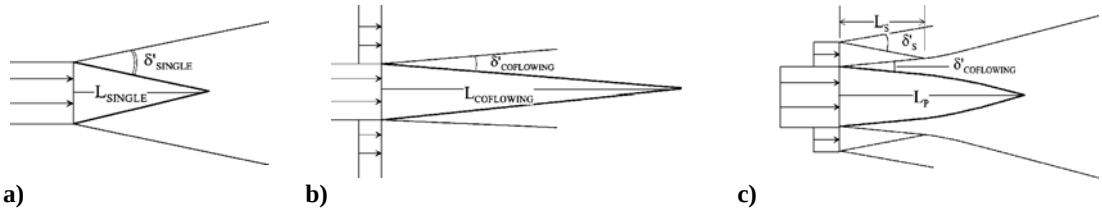

Figure 2.7. Potential core length model for a) a single jet b) the single jet with infinite coflow and c) the dual-stream jet, Murakami & Papamoschou. (From Ref. 8, Fig. 9)

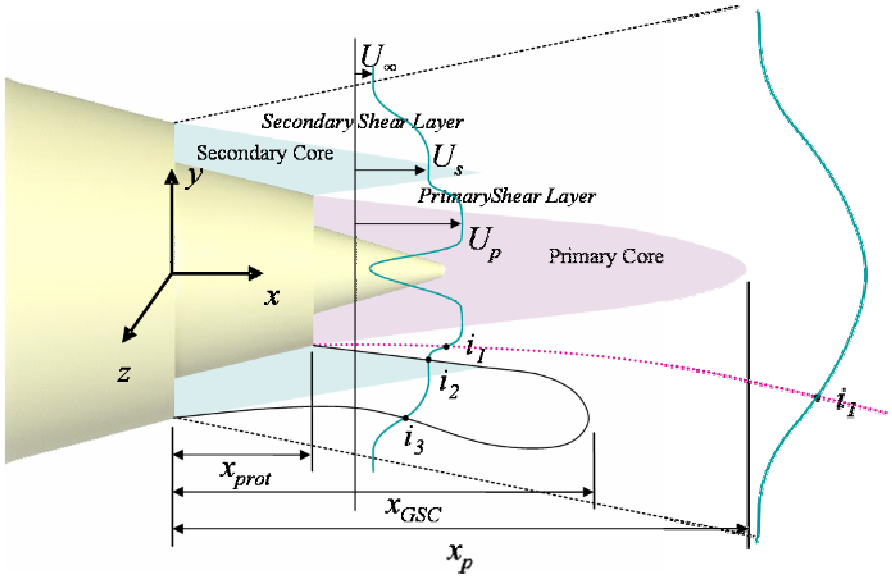

Figure 2.8. Primary potential core length, x_p, generalized secondary core (GSC) length, x_{GSC}, and protrusion of inner nozzle, x_{prot}. The maximum gradient of the mean velocity profile lies along the first locus of inflection points, i_1.

Chapter 3

Experimental Program

The experimental program was part of a collaborative investigation between the University of California Irvine (UCI) and NASA Glenn Research Center (GRC), aiming toward the development and implementation of technology for noise suppression in turbofan engines. The research objectives necessitated an experimental program that encompassed noise and flow-field surveys of asymmetric dual-stream jets. Pitot-rake experiments were conducted in the UCI Jet Aeroacoustics Laboratory, and hot-wire experiments were conducted in the GRC Engine Research Building CW-17 Free Jet Facility. The advantages of utilizing the NASA facility include the ability to resolve the fluctuating velocity field and the opportunity to confirm trends observed at UCI in a larger facility.

3.1 University of California, Irvine

The Jet Aeroacoustics Laboratory at the University of California Irvine has limited flow capacity, and its facilities are suitable for conducting investigations of noise emissions from small-scale models of turbofan engine nozzles. The nozzles used are $1/64^{th}$ of the actual size. The experiments are run at room temperature, and realistic

exhaust conditions are simulated by using helium-air mixtures for the microphone noise measurements. Mean velocity measurements are conducted using a Pitot-probe rake to investigate the relationship between noise and flow field of the jets. The details of the noise and flow measurements are provided here, and data analysis is in the next chapter.

3.1.1 UCI Nozzles

The UCI experiments (explained in Chapter 5) used two dual-stream nozzles, one with rapidly converging exit streamlines, and one with nearly parallel exit streamlines, Fig. 3.1. At nominal exhaust conditions both nozzles have a bypass ratio of approximately 5. The motivation for this study was Ref. 14, in which minimal noise reduction was observed when a wedge-shaped deflector was placed on a nozzle with parallel exit flow lines at NASA Glenn Research Center, while at the same time, dramatic noise reductions were being observed at UCI when the same type of deflector was placed on a nozzle with converging streamlines. The UCI classic nozzle was selected because at nominal exhaust conditions it has approximately the same bypass ratio as the UCI 3BB nozzle. The two nozzles are described below. Both nozzles were made from epoxy resin using rapid-prototyping methods. The nozzles were epoxied to a threaded aluminum pipe fitting, shown in Fig. 3.2, taking care to keep the axes aligned.

The nozzle with parallel exit streamlines is called the UCI ‘Classic’ nozzle. This nozzle is used in two configurations. One is in a coplanar arrangement where the exit of the core nozzle is aligned with the exit of the fan nozzle. The second arrangement of the UCI ‘Classic’ nozzle has an inner nozzle protrusion of 9.5-mm. The nozzle had been used

in past UCI experiments, before coordinates for realistic turbofan engine nozzles were obtained, this is why it is referred to as the UCI 'Classic' nozzle.

The nozzle with convergent exit flow lines and a geometry that is representative of actual separate-flow turbofan engines is referred to as the UCI '3BB' nozzle throughout the thesis. The nozzle was named '3BB' because it was the third nozzle on the separate-flow test program in the Aeroacoustic Propulsion Laboratory (AAPL) at NASA Glenn Research Center, Ref. 37. The positions of the letters denote the configuration for the core and fan nozzles, repsectively. 'B' means baseline. At UCI, the nozzle used is a scaled-down version of the baseline separate-flow nozzle used on the Nozzle Acoustic Test Rig (NATR). The coordinates of the NATR nozzle were divided by a factor of eight to fit within the flow capacity of the UCI lab.

The nozzle assemblies includes three elements: secondary (fan) nozzle, primary (core) nozzle, and center plug, Fig. 3.2b. Figures 3.1 and 3.2 show 3D views generated from the stereolithography files for the nozzles. Figure 3.3 shows the radial coordinates of the nozzles. Figure 3.4 shows a photograph of the nozzles with one pair of vanes installed. Tables 3.1 and 3.2 list the nozzle exit conditions. The reader is referred to Ref. 10, for further details of the UCI '3BB' nozzle.

3.1.2 UCI Deflectors

The purpose of the airfoil-shaped vanes and wedge-shaped deflectors is to create asymmetry in a dual-stream jet by imparting an aerodynamic force on the secondary fluid, thereby diverting some of the secondary flow to the side and underneath the high-speed primary jet. The deflector force creating the asymmetry, or deflector "turning

effort," is quantitatively defined in Chapter 5. The asymmetry that results is in the form of a thickened low speed fluid in the hemicylinder underneath the jet centerplane, targeting the dominant noise sources near the end of the primary potential core. Figure 1.5 shows the concept.

All vanes were constructed by hand from strips of 0.35-mm thickness brass sheet metal, cut to the desired chord width. The metal was folded at an angle so that there was no sweepback upon installation, Fig. 3.5.a. The bending angle θ was equal to the surface angle of the nozzle with respect to the centerline. Each vane in a pair was made to be a mirror image of the other. Using the outer nozzle as a guide, the length of the vanes were determined such that the vanes were full span upon installation. The leading edge was generally about 1-mm longer in span than the trailing edge for the '3BB' nozzle vanes. The difference in leading edge and trailing edge span was less than 1-mm for the 'Classic' nozzle vanes because of the difference in the fan duct geometries. The base of each vane was about 3-mm by 3-mm and was given slight curvature so that it could be firmly attached to the nozzle surface, Fig. 3.5.b. Smooth electric tape (the thickness of the electric tape was 0.18-mm) was used to give curvature to the leading edge of the vane. Starting with a clean, smooth nozzle, the azimuth angles were measured from the ground position; to assist with this, guide lines were drawn using pencil. The angle of attack was carefully measured using specialized tooling developed specifically for the construction of the vanes, and accuracy is estimated to within ±1° If the vanes were reused, they were cleaned using acetone before installation, new tape was applied, and the vanes were squared to ensure that camber, dihedral, or twist were not present. Using a drop of super glue, the base of the vane was attached to the inner nozzle, at the desired trailing edge

position. The vanes were then examined under a magnifying lens to check symmetry, and finally, the nozzle assembly, Fig. 3.2, was attached to the dual-stream apparatus, described in the next section.

The wedge-shaped deflectors were cut out of 4.5-mm thick nylon sheet. The nylon sheet was taken from flexible hosing, so it had curvature. This facilitated attachment of the deflector to the nozzle. The same means are used to determine the half angle of the wedge, as was used for the vane angle of attack. The sidewalls of the wedge were vertical, and height of the wedge was approximately the same as the annular gap width of the nozzle. The accuracy in cutting the wedge side length is estimated to be ± 0.5-mm.

For details of the aerodynamic forces of the deflectors, and how the forces differ depending on which nozzle is used, and depending on choice of deflector leading edge position, the reader is referred to Chapter 5.

3.1.3 UCI Noise Measurements

For acoustic simulation of hot jets, the nozzles were attached to the dual-stream apparatus, shown in Fig. 3.6.a, and cold mixtures of helium and air are supplied to the primary and secondary nozzles. Helium-air mixtures have been shown to simulate reasonably well the acoustics of hot jets, Refs. 40-41. The exit flow conditions, listed in Tables 3.1 and 3.2, matched the typical exit conditions of a turbofan engine with bypass ratio 4.8 at takeoff setting. The Reynolds number of the jet, based on fan diameter, was 0.6×10^6. For more information on the helium-air mixture matching method, the reader is referred to Refs. 40 and 41.

The microphone phased array consists of eight 3.2-mm condenser microphones (Bruel & Kjaer, Model 4138) arranged on a circular arc centered at the vicinity of the nozzle exit. The polar aperture of the array is 30º and the array radius was 1m. The angular spacing of the microphones is logarithmic. The entire array structure is rotated around its center to place the array at the desired polar angle. Positioning of the array is done remotely using a stepper motor. An electronic inclinometer displays the position of first microphone. The arrangement of the microphones inside the anechoic chamber, and the principal electronic components, are shown in Fig. 3.8. A photograph is shown in Fig. 3.9. The microphones were connected, in groups of four, to two amplifier/signal conditioners (Bruel & Kjaer, Model 4138) with low-pass filter set at 300 Hz and high-pass filter set at 100 kHz. The four-channel output of each amplifier was sampled at 250 kHz per channel by a multi-function data acquisition board (National Instruments PCI-6070E). Two such boards, one for each amplifier, were installed in a Pentium 4 personal computer. National Instruments LabView software was used to acquire the signals. Even though the array provides noise source location maps, in this study it was used only to survey the far-field sound emitted by the jets. Only the downward azimuthal direction was surveyed. The sound pressure level spectrum was corrected for actuator response, free-field correction, and atmospheric absorption. The overall sound pressure level (OASPL) was obtained by integrating the corrected spectrum. All acoustic data are referenced to a distance of $100D_f$ from the nozzle exit. For more details on the array setup, the reader is referred to Ref. 42.

3.1.4 UCI Velocity Measurements

Pitot-pressure measurements were conducted and the mean velocity was calculated using the equations presented in Chapter 4. The nozzles were attached to the dual-stream apparatus, shown in Fig. 3.6.a. Compressed air was supplied to both the primary (core) and secondary (fan) nozzles at room temperature. Velocity measurements cannot be obtained using helium-air mixtures, because the concentration, and therefore the gas constant would be unknown, Ref. 40. Since cold air is used to feed both streams, this means that only the velocity ratio or the Mach number ratio at the jet exit can be matched to a realistic turbofan exhaust. The velocity ratio was chosen to preserve some of the important physics, and therefore the trends are also expected to be preserved. The exhaust conditions are listed in Tables 3.1 and 3.2. The Reynolds number of the jet, based on fan diameter, was 0.9×10^6. Even though the velocities were lower than those of a realistic turbofan exhaust, which was used in the acoustic tests, the trends of some of the essential flow characteristics were expected to be preserved. The velocity ratio used was 0.7, representative of the exhaust velocity ratio in turbofan engines, and it matched the velocity ratio used in the acoustics tests.

A Pitot-probe rake, shown in Fig. 3.6.b and in Fig. 3.7, was used to survey the total pressure in the jet plume. The rake consisted of five stainless steel tubes, each 70-mm long, supported by a streamlined fitting. The tubes were mounted 10-mm apart and their inner diameter is 1.0-mm, limiting the spatial resolution to 1.0-mm. The motion in the y-direction was automated and the positioning in the x- and z-directions was manual. 11,000 data points are collected in the y-direction over a distance of $4D_f$. In the x-direction, 25 data points were regularly spaced at intervals $0.42D_f$ apart. For each axial

station, the rake traversed the plume in the y-direction a total of four times. Each time, the rake was moved by a z-increment of 2.5-mm, i.e., one fourth of the probe spacing. This resulted in 20 z-locations being surveyed for each axial position. The spatial resolution was 2.5-mm in z and 1.0-mm in y.

The second probe from the top is the reference probe, and it is initially positioned at the tip of the plug. The negative y-direction defines the direction of the ground (ϕ=0^o). The five probes of the rake were connected individually to five pressure transducers (Setra Model 207). The transducers were mounted on the traverse assembly in order to minimize the length of the tubing between each probe and transducer. This arrangement allowed the response time of the probe-transducer system to be low enough to resolve the steep gradients near the nozzle exit. The typical carriage speed was 10mm/s, and the transducers were sampled each at 1000 samples per second by a National Instruments analog-to-digital data acquisition board.

Mach number and velocity were computed from the total pressure measurements assuming constant total temperature, equal to the ambient temperature, and uniform static pressure, described in Chapter 4. Symmetry of the velocity field was assumed about the plane z=0. Therefore, the region $z\geq 0$ and a small portion of the region $z<0$ were resolved. Velocity data from the latter region were used to determine the true plane of symmetry of u, which may differ slightly from the geometric plane z=0. The true plane of symmetry was then used in mirror-imaging the velocity data.

3.2 NASA John H. Glenn Research Center (GRC)

In a complementary study to the UCI mean velocity measurements, hot-wire velocity measurements were conducted in the CW-17 Free Jet Facility at NASA Glenn Research Center to acquire the mean and RMS velocity fields using wedge-shaped deflectors. Due to the stringent safety permits required to run at high pressures, only very low pressures were approved, about one psig, at the time the experiments were performed. Therefore the experiments were run at very low Mach number; the primary exit Mach number was 0.18, and the secondary Mach number was 0.13. The secondary-to-primary velocity ratio of 0.7. Mean and turbulent flow-field surveys were acquired. Full pressure capabilities (and therefore Mach number) were not restored to the facility upon completion of the thesis, and noise measurements were not obtained. Details of the experiments are provided in the sections that follow. Data analysis is provided in Chapter 4.

3.2.1 GRC Nozzle and Deflectors

It is practical to test replica aircraft engine nozzles that are also being tested by NASA and industry with the aim of implementing them on efficient airliners. The bypass ratio 8 nozzle used at GRC was selected because it is representative of next generation high bypass ratio turbofan engine nozzles. This nozzle, like the ‘3BB’ nozzle, has converging exit geometry, and is referred to as the GRC ‘5BB’ nozzle throughout this document. It was named ‘5BB’ because it was the fifth nozzle on the separate-flow test program in the Aeroacoustic Propulsion Laboratory (AAPL) at NASA Glenn Research Center, Ref. 37. The positions of the letters denote the configuration for the core and fan nozzles, repsectively. ‘B’ means baseline. In the GRC CW-17 Open Jet Facility, the nozzle used

was a scaled-down version of the baseline separate-flow nozzle used on the Nozzle Acoustic Test Rig (NATR). The coordinates of the NATR nozzle were divided by 4.67. The Reynolds number of the jet, based on fan diameter, was 0.2×10^6. Figure 3.10 shows a photograph of the GRC '5BB' Nozzle. Figure 3.11 shows the nominal radial coordinates of the GRC '5BB' nozzle. Table 3.3 lists the actual nozzle exit conditions. The nominal bypass ratio is 8 when operated at realistic engine conditions. Ref. 12 also uses this nozzle.

The alignment of the hot-wire probes and the jet axis was verified by taking mean *y*- and *z*- velocity profiles at the nozzle exit and at a location far downstream of the nozzle exit, $20D_f$. The alignment of the profiles provided information about how well aligned the entire setup was. By measuring the shift of the location of the peak velocity, it was determined that the probe was off-axis by about a tenth of a degree. The nozzle axisymmetry was determined as precisely as possible by measuring the width of the secondary annulus using a hole diameter gauge. It was possible to match the annular gap width to within 0.005" of the values measured at three points around the nozzle. The nozzle was left in place between baseline and external wedge experiments. The outer nozzle was necessarily removed for installation of the internal wedges.

Several wedge deflector configurations and a pylon with an external half wedge on either side were tested. Since the geometry of the internal pylon structure is likely to have an impact on turbulent-mixing noise, internal wedge configurations were also examined with the GRC '5BB' nozzle. The wedges were fabricated from DuraForm® EX Plastic and attached using epoxy. Photographs of the wedges and pylon with flaps are in Fig.

3.12. Further details of the wedge-shaped deflectors and pylon configuration design are provided in Chapter 6.

3.2.2 GRC Velocity Measurements

Hot-wire experiments were conducted in the CW-17 Open Jet Facility open jet facility at NASA Glenn Research Center, Fig. 3.13. The primary plenum chamber has a 0.76m. diameter. Dual-stream coannular flow is achieved via a secondary plenum chamber located just upstream of the nozzles. The secondary annular flow, supplied by four equally spaced ports, is routed through contoured interior and screens to provide a uniform velocity profile at the exit. Further details of this facility may be found in Ref. 38.

Separate centrifugal blowers were used to supply the primary and the secondary flows. All results were obtained using cold air. This matched the UCI experiment. Also, using the hot-wire technique, if there are temperature gradients in the jet, heat transfer from the hot-wire probe is not strictly a function of velocity. Since air at room temperature was used to supply the two streams, the total temperature everywhere was approximately the same as ambient temperature, assuming a Prandtl number of unity. The facility had very limited flow capacity, and a safety permit was obtained for operation at one psig. The GRC '5BB' nozzle exhaust conditions are listed in Table 3.3. Although the tests were run at very low Mach number, M_p=0.18, and M_s=0.13, the secondary-to-primary velocity ratio was 0.7, and thus, some of the fundamental fluid mechanics were expected to be preserved. The velocity ratio also matched the UCI velocity measurements.

Two pairs of crossed hot-wires, illustrated in Fig. 3.14, were used to survey the mean and fluctuating velocity components in the jet plume. One was in a *u*-*v* configuration, the other in a *u*-*w* configuration. Only the normal velocity component to each wire can be measured, so a single hot-wire cannot measure Reynolds stresses and turbulent kinetic energy. The wires were spaced 1.0-mm apart, limiting the spatial resolution to 1.0-mm in the *y*- and *z*- directions. The probes were mounted on a streamlined strut, visible in Fig. 3.13, and the positioning was automated under computer control in all three directions. The two probes were located at the same *y*-location (vertical) and spaced apart from one another by 23-mm in the *z*-direction (horizontal), Fig. 3.14. The step size in the *z*-direction was chosen to be a submultiple of the separation distance so that a shift of the *v*-array by an integral number of steps matched the corresponding *w*-array.

With axial distance, both spatial resolution and the sampling rate were decreased. Fig. 3.15 shows the grid used for data point spacing. Smaller grid intervals were used where sharp spatial gradients exist in the initial region of the jet. An exponential function was used to decrease the spatial resolution with axial distance. In the *x*-direction, 16 data points were acquired, spanning $8.23D_f$. Grid spacing in the *x*-direction started with a separation of $0.114D_f$ or 6.1-mm between the first and second data points and ended with a separation of $1.47D_f$ between the last two data points. The first data point was taken $0.024D_f$ from the tip of the nozzle center plug in *x* and $0.62D_f$ from the jet centerline in *y,* where the velocity was small. For each axial station, 19 data points were collected along *y,* uniformly spaced. At each axial station, the grid spacing in *y* was adjusted so that the outer data point formed an angle of 5.35º with the axis. The upstream-most position used uniform intervals of $0.0715D_f$ and the furthest position downstream used uniform

intervals of $0.157D_f$. This corresponds to a spatial resolution of 3.8-mm in y at the upstream-most position and 8.3-mm in y at the downstream-most position.

Further downstream, where turbulent structures convect with lower frequencies, larger sampling times were required. For distances upstream of $4.28D_f$, the sampling rate used was 500 hz, and for distances downstream of $4.28D_f$ from the plug tip, the sampling rate used was 200 hz. The ensemble size was 2000. Thus, sampling times of 4s or 10s were used depending on the axial location. At each data point, mean and RMS velocities were sampled in all three directions. Reynolds stress $u'v'$ and $u'w'$ components were obtained.

In addition to the crossed wire surveys, a single wire was used separately to survey the GRC '5BB' nozzle exit boundary layers. The boundary layers were found to be nominally laminar and their characteristics are listed in Table 3.4; here, location 1 refers to the inner layer of the primary (core) nozzle, location 2 refers to the outer layer of the primary (core) nozzle, and location 3 refers to the inner layer of the secondary (fan) nozzle.

The calibration procedure used the coannular nozzle in order to produce a top-hat velocity profile. The voltage of each probe was recorded and plotted against the calculated velocity for several total pressures ranging from very low speeds, close to zero, up to the highest velocity tested. The jet exit velocity was calculated based on the total pressure supplied to the jet, using an assumption of isentropic expansion through the nozzle, and knowledge of the total temperature and atmospheric pressure. A fourth order polynomial was used to fit the calibration curve to the points.

In order to validate the setup, single hot-wire profiles were compared with crossed hot-wire profiles. Mean velocity profiles measured in the initial, intermediate, and fully-

developed regions of a coaxial jet with secondary-to-primary velocity ratio 0.5 are shown in Fig. 3.16. The mean velocity profiles measured using a single hot-wire probe agree closely with the profiles measured using a pair of crossed hot-wire probes. Also compared were mean velocity profiles that were obtained with the *u*-*v* probe and the *u*-*w* probe. These are not shown, but it is noted that these comparisons displayed remarkable agreement. The coannular nozzle exit conditions are listed in Table 3.5.

Also, mean velocity profiles were measured at two axial locations in the initial mixing region of the jet, and compared with experimental data from Fig. 2 of Ko and Kwan, see Fig. 3.17. It was desired to look at the similarity of the shear layer in the jet, as well as to validate the experimental setup. The conventional similarity parameter was used, $\eta = y/x$, where y is measured with respect to the lip of the secondary (fan) nozzle. The local mean velocity ratio is taken with respect to the exit velocity of the secondary jet, U_s.

Table 3.1 ***UCI 'Classic' Nozzle Exit Conditions***

Quantity	Primary	Secondary
Nozzle diameter (mm)	14.3	23.6
Plug diameter (mm)	10.0	-
Lip thickness (mm)	0.74	-
Protrusion (mm)	9.5	-
Velocity[a] (m/s)	460	335
Mach number[a]	0.86	0.95
Bypass ratio[a]	-	4.93
Velocity[b] (m/s)	310	220
Mach number[b]	1.0	0.66
Bypass ratio[b]	-	1.92

Table 3.2 ***UCI '3BB' Nozzle Exit Conditions***

Quantity	Primary	Secondary
Nozzle diameter (mm)	17.0	31.0
Plug diameter (mm)	11.5	-
Lip thickness (mm)	0.8	-
Protrusion (mm)	16.2	-
Velocity[a] (m/s)	460	335
Mach number[a]	0.86	0.95
Bypass ratio[a]	-	4.8
Velocity[b] (m/s)	310	220
Mach number[b]	1.0	0.66
Bypass ratio[b]	-	1.87

Table 3.3 ***GRC 5BB Nozzle Exit Conditions***

Quantity	Primary	Secondary
Nozzle diameter (mm)	28.0	53.3
Plug diameter (mm)	20.4	-
Lip thickness (mm)	0.70	-
Protrusion (mm)	25.3	-
Velocity (m/s)	63.1	44.2
Mach number	0.18	0.13
Bypass ratio	-	2.67

[a] acoustic measurements

[b] mean velocity measurements

Table 3.4 ***GRC 5BB Nozzle*** *Boundary Layer Surveys*

Boundary Layer Survey Location	Momentum thickness, δ_2 (mm)	Displacement thickness, δ_1 (mm)	Shape factor, δ_1/δ_2	Maximum turbulence, u'_{max}/U_p
Inner Primary Nozzle	0.043	0.10	2.36	0.017
Outer Primary Nozzle	0.081	0.20	2.50	0.057
Inner Fan Nozzle	0.043	0.043	2.46	0.015

Table 3.5 ***GRC Coannular Nozzle Exit Conditions***

Quantity	Primary	Secondary
Nozzle diameter (mm)	37.6	53.3
Lip thickness (mm)	0.76	-
Protrusion (mm)	3.18	-
Velocity (m/s)	293	147
Mach number	0.26	0.13
Bypass ratio	-	0.50

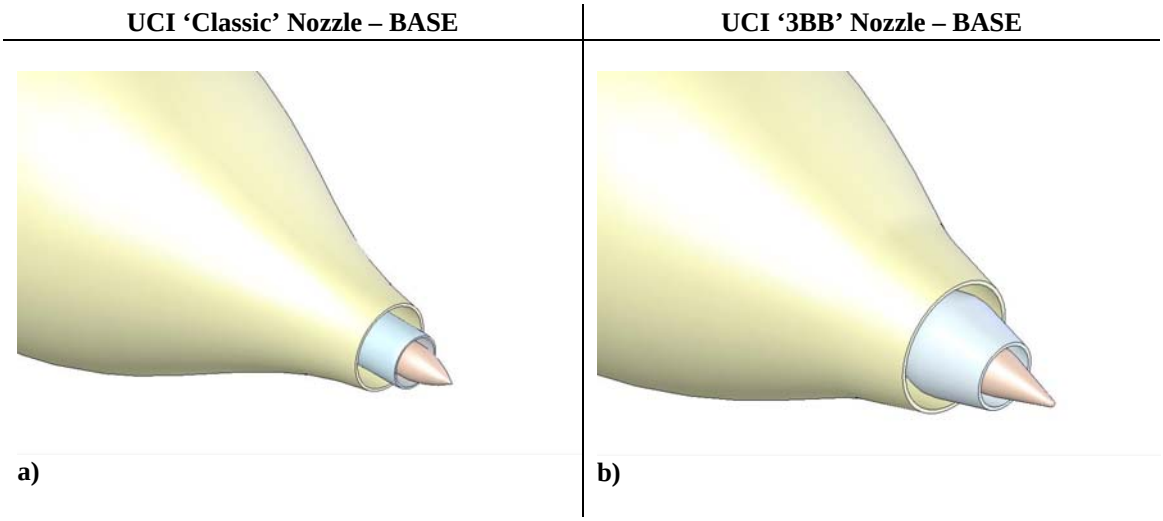

Figure 3.1. 3D views of UCI a) 'Classic' and b) '3BB' nozzles.

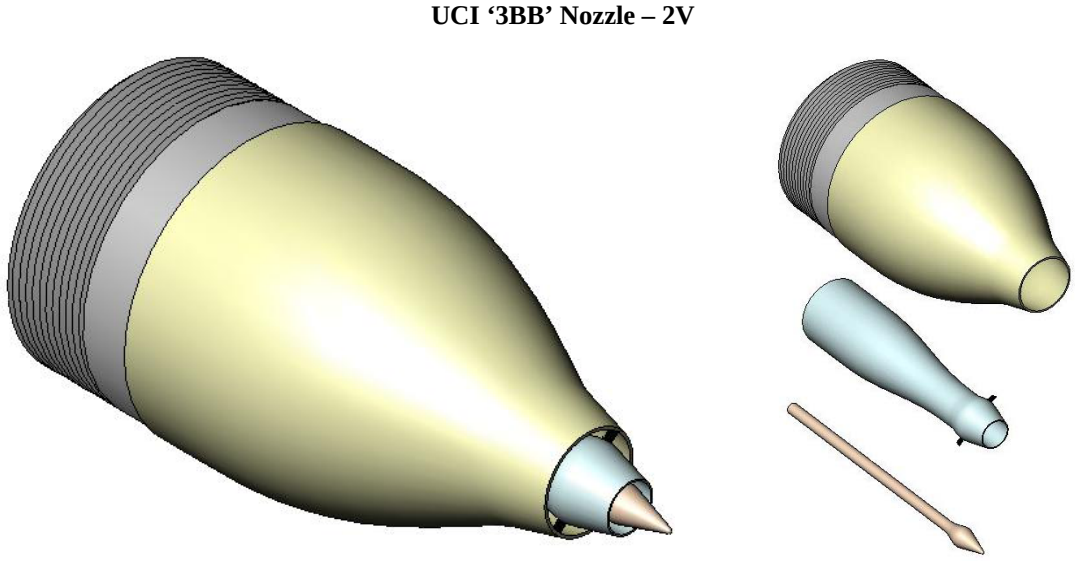

Figure 3.2. Solidworks model of entire assembly for the UCI '3BB' nozzle: threaded aluminum fitting, fan nozzle, core nozzle, one pair of vanes, and center plug.

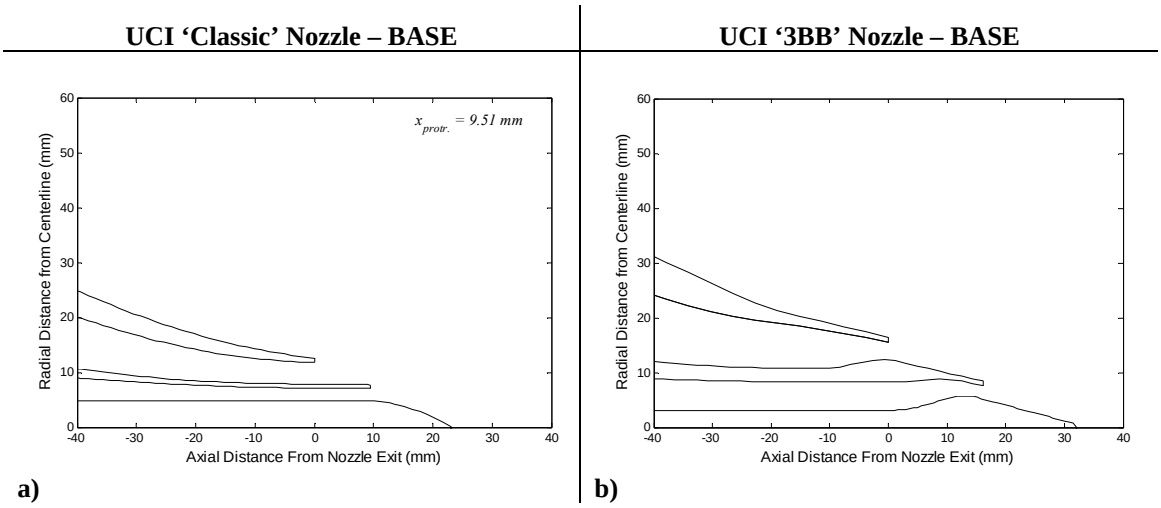

Figure 3.3. Radial coordinates of UCI a) 'Classic' and b) '3BB' nozzles in millimeters.

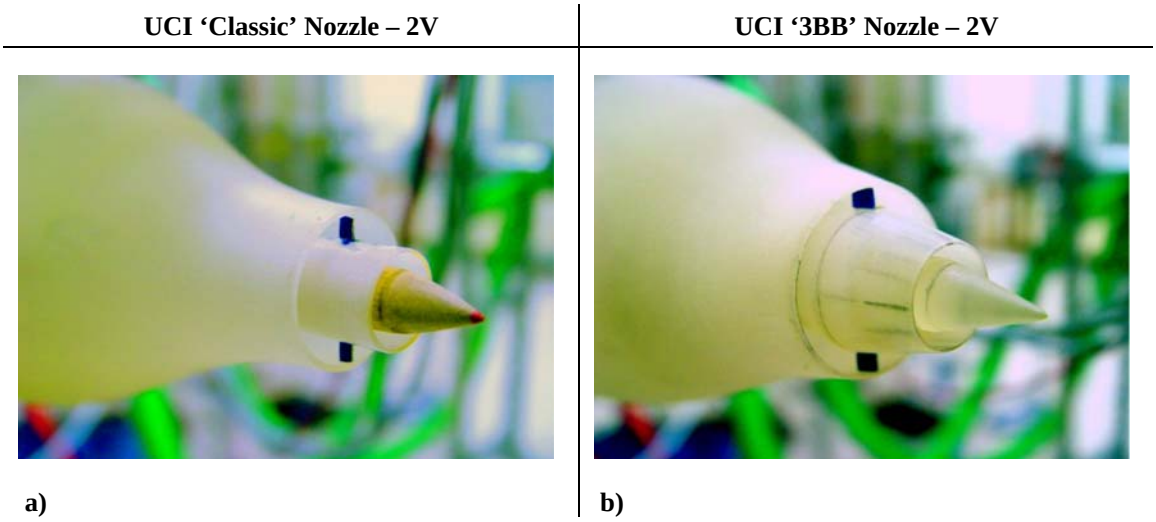

Figure 3.4. Photographs taken in the UCI Jet Aeroacoustics Laboratory with one pair of vanes in the UCI a) 'Classic' and b) '3BB' nozzles.

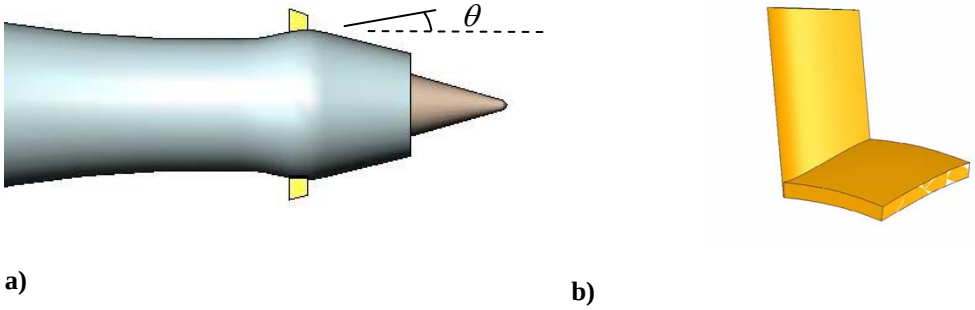

Figure 3.5. a) Bending angle for zero sweepback and b) base curvature for secure attachment.

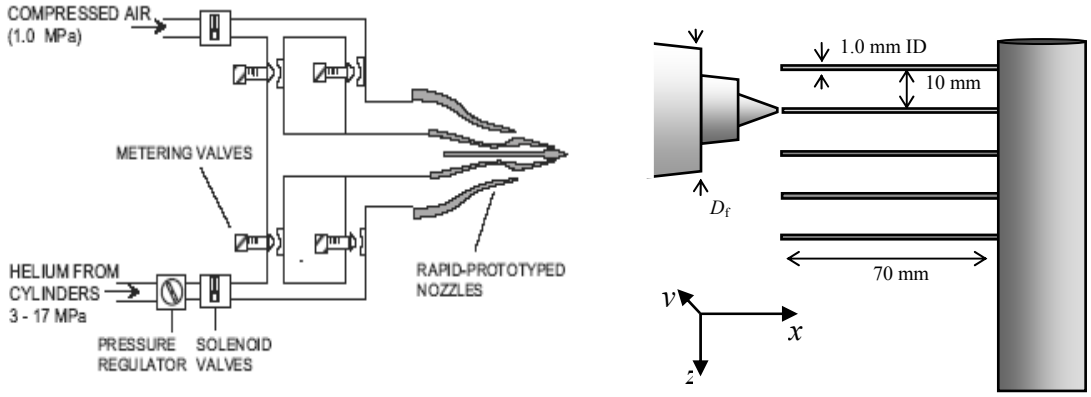

a) Dual-Stream Apparatus **b) Pitot-Probe Rake**

Figure 3.6. UCI Jet Aeroacoustics Facility.

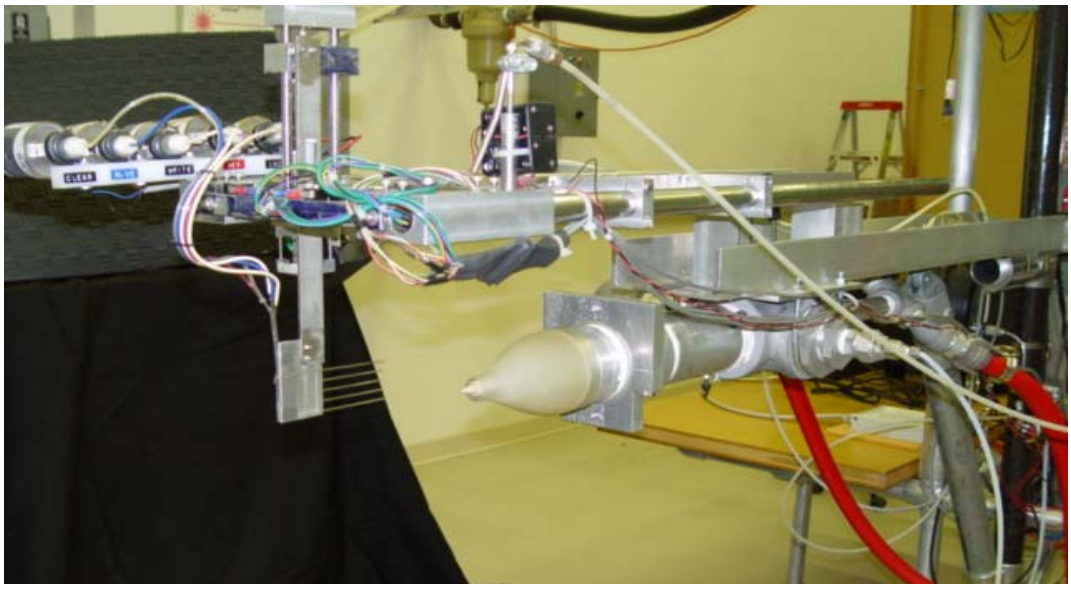

Figure 3.7. UCI Mean Flow Apparatus.

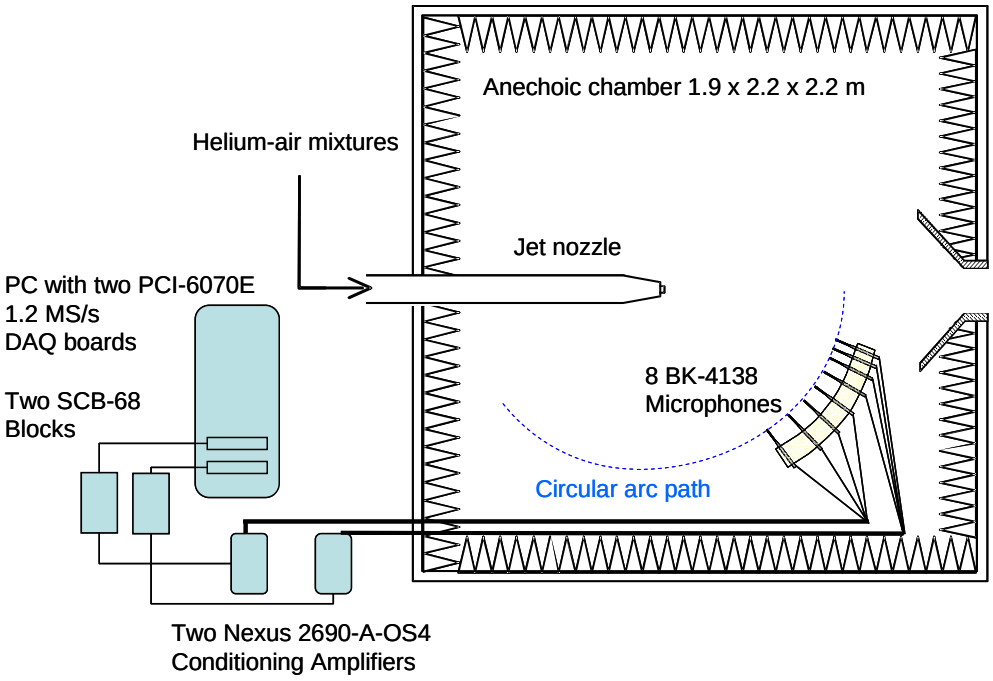

Figure 3.8. UCI Jet Aeroacoustics Facility. Anechoic Chamber

Figure 3.9. UCI Phased-Microphone Array.

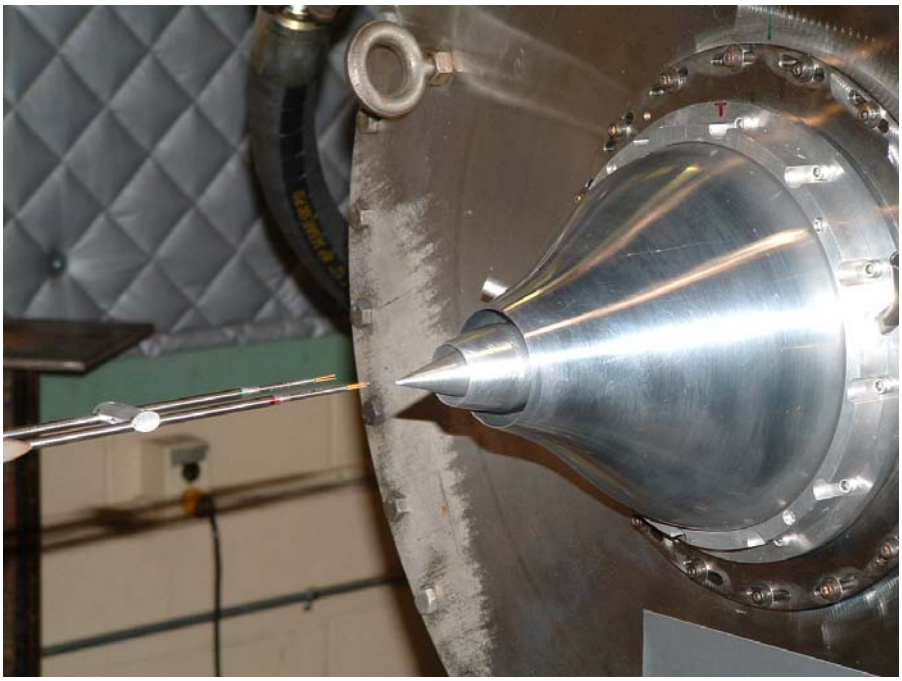

Figure 3.10. Photograph taken in the GRC CW-17 Open Jet Facility of the GRC '5BB' nozzle and a pair of crossed hot-wire probes.

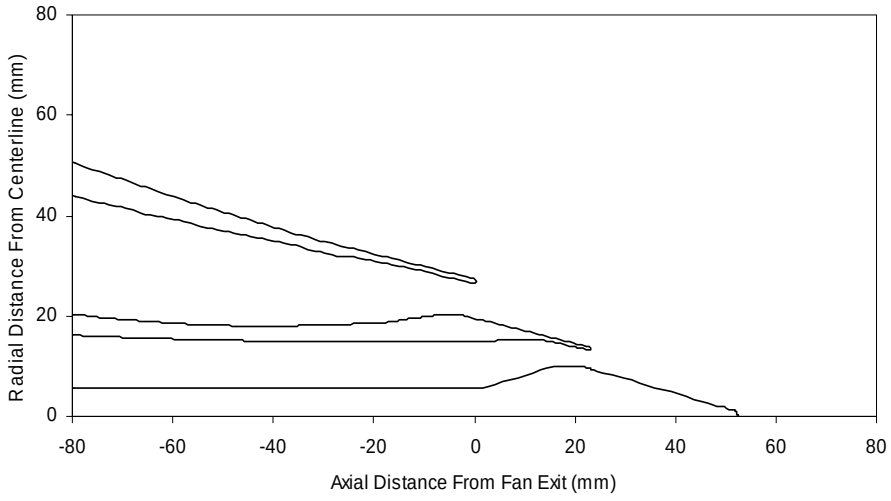

Figure 3.11. Radial coordinates of GRC '5BB' nozzle in millimeters.

a) b)

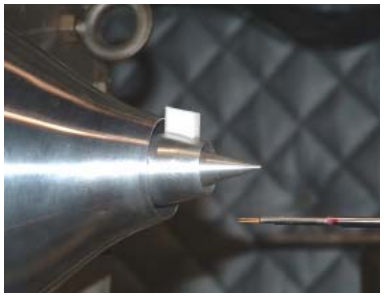

c) d)

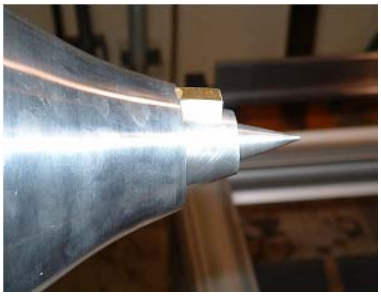

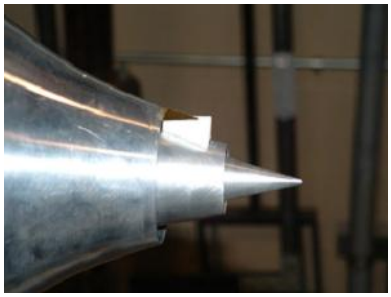

Figure 3.12. Photographs taken in the GRC CW17 Open Jet Facility. GRC '5BB' nozzle and a) W_1 b) Pylon + Flap c) W_2 + Cap 1 d) W_2 + Cap 3.

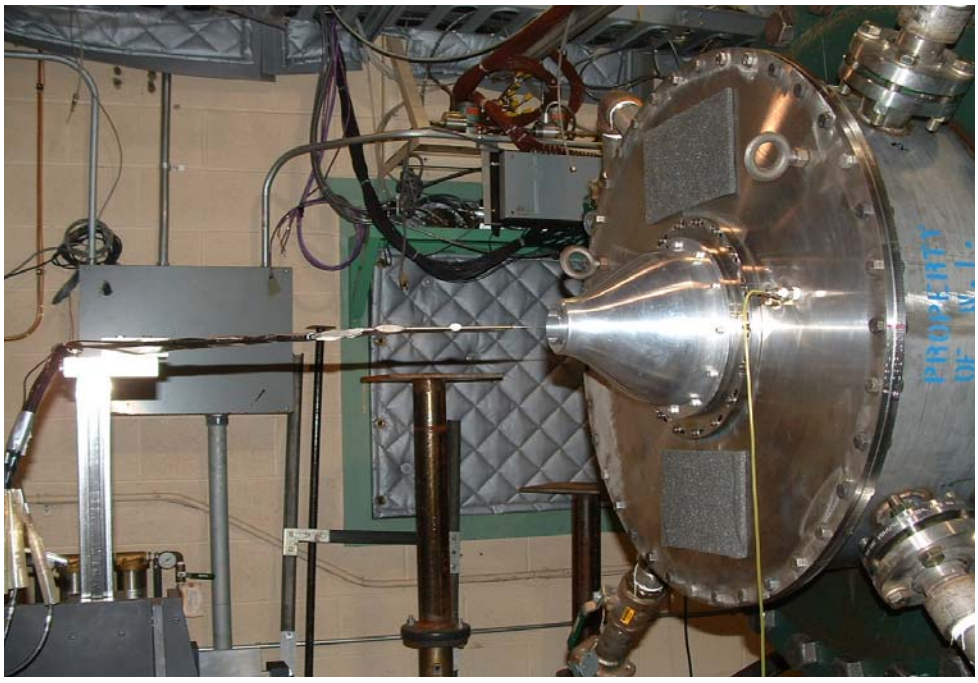

Figure 3.13. Photograph taken in the GRC CW-17 Free Jet Facility of the GRC coannular nozzle and automated traversing mechanism.

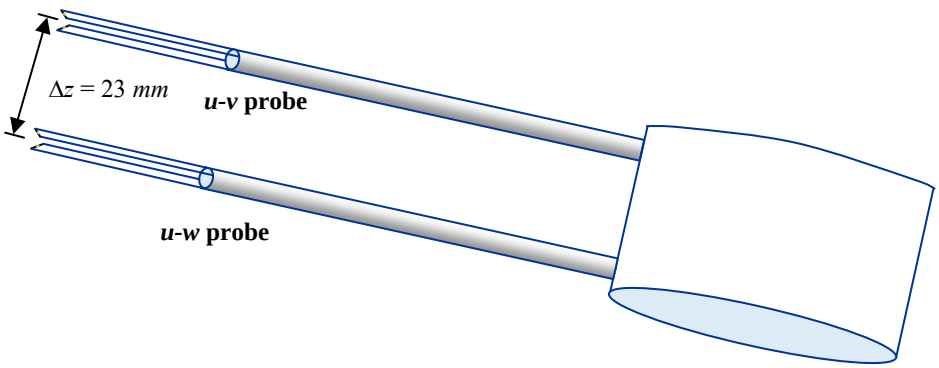

Figure 3.14. Illustration of *u-v* and *u-w* cross-wire probe separation in the *z*-direction.

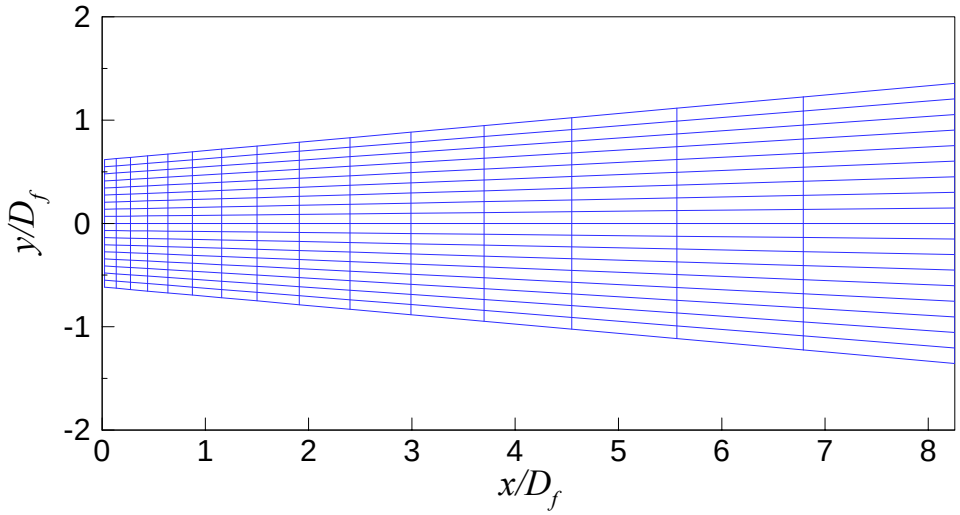

Figure 3.15. Grid used for positioning of the *u-v* probe in the *xy*-plane.

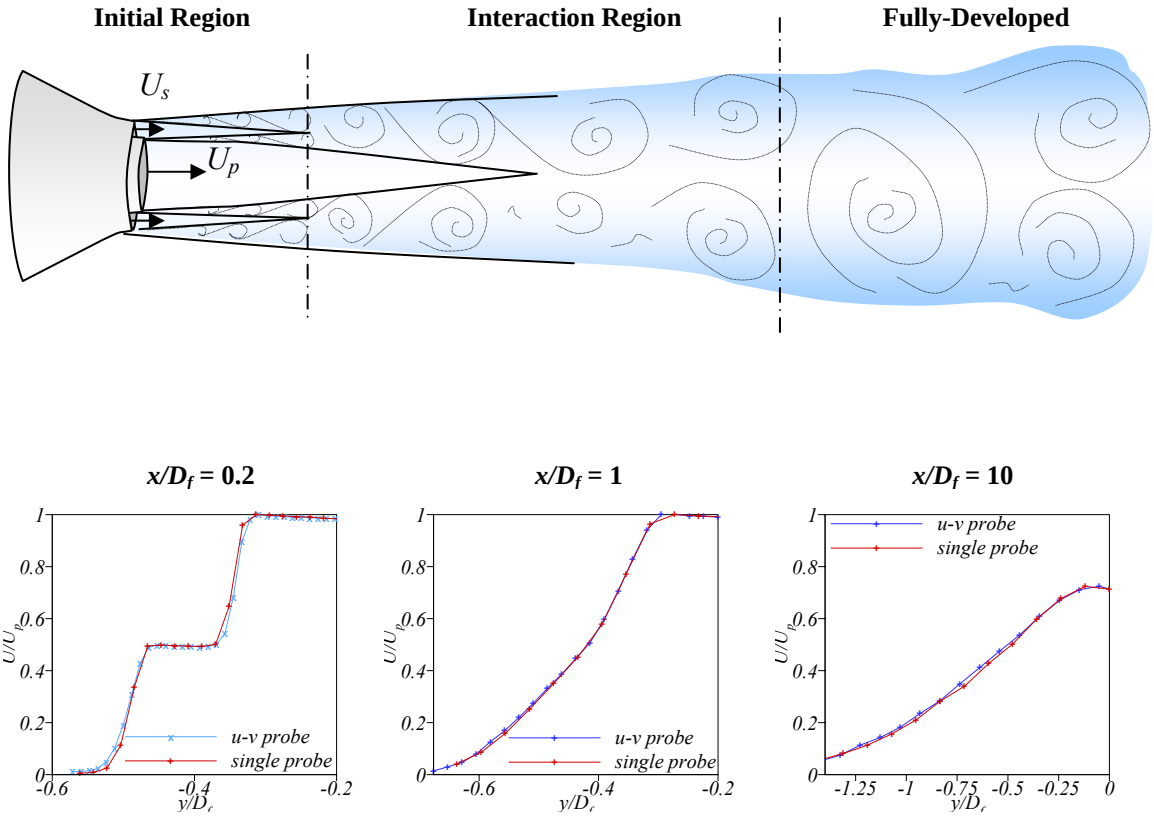

Figure 3.16. Three regions of a coaxial jet (top). Mean velocity profiles (bottom) measured at x/D_f = 0.2,1, and 10 in a coaxial jet exhaust with secondary-to-primary velocity ratio 0.5.

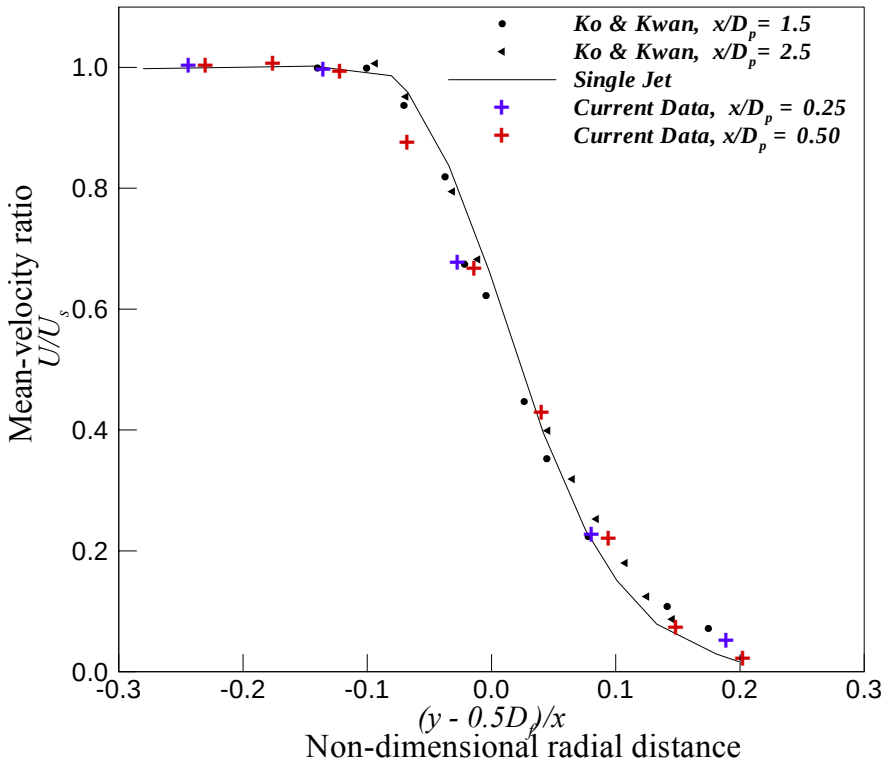

Figure 3.17. Secondary shear layer mean velocity profiles. Values are non-dimensionalized for similarity.

Chapter 4

Data Analysis

4.1 Pitot-Pressure Signal Processing

The details of the UCI Jet Aeroacoustics Facility Pitot-pressure and noise measurements are outlined in Chapter 3. Signal processing techniques are described here. For details of the acoustics post-processing, the reader is referred to Ref. 42.

4.1.1 Savitzky-Golay Smoothing Filter

A Savitsky-Golay, Refs. 64-65, subroutine was used to smooth the Pitot-pressure data and to calculate 1^{st} and 2^{nd} derivatives of the velocity. The Savitsky-Golay filter differs from a moving window average in that it uses a polynomial regression to determine the smoothed value or derivative at a given location. This technique preserves important features of the flow profiles that would otherwise be blurred out by a moving window average. The filter size and order of the polynomial are selected based on the size of the feature that is to be preserved. Different filter sizes were used and the effect on velocity gradient, and inflection points were weighed in order to determine the optimal filter size.

4.1.2 Velocity Calculation

The mean velocity in the jet plume is determined from the measured Pitot-pressure measurements by assuming that the static pressure and total temperature are constant throughout the jet plume. The idea of constant pressure for the turbulent jet is analogous to a subsonic, laminar free jet; one can reason that the pressure must be equal to ambient pressure throughout, since the slipline would move if it were not. For the turbulent jet, it can be shown that there is only a very small change in the mean static pressure across a planar turbulent shear layer, under a thin boundary layer approximation. Since all experiments here consider subsonic jets, there is communication with the ambient fluid, and the static pressure at the nozzle lip line is matched to ambient pressure. The second assumption can be shown to be rather valid for a turbulent jet with Prandtl number approximately unity by studying the result of the theory of Crocco and Busemann. Since the jet is supplied with cold air, at a reservoir temperature equal to the ambient temperature, total enthalpy is constant throughout the jet shear layer. The equations used to calculate velocity are outlined below.

In all of the experiments, the exit conditions of the jet were subsonic, so we did not need to consider shock formation in front of the Pitot-tube opening. The Pitot pressure is equal to the total pressure, as long as the flow is brought to rest isentropically in the Pitot probe. The definition of total pressure is

$$p_0 = p\left(1+\frac{\gamma-1}{2}M^2\right)^{\frac{\gamma}{\gamma-1}}, \tag{4.1}$$

where γ is the ratio of specific heats of the gas.

From the definition of total pressure in Eq.4.1, the Mach number is determined to be

$$M = \left\{ \frac{2}{\gamma - 1} \left[\left(\frac{p_0}{p} \right)^{\frac{\gamma - 1}{\gamma}} - 1 \right] \right\}^{\frac{1}{2}} , \tag{4.2}$$

where p is taken to be constant throughout the jet plume and equal to the ambient pressure. The reservoir temperature T_0 is equal to ambient temperature, and so the local static temperature T can be determined from the definition of total temperature

$$T = \frac{T_0}{\left(1 + \frac{\gamma - 1}{2} M^2 \right)} , \tag{4.3}$$

taking the total temperature to be constant and equal to ambient temperature throughout the jet plume. The definition for the local speed of sound is

$$a = \sqrt{\gamma R T} , \tag{4.4}$$

where R is the gas constant.

The definition for local Mach number depends upon local speed of sound and is given by

$$M = \frac{U}{a} . \tag{4.5}$$

The local mean velocity is determined from Eq.4.4 and 4.5 now that M and T are known from the pressure measurements and the total temperature. The equation for determining the local velocity from the Pitot-pressure measurements is

$$U = \left\{ \frac{\gamma R T_0}{\left(1/M^2 + (\gamma - 1)/2 \right)} \right\}^{\frac{1}{2}} , \tag{4.6}$$

and if the measurement is taken in air, the specific heat ratio is $\gamma = 1.4$.

4.2 Hot-Wire Signal Processing

The hot-wire experimental setup used in the NASA GRC CW-17 Open Jet Facility is outlined in Chapter 3. Post-processing techniques are described in this section.

4.2.1 Velocity Calculation

The specific details of the crossed hot-wire experimental setup are described in Chapter 3. The text by Bruun, Ref. 66, provides a comprehensive overview of hot-wire techniques. Here, an explanation is provided for calculation of the velocity components in all three directions. In a typical crossed hot-wire configuration, the wires are placed perpendicular to one another. The orientation of the wires is such that the in-plane velocity component can be measured, provided that the other component is much smaller in comparison. For turbulent jet measurements, the probes are placed in the same plane as the axial velocity component and one of the other velocity components to be measured, either the vertical or horizontal component. We use a *u*-*v* orientation to measure the axial and vertical components, and a *u*-*w* orientation to measure the axial and horizontal components.

In the current experimental setup, the probe axis is parallel to the *x*-axis. Let V be the total velocity of the in-plane component, inclined at an angle θ with respect to the *x*-axis, Fig.4.1. Using the trigonometric identity for cosines, the measured (normal) velocity components for each probe are

$$\begin{aligned} u_{n1} &= V\cos(\theta + 45°) = V\cos\theta\cos 45° - V\sin\theta\sin 45° \\ u_{n2} &= V\cos(\theta - 45°) = V\cos\theta\cos 45° + V\sin\theta\sin 45° \end{aligned} \tag{4.7}$$

The axial and transverse velocity components are $u = V\cos\theta$ and $v = V\sin\theta$.

Combining with Eq.4.7, the velocity components are expressed based on the measured (normal) components of each probe

$$u = \frac{1}{\sqrt{2}}\left(u_{n1} + u_{n2}\right) \quad , \quad v = \frac{1}{\sqrt{2}}\left(u_{n1} + u_{n2}\right) \tag{4.8}$$

The same procedure was used to determine u and w from the recorded voltages of the second crossed hot-wire probe. The Savitsky-Golay filter explained in 4.1.1 is used to smooth raw velocity data. The velocity components of Eq.4.8 represent total instantaneous velocities and are functions of space and time. This means they consist of an average and a fluctuating component. Due to the random nature of turbulent flows, statistical tools are necessary to interpret the data in a meaningful fashion. These are described in the next section.

4.2.2 Statistical Quantities

For a stationary ergodic process, the statistical quantities do not vary with time, and several quantities of interest can be expressed by the equations presented in this section. Many values can be measured in a flow field, such as velocity, pressure, or temperature. We are interested in a turbulent process, for which these quantities have a mean and a fluctuating component. The total turbulent velocity is a function of position in space and time, $\underset{\sim}{u}(x, y, z, t)$. The fluctuating component, $\underset{\sim}{u}'(x, y, z, t)$, is the difference between the total velocity and the average velocity, $\underset{\sim}{u}'(x, y, z, t) = \underset{\sim}{u}(x, y, z, t) - \underset{\sim}{\bar{u}}(x, y, z)$. The mean

value, $\bar{\tilde{u}}(x,y,z)$, is the average of many samples over a given time period. This quantity is also called the first moment.

$$\bar{\tilde{u}}(x,y,z) = \lim_{T\to\infty} \frac{1}{2T} \int_{-T}^{T} \tilde{u}(x,y,z,t)dt \tag{4.9}$$

The mean square, ψ^2, is the average value of the squares of many individual samples over a long period of time. This quantity is also called the second moment

$$\psi^2(x,y,z) = \lim_{T\to\infty} \frac{1}{2T} \int_{-T}^{T} \tilde{u}^2(x,y,z,t)dt \tag{4.10}$$

and the variance, σ^2, or the second central moment is taken with respect to the mean value, $\bar{\tilde{u}}(x,y,z)$ as follows

$$\sigma^2(x,y,z) = \lim_{T\to\infty} \frac{1}{2T} \int_{-T}^{T} \left(\tilde{u}(x,y,z,t) - \bar{\tilde{u}}(x,y,z)\right)^2 dt \tag{4.11}$$

The root mean square (RMS), σ, is the square root of the variance. This value is often used to describe the turbulence intensity. The turbulent kinetic energy (TKE) will be used to describe the turbulence intensity in subsequent chapters. Its value is determined by squaring the individual RMS components.

$$k(x,y,z) = \frac{1}{2}\left(\sigma_x^2 + \sigma_y^2 + \sigma_z^2\right) \tag{4.12}$$

In post-processing of the data, the turbulent kinetic energy can be approximated by

$$k(x,y,z) \approx \frac{1}{2}\left(\sigma_x^2 + 2\cdot\sigma_z^2\right) \tag{4.13}$$

since the horizontal and transverse components are of the same order of magnitude. In subsequent chapters, these statistical quantities are non-dimensionalized using either the primary jet exit velocity U_p or its square.

The skewness is the third central moment and the kurtosis is the fourth central moment, but these are not presented here. For an excellent reference on statistical engineering analysis, the reader is referred to Bendat and Piersol, Ref. 67.

The one-point velocity cross-correlations between the axial and vertical and the axial and horizontal velocity components, *u'v'* and *u'w'* respectively, can be obtained using the current hot-wire setup. These are directly related to the Reynolds stresses. In this work, the term Reynolds stress is used synomonously with the cross-correlation defined below.

$$R_{uv}(x,y,z) = \lim_{T\to\infty} \frac{1}{2T} \int_{-T}^{T} u'(x,y,z,t)v'(x,y,z,t)dt \tag{4.14}$$

$$R_{uw}(x,y,z) = \lim_{T\to\infty} \frac{1}{2T} \int_{-T}^{T} u'(x,y,z,t)w'(x,y,z,t)dt$$

Commonly, the incompressible Reynolds stress definition includes density and a negative sign as coefficients to the above definition, for example, Ref. 68.

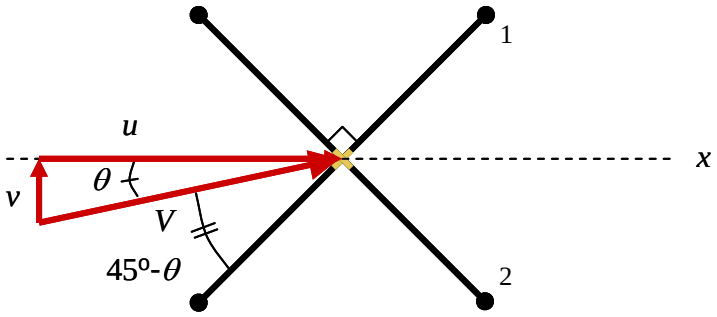

Figure 4.1. Crossed hot-wire orientation. The velocity vector is oriented at an angle θ with respect to the probe axis, and each wire is oriented at 45^{o} with respect to the axis.

Chapter 5

Effect of Nozzle Geometry on Jet Noise Reduction using Fan Flow Deflectors

Marginal noise reduction had been observed at UCI, after an internal wedge was placed on the UCI ‘Classic’ nozzle, described in Chapter 3. Subsequently, the wedge was discarded because it was thought to be inferior to vanes in noise suppression capability. The wedge showed much improved efficacy when placed on a nozzle with realistic (converging) exit geometry, such as the UCI ‘3BB’ nozzle, Refs.12-13. Subsequent measurements taken at NASA GRC showed the same trends, Ref.14. Figure 5.1 shows noise reduction achieved in the ‘3BB’ nozzle using an internal wedge deflector. On the left is the UCI measurement and on the right is the GRC measurement. Figure 5.2 shows the limited noise reduction observed when an internal wedge was placed on a nozzle with parallel exit flow lines at NASA.

It was hypothesized that the convergent nozzle contours helped the wedge displace the fluid in the downward and sideward directions, while the parallel exit contours limited the fluid displacement strictly to the sideward direction. Figure 5.3 illustrates the hypothesis. Mean flow measurements conducted at UCI confirmed the expected flow

behavior, Fig.5.4. Additionally, uniformly reduced velocity gradients were revealed underneath the jet issuing from the ‘3BB’ nozzle.

The experiments conducted at UCI illuminated the relation between mean flow gradient and noise reduction. By using two different nozzles, they augmented the database for correlating the mean flow field with noise emissions. The noise and mean flow fields for ten nozzle-deflector configurations are presented here, and important trends are highlighted.

5.1 Nozzle-Deflector Comparisons

The baseline nozzles and deflector fabrication are described in Chapter 3. Experiments covered two nozzle geometries, four deflector configurations, and two types of comparisons using internal vanes: equal deflector turning effort, and equal chord length. Comparisons at equal turning effort, to be defined below, were necessary to distill the effect of nozzle geometry from the effect of deflection force.

5.1.1 UCI Nozzles

The nozzles used for the comparisons outlined here included one with parallel exit streamlines and one with convergent exit streamlines, described in Chapter 3. The initial measurements of Fig. 5.4 were taken using a coplanar configuration of the UCI ‘Classic’ nozzle and the UCI ‘3BB’ nozzle and internal wedge, Fig. 5.5. The nozzle coordinates with deflector placement for all subsequent comparisons are shown in Figs. 5.11-5.14. The UCI ‘Classic’ nozzle was tested with a protrusion of the core nozzle so that a one-to-one comparison could be performed with the UCI ‘3BB’ Nozzle. Exit conditions are

listed in Tables 5.1 and 5.2. The principal difference between the two nozzles, as far as deflector aerodynamics is concerned, is in the internal Mach number distribution. In the nozzle with rapidly convergent exit streamlines, the Mach number decreases quickly moving upstream of the fan exit, while in the nozzle with parallel streamlines, the Mach number changes slowly in the vicinity of the nozzle exit. The Mach-area relation is used to obtain the dynamic pressure distribution inside the nozzle fan ducts, Fig. 5.6.

5.1.2 Deflector Turning Effort, ε

In order to isolate the effect of nozzle geometry on the ability of fan flow deflectors to reduce noise, it was necessary to conduct comparisons between deflectors on an "equal turning effort" basis, meaning that the deflector force, normalized by the thrust of the bypass stream, is approximately the same in both nozzles. The turning effort can be seen as an overall deflection angle based on the force of the deflectors alone (i.e., without considering any additional forces created by the nozzle surface). Its definition is

$$\varepsilon = \frac{1}{F_s} \sum_{i=1}^{N} L_i \,, \tag{5.1}$$

where L_i is the lift, or sideforce, generated by each deflector and N is the total number of deflectors. Both nozzles produced approximately the same secondary (bypass) thrust F_s, while the dynamic pressure distributions in the fan ducts of the two nozzles differ drastically. Experiments were conducted using internal vanes with approximately matched lift forces in the two nozzles, achieved by reducing the chord length of the vanes in the UCI 'Classic' nozzle. The external wedge side forces were approximately matched without altering the wedge geometry. The internal wedge forces were not matched,

however qualitative trends are not expected to change depending on the magnitudes of the deflector forces. The equations in this section provided guidance for selection of the deflector parameters.

Recent pressure coefficient measurements have been obtained for a wedge placed in a compressible jet issuing from a rectangular nozzle, Ref. 17. This problem differs significantly from the classic wedge problem because the top and base of the wedge are in communication with ambient fluid. It is well worth noting that the drag force was found to be about 75% less than a fully-immersed two-dimensional cylindrical wedge. For the wedge placed in a finite thickness jet exhaust, one can reasonably assume

$$L_{We} = C_L(\alpha) q_s S \,, \tag{5.2}$$

where C_L is a sideforce coefficient that depends only on the wedge half-angle α, q_s is the dynamic pressure at the nozzle exit, and S is the wetted area of the wedge. Given that q_s is the same for both nozzles, equal sideforce is achieved by wedges of equal half-angle and wetted area.

For internal vanes, a computational study, Ref. 16, showed that the lift coefficient of the vane airfoil (in that case a NACA 0012 section) approximately matched the lift coefficient of the same airfoil in external flow if the reference conditions were taken at the axial position of the leading edge of the vane. Reference conditions are taken at vane leading edge. With this selection of reference conditions, the lift coefficient of the vane airfoil is given by the familiar relation

$$C_L = a_{2D}\alpha \,, \tag{5.3}$$

where a_{2D} is the two-dimensional lift curve slope (typically 0.11 deg^{-1}). Therefore, the vane lift is

$$L_V = a_{2D}\alpha q_{le} cw\,, \tag{5.4}$$

where w is the average vane span. Equations 5.2 and 5.4 provided guidance for the design of deflectors that would allow comparisons at equal turning effort ε. Other comparisons were performed on an equal chord length basis. Details of the deflector designs are provided in the next section. The interested reader is referred to Shevell, Anderson, and Liepmann and Roshko, Refs. 73, 75, and 77, for three excellent aerodynamics texts.

5.1.3 Deflector Configurations

The deflector parameters were similar to those used in earlier exploratory studies, Refs. 10-12. They do not represent optimal design configurations. Four configurations were tested: internal wedge (W_i), external wedge (W_e), a single pair of internal vanes (2V), and two pairs of internal vanes (4V). Figure 5.7 depicts the four configurations tested. The deflector geometries are shown together with the nozzle coordinates in Figs. 5.8-5.11. Tables 5.3 and 5.4 list the deflector parameters.

Both external wedges (W_e) were mounted at the top of the two nozzles (ϕ=180^o) and had the same half-angle. It was thus assumed that the sideforce coefficient, C_L was the same. In order for the sideward forces imparted by the wedges to be matched, the wetted area, S, of the deflectors must be consistent between nozzles, Eq.5.2. Since the fan duct thickness is 3.9 mm for the classic nozzle and 3.1 mm for the UCI 3BB nozzle, it was thought that the wedge side lengths could be varied to match the wetted areas. This was not necessary, however, since the wetted areas were estimated to be approximately the same for a wedge that was 4.5 mm in height.

The wetted area of the external wedge (W_e) was estimated as follows: along the free surface of the fluid passing over the wedge, the pressure is ambient. Assuming isentropic flow, the Mach number is constant on the free surface. This means that the temperature and therefore the density are also constant. It follows, from the continuity equation, that the area filled by the flow must be constant. The surface of the '3BB' nozzle downstream of the fan duct exit is convergent, so the streamlines cannot remain parallel to the surface. Fig. 5.12. shows the idea. A simple program was written to calculate the position of the free surface when a wedge with half angle $\alpha = 17^o$ is placed on the UCI '3BB' nozzle. The projection of the free surface of the fluid passing along the side of the wedge onto the plane of symmetry is plotted in Fig.5.13. The outcome showed that the wetted area of the wedge on the UCI '3BB' nozzle for a wedge with half angle $\alpha = 18^o$ and side length l=10 mm is 37mm^2. The wetted area for a wedge with the same half angle and side length on the 'Classic' nozzle is rectangular assuming parallel flow lines, and it is 39mm^2, a difference of only about 5%. Altering the side length by 0.5 mm would have resulted in a matched wetted area, but construction of the wedge-shaped deflector is very painstaking, and the accuracy in making them was not better than ± 0.5 mm. Thus, the comparison was performed using the same external wedge (W_e) geometry in both nozzles. This force estimation procedure does not take into account the upwash that was noted in the flow visualization experiments of Ref. 17. (Chapter 7 presents computational and experimental surface flow data for an external wedge that are in contrast to the analysis here. However, the estimate is still valid for matching force between nozzle geometries.)

Determining the turning effort provided by the internal wedge (W_i) is more complicated because of the favorable pressure gradient inside the fan duct. This

comparison was performed using the same internal wedge half-angle and side length in both nozzles. Without estimating the sideforce, it is noted that it will be larger in the 'Classic' nozzle than in the '3BB' nozzle because of the larger average dynamic pressure q_s in the 'Classic' nozzle. The wedge deflectors were constructed by hand from 4.5-mm-thick nylon sheet. The internal wedge cross-section was rectangular with height 3.9 mm in the 'Classic' nozzle. The top of the internal wedge was carved to match the contours of the fan duct in the '3BB' nozzles.

Two types of comparisons using internal vane deflectors (2V and 4V) were performed between the 'Classic' and '3BB' nozzles: equal turning effort ε and equal chord length c. In the '3BB' nozzle, the Mach number and dynamic pressure increase rapidly near the fan exit because of the rapidly converging duct. As a consequence, at fixed axial position, the Mach number and dynamic pressure in the '3BB' nozzle are smaller than those in the 'Classic' nozzle. In the first type of comparison, the lift force, calculated from Eq.5.4, was matched by reducing the chord length of the vanes in the classic nozzle to compensate for the larger dynamic pressure relative to the '3BB' nozzle. The trailing edges of the vanes were placed at the exit plane of the fan duct, x_{te}=0, a choice necessitated by the constraints of this study, and not an ideal placement from an optimal design point of view.

Placement of the trailing edge of the vanes at the fan exit allowed for matched lift force comparisons between the nozzles without an exceedingly small chord length in the 'Classic' nozzle. Placing the vane trailing edge at x_{te}=-2mm inside the fan duct would have required a chord length of 1.5mm in the 'Classic' nozzle, see Fig. 5.14b. Placed at the trailing edge, the required chord length was 1.8mm (this was rounded up to 2mm) in

order to match the lift forces of in the two nozzles. Increasing the chord length in the '3BB' nozzle had little effect on the lift force past c=4mm. Instead of varying the chord length, the angle of attack could have been varied to match lift force. For vane deflectors with chord lengths of 4mm, approximately matched lift forces would be achieved by angles of attack less than 5^o in the 'Classic' nozzle and 10^o in the '3BB' nozzle. It was decided that placing the trailing edge position of the vanes at the fan exit, or x_{te}=0mm, was more practical from a fabrication standpoint in achieving the matched turning effort than placing it at x_{te}=-2mm based on the predictions. It was decided that the chord length should be changed as opposed to angle of attack to provide downwash at a consistent angle. This was thought to be a more consistent decision with the experimental necessity to isolate the effect of the force provided by the nozzle from the force provided by the deflector. Figure 3.4 shows photographs of the internal vane deflectors with c=2mm in the 'Classic' nozzle, and c=4mm in the '3BB' nozzle.

In the second type of comparison, the chord length of the vanes in the 'Classic' nozzle matched the chord length of the vanes in the '3BB' nozzle. The angle of attack, $\alpha = 10^o$ was selected to achieve a large turning effort while avoiding flow separation. Azimuth placement of the vanes was determined based on previous experiments that showed significant noise suppression. The vane parameters are listed in Tables 5.3 and 5.4. Vane fabrication is described in Chapter 3.

5.2 Noise and Mean Flow Measurements

Mean velocity and acoustic measurements were conducted in the Jet Aeroacoustics Laboratory at the University of California, Irvine, for ten nozzle-deflector combinations.

The results here were also published in Ref. 11. The data is referenced to the axial location of the plug tip, so x/D_f =0 corresponds to the plug tip, and the first measurement location.

First, in Fig.5.15, the velocity results for the baseline 'Classic' and '3BB' nozzles are presented. Two types of isocontours are presented: the velocity on the plane of symmetry, or the z=0 plane, normalized by the primary jet velocity, $u(x,y,0)/U_p$, and the velocity on various $x=x_0$ planes, normalized by the local maximum velocity, $u(x_0,y,z)/u_{max}(x_0)$. The same types of plots will be shown for the cases with deflectors in subsequent figures. For the baseline nozzles, we observe near-perfect axisymmetry of the mean flow, indicating good alignment of the nozzles and the Pitot rake.

For the cases with deflectors, shown in Figs. 5.16-5.21, the following information is provided:

- Mean-velocity profiles, following the format in Fig. 5.15.
- Plots of $u(x_p,y,z)/u_{max}(x_p)$, where x_p denotes the axial location where the maximum velocity drops to 80% of the primary exit velocity. This is a short distance past the end of the primary potential core. x_p is thus an indicator of the extent of the noise source region, with reduced x_p indicating greater mixing and thus a smaller noise source region. Each plot is presented alongside corresponding baseline $u(x_p,y,z)/u_{max}(x_p)$ isocontours.
- Overall sound pressure level (OASPL) versus polar angle from the jet axis, with comparisons to the corresponding baselines, measured in the $\phi=0^o$ plane. OASPL reductions are listed in Tables 5.3 and 5.4.

- Far-field, narrowband sound pressure level (SPL) spectra in the direction of peak emission, with comparisons to the respective baseline emissions.

In all figures, the results for the 'Classic' and '3BB' nozzles are presented on the left- and right-hand sides, respectively. All axial distances are scaled by the respective fan nozzle diameters D_f.

The mean-velocity and acoustic results for the internal wedge (W_i) are shown in Fig.5.16. While there is no great difference in the $u(x,y,0)/U_p$ contours between 'Classic' and '3BB' nozzles (top of Fig. 5.16a), there are significant differences in the cross-sectional isocontours (bottom of Fig. 5.16.a, and Fig. 5.16.b). The internal wedge on the 'Classic' nozzle produces a heart-shaped plume cross-section with deflection mostly sideward and some thinning of the low-speed region on the underside of the jet. In contrast, the internal wedge on the '3BB' nozzle deflects flow downward and sideward, producing a pear-shaped plume cross-section with reduced velocity gradients not only downward but also over a wide range of sideline directions.

The OASPL plots show that the internal wedge (W_i) on the 'Classic' nozzle gives marginal noise reduction, about 1.5 dB, only at very small polar angles, and no noise reduction (and some noise increase) for the rest of the arc. This is consistent with earlier acoustic measurements, Ref.14. On the other hand, the internal wedge on the '3BB' nozzle produces strong noise reduction in the direction of peak emission (5.3 dB) and appreciable OASPL reduction up to $\theta = 70^o$. The spectra in the directions of peak emission, Fig. 5.16.d, confirm the superiority of the '3BB' nozzle, which reduces noise levels over the entire range of frequencies measured. For the 'Classic' nozzle, there is noise decrease at low frequencies but significant noise increase at high frequencies.

The trends for the external wedge (W_e), shown in Fig. 5.17, are similar to those for the internal wedge discussed above. There is a small improvement in the OASPL of the 'Classic' nozzle at low polar angles, possibly because the low speed region on the underside of the jet, Fig. 5.17.b, is not thinned as much as for the internal wedge (Fig. 16.b), however, there is excess noise at large polar angles. The peak OASPL reduction for '3BB' nozzle is slightly lower than for the internal wedge. The behavior of SPL in the direction of peak emission mirrors that observed for the internal wedge.

We now examine the case of a single pair of vanes (2V) compared at equal turning effort, Fig. 5.18. The vanes in the 'Classic' nozzle produce oblong mean velocity isocontours with reduced gradients in the downward direction but sharpened gradients in the sideline direction. The vanes in the '3BB' nozzle generate velocity contours that are pear-shaped (similar to those observed with the wedges) and increase the thickness of the low-speed layer in the downward and sideline directions. The differences in OASPL and SPL between 'Classic' and '3BB' nozzles are quite dramatic. The 'Classic' nozzle reduces levels marginally at small polar angles and increases levels at large polar angles. In contract, the 3BB nozzle gives a strong reduction in the direction of peak emission and appreciable noise reduction up to $\theta = 60^o$. Importantly, there is no significant excess OASPL at larger polar angles. For the 'Classic' nozzle, the spectra in the direction of peak emission reduce only at low frequencies and increase at high frequencies. The peak-emission spectra in the '3BB' nozzle decline for all measured frequencies.

Figure 5.19 compares the 2V configuration between 'Classic' and '3BB' nozzles, with the vanes having equal chord length. Now the vanes of the 'Classic' nozzle produce a larger turning effort than the vanes of the '3BB' nozzle. The only significant difference

when compared with Fig. 5.18 (equal turning effort) is that the velocity cross-section of the ‘Classic’ nozzle has some lateral “fattening” on the underside of the jet, probably a result of turning the flow earlier inside the fan duct, and complex flow interactions with the nozzle inner walls. The apparent effect of this fattening on the OASPL is that the noise excess observed in the equal-turning-effort comparison (Fig. 5.18b) is somewhat reduced. Overall, the performance of the ‘Classic’ nozzle is still inferior to that of the ‘3BB’ nozzle.

In the equal-turning effort and equal-chord comparisons with two pairs of vanes (4V), shown in Figs. 5.20 and 5.21, respectively, we observe the same general trends as in the 2V comparisons. Noise reduction in the direction of peak emission is now more pronounced for the ‘Classic’ and ‘3BB’ nozzles, owing to the larger deflection of the flow. Still, the ‘Classic’ nozzle produces OASPL reduction only for angles very close to the jet axis, while the ‘3BB’ nozzle reduces OASPL up to about $\theta = 60^{o}$. A larger turning effort in the ‘Classic’ nozzle (Fig. 5.21 vs. Fig. 5.20) produces some lateral motion of the air, which apparently mitigates excess noise at large polar angles. The peak-emission spectra in the ‘3BB’ nozzle shows reduction across all frequencies while in the ‘Classic’ nozzle there are crossovers at higher frequencies.

5.3 ΔOASPL vs. *G*

From the mean flow measurements presented in Figs. 5.16 – 5.21, it is clear that there is a reduction in mean velocity gradient associated with the noise reduction measured on the underside of the jet. The best noise reduction case (internal wedge (W_i) placed on the UCI ‘3BB’ nozzle) is accompanied by uniformly reduced radial velocity gradients. The

uniform reduction in radial velocity gradient is characterized by a "pear-shaped" cross-section of velocity isocontours, Fig. 5.16b (right). To quantify the velocity gradient, a parameter *G*, is defined

$$G = \frac{x_p}{U_p} \frac{\partial u(x_p, y_{i1}, 0)}{\partial y}, \tag{5.5}$$

where i_1 corresponds to the location of the first inflection point, and the location of the maximum radial mean velocity gradient (the inflection points were explained in Chapter2, Fig. 2.6.). The maximum gradient is measured at the end of the primary potential core, x_p, and is non-dimensionalized by the primary potential core length and the primary jet exit velocity, U_p.

In Figs. 5.22 and 5.23, a preliminary correlation between ΔOASPL and the reduction in maximum velocity gradient with respect to the baseline case, ΔG is shown on the $\phi = 0^o$ plane for different nozzle-deflector combinations. This preliminary attempt does not incorporate the velocity gradient on non-zero ϕ-planes underneath the primary jet, which will have a significant impact on the noise measured in the $\phi = 0^o$ plane. In Fig. 5.22, the internal wedge shows greatest reduction in OASPL with least reduction in maximum radial velocity gradient. The vane cases show larger gradient reduction on the $\phi = 0^o$ plane but with less acoustic benefit. Figure 5.23 shows that the internal wedge results in an increased gradient underneath the jet. The external wedge reduces the maximum gradient underneath the jet as do the vanes, but there is wide scatter. It is thought that a different definition of *G* would result in an improved correlation.

The correlations presented in Chapter 6 between *G* and turbulent kinetic energy *k*, show the connection between peak turbulent kinetic energy and *G* when it is measured at

the end of the generalized secondary core (GSC). This provides intuition for choosing a better definition for G in correlating OASPL. The internal and external wedges (W_i and W_e) have a finite length GSC (it is shorter than the primary potential core). For these cases, the definition of G was adjusted so that the radial velocity gradient was measured at the end of the generalized secondary core, see Eq. 5.6.

$$G = \frac{x_p}{U_p} \frac{\partial u(x_{GSC}, y_{i1}, 0)}{\partial y}, \tag{5.6}$$

Figure 5.24 shows that the correlation is improved, however, there is still scatter in the point corresponding to the internal wedge (W_i). This could be because the internal wedge alters the mass flow rate of the nozzle, but this is not yet clear. Since the primary potential core is covered by the generalized secondary core for the 2V and 4V cases, one can argue that taking G at the end of the primary potential core is equivalent to taking it at the end of the generalized secondary core for correlating with noise.

A still improved correlation would include the gradient reduction on more than one planar slice of the flow field, over a range of azimuthal directions, and G would have the form

$$G = \frac{1}{\pi} \int_{-\pi/2}^{\pi/2} \frac{x_p}{U_p} \cdot \frac{\partial u(r_{i1}, \phi, x_{GSC})}{\partial r} d\phi, \tag{5.7}$$

Examining the flow characteristics on the ϕ=0^o plane is a first step toward understanding the flow characteristics and their impact on noise emissions. It is also an important intermediate step in developing the algorithm that will integrate the flow characteristics from several ϕ-planes. A correlation using Eq. 5.7 will be the focus of subsequent works.

5.4 Summary of Trends

This investigation of the effect of baseline nozzle shape on the acoustic performance of fan flow deflectors for turbofan engine noise suppression resulted in the observation of several important trends. A coaxial nozzle with parallel flow lines, the UCI 'Classic' nozzle, and a realistic coaxial nozzle with convergent flow lines, the UCI '3BB' nozzle, were compared. For all types of comparisons and all deflector arrangements, the '3BB' nozzle produced superior acoustic performance along with more uniform reduction of velocity gradients on the underside of the primary jet. The deflectors comprised internal vanes as well as internal and external wedges. Comparisons at equal deflector turning effort and equal deflector geometry were performed. The study consisted of mean axial velocity measurements and far-field acoustic surveys in the downward direction. The results helped to illuminate the desired shape of the mean flow field for effective noise suppression. The following general observations can be inferred from the results:

- A wedge-type deflector in a nozzle with parallel flow lines pushes flow mainly in the sideward direction and can thin the low-speed layer on the underside of the jet. This works contrary to the desired effect of fan flow deflection and gives marginal noise reduction and even noise increase.
- A nozzle with convergent flow lines helps the wedge-type deflector displace fluid downward and in the sideline direction. Velocity gradients are reduced for most of the downward perimeter of the jet. Appreciable noise reduction is achieved for a large range of polar angles.
- With internal vanes, the nozzle with parallel flow lines produces an oblong jet plume cross-section with reduced gradients in the strictly-downward direction

and enhanced gradients in the sideline direction. An apparent consequence of this is that noise reduction is confined to small polar angles and noise excess is often observed at large polar angles.

- Internal vanes in a nozzle with convergent flow lines displace flow downward and in the sideline direction, hence reducing gradients in those directions. Noise reduction in the direction of peak emission is substantial and observed across all measured frequencies. OASPL benefit is observed for polar angles up to $\theta = 60^{o}$ with respect to the jet axis.
- As a general conclusion, the best noise reduction is attained when a low-speed layer is concentrated uniformly on the underside of the jet. The resulting velocity cross-section is “pear-shaped.”

Table 5.1 UCI 'Classic' Nozzle Exit Conditions

Quantity	Primary	Secondary
Nozzle diameter (mm)	14.3	23.6
Plug diameter (mm)	10.0	-
Lip thickness (mm)	0.74	-
Protrusion (mm)	9.5	-
Velocity[a] (m/s)	460	335
Mach number[a]	0.86	0.95
Bypass ratio[a]	-	4.93
Velocity[b] (m/s)	310	220
Mach number[b]	1.0	0.66
Bypass ratio[b]	-	1.92

Table 5.2 UCI '3BB' Nozzle Exit Conditions

Quantity	Primary	Secondary
Nozzle diameter (mm)	17.0	31.0
Plug diameter (mm)	11.5	-
Lip thickness (mm)	2.2	3.1
Protrusion (mm)	16.2	-
Velocity[a] (m/s)	460	335
Mach number[a]	0.86	0.95
Bypass ratio[a]	-	4.8
Velocity[b] (m/s)	310	220
Mach number[b]	1.0	0.66
Bypass ratio[b]	-	1.87

[a] acoustic measurements

[b] mean velocity measurements

Table 5.3 UCI 'Classic' Nozzle Deflector Configurations

Case	Configuration	ε	**ΔOASPL**
W_i	$\alpha = 17^o$, l = 5 mm, x_{apex} = -4.8 mm.	-	1.4
W_e (equal ε)	$\alpha = 18^o$, l = 10 mm, x_{apex} = 0 mm.	-	2.8
2V (equal ε)	ϕ=90°, c = 2 mm, $\alpha = 10^o$, x_{te} = 0 mm.	0.03	1.5
2V (equal c)	ϕ =90°, c = 4 mm, $\alpha = 10^o$, x_{te} = 0 mm.	0.06	2.4
4V (equal ε)	ϕ =70° and ϕ =110°, c = 2mm, $\alpha = 10^o$, x_{te} = 0 mm.	0.07	3.5
4V (equal c)	ϕ =70° and ϕ =110°, c = 4mm, $\alpha = 10^o$, x_{te} = 0 mm.	0.13	3.8

Table 5.4 UCI '3BB' Nozzle Deflector Configurations

Case	Configuration	ε	**ΔOASPL**
W_i	$\alpha = 17^o$, l = 5 mm.	-	5.3
W_e	$\alpha = 18^o$, l = 10 mm.	-	4.2
2V	ϕ =90°, c = 4 mm, $\alpha = 10^o$, x_{te} = 0 mm.	0.03	3.8
4V	ϕ =70° and ϕ =110°, c = 4 mm, $\alpha = 10^o$, x_{te} = 0 mm.	0.06	5.0

α = angle of attack for vane, half-angle for wedge

c = chord length of vane airfoil

l = length of side of wedge

ϕ = azimuth angle measured from the downward vertical direction

x_{te} = axial location of trailing edge relative to exit of fan nozzle

x_{apex} = axial location of wedge apex relative to exit of fan nozzle

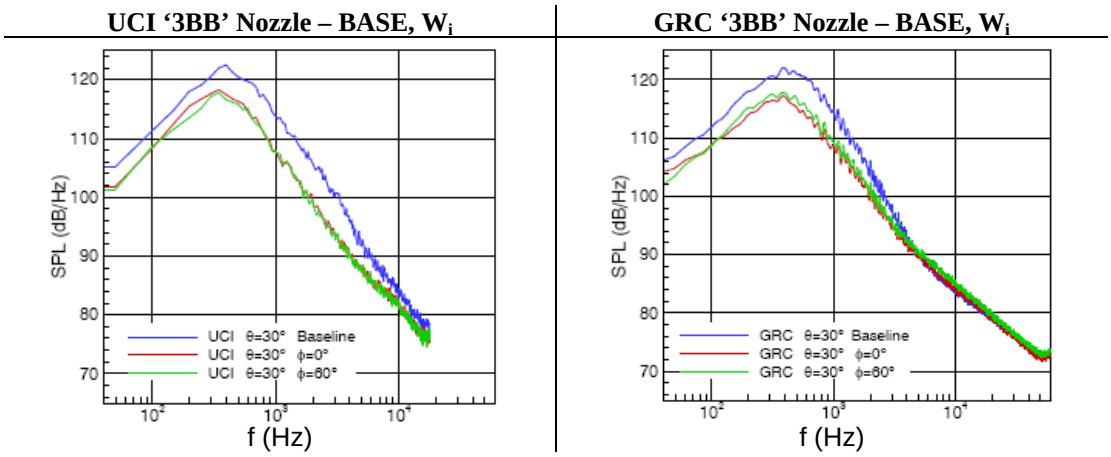

Figure 5.1. Sound pressure level (SPL) measurements for an internal wedge in a nozzle with converging exit streamlines. Similar trends are observed at a) UCI and b) at NASA. (Fig. 5 of Ref. 14)

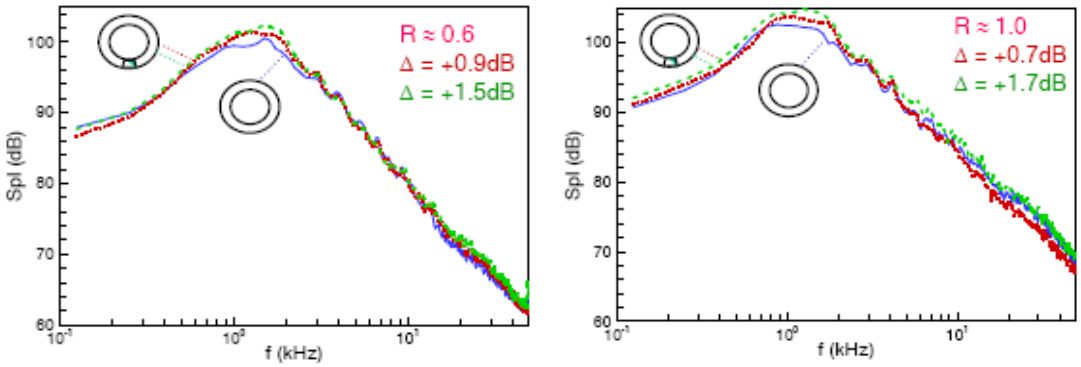

Figure 5.2. Sound pressure level (SPL) measurements for an internal wedge and nozzle with parallel exit streamlines. The wedge causes a noise increase. (Fig. 9 of Ref. 14)

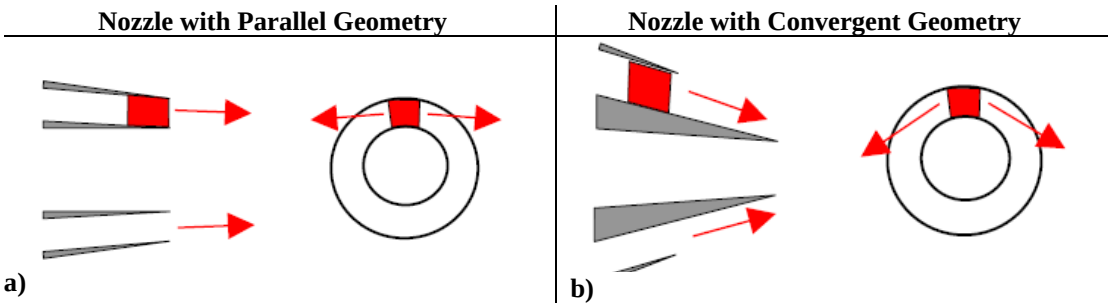

Figure 5.3. Illustration showing hypothesis of deflection of flow in the nozzle with a) parallel geometry and b) with convergent geometry. (Fig. 11 of Ref. 14)

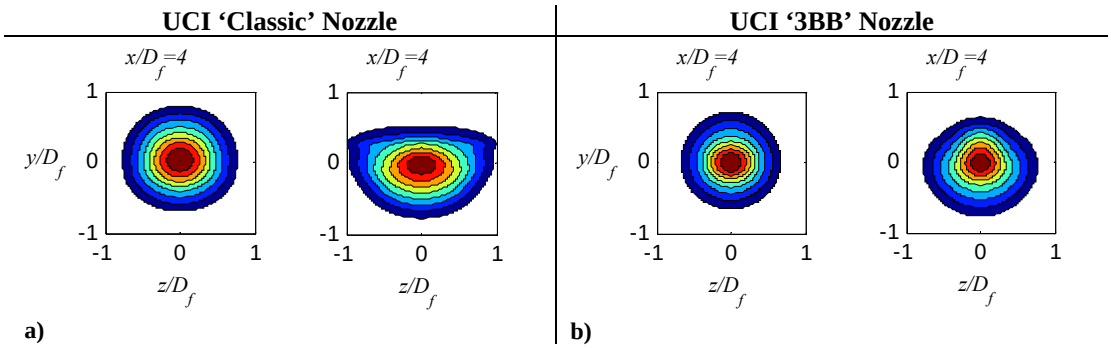

Figure 5.4. Mean flow measurements supporting the hypothesis in Fig. 5.3. Axial velocity isocontours of $u(x,y,0)/U_p$ and $u(x_0, y, z)/u_{max}(x)$ taken at $4D_f$ downstream of the plug tip. a) UCI 'Classic' and b) UCI '3BB' nozzles.

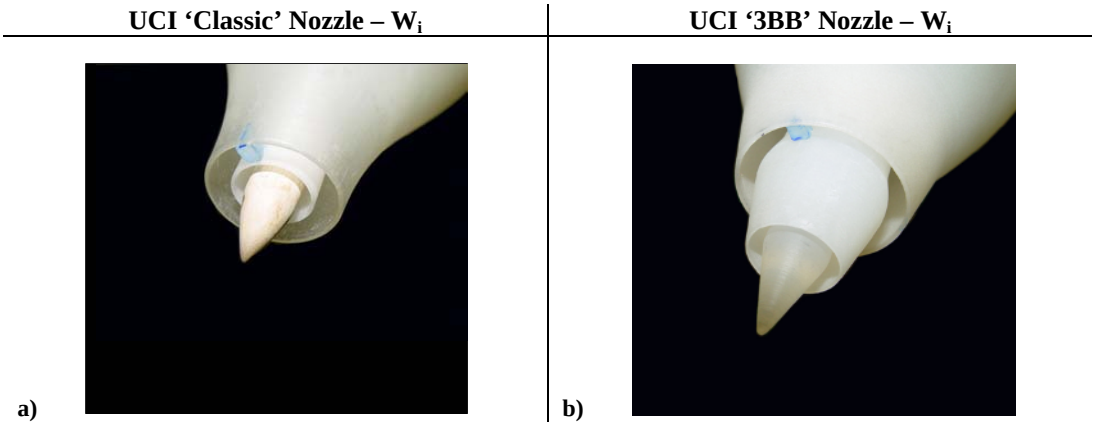

Figure 5.5. Nozzle and internal-wedge configurations that produced the results in Fig.5.4. a) UCI 'Classic' coplanar and b) UCI '3BB' nozzles.

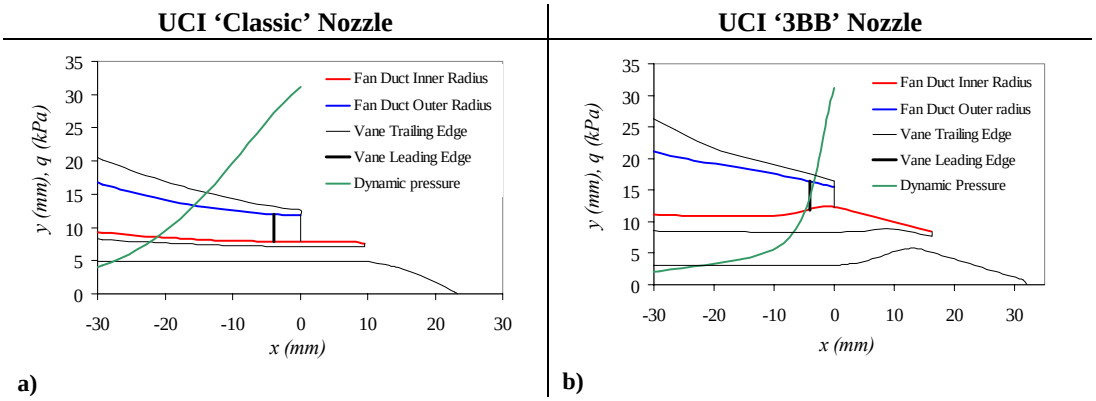

Figure 5.6. Dynamic pressure distributions in a) UCI 'Classic' and b) UCI '3BB' nozzles. Cross-section of a vane with chord length, *c* = 4mm is shown. (Note: The plot in b) is corrected from original print in Ref. 11)

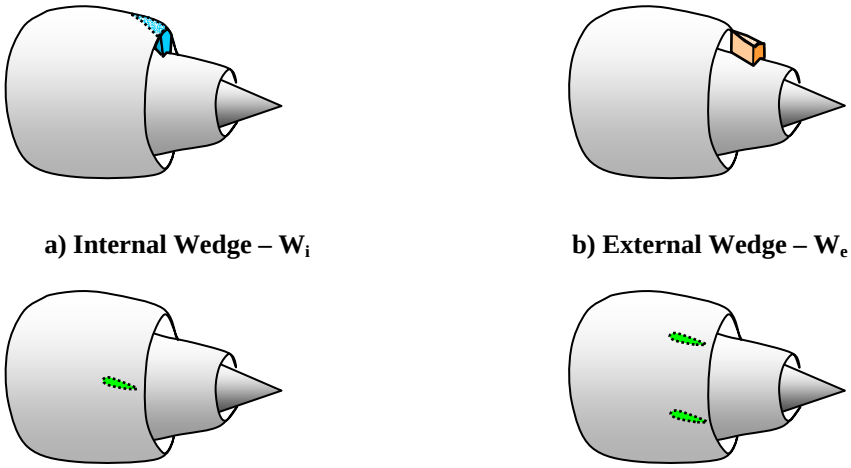

a) Internal Wedge – W_i

b) External Wedge – W_e

c) Single Vane Pair – 2V

d) Two Vane Pairs – 4V

Figure 5.7. Illustrations of deflector configurations tested.

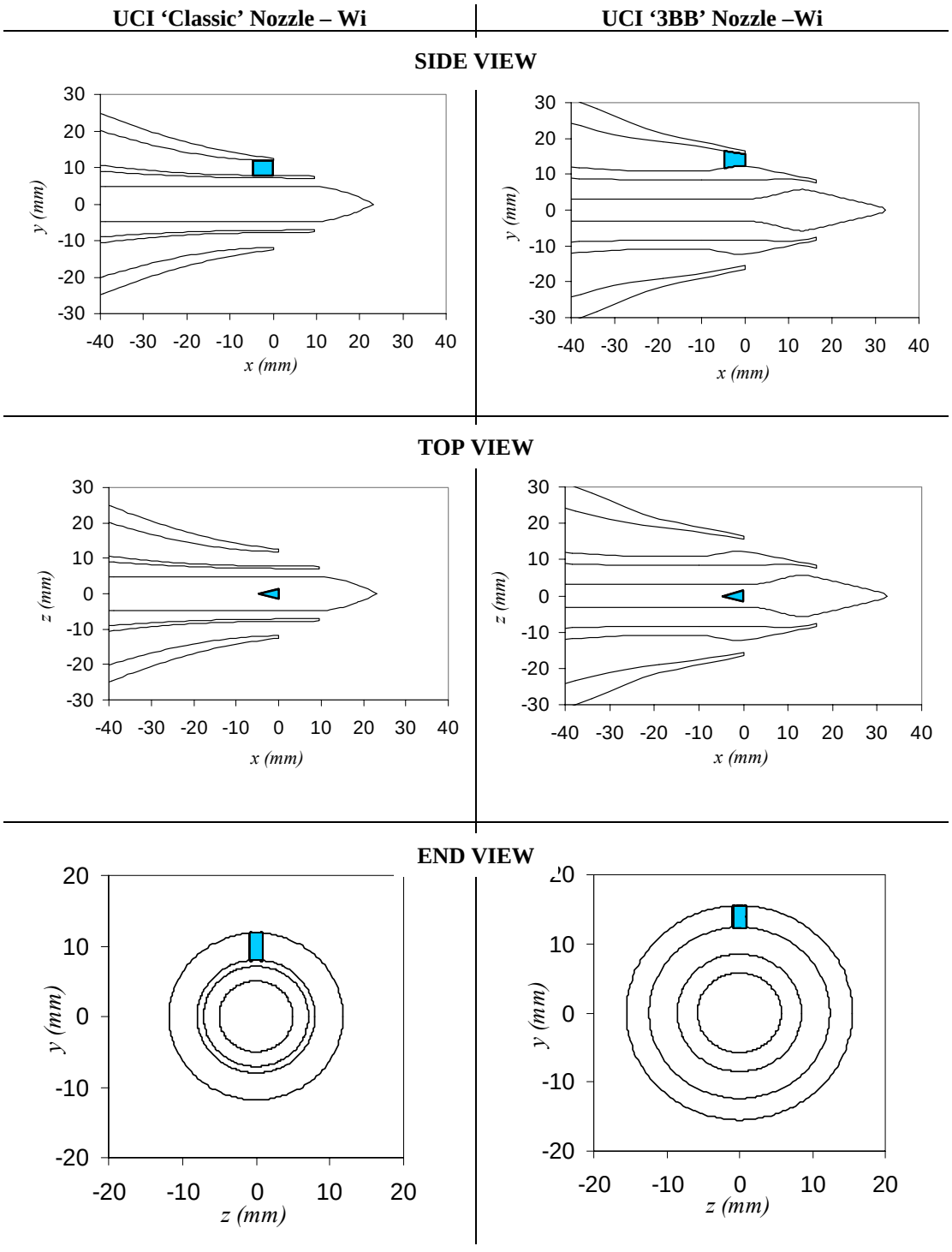

Figure 5.8. Coordinates of UCI 'Classic' (left) and '3BB' (right) nozzles. W_i – an internal wedge. The side length is 5 mm, and the half angle is 17°. The base is placed at x = 0, on the fan exit plane.

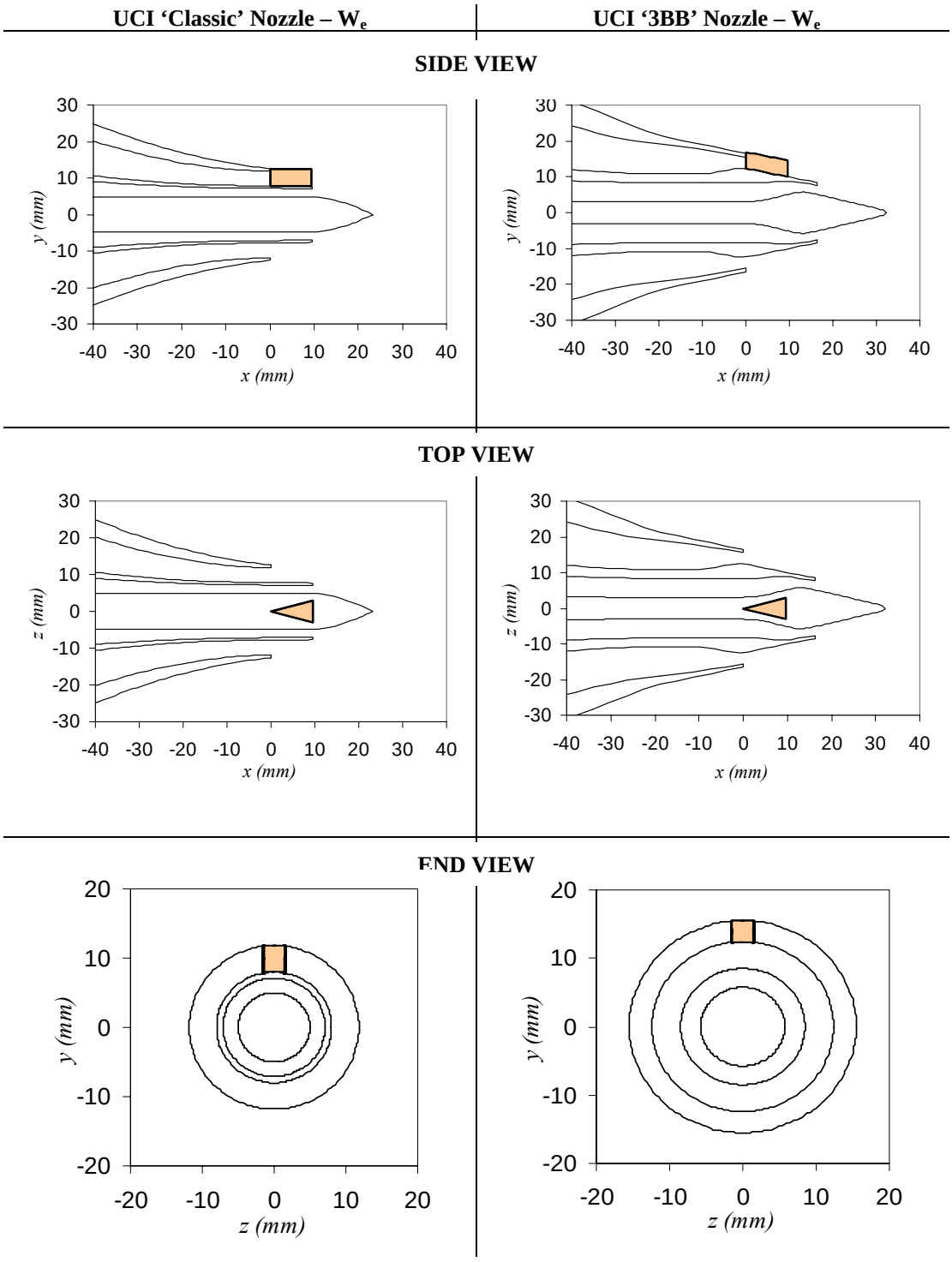

Figure 5.9. Coordinates of UCI 'Classic' (left) and '3BB' (right) nozzles. W_e – an external wedge. The side length is 10 mm, and the half angle is 18°. The apex is placed at x = 0 mm , on the fan exit plane.

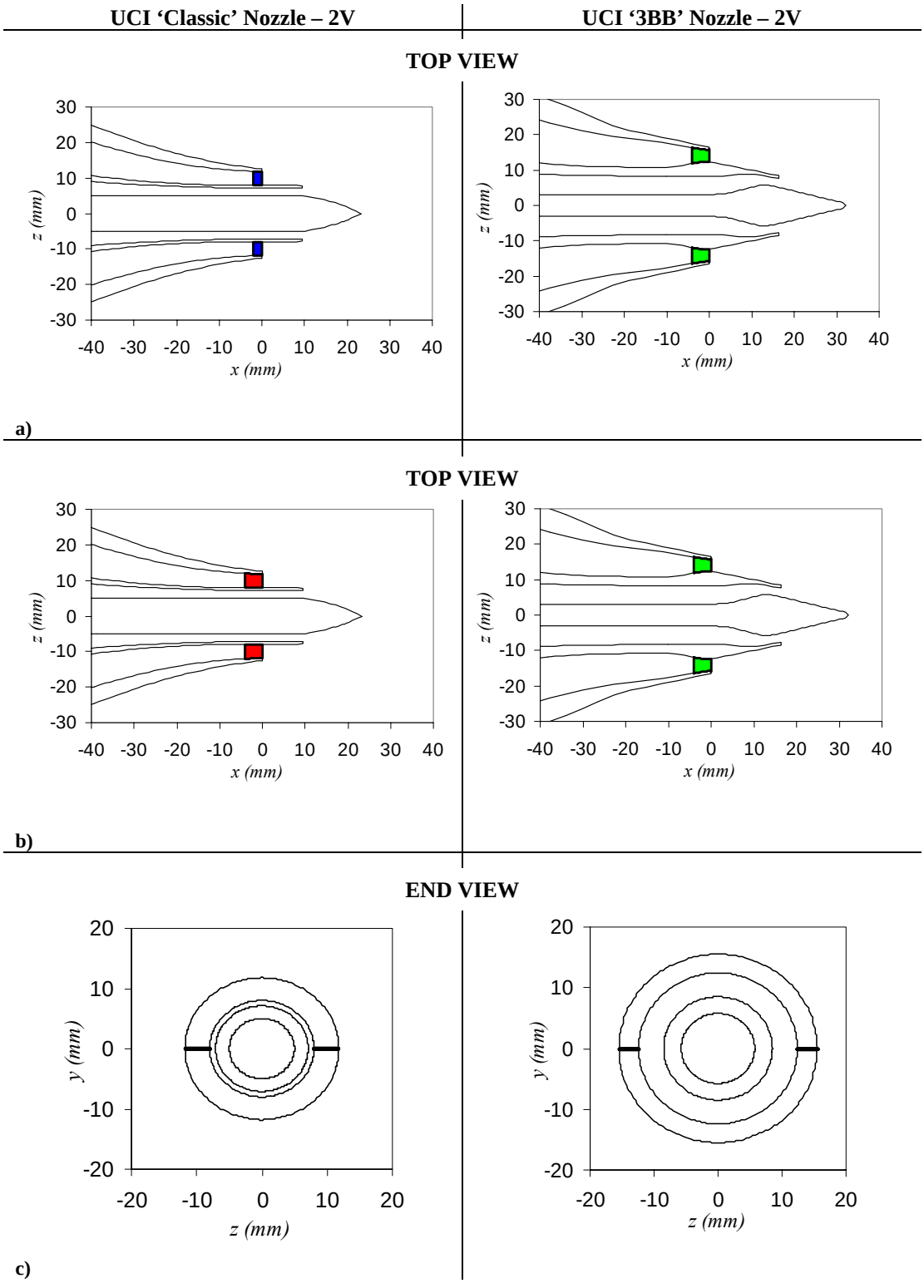

Figure 5.10. Coordinates of UCI 'Classic' (left) and '3BB' (right) nozzles. 2V – a single pair of vanes. a) Equal turning effort comparison, *c* = 2 mm in the 'Classic' nozzle and c = 4mm in the '3BB' nozzle. b) For the equal chord comparison, *c* = 4 mm in both nozzles. c) End views.

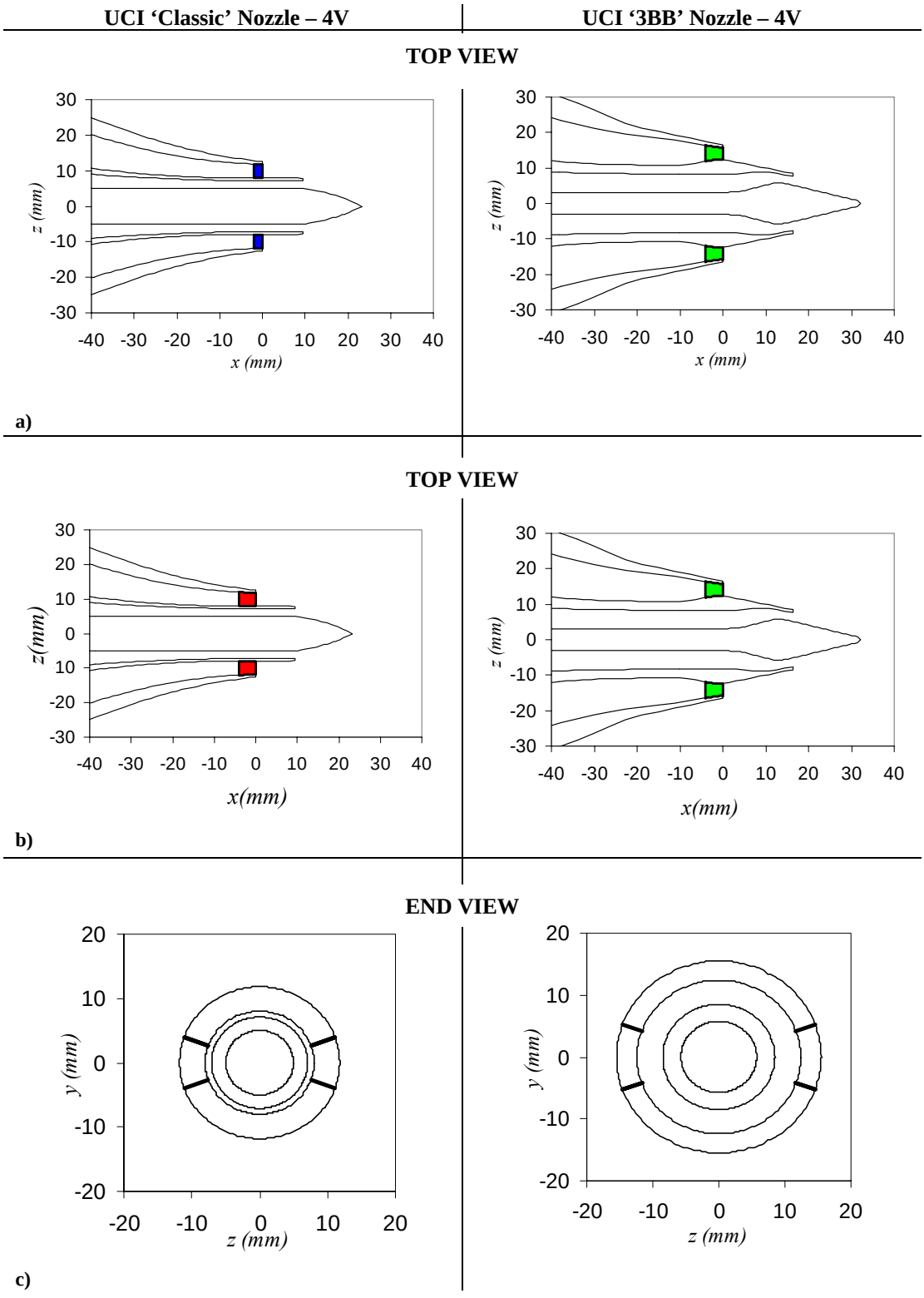

Figure 5.11. Coordinates of UCI 'Classic' (left) and '3BB' (right) nozzles. 4V – two pairs of vanes. a) Equal turning effort comparison, *c* = 2 mm in the 'Classic' nozzle and c = 4 mm in the '3BB' nozzle. b) For the equal chord comparison, *c* = 4 mm in both nozzles. c) End views.

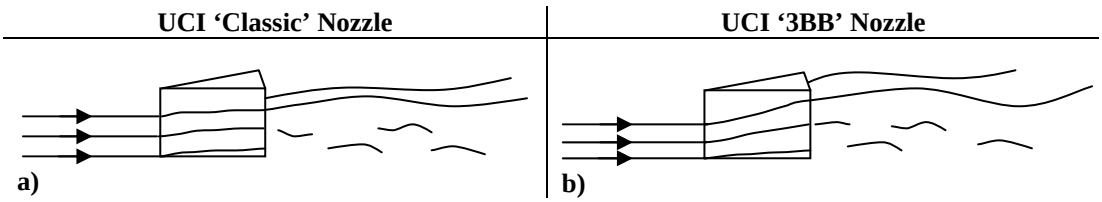

Figure 5.12. The wetted surface area of the wedge. (a) UCI 'Classic' nozzle. (b) UCI '3BB' nozzle.

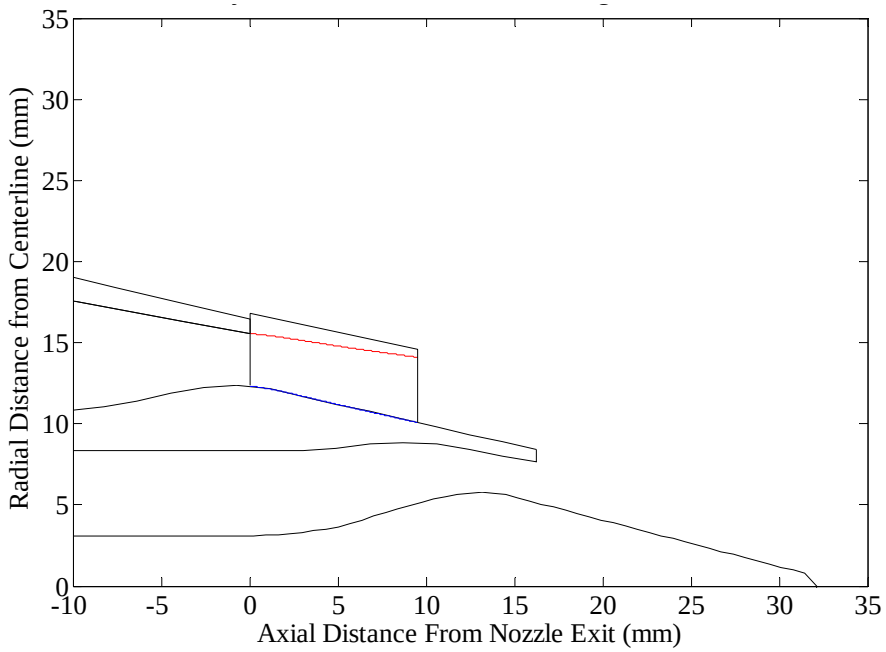

Figure 5.13. Deflector wetted area is estimated for the UCI '3BB' nozzle.

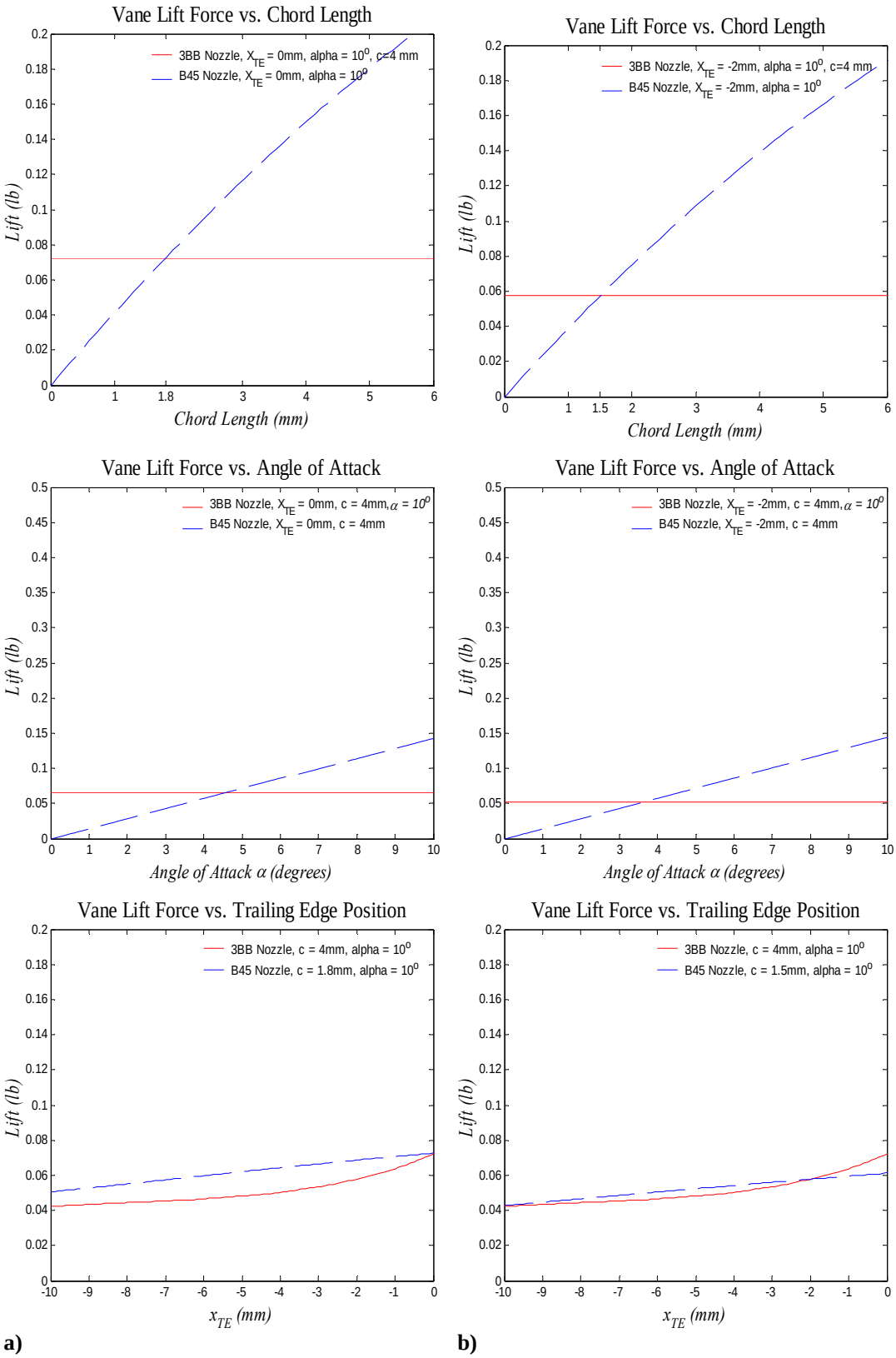

a) **b)**

Figure 5.14. Lift estimates for vane deflectors with trailing edge postion a) x_{te}=0mm and b) x_{te} =-2mm. – UCI '3BB' nozzle -- UCI 'Classic' nozzle.

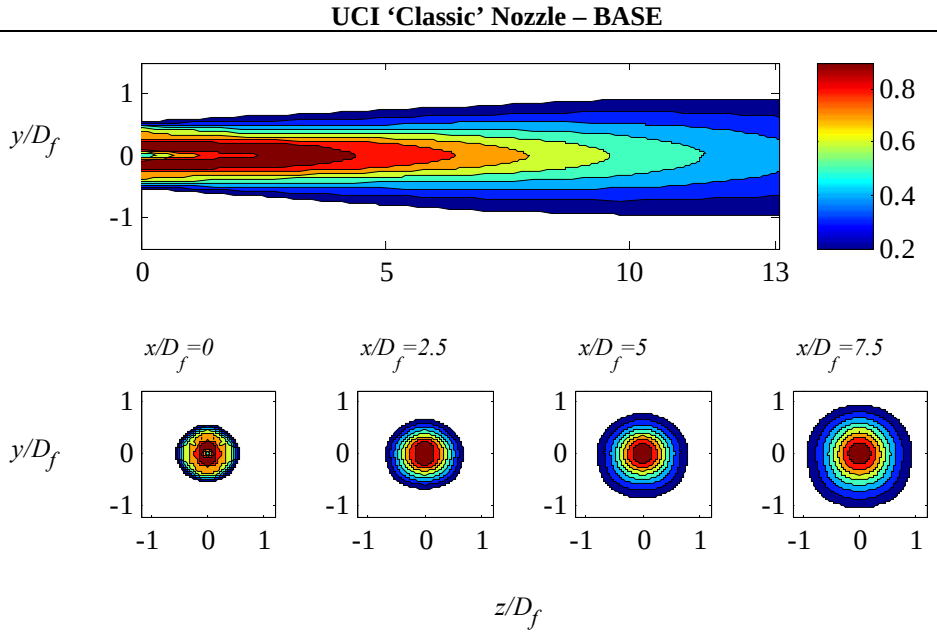

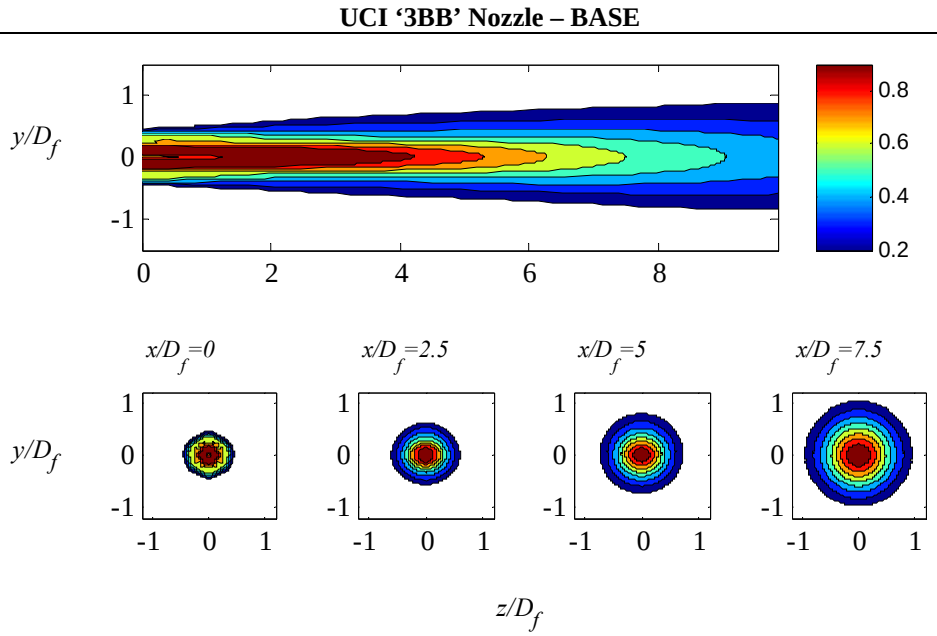

Figure 5.15. Isocontours of $u(x,y,0)/U_p$ on the plane of symmetry, and $u(x_0, y, z)/u_{max}(x)$ at several axial stations, measured with respect to the plug tip. UCI 'Classic' (top) and '3BB' (bottom) baseline nozzles.

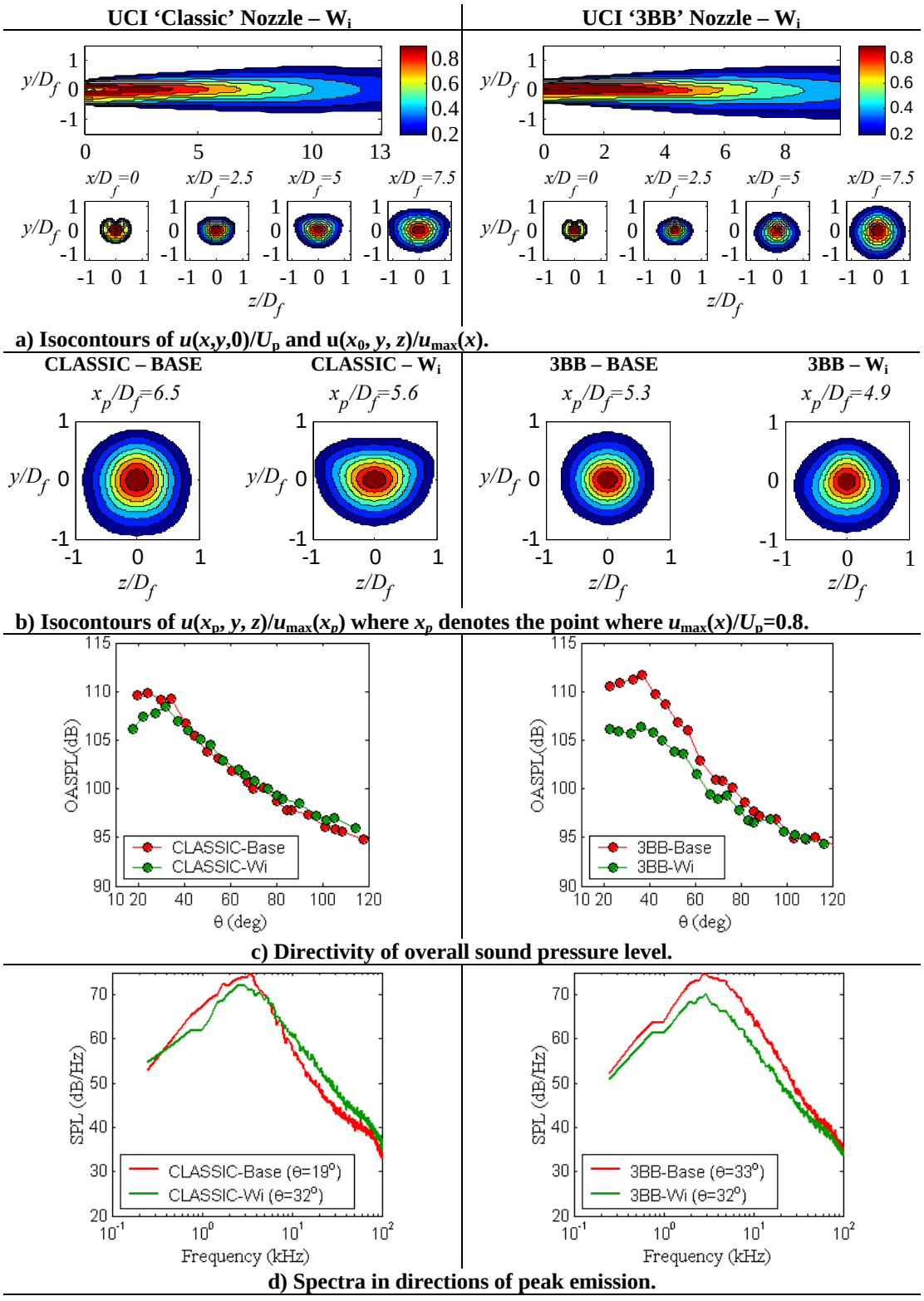

Figure 5.16. UCI 'Classic' (left) and '3BB' (right) nozzles with W_i (internal wedge). The measurements support the hypothesis in Fig. 5.3.

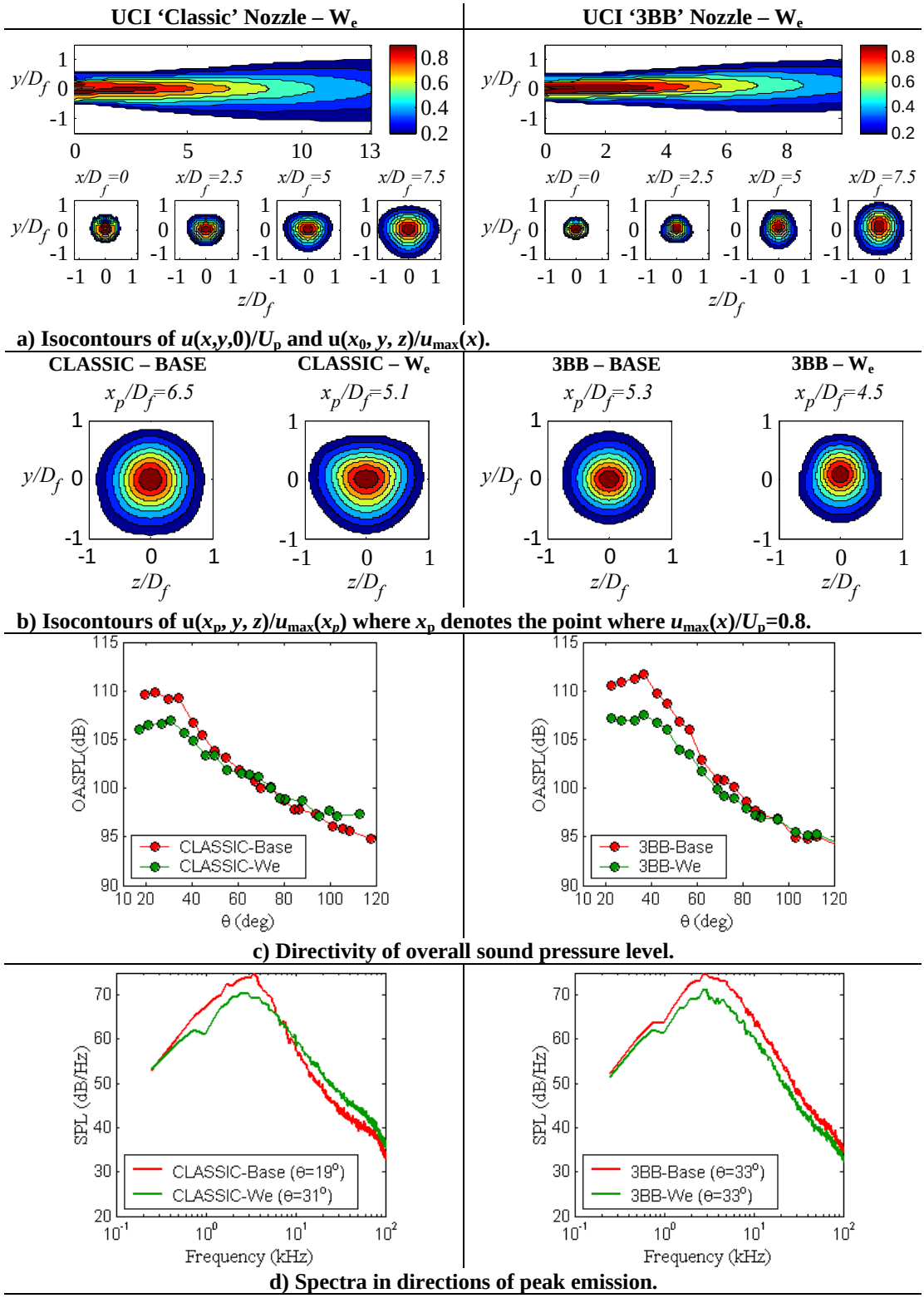

Figure 5.17. UCI 'Classic' (left) and '3BB' (right) nozzles with W_e (external wedge). The measurements support the hypothesis in Fig. 5.3.

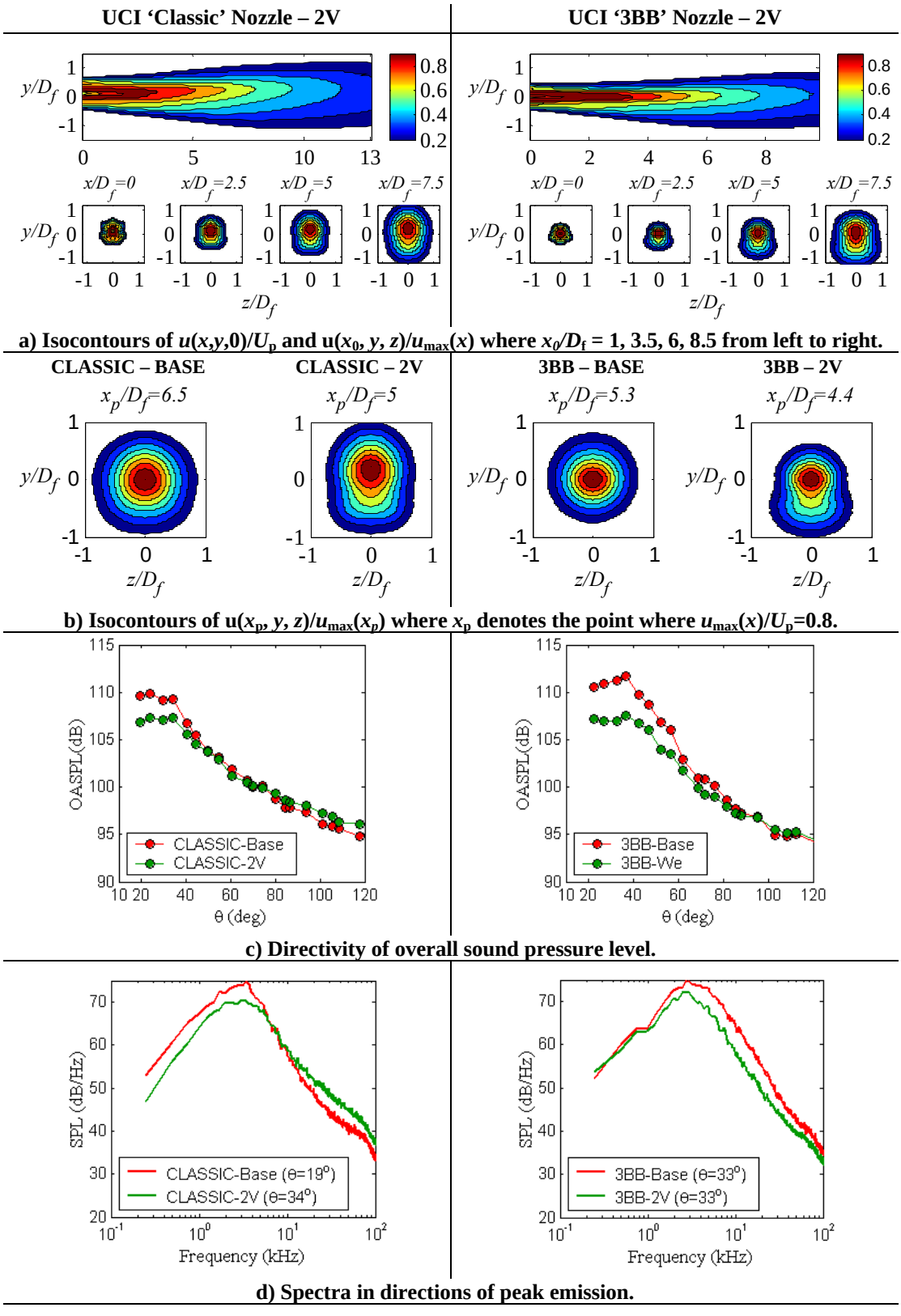

Figure 5.18. UCI 'Classic' (left) and '3BB' (right) nozzles with 2V (pair of vanes.) Equal turning effort, ε.

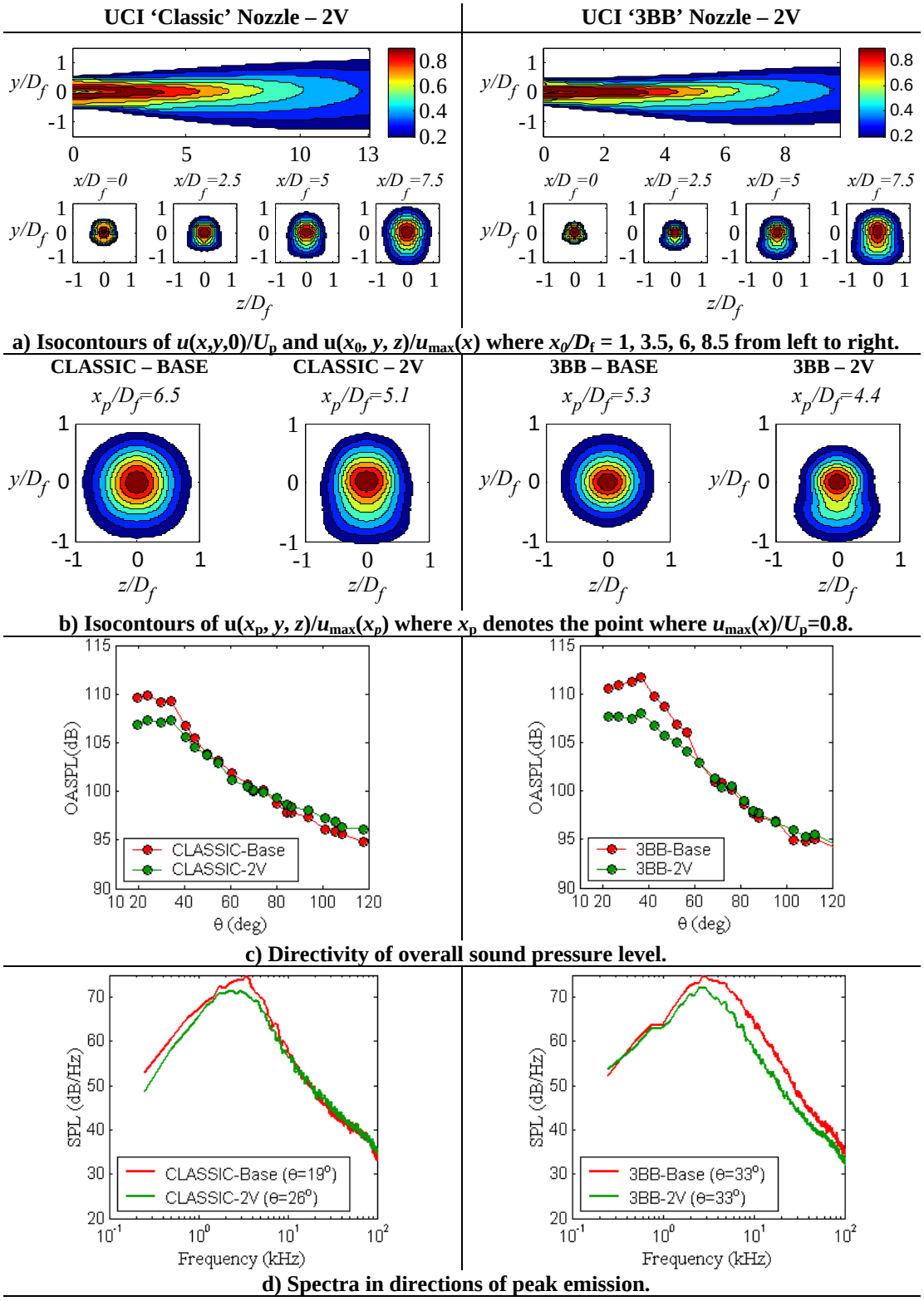

Figure 5.19. **UCI 'Classic' (left) and '3BB' (right)** nozzles **with** 2V **(**pair of vanes**). E**qual chord length**, *c*.**

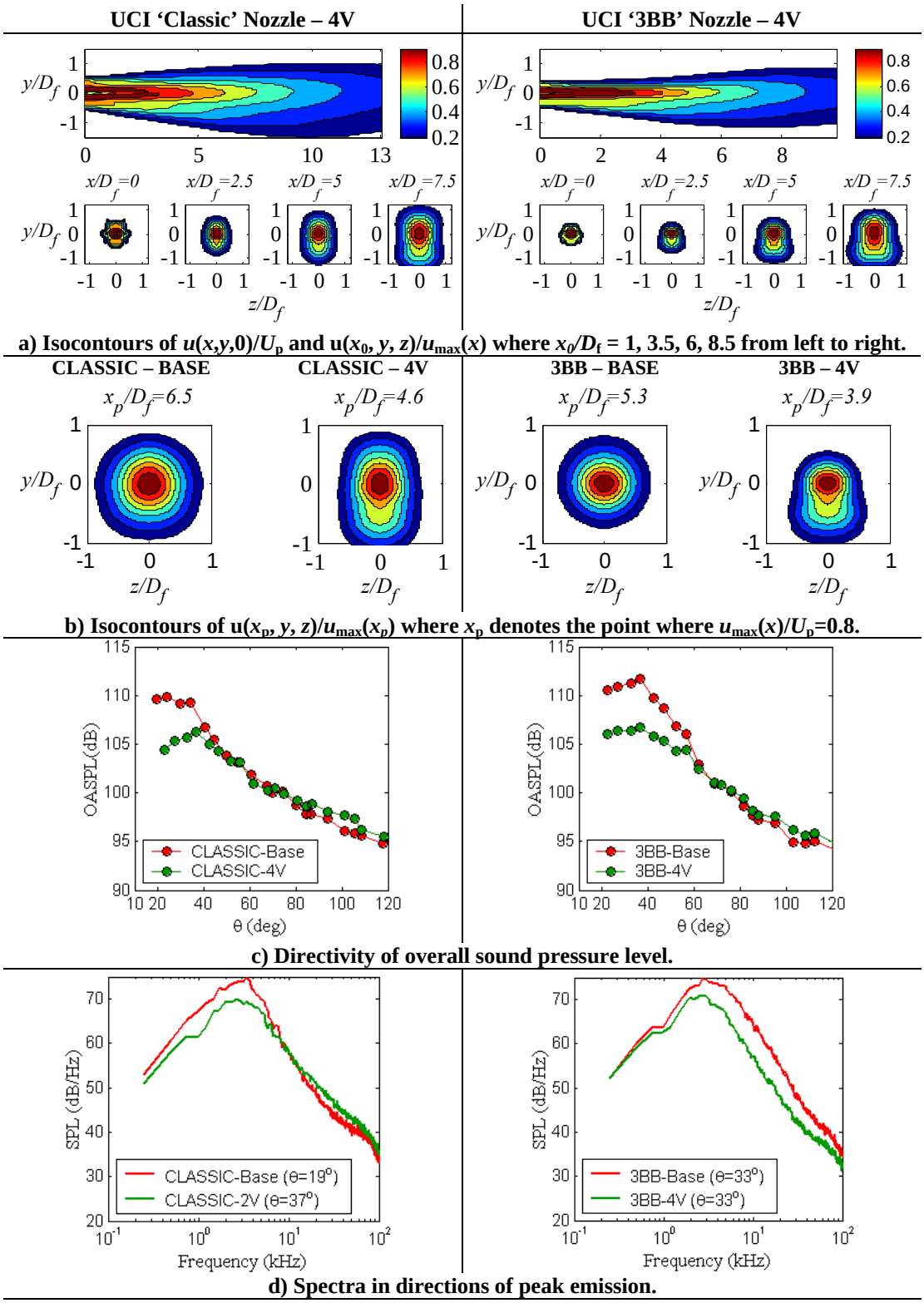

Figure 5.20. UCI 'Classic' (left) and '3BB' (right) nozzles with 4V (two pairs of vanes). Equal tuning effort, ε.

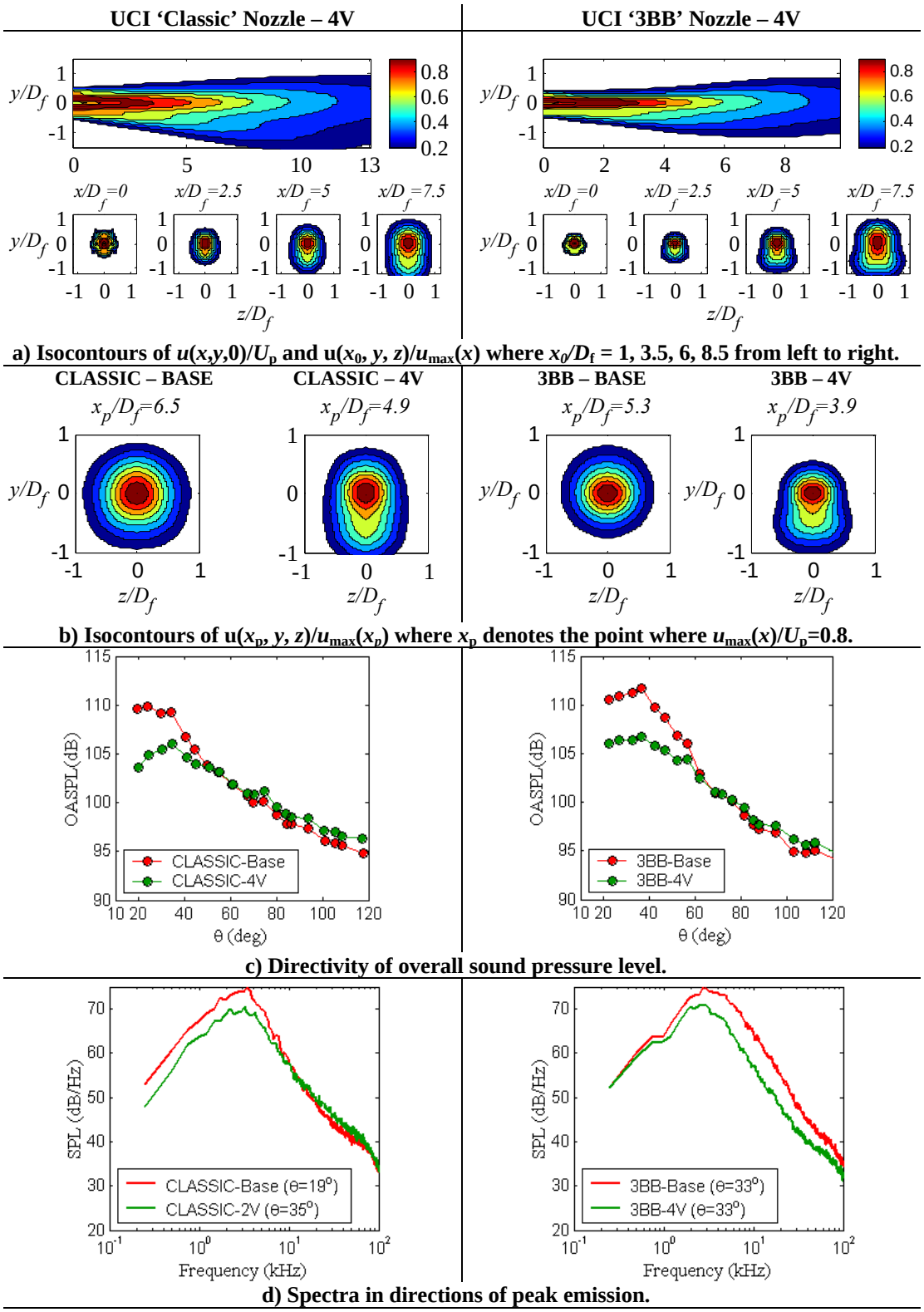

Figure 5.21. Flow field and acoustics of jets issuing from CLASSIC and 3BB nozzles with 4V (two pairs of vanes). Equal chord length, *c*.

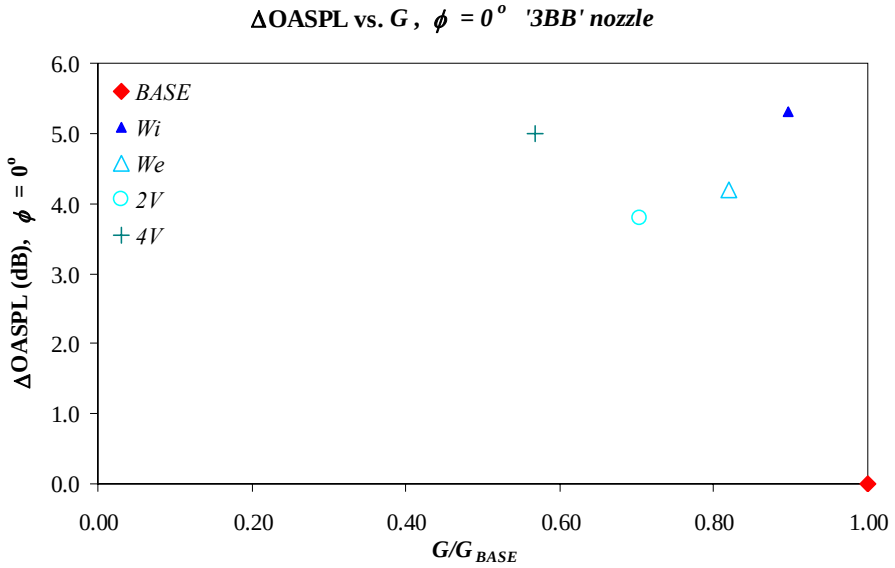

Fig. 5.22. Preliminary correlation on $\phi = 0^{o}$ plane for the UCI '3BB' nozzle.

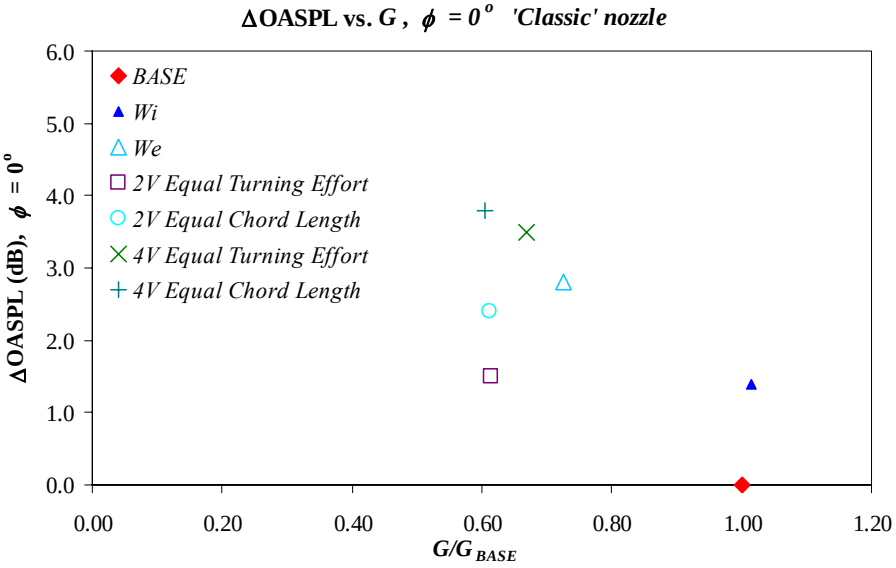

Fig. 5.23. Preliminary correlation on $\phi = 0^{o}$ plane for the UCI 'Classic' nozzle.

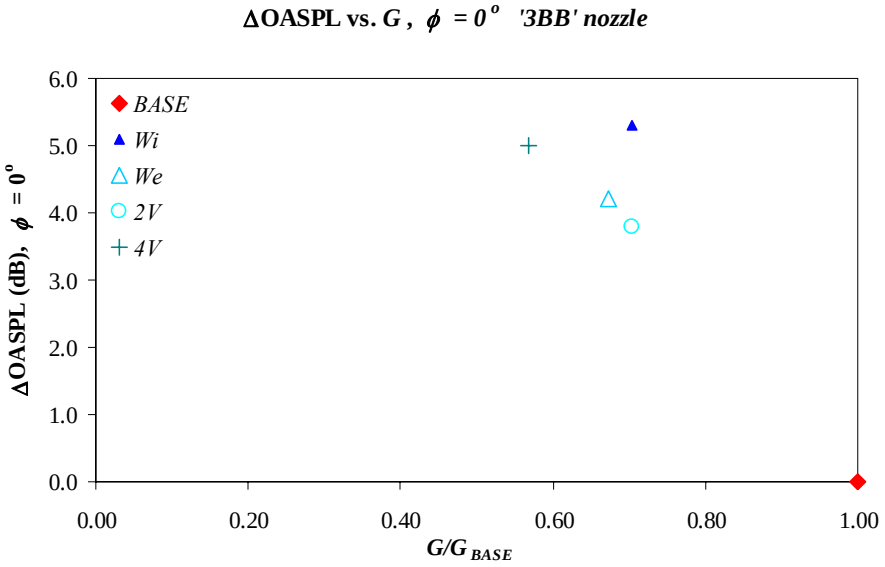

Fig. 5.24. Preliminary correlation on $\phi = 0^{o}$ plane for the UCI '3BB' nozzle. For W_i and W_e, G is calculated using Eq.5.6. For 2V and 4V, Eq.5.5 is used.

Chapter 6

Mean and Turbulent Flow Fields of Asymmetric Dual-Stream Jets

Hot-wire experiments conducted at NASA Glenn Research Center in the CW-17 Open Jet Facility produced mean and turbulent velocity data for several asymmetric jet configurations and a baseline symmetric configuration. It was desired to investigate the mean flow gradient reduction, observed in the UCI experiments (Chapter 5), that was achieved by a wedge-shaped deflector on a nozzle with convergent geometry, and the relation to the turbulent flow field. Mean and turbulent velocity data are presented here. In addition, a correlation between the mean and turbulent flow fields was obtained and it is described here; specifically, a correlation is obtained between the maximum mean velocity gradient in the vicinity of the peak turbulent kinetic energy.

In choosing the deflector configurations, the flow visualization experiments of Ref. 17 were considered, and an attempt to suppress upwash was made. Figure 6.1 shows similar surface flow visualizations using water color paint. As is made evident by the streaklines on the wedge surface, there is spillover at the top of the short wedge, while, there appears to be minimal spillover at the top of the taller wedge. This aerodynamic effect will be important for drag considerations. As pointed out in Chapter 5, a wedge that is in contact

with ambient fluid on the top and at its base has been demonstrated to have 75% less drag than a traditional cylindrical wedge placed in a freestream with a recirculation region forming behind it in the experiments of Ref. 17. Thus, it was desired to look at the effect of upwash or suppressing the upwash on the ability of the deflectors to reduce gradients, and therefore noise, in the downward direction.

The four base wedge configurations are depicted in Fig. 6.2. The subscripts 1 and 2 refer to the external wedges, and the subscripts 3 and 4 denote internal wedges. The tall external wedge (W_1) is twice the height of the annular gap width. The height of the wedge was chosen to be much taller than the annular gap to prevent the air from flowing over the wedge. The second wedge is shorter, starting at a height equal to the annular gap, it flares upward ending with a height 1.25*H*. The cross-sections of the external wedges are shown in Fig. 6.3a.

The third and fourth wedges are internal wedges. One of the internal wedges, (W_3) has a cross-section that matches that of the external wedges (W_1 and W_2). The other has a cross-section corresponding to the internal portion of a pylon design, Fig. 6.3.b. Figure 6.3.c. shows top views of the short wedge (W_2) tested with caps of different cross-sections. The caps were used to investigate the effect of suppressing upwash. Fig. 6.4a illustrates the three caps placed on the wedge.

Since the pylon structure is likely to have an impact on turbulent-mixing noise, the pylon ensemble is composed of three pieces: an internal component, terminating at the fan exit plane (W_4), an external component that is flush mounted against the internal component (pylon), and two side-mounted half wedges (flaps), Fig. 6.4.b. The interior portion of the pylon cross-section is a fast-diverging wedge, deep inside the fan duct,

with a half angle of 30°, with the sides becoming parallel close to the fan exit, Fig. 6.3b. The distance from the apex to the base for all of the wedges is three times the annular gap width, *H*. The half wedges have an angle of approximately 7°. Photographs of the external wedge configurations on the GRC '5BB' nozzle in the CW17 Open Jet Facility are shown in Fig. 6.5, and a photograph of the pylon with flaps is shown in Fig. 6.5.f

6.1 Mean and Turbulent Flow Fields

Figure 6.7 shows the evolution of mean and turbulent kinetic energy velocity profiles for the axisymmetric case from x/D_f=0 to x/D_f=4, referenced to the location of the plug tip. Despite the painstaking effort to eliminate asymmetry from the nozzle upon installation, the flow is evidently very sensitive to asymmetries present in the nozzle geometry. The strong sensitivity of flow to asymmetries in geometry was first pointed out by Birch et al., Ref. 46. As was noted in Chapter 3 the secondary annulus was matched to within 0.005" at three different points using specialized tooling, namely a hole diameter gauge. In Fig. 6.6.a, a thicker annulus is observed on the upper-side of the jet, and in Fig. 6.6.b, lower peak turbulent kinetic energy values are observed on the upper-side of the jet. On the underside of the jet, corresponding to the thinner annulus, higher peak turbulent kinetic energy levels are observed for the "axisymmetric" baseline case.

6.1.1 Mean Velocity and Radial Velocity Gradient

Figures 6.8–6.23 show evolution of the mean velocity profiles and the radial velocity gradient profiles for seven asymmetric configurations and for the baseline case. Figures 6.8 and 6.9 show evolution of the baseline jet, and the profiles are nearly

symmetric. Transverse profiles at 8 axial positions referenced from the plug tip are shown. The first four cases presented are for the wedge deflectors alone and the latter three are for external wedges with caps. In the initial region of the jet, there are two distinct streams, evident as bumps in the profile that have not yet been mixed with one another. They are typically flat until they have been mixed. The primary stream is longer because it represents the higher velocity stream. The two 'shoulders' on either side of the primary stream correspond to the secondary flow, with slower velocity. There is a defect in the middle of the primary stream because the center plug creates a wake flow region. There are steep gradients surrounding the plug wake because a shear layer forms between the wake flow and between the primary stream. Between the primary and secondary streams, the primary mixing layer is characterized by steep mean velocity gradients. Between the ambient and the secondary stream, the secondary mixing layer is also characterized by steep gradients in the mean velocity. After the primary and secondary shear layers merge, the secondary core is no longer distinguishable as two flat humps. Soon, the effect of a secondary flow is no longer evident at all, marking the end of the generalized secondary core (GSC), which was defined in Chapter 2. Past this complex region, the behavior of the jet is characteristic of a single stream jet (sometimes referred to as the simple region) and the mean velocity profiles have Gaussian-like distributions, with one inflection point.

Figures 6.10 and 6.11 are for the tall external wedge, W_1, with height equal to two times the annular gap width, *H*. The effect of the wedge is to displace some of the low speed flow from above and thicken the low speed region on the underside of the jet, or equivalently, to reduce the peak velocity gradients underneath the jet. The peak velocity

gradient is reduced at all axial positions underneath the jet. Above the primary jet, the peak velocity gradient is reduced for most axial positions, and increased in the initial region, just behind the wedge where the primary jet is left exposed to the ambient air. The mean flow profiles of all asymmetric cases shown here decay more rapidly than the baseline jet, indicating enhanced mixing.

Figures 6.12 and 6.13 are for the short external wedge, W_2, with base height equal to 1.25 times the annular gap width, *H*. Similar to W_1, this wedge reduces the maximum gradients in mean velocity at all axial positions underneath the jet, and the increase above the jet is not as much as for W_1. This could be an important consideration in choosing the ultimate deflector design, since an increase in velocity gradient and mixing on the upper side of the jet could increase noise and is not desireable. The wedge height did not need to be taller than the free surface of the secondary jet stream for the wedge to maintain its effectiveness, as is made evident by the difference between the flow characteristics of W_1 and W_2. This could also an important for aerodynamic considerations, such as reducing drag when the wedge is deployed.

Figures 6.14 and 6.15 are for the internal wedge, W_3, which uses the same cross-section as W_1 and W_2. This wedge dramatically reduces the maximum velocity gradients at all axial positions underneath the jet and at most axial positions above the jet except just behind the wedge in the initial region of the jet, where a steep increase is noted, much steeper than any other asymmetric case presented here. The mean flow profiles decay more rapidly than those of W_1 or W_2 with respect to the baseline, and also more rapidly than all other asymmetric cases presented. This marks a reduced potential core length, and therefore, a reduced turbulent mixing noise source volume.

Figures 6.16 and 6.17 are for the internal wedge, W_4, with a rapidly converging cross-section deep inside the fan duct to nearly parallel sidewalls at the fan exit, see Fig. 6.3b. This wedge results in reduction of peak velocity gradients underneath the jet and above the jet, except just behind the wedge in the initial region of the jet, similar to those observed in the case external wedge case, W_1.

Figures 6.18 and 6.19 are for the external wedge, W_2, with a rectangular cap to suppress any upwash that may cause spillover at the top of the wedge. The rectangular cap has a width equal to the wedge base width, B = 1.04 cm, and is referred to as Cap1. Figs. 6.20 and 6.21 use a rectangular cap with width equal to twice the wedge base width, Cap2, and Figs. 6.22 and 6.23 show results for the trapezoidal shaped cap, Cap3. The results here are not too different from the results for the wedge alone, Figs. 6.12 and 6.13.

Figs. 6.24–6.31 show loci of inflection points for the same cases. Figure 6.24 shows inflectional loci for the baseline case. The generalized secondary core (GSC) of a dual-stream jet is defined by the loop formed by the second and third inflectional loci of the mean velocity profile, Ref. 7 (not looking at the inflection points contributed by the presence of the plug wake). The lengths of the GSC above and below the jet are listed in Table 6.1 for each case. The length of the GSC is very important from a jet noise standpoint. The primary potential core should not be left exposed to ambient, but covered by the GSC, if possible. In all of the asymmetric cases presented here except W_4, the GSC is elongated on the underside of the jet (solid blue line) and reduced on the upperside of the jet (solid red line) with respect to the baseline jet. In the case of W_4 corresponding to the internal structure of the pylon, the GSC was shortened underneath the jet. This may be a result of poor nozzle alignment after installation of this internal

wedge. In the cases in which the GSC was determined to be zero above the jet, the primary stream mixed directly with the ambient stream behind the wedge. This was true for the internal wedges and for W_2 + Cap2, in which neither upwash nor spillover were present at the top of the wedge, and recirculation regions were not allowed to develop behind the wedge. This could be important for drag considerations, since elimination of a recirculation region would reduce form drag. It must be weighed with other design considerations since placing a cap on the external wedge would add skin friction and may offset the potential benefit.

Figures 6.32–6.39 show the axial distribution of the maximum mean velocity and maximum radial velocity gradient for the baseline and for seven asymmetric cases. The velocity is normalized by the primary jet exit velocity, U_p. In each of the asymmetric cases, the maximum velocity profile decays faster than for the baseline case. Defining the primary potential core to end where the maximum velocity decays to 90% of the primary jet exit velocity, Table 6.1 lists the values of primary potential core lengths for each case. The distributions of velocity gradient (right) show the effect of the deflector on the mean velocity gradient on the ϕ=0° plane. In all cases, the maximum gradient was reduced underneath the jet across for every axial position. Exceptional reduction is observed for W_3 compared with the other cases.

The plots showing distributions in the reduction in maximum velocity gradient are extremely important to noise reduction applications. In Chapter 5 it was shown that the most successful deflector configurations in achieving noise reductions were accompanied by reduced gradients underneath the jet. These plots show the potential that each configuration has in reducing noise emitted toward the ground. Initially, the maximum

gradient decreases rapidly. When the primary and secondary shear layers begin to merge there is an increase. Finally, the maximum gradient reaches a local maximum value before it continues to decay. All of the cases display this behavior, except for W_3, which does not show an increase after the initial rapid decay.

Figures 6.40–6.47 show the mean velocity isocontours on the *xy*-plane (the plane of symmetry). The velocity is normalized by the primary jet exit velocity, U_p and the contours from 0.2 to 0.9 are shown. Figure 6.40 is for the baseline nozzle, and it is nearly perfectly symmetric. The lengths of the primary potential cores can be determined by viewing these plots. The primary potential core is defined to end where the maximum velocity is 90% of the primary jet exit velocity, so the first contour, or the dark brown contour, corresponds to the primary potential core. In all of the asymmetric cases that follow, the length of the primary potential core, and therefore, the volume of the dominant noise source region is reduced. Potential core lengths non-dimensionalized by the fan diameter are listed in Table 6.1. Also visible in these figures is the velocity defect due to the placement of the wedge. One can see that the wedge has affected the flow on the upper side in the initial region of the jet. The region behind the wedge would ideally be filled with ambient fluid, and there would be no recirculation. This would be the most ideal configuration for aerodynamic performance considerations, Ref. 17. The wake due to the plug, along the centerline of the jet is visible.

Figures 6.48–6.53 show the mean velocity isocontours on the *yz*-plane, or the plane of symmetry for the baseline case and for W_1–W_3 at x/D_f=0 and at x/D_f=4. In Fig. 6.48, the cross-sectional velocity isocontours of the jet plume are very nearly circular as is to be expected for good axisymmetry of the nozzles. In Figs. 6.49–6.51 the defect due to the

wake of the wedge is apparent at x/D_f=0, and at x/D_f=4 the cross-sectional velocity isocontours of the jet plume are pear-shaped. The pear-shaped contours were determined to be acoustically superior to other shapes in the UCI experiments, as noted in Chapter 5. Based on the results of the UCI experiments, the mean flow cross-sectional shape suggests that the wedges may achieve a noise reduction in the '5BB' nozzle, but acoustic measurements are still required to confirm this, and they are also needed to determine by how much the noise can be reduced. Note the augmented pear-shape in Fig. 6.51.b due to the internal wedge W_3 as compared to the pear-shapes in Figs. 6.49.b and 6.50.b due to the external wedges. Figure 6.52a shows similar pear-shape in cross-sectional velocity profile of the jet plume with internal wedge, W_4.

Figures 6.52 and 6.53 show comparisons between the internal wedge, W_4 corresponding to the internal pylon structure, and the external pylon structure and external flaps. Figure 6.52 shows that there is not much change in the mean flow field between W_4 and W_4 + pylon. This revealed that the internal portion of the pylon is responsible for most of the deflection of the flow, and the external portion of the pylon does not intrude much into the jet plume. Rather, it sits in the dead-flow region created by W_4. Figure 6.53 shows that the addition of external flaps alters the shape of the cross-sectional mean velocity profile. It would be worthwhile to conduct an optimization for flap angle by taking noise measurements. The flaps would be ideally deployed during takeoff and retracted during flight.

6.1.2 Turbulence Field

Figures 6.54–6.69 show the evolution of the RMS axial velocity component and of the turbulent kinetic energy for the baseline case and for seven asymmetric configurations. Transverse profiles at 8 axial positions referenced from the plug tip are shown. Figures 6.54 and 6.55 are for the baseline case, and the profiles are nearly symmetric. The maximum turbulence intensity occurs just past the end of the primary potential core, around $5D_f$–$6D_f$. The RMS profiles are qualitatively very similar to the turbulent kinetic energy profiles because the axial component is the dominant component in the turbulent kinetic energy. A larger view of the baseline profiles is shown in Fig. 6.7 up to x/D_f=4. Three distinct turbulence regions are notable in the initial region of the jet. In the wake behind the plug, there is non-zero turbulence; the bump on y = 0 corresponds to this turbulence region. The turbulence in the primary mixing region is noteable in Fig. 6.7, and turbulence in the secondary mixing region is the outside peak. The profile never reaches zero because the hot-wire probe never measures zero turbulence. This is a result of the finite spacing between the crossed probes, making it difficult to measure accurate values in regions where high spatial resolution is required. Downstream of the plug tip, about 1.5–2D_f, the two mixing layers are completely merged, and there is only one turbulence peak radially outward from the jet centerline.

Figures 6.56 and 6.57 are for the tall external wedge, W_1, with height equal to two times the annular gap width, H. Similar to the velocity gradient, the peak turbulence intensity is reduced at all axial positions underneath the jet. Above the primary jet, the peak turbulence intensity is increased for most axial positions. A correlation is beginning

to appear between the effect that the wedge-deflectors have on the mean flow gradient and on the turbulence intensity.

Figures 6.58 and 6.59 are for the short external wedge, W_2, with base height equal to 1.25 times the annular gap width, H. Similar to W_1, this wedge reduces the peak turbulence intensity at all axial positions underneath the jet. Above the primary jet, the peak turbulence intensity is slightly increased for most axial positions up to about x/D_f=7.

Figures 6.60 and 6.61 are for the internal wedge, W_3, with congruent cross-section to W_1 and W_2. This wedge dramatically reduces the peak turbulence intensity at all axial positions underneath the jet and significantly increases the values in the initial region of the jet, up to about x/D_f = 5.

Figures 6.62 and 6.63 are for the internal wedge, W_4, with rapidly converging cross-section deep inside the fan duct to nearly parallel sidewalls at the fan exit. This wedge results in redistributions of turbulence intensity similar to W_2.

Figures 6.64–6.69 are for the external wedge, W_2, with caps. The caps are shown in Figs. 6.3.b and 6.4.b. Figures 6.64 and 6.65 are for the external wedge, W_2, with Cap1. Figs. 6.66 and 6.67 are for W_2, with Cap2, and Figs. 6.68 and 6.69 are for W_2, with Cap3. In these cases reduction in turbulence intensity, similar to W_2, is observed underneath the jet, while the behavior above the jet is similar to that of the internal wedge. Above the primary jet, the peak turbulence intensity is increased up to about x/D_f=5. The cap appears to assist in reduction of the peak turbulent kinetic energy levels underneath the jet, with the tradeoff being an increase on the upper side of the jet. The largest cap results in increased levels of reduction, and the smallest cap results in minimal reduction

compared to W_2 alone. Acoustic measurements are necessary to further assess the potential benefits of having a cap.

Figures 6.70–6.77 show the axial distributions of maximum turbulent kinetic energy, k, normalized by the primary jet exit velocity, U_p^2, above and below the jet centerline for the baseline and for seven axymmetric configurations. Underneath the jet, the peak value of k is always reduced with respect to the baseline symmetric configuration. Above the jet centerline, the peak value of k is increased up to a given axial location, thereafter, it is reduced. An important design consideration may be how much the turbulence levels can be reduced on the underside of the jet without the compromise of an increase above the jet. Increased turbulence above the jet could very well affect sideline noise emissions, and it is a compromise that one must take into account when designing a wedge-shaped deflector for noise-emissions reduction. Table 6.1 lists the values of peak k above and below jet centerline for each case.

Figure 6.70 shows the axial distribution of the maximum turbulent kinetic energy for the baseline jet above and below the centerline. The profiles are nearly symmetric with respect to one another, about the jet centerline. The peak turbulence level occurs past the end of the primary potential core, close to x/D_f=6 on both sides. Between x/D_f=2 and x/D_f=3 the maximum turbulent kinetic energy does not grow as rapidly as it does both upstream and downstream of this location. This can also be seen in Fig. 6.7.b by observing the peaks on either side of the jet centerline for x/D_f=2–3.

Figure 6.71 shows the axial distribution of the maximum turbulent kinetic energy for W_1 overlaid with the baseline jet both above and below the centerline. The turbulent kinetic energy is reduced underneath the jet for all axial locations, and the most

significant reduction occurs for the peak value. Above the jet centerline, the turbulent kinetic energy is increased up to about x/D_f=6.

Figure 6.72 shows the axial distribution of the maximum turbulent kinetic energy for W_2 overlaid with the baseline jet both above and below the centerline. Similar to W_1, reduction in turbulent kinetic energy underneath the jet is observed. The increase in the initial region of the jet is less on the upperside of the jet centerline. This feature is a consequence of the difference in wedge geometries. It would be interesting to look at noise measurements on the sideline and see if this difference does indeed play a role in sideline noise emissions.

Figure 6.73 shows the axial distribution of the maximum turbulent kinetic energy for W_3 overlaid with the baseline jet both above and below the centerline. Dramatic reduction in peak levels is observed, much more than that which was observed due to the external wedges. While the significant amount of reduction at first may look very attractive, it is accompanied by a similarly dramatic increase in peak values of turbulent kinetic energy above the jet centerline, which may offset any groundward emissions reduction.

Figure 6.74 shows the axial distribution of the maximum turbulent kinetic energy for W_4 overlaid with the baseline jet both above and below the centerline. The distributions are similar to those for W_1. The internal wedge is not as attractive for noise emissions reduction as the external wedge because it alters the mass flow rate and the bypass ratio. For this reason, the external wedge is thought to be the most likely candidate as a fan flow deflector for noise suppression.

Figures 6.75–6.77 show the axial distributions of the maximum turbulent kinetic energy for W_2 and caps overlaid with the baseline jet both above and below the centerline. The distributions are similar to those for W_2 below the jet centerline. Above the jet centerline, the turbulence is increased at levels comparable to the internal wedge (W_3). The caps do not look like potentially good design solutions, not withstanding skin friction that would add to thrust loss of the design. However, this is still speculative without noise measurements.

Figures 6.78–6.85 show the RMS distributions of the axial velocity component on the *xy*-plane for the baseline and for seven axymmetric configurations. $u_{RMS}(x,y,0)$ is normalized by the primary jet exit velocity, U_p. In Fig. 6.78, the baseline case is shown. The turbulence intensity is slightly greater underneath the jet centerline. In this plot it is possible to see both the primary and secondary cores. These are the regions of low turbulence intensity. The peak turbulence intensity occurs just past the end of the primary potential core.

Figure 6.79 and 6.80 are for the external wedges W_1 and W_2. They show similar redistribution in turbulence intensity. The values underneath the jet are reduced significantly, with an increase above the jet centerline. In Fig. 6.80 the increase in turbulence intensity above the jet in the initial region is not as much as it is in Fig. 6.79. Both show significant reduction underneath the jet, indicating their potential to reduce noise in the downward direction.

Figure 6.81 is for the internal wedge with similar cross-section (W_3). The redistribution for this case is the most dramatic observed of all seven cases. The turbulence intensity levels are reduced quite significantly on the underside of the jet, but

the reduction is accompanied by increased levels above the jet centerline. This wedge is expected to reduce noise emissions in the downward direction when placed on a nozzle with converging exit streamlines. It is not clear what impact the increased turbulence on the upper side of the jet will have on noise emissions, if any.

Figure 6.82 is for internal wedge corresponding to the pylon structure (W_4). The redistribution is modest in comparison with (W_3), and it is comparable to that of the first two external wedge cases, in Figs. 6.79 and 6.80. Figs. 6.73-6.76 show similar redistribuitions, and peak values are listed in Tables 6.1.

Figures 6.83–6.85 are for the short external wedge W_2 with caps. Similar distributions are observed beneath the jet centerline to the base external wedge (W_2) while, distributions similar to the internal wedge (W_3) are observed above the jet, indicating that some of the flow physics of the internal wedge are mimicked by the caps. The presence of the caps increases turbulence on the upperside of the jet.

A very important turbulence parameter for noise considerations is Reynolds stress. In fact, it has been stated in Ref. 48 that if one flow parameter should be chosen for code validation, it should be peak shear stress because this is the parameter that governs the turbulent mixing process. Figures 6.86–6.93 show isocontours of the $\overline{u'v'}$ and $\overline{u'w'}$ components of the Reynolds stresses at x/D_f=4. Isocontours are shown for the baseline and for seven asymmetric configurations. The first four asymmetric configurations correspond to the base wedge configurations (W_1 – W_4). Only one cap configuration is presented here, that is for W_2, with Cap1. Instead of the other two cap configurations, Figs. 6.83 and 6.84 show pylon comparisons. One is for the baseline pylon alone (W_4 + pylon), and the other is for the pylon with flaps (W_4 + pylon + flaps). As mentioned

above, the pylon ensemble is composed of three components. Peak values are listed in Table 6.2, and stated in the text below.

For the baseline case, shown in Fig. 6.86, the profiles are nearly symmetric. The peak $\overline{u'v'}$ value above the jet is 0.0037, and below the jet is -0.0043. The peak $\overline{u'w'}$ positive value is 0.0043, and the negative peak value is -0.0051. The sign of the Reynolds stress depends upon the slope of the mean velocity profile, and it is positive on the positive axis in both plots. The shape of the $\overline{u'w'}$ Reynolds stress contours are generally pear-shaped for all of the axymmetric jet cases because of the coupling of the turbulence with mean velocity.Figure 6.87 is for the tall external wedge (W_1). The peak $\overline{u'v'}$ value above the jet is 0.0057, a steep increase from the baseline. Below the jet, it is -0.0039, a reduction in magnitude of about 10%. The peak $\overline{u'w'}$ positive value is 0.0042, and the negative peak value is -0.0048, both reduced in magnitude from the baseline values. This is important for suggesting the potential of the external wedge in comparison with the baseline to reduce noise. Since the peak values occur near the axis, the reduction suggests that sideline radial gradients are reduced. This means that it is likely that sideline noise emissions will also be reduced using the external wedge. Note the characteristic pear-shape formed by the two halves of the $\overline{u'w'}$ distribution, a feature to be noted in all subsequent cases.

Figure 6.88 is for the short external (W_2). The peak $\overline{u'v'}$ value above the jet is 0.0051, much less of an increase from the baseline. Below the jet, it is -0.0040, a reduction in magnitude of about 7%. The peak $\overline{u'w'}$ positive value is 0.0040, and the negative peak value is -0.0041, both reduced significantly in magnitude from the baseline values, even more than the reduction observed for the tall wedge. Looking at the balance of increase

on the top of the jet and the reduction underneath and on the side of the jet, the shorter wedge looks to have more potential to reduce noise than does the tall wedge. Noise measurements are needed to confirm this.

Figure 6.89 is for the internal wedge with matching cross-section (W_3). The peak $\overline{u'v'}$ value above the jet is 0.0053, increased from the baseline value by 36%. Below the jet, however, a marked reduction is observed. It is -0.0033, a 26% decrease compared to the baseline value of -0.0043. The peak $\overline{u'w'}$ positive value is 0.0061, and the negative peak value is -0.0057, both steeply increasing in magnitude from the baseline values of 0.0043 and -0.0051. This behavior differs from the external wedge deflectors, both of which reduced the $\overline{u'w'}$ values. Note, the augmented pear-shape formed by the two halves.

Figure 6.90 is for the internal wedge (W_4). Similar behavior to the external wedges is observed. The peak $\overline{u'v'}$ value above the jet is 0.0049, increased from the baseline value by about 30%. Below the jet, the peak value is -0.0038, reduced by 12%. The peak $\overline{u'w'}$ positive value is 0.0045, and the negative peak value is -0.0049, similar in magnitude to the baseline values.

Figure 6.91 is for W_2+Cap1. The peak $\overline{u'v'}$ value above the jet is 0.0048, increased from the baseline value by about 26%. Below the jet, the peak value is -0.0040, a reduction in magnitude of 7%. The peak $\overline{u'w'}$ positive value is 0.0040, and the negative peak value is -0.0042, both decreased significantly in magnitude compared to the baseline values, agreeing with the behavior of the external wedge deflector.

Figure 6.92 is for W_4+pylon. The peak $\overline{u'v'}$ value above the jet is 0.0043, increased from the baseline value by 15%. Below the jet, the peak value is -0.0042, reduced by 2%

The peak $\overline{u'w'}$ positive value is 0.0047 and the negative peak value is -0.0049 both increased compared to the baseline values, and compared to the internal portion of the pylon structure W_4 alone. This shows that the external pylon used in these experiments intruded somewhat into the flow, and it increased turbulence.

Figure 6.93 is for the entire pylon ensemble including flaps (W_4+pylon+flaps). The peak $\overline{u'v'}$ value above the jet is 0.0050, increased from the baseline pylon value of 0.0043. Below the jet, the peak value is -0.0036, a reduction in magnitude compared with -0.0042. The peak $\overline{u'w'}$ values are 0.0056 and -0.0062 both steeply increased compared with baseline pylon values. These results are similar to the behavior of the internal wedge, (W_3).

Peak Reynolds stresses occur where peak mean velocity gradients occur. The peak $\overline{u'v'}$ Reynolds stress component underneath the jet (measured in the region near the end of the primary potential core) was reduced in all cases, as a consequence of the reduction in maximum radial velocity gradient underneath the jet. In all cases, the peak $\overline{u'v'}$ Reynolds stress component above the jet was increased, corresponding to the increase in velocity gradient. In a few cases, for example, the external wedge-deflectors, the peak $\overline{u'w'}$ Reynolds stress components were also reduced. This corresponds to a reduction in mean velocity gradient in the *z*-direction (sideline direction), and this result is very important to noise emissions. Ideally, the best design for reduced jet noise emissions in the direction of the ground would not be accompanied by an increase in the sideline direction. The external wedge looks very promising from this perspective, and the sideline noise measurements shown in Fig. 1.7 already show its potential. In the

discussion that follows peak radial velocity gradients are correlated with the turbulence field.

6.2 Correlation Between Mean and Turbulent Flow Field

In the previous section, it was observed that a reduction in mean velocity gradient on the underside of the jet was accompanied by a reduction in turbulence levels underneath the jet. The reverse occurred on the top side of the jet. Thus, it became a research goal to seek a correlation between the maximum turbulent kinetic energy and mean flow gradient both for the top and bottom of the jet. In this section the process for obtaining the correlation is described.

Peak turbulent kinetic energy is a good metric for correlating with noise emissions of jets because it describes the intensity of the turbulence mixing. For mean flow, the velocity gradient is a good parameter for correlating with noise reduction because it can be used to quantify the thickness of the low-speed region underneath the jet with respect to the baseline jet. In all cases where noise reduction was observed, in Chapter 5, a reduction of velocity gradient was also observed.

A mean flow parameter used to correlate with peak turbulent kinetic energy was described in Eq. 5.5. It is a radial gradient, measured at the end of the primary potential core and normalized by the primary potential core length, restated here:

$$G = \frac{x_p}{U_p}\left|\frac{\partial u}{\partial y}\left(x_p, y_{i1}, 0\right)\right|, \tag{6.1}$$

In an effort to improve upon the preliminary correlation, other methods for measuring and non-dimensionalizing the gradient parameter were performed. One variation of G is

to on the axial location where the maximum gradient is obtained. For example, an average of the maximum radial gradient between x_p and x_{GSC} could yield a good correlation with peak turbulence. Several non-dimensionalizing schemes using the fan diameter, D_f, the primary potential core length, x_p, and $x_p - x_{GSC}$, were considered. Also of importance to noise is the primary jet velocity, so U_p is used for non-dimensionalization.

Figure 6.94 shows the best correlations obtained. The mean radial gradient parameter value, G, was obtained at the end of the generalized secondary core, x_{GSC}, see Eq. 6.2. Taking G at this location resulted in good correlations both above and below the jet centerline. This correlation was instrumental in improving the noise correlation in Fig.5.24, when normalizing by the primary potential core length, x_p.

$$G = \frac{x_p}{U_p}\left|\frac{\partial u}{\partial y}\left(x_{GSC}, y_{i1}, 0\right)\right|, \tag{6.2}$$

The correlations above and below the jet are superimposed to form one curve in Fig. 6.96. Because the baseline case was not perfectly symmetric, two points are obtained for the baseline, one above, and one below the centerline. The least squares quadratic fit displayed is $k = 0.000884G^2 - 0.002621|G| + 0.002955$.

Since the peak turbulent kinetic energy can be thought of as a measure of how intense the turbulent mixing is, it is logical that it should also provide a measure for turbulent mixing noise. Therefore, this correlation yields insight into the important mean flow parameter that will yield a correlation with noise. This is important, since a large number of experiments have been conducted at UCI for which there are only mean flow measurements to be correlated with the noise measurements. The direct correlation between the mean flow parameter measured at the end of the generalized secondary core

and the peak turbulent kinetic energy suggests that it may be possible to obtain a correlation, a topic of future research.

In constructing correlations with the acoustics, the gradient parameter

$$G = \frac{x_p}{U_p}\left|\frac{\partial u}{\partial y}\left(x_{GSC}, y_{i1}, 0\right)\right|, \tag{6.3}$$

may be more physical because it includes the potential core length, x_p. Figure 6.95 shows that the correlation is very good. This parameter was used in Chapter 5 to provide a slight improvement to the preliminary correlation between ΔOASPL and G on the ϕ=0° plane, in Fig. 5.24. One of the remaining challenges in obtaining a robust correlation between acoustics and mean flow is to extend the procedure to include the azimuthal variations of the gradient.

Table 6.1 ***GRC Flow Field Parameters***

GRC Experiment	Peak k/U_p^2 Below	Peak k/U_p^2 Above	G Below	G Above	x_{GSC}/D_f Below	x_{GSC}/D_f Above	x_p/D_f
Baseline	0.0172	0.0154	2.27	2.30	1.22	1.66	4.79
W1	0.0142	0.0164	2.14	2.36	1.26	0.19	4.13
W2	0.0144	0.0168	2.15	2.42	1.23	0.14	4.30
W3	0.0103	0.0206	1.70	2.49	2.55	0.00	3.40
W4	0.0144	0.0179	2.22	2.45	1.15	0.00	4.17
W2+Cap1	0.0134	0.0179	2.08	2.45	1.35	0.12	4.14
W2+Cap2	0.0135	0.0208	2.10	2.51	1.36	0.00	3.71
W2+Cap3	0.0140	0.0163	2.10	2.41	1.33	0.15	4.33

Table 6.2 ***GRC Reynolds Stresses***

GRC Experiment	Peak $u'v'$ Below (-)	Peak $u'v'$ Above (+)	Peak $u'w'$ (-)	Peak $u'w'$ (+)
Baseline	-0.00427	0.00368	-0.00505	0.00425
W1	-0.00388	0.00569	-0.00480	0.00425
W2	-0.00399	0.00509	-0.00411	0.00398
W3	-0.00330	0.00529	-0.00570	0.00609
W4	-0.00379	0.00489	-0.00490	0.00450
W2+Cap1	-0.00398	0.00479	-0.00422	0.00400
W4+Pylon	-0.00417	0.00434	-0.00493	0.00470
W2+Pylon+Flaps	-0.00358	0.00500	-0.00616	0.00560

a) b)

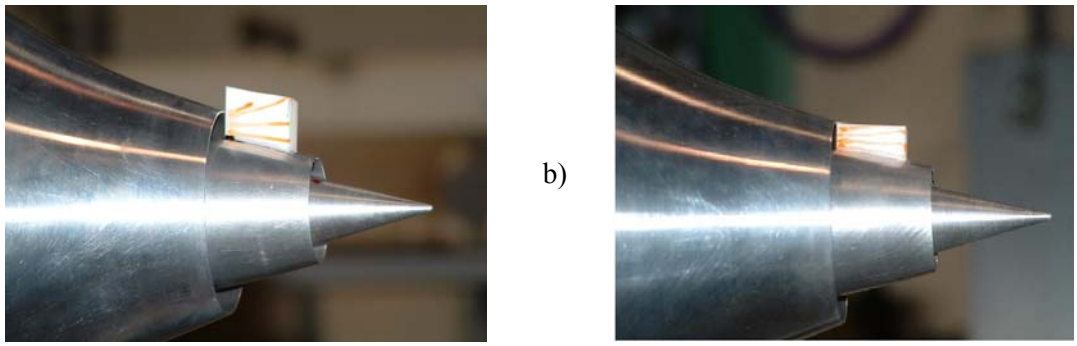

Figure 6.1. Crude surface flow visualizations using orange water color paint for a) W_1 and b) W_2.

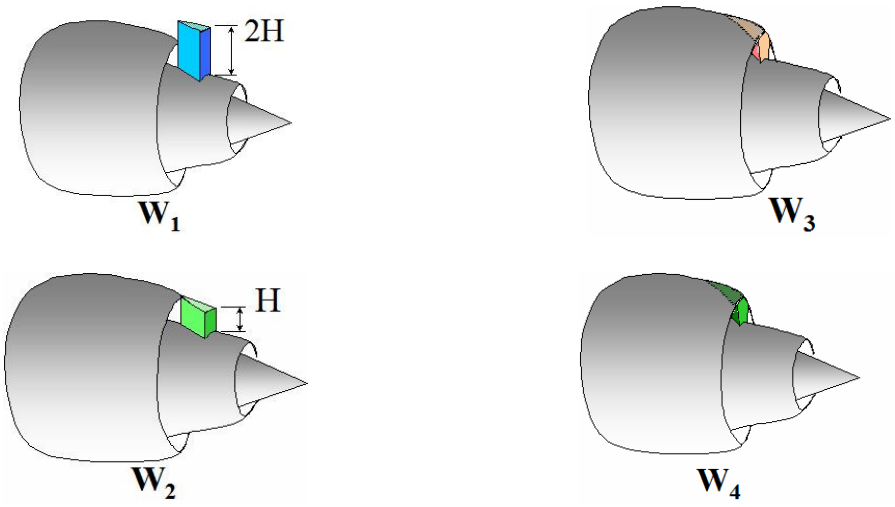

Figure 6.2. Wedge-shaped deflector configurations tested at NASA Glenn Research Center. W_1, W_2, W_3, and W_4. *H* = 0.269 in. is the annular gap width. (Cartoons by D. Papamoschou).

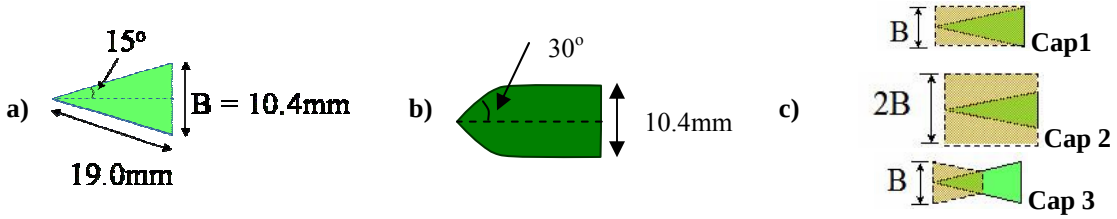

Figure 6.3. Cross-section of a) W_1, W_2, and W_3 and b) W_4 c) Three caps (top views are shown).

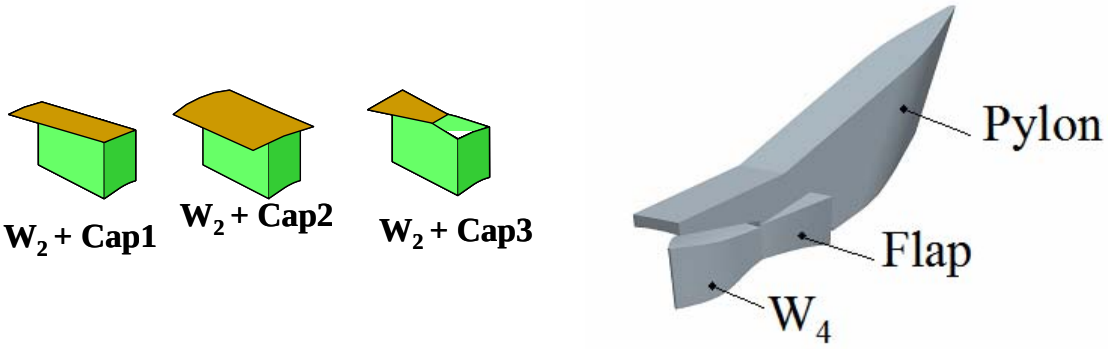

Figure 6.4. W_4 + pylon + external flap. Cap configurations tested. (Pylon coordinates provided by Henry Haskins at NASA Langley).

a) 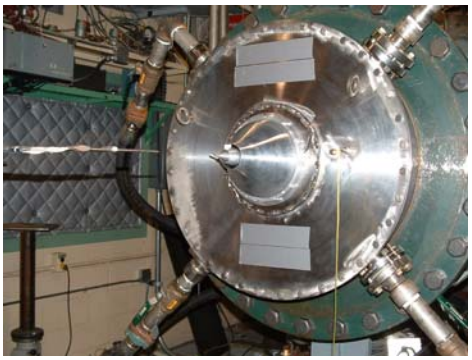

b) 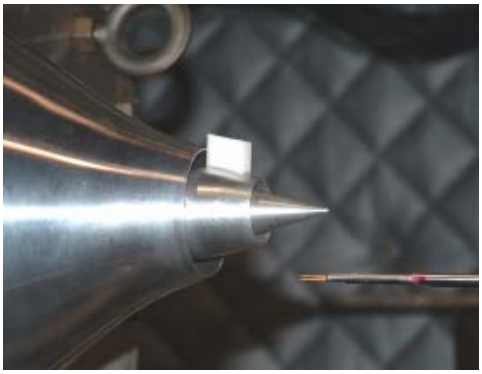

c) 

d) 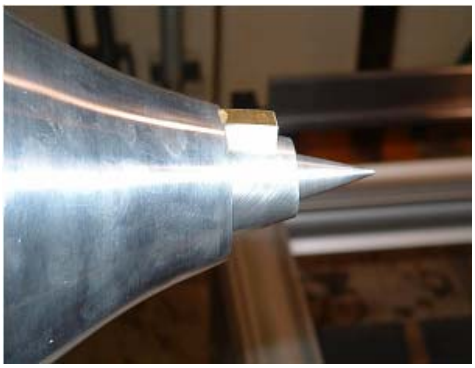

e) 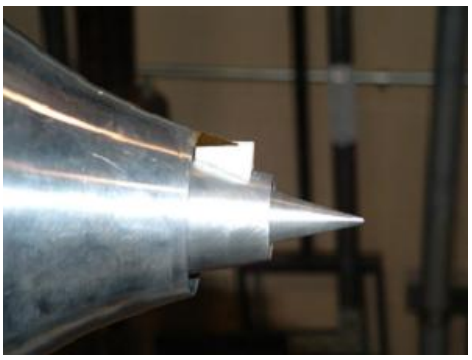

f) 

Figure 6.5. a) GRC CW-17 jet facility and '5BB' nozzle. Hot-wire apparatus is visible in the foreground. b) W_1 c) W_2 d) W_2 + Cap 1 e) W_2 + Cap 3 f) W_4 + Pylon + Flaps. (Photos by K.B.M.Q. Zaman).

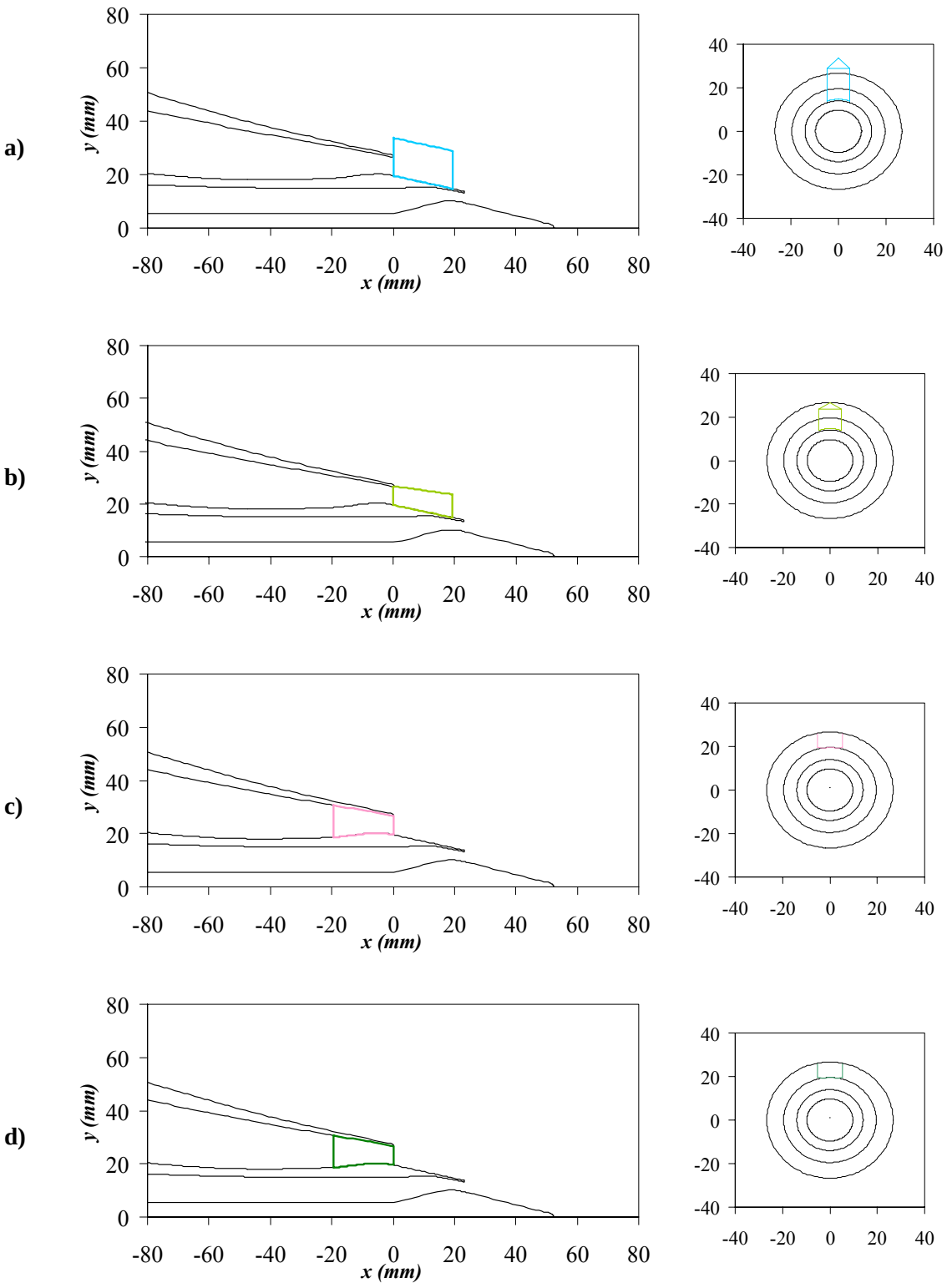

Figure 6.6. Radial coordinates for the CW17 5BB nozzle with a) W_1 b) W_2 c) W_3 d) W_4.

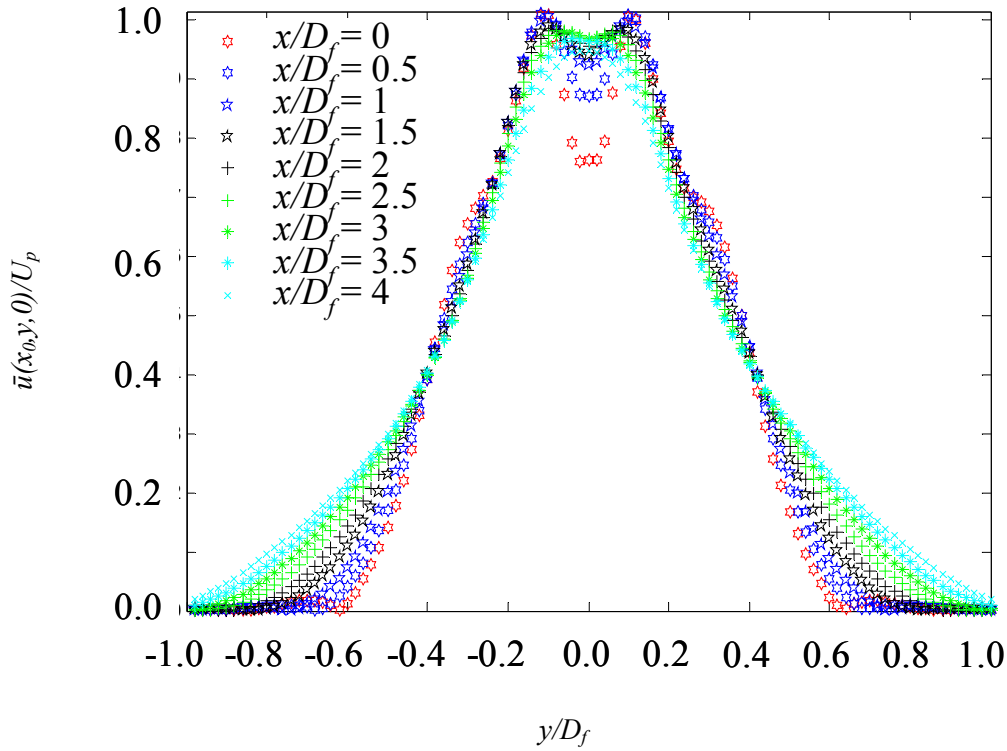

a)

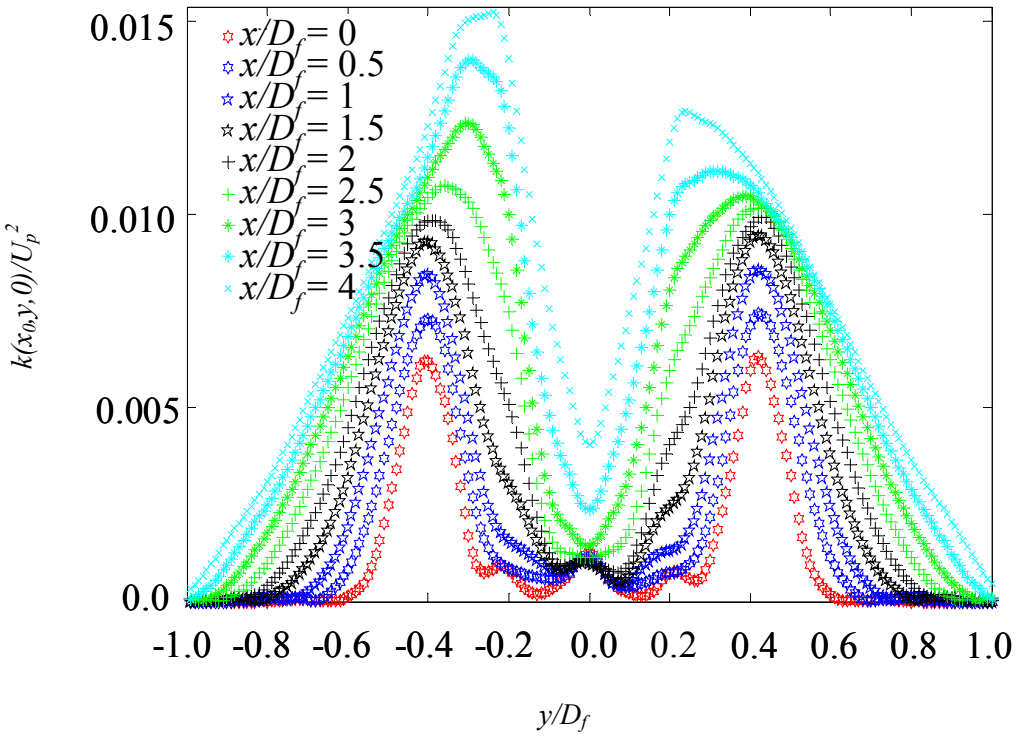

b)

Figure 6.7. Evolution of baseline jet a) mean axial velocity profiles and b) turbulent kinetic energy profiles with axial distance from plug tip to 4 fan diameters downstream.

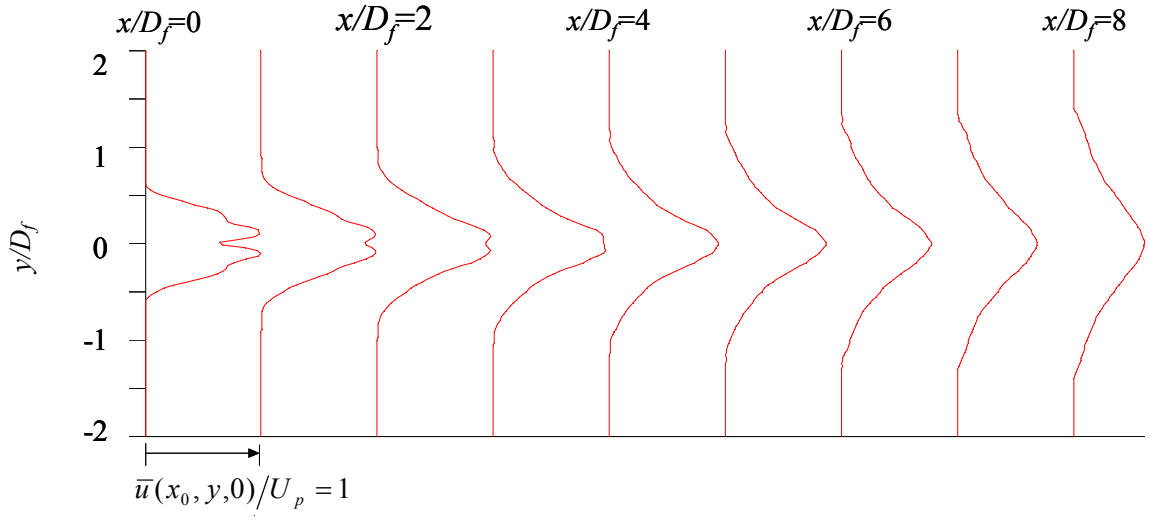

Figure 6.8. Evolution of mean axial velocity profiles. Baseline jet.

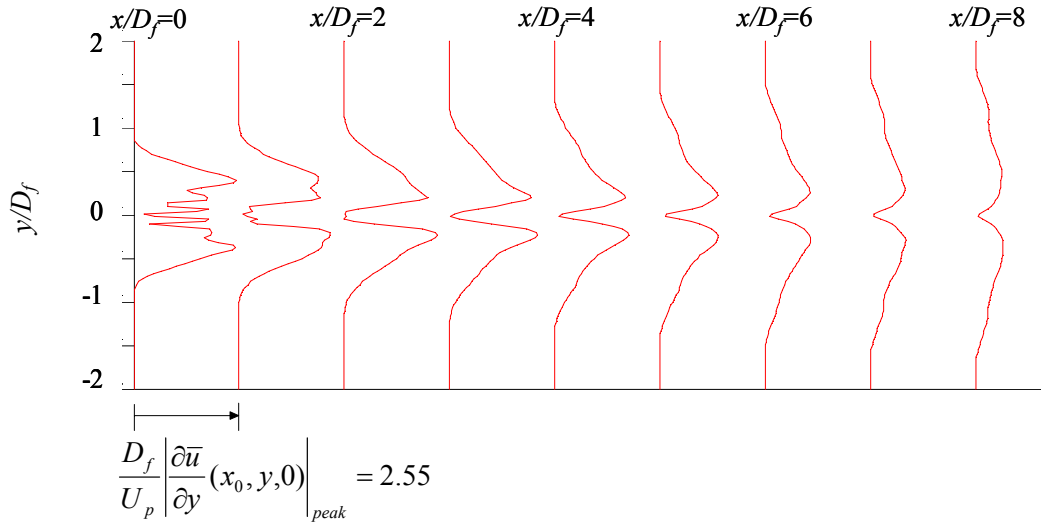

Figure 6.9. Evolution of mean velocity gradient profiles. Baseline jet.

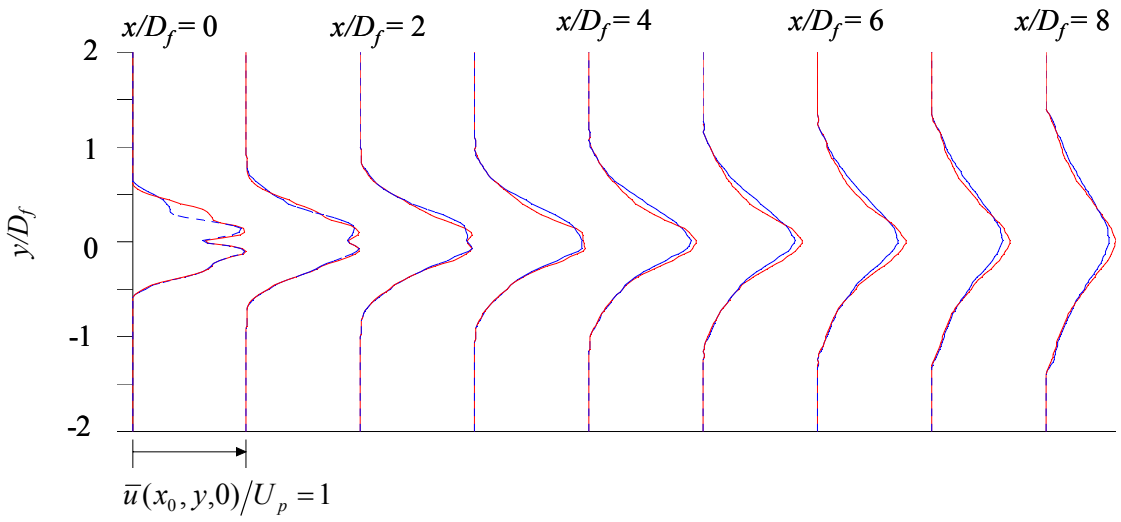

Figure 6.10. Evolution of mean axial velocity profiles. W_1 - - - overlaid with baseline —.

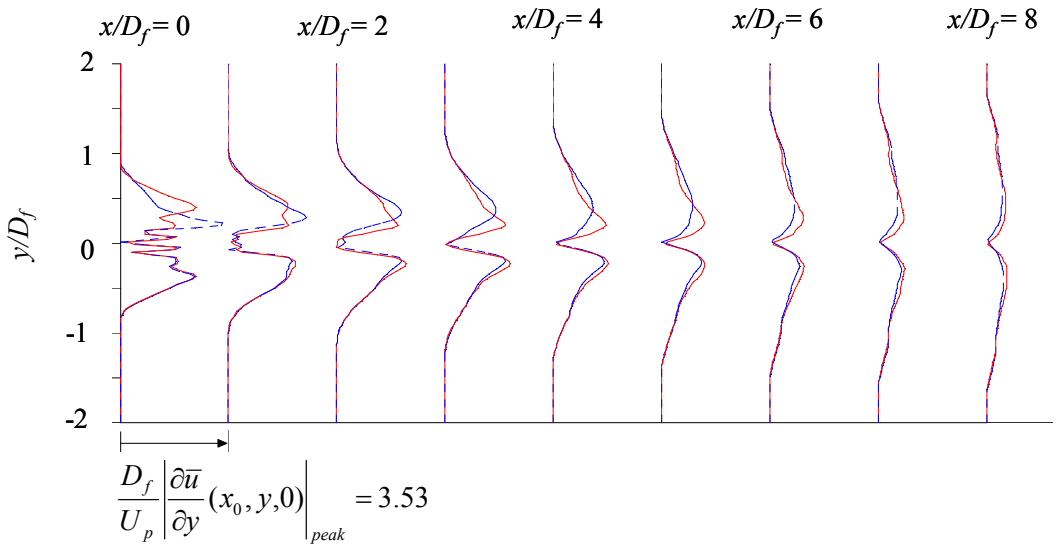

Figure 6.11. Evolution of mean velocity gradient transverse profiles. W_1 - - - overlaid with baseline —.

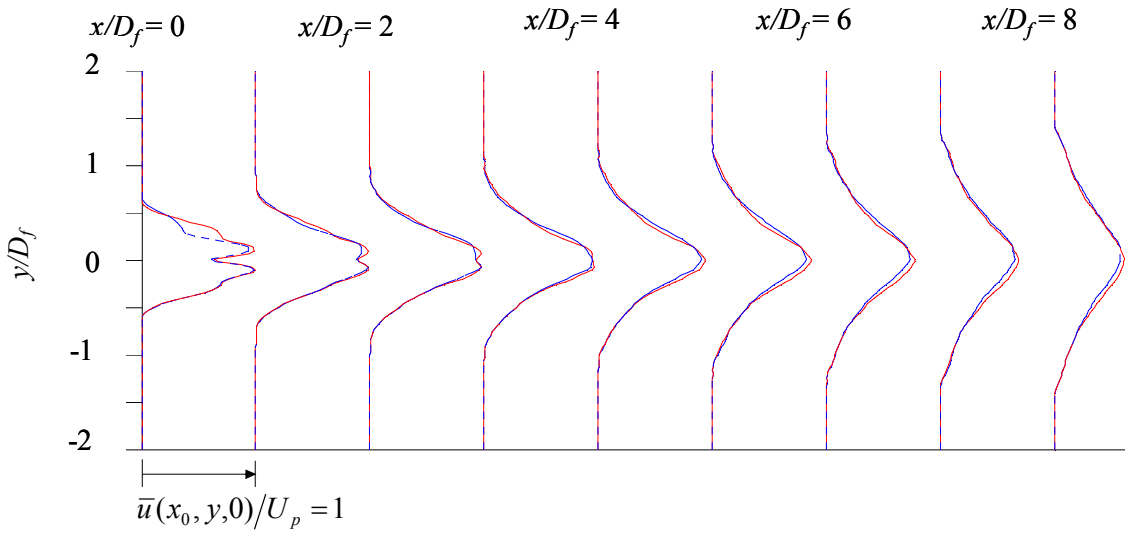

Figure 6.12. Evolution of mean axial velocity profiles. W_2 - - - overlaid with baseline —.

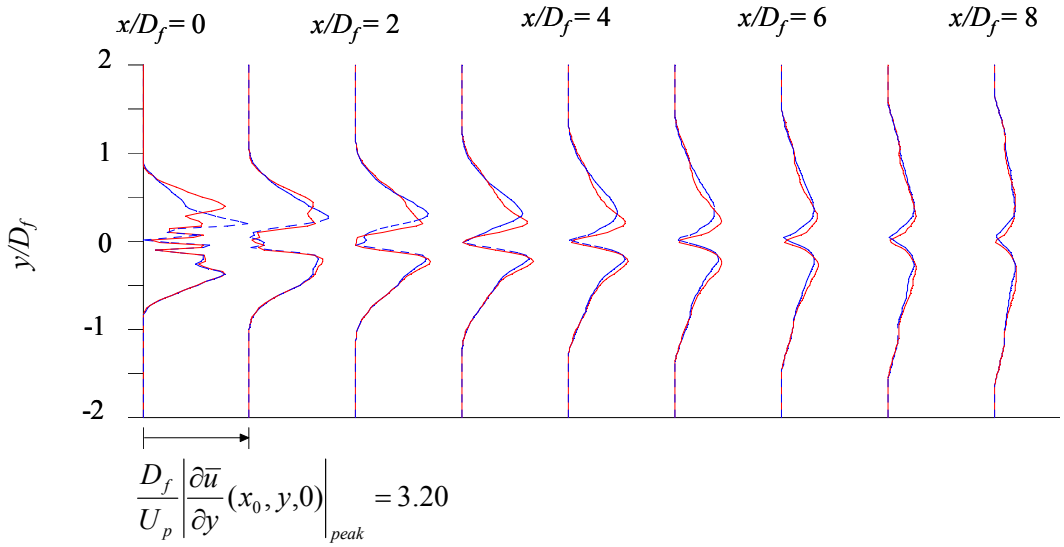

Figure 6.13. Evolution of mean velocity gradient transverse profiles. W_2 - - - overlaid with baseline —.

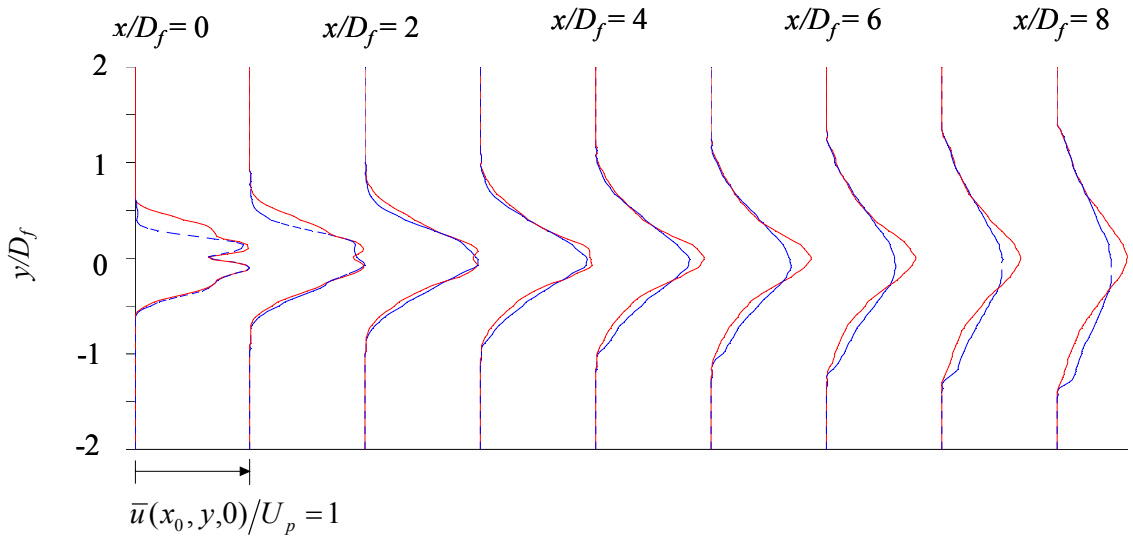

Figure 6.14. Evolution of mean axial velocity profiles. W_3 - - - overlaid with baseline —.

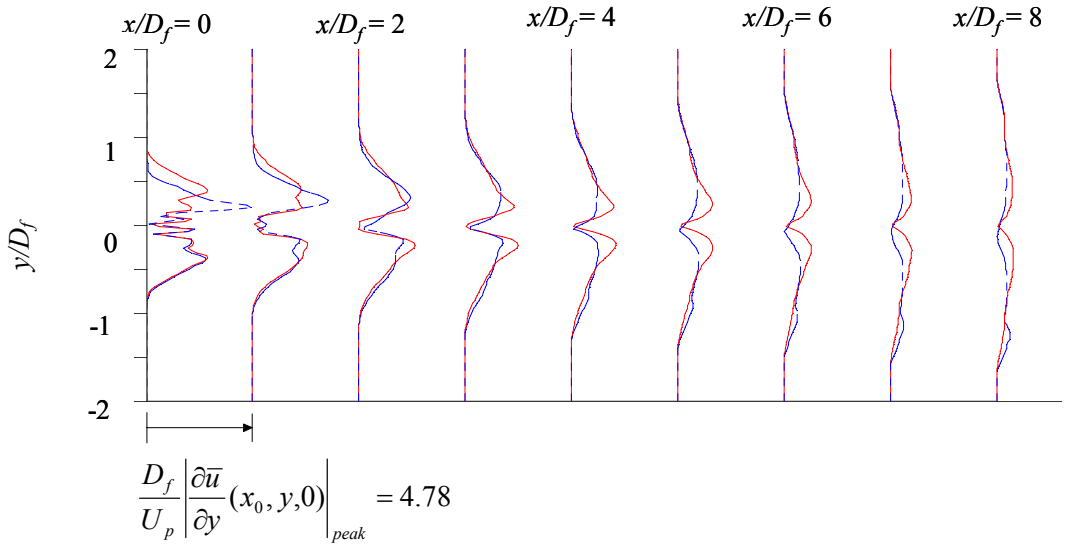

Figure 6.15. Evolution of mean velocity gradient transverse profiles. W_3 - - - overlaid with baseline —.

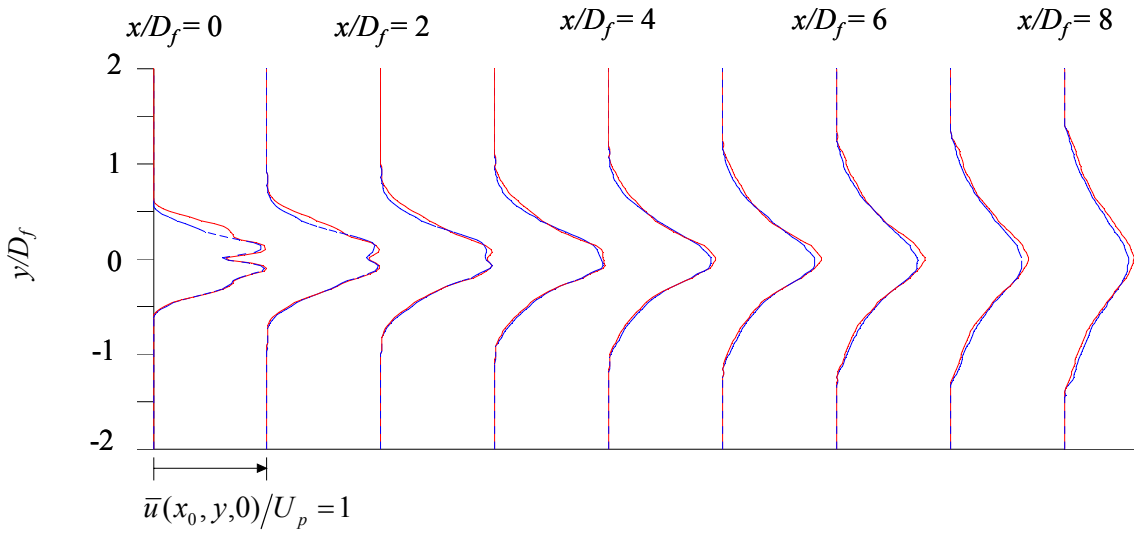

Figure 6.16. Evolution of mean axial velocity profiles. W_4 - - - overlaid with baseline —.

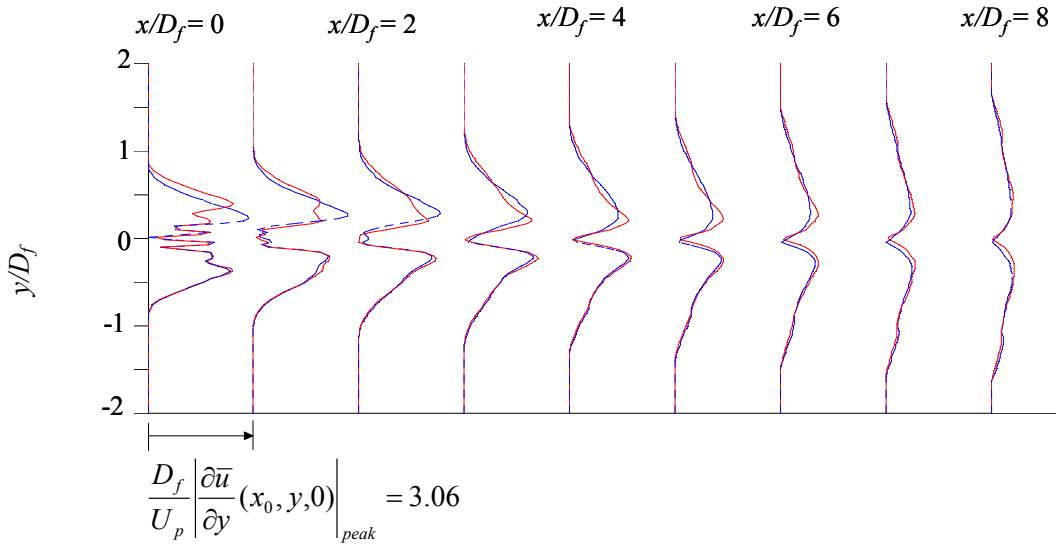

Figure 6.17. Evolution of mean velocity gradient transverse profiles. W_4 - - - overlaid with baseline —.

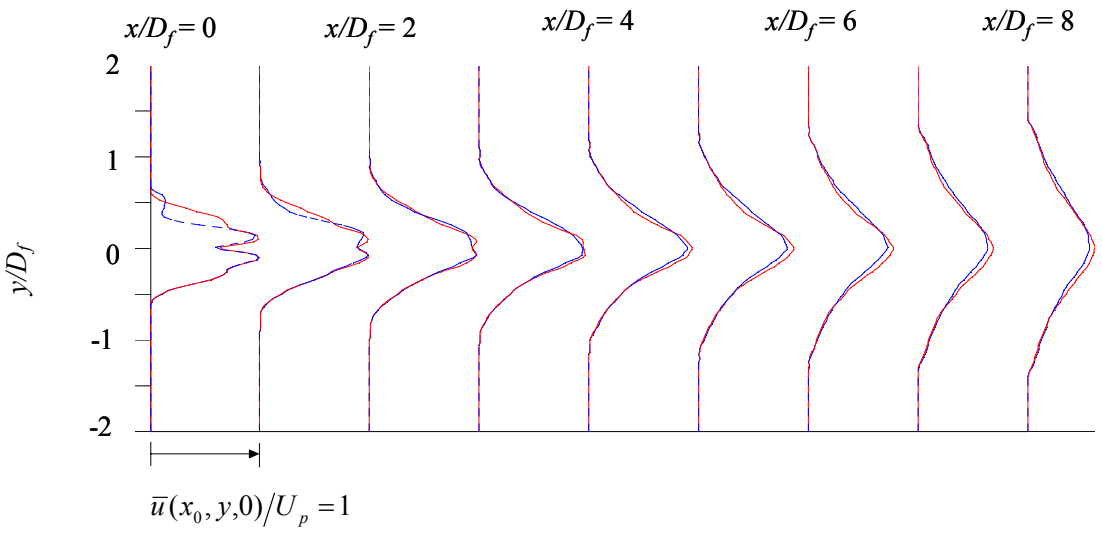

Figure 6.18. Evolution of mean axial velocity profiles. W_2 + cap 1 - - - overlaid with baseline —.

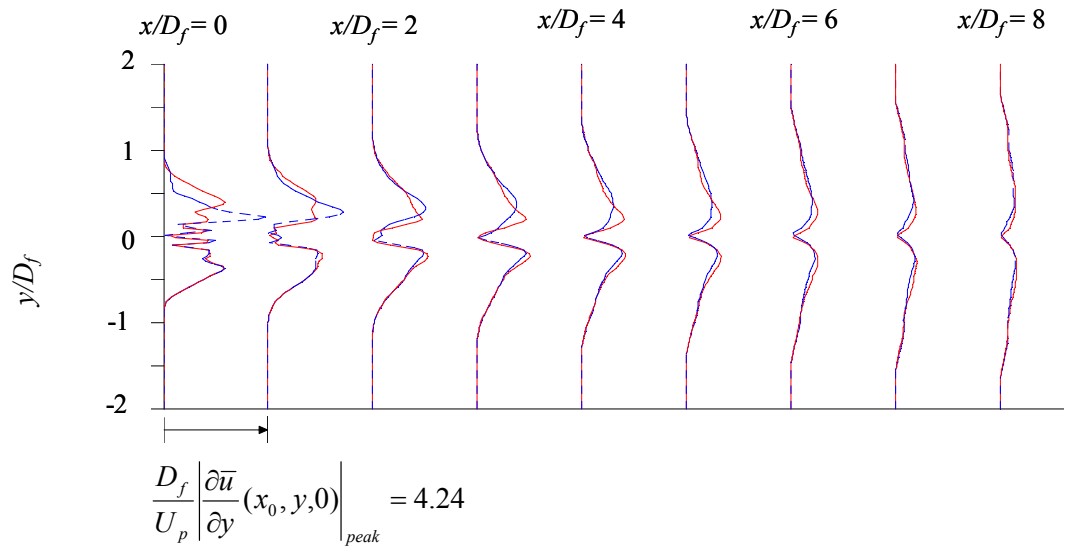

Figure 6.19. Evolution of mean velocity gradient transverse profiles. W_2 + Cap1 - - - overlaid with baseline —.

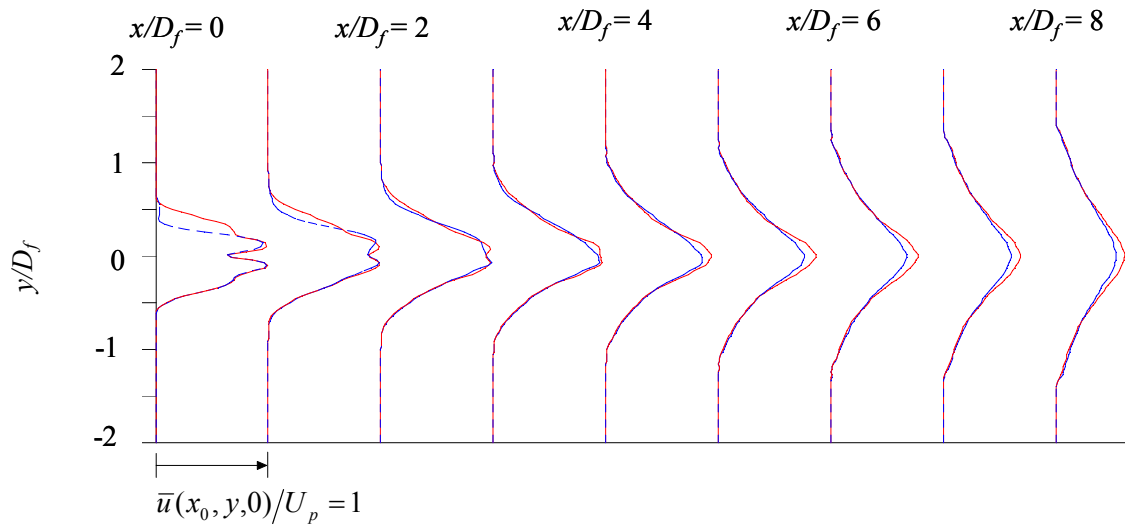

Figure 6.20. Evolution of mean axial velocity transverse profiles. W_2 + cap 2 - - - overlaid with baseline —.

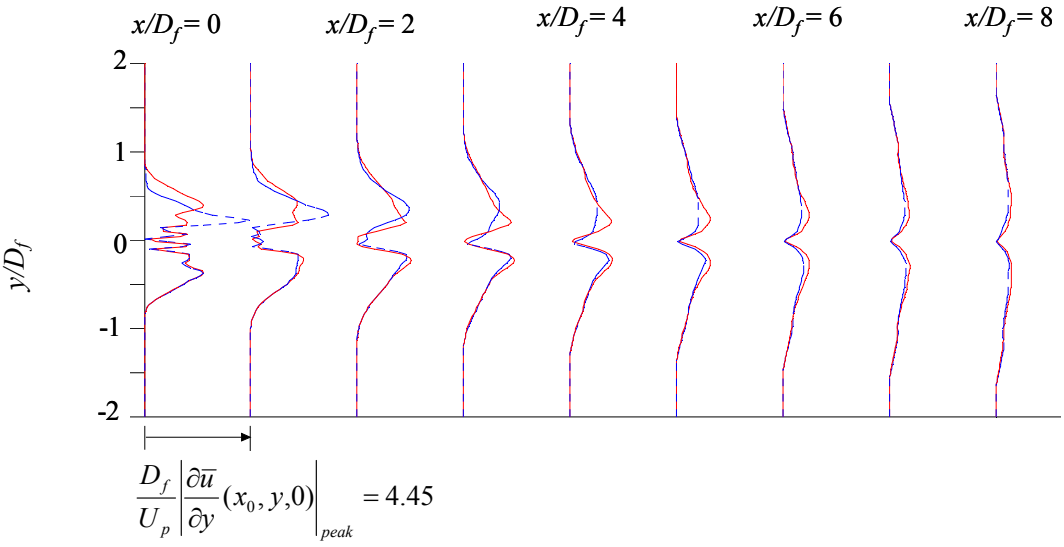

Figure 6.21. Evolution of mean velocity gradient profiles. W_2 + Cap 2 - - - overlaid with baseline —.

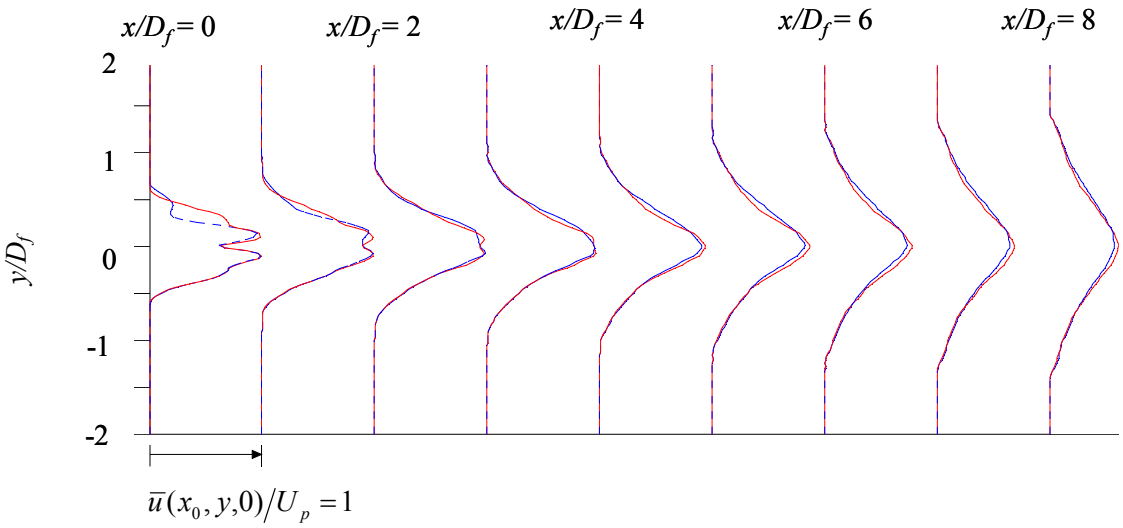

Figure 6.22. Evolution of mean axial velocity profiles. W_2 + Cap 3 - - - overlaid with baseline —.

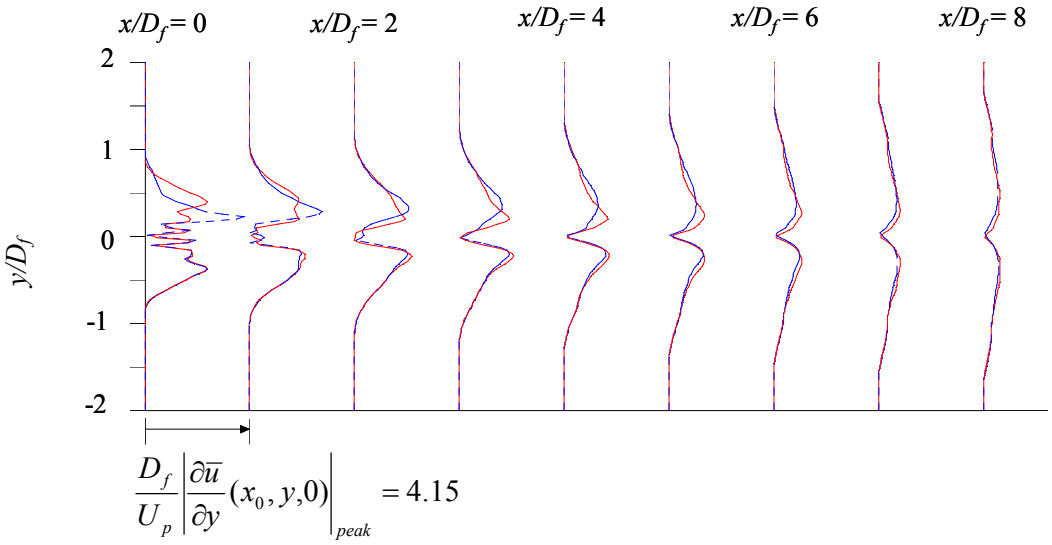

Figure 6.23. Evolution of mean velocity gradient transverse profiles. W_2 + Cap 3 - - - overlaid with baseline —.

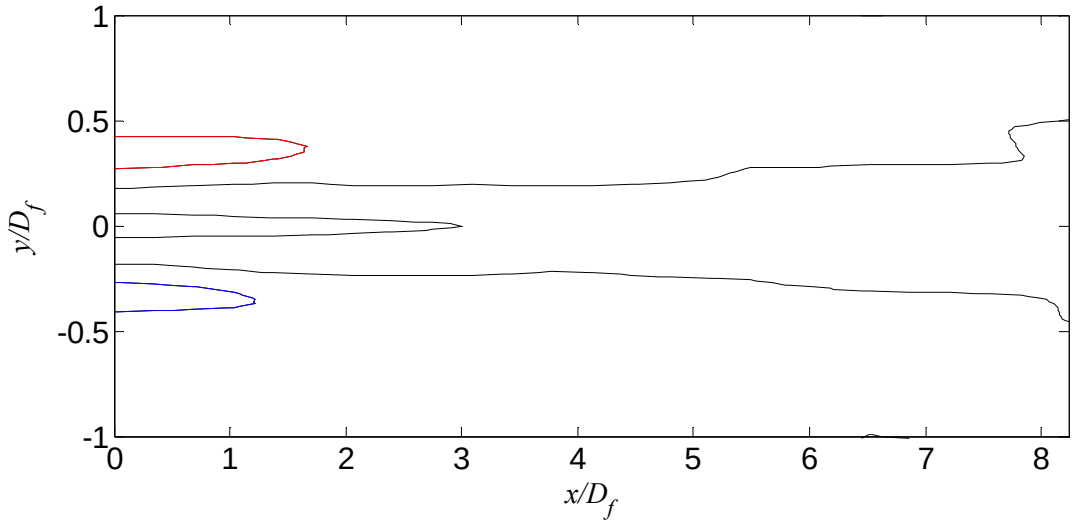

Figure 6.24. Loci of inflection points of $\bar{u}(x,y,0)/U_p$ for baseline.

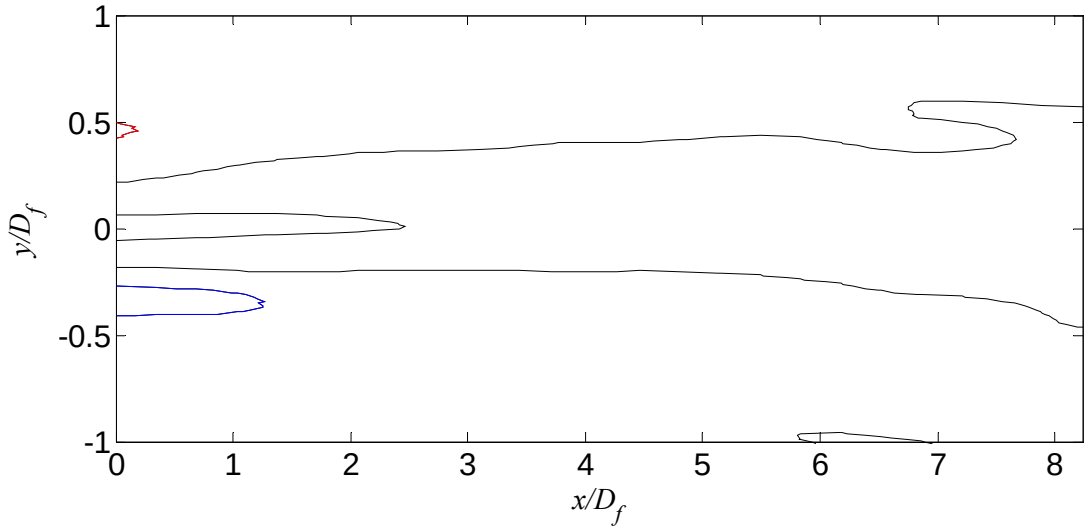

Figure 6.25. Loci of inflection points of $\bar{u}(x,y,0)/U_p$ for W_1.

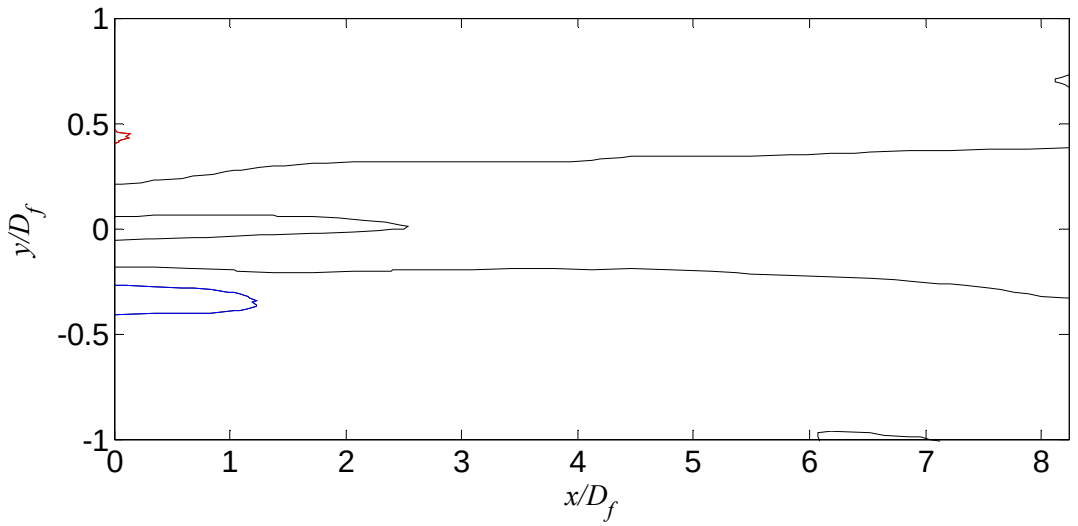

Figure 6.26. Loci of inflection points of $\bar{u}(x,y,0)/U_p$ for W_2.

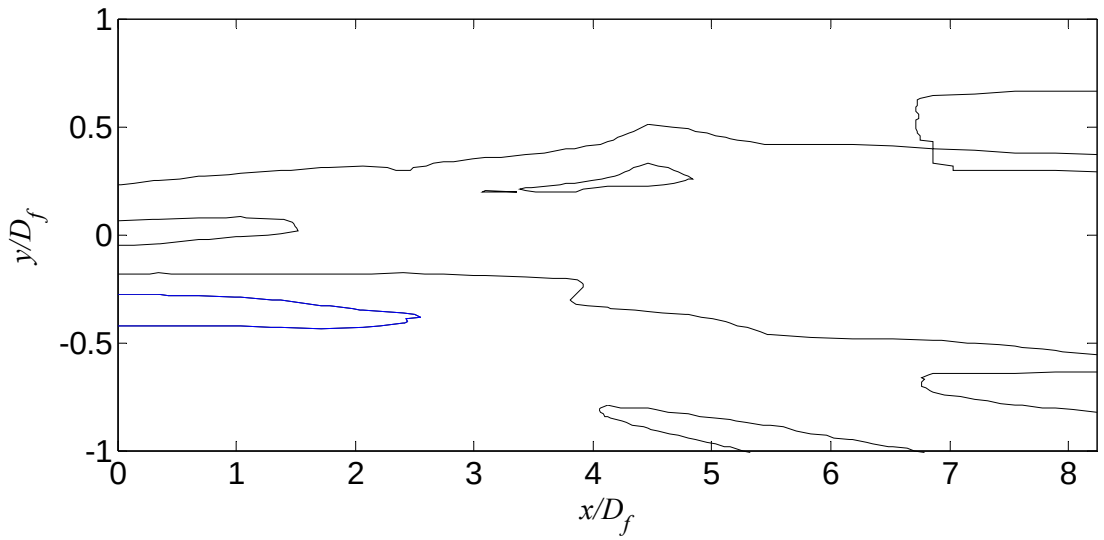

Figure 6.27. Loci of inflection points of $\bar{u}(x,y,0)/U_p$ for W_3.

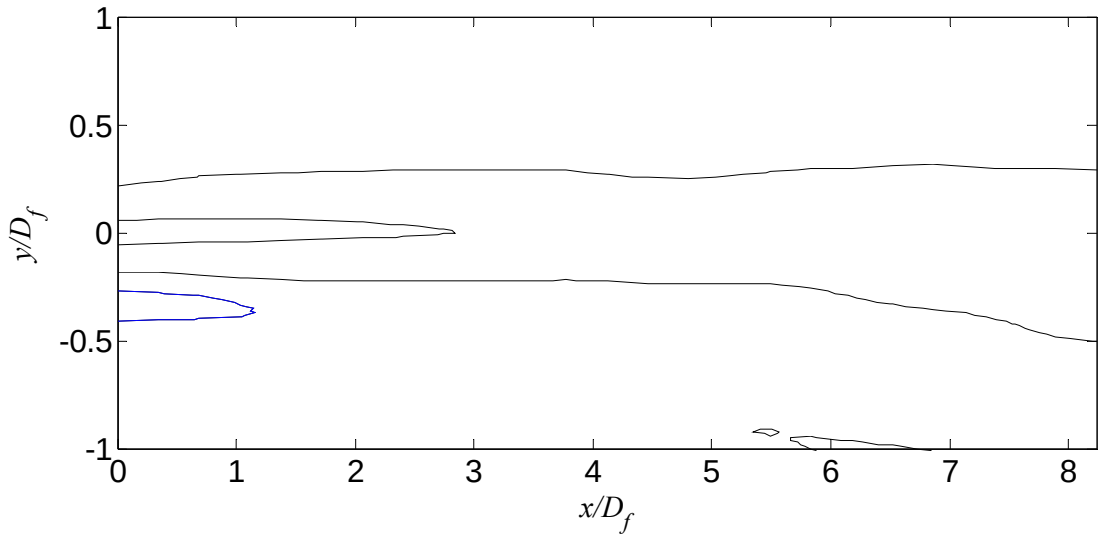

Figure 6.28. Loci of inflection points of $\bar{u}(x,y,0)/U_p$ for W_4.

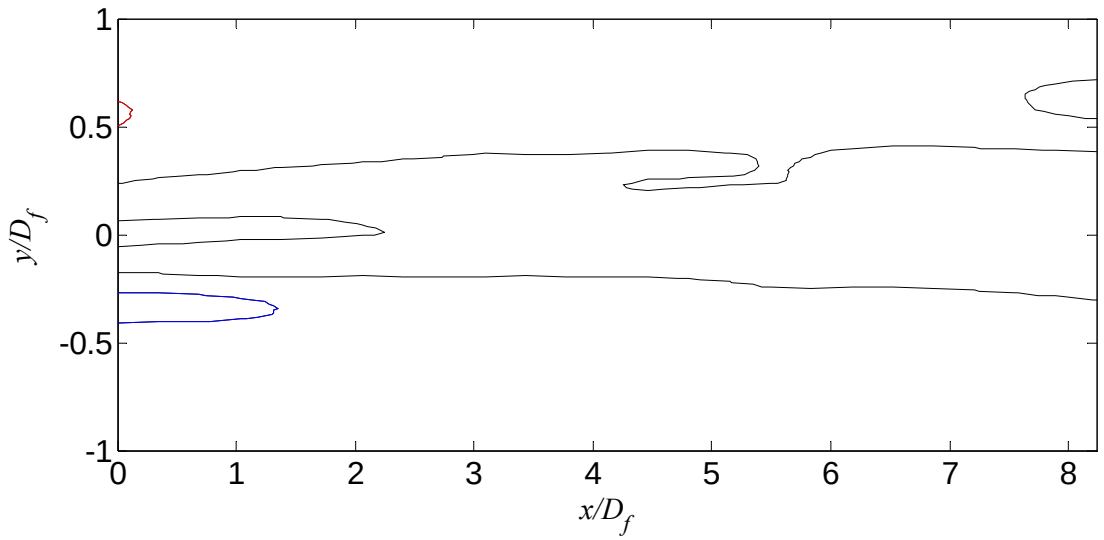

Figure 6.29. Loci of inflection points of $\bar{u}(x,y,0)/U_p$ for W_2 + Cap 1.

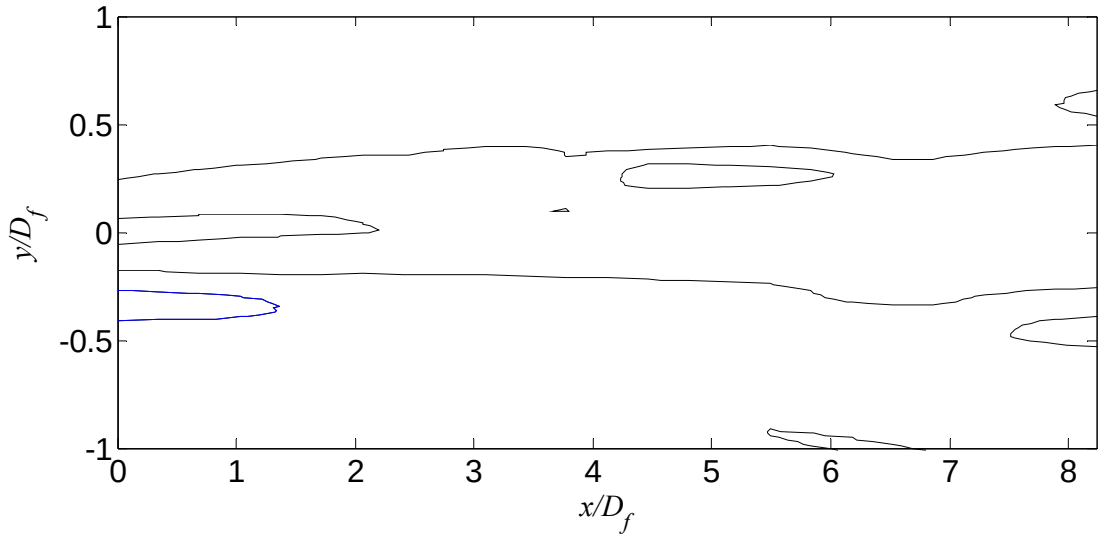

Figure 6.30. Loci of inflection points of $\bar{u}(x,y,0)/U_p$ for W_2 + Cap 2.

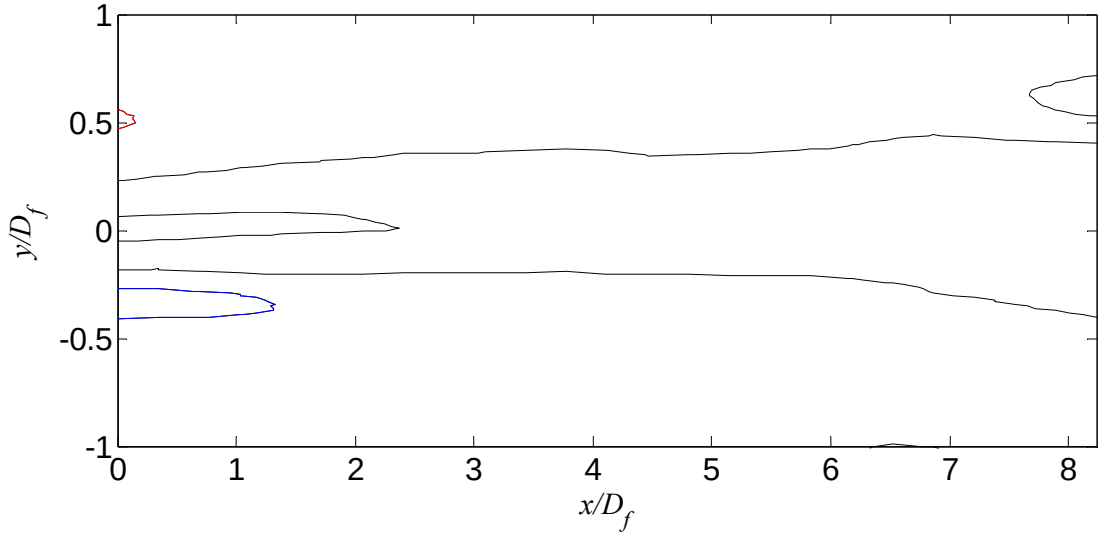

Figure 6.31. Loci of inflection points of $\bar{u}(x,y,0)/U_p$ for W_2 + Cap 3.

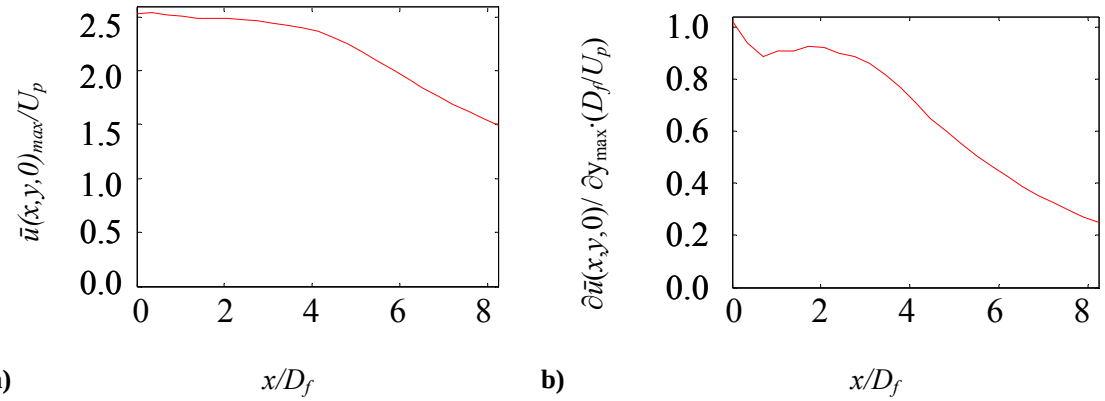

Figure 6.32. Axial distributions of a) maximum mean velocity and b) maximum radial velocity gradient, baseline jet.

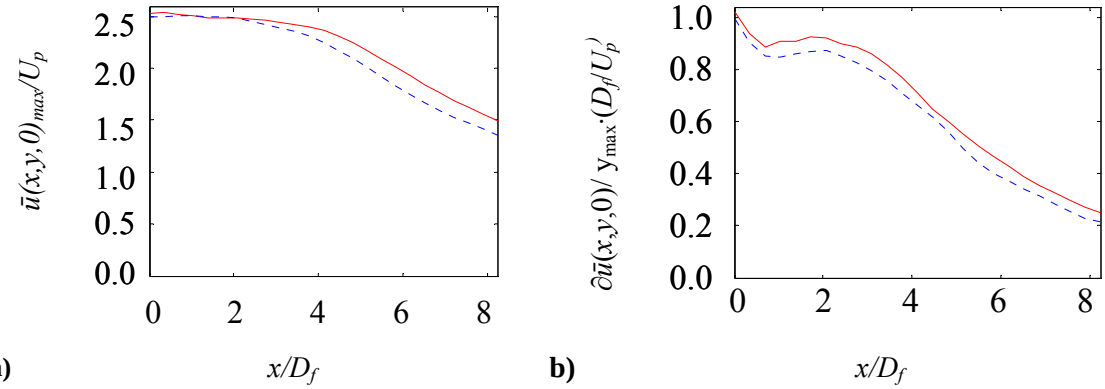

Figure 6.33. Axial distributions of a) maximum mean velocity and b) maximum radial velocity gradient, W_1 - - - overlaid with baseline —.

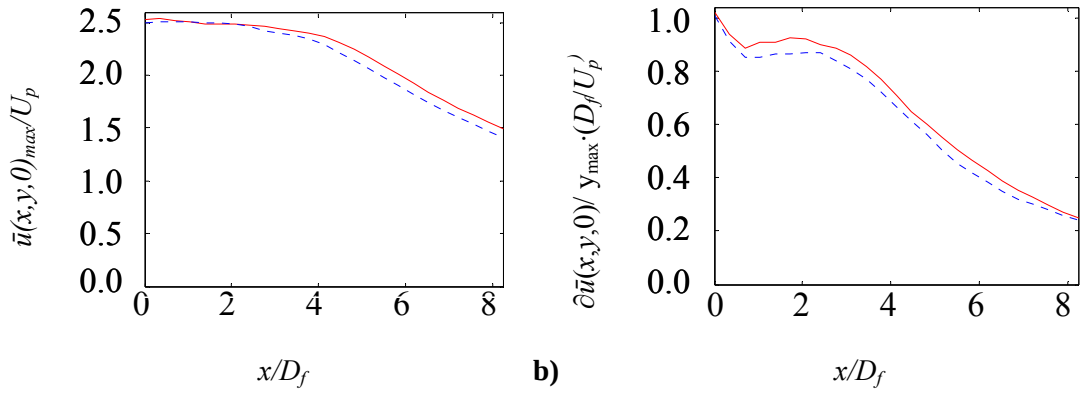

Figure 6.34. Axial distributions of a) maximum mean velocity and b) maximum radial velocity gradient, W_2 - - - overlaid with baseline —.

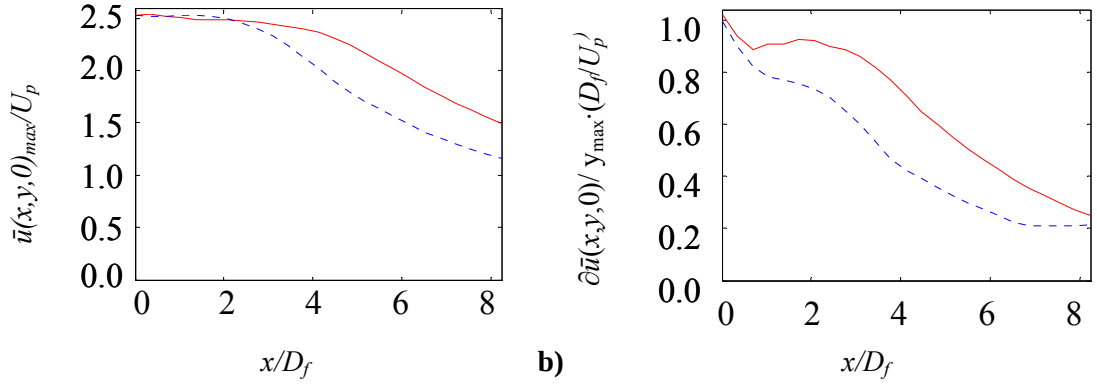

Figure 6.35. Axial distributions of a) maximum mean velocity and b) maximum radial velocity gradient, W_3 - - - overlaid with baseline —.

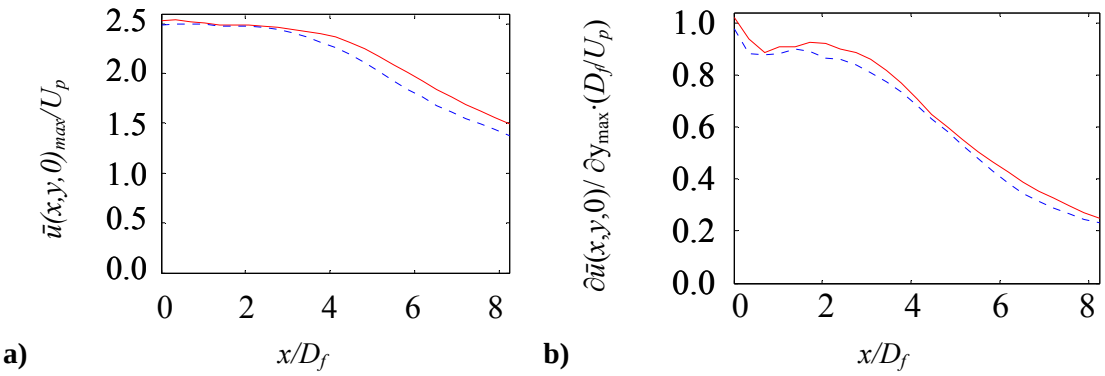

Figure 6.36. Axial distributions of a) maximum mean velocity and b) maximum radial velocity gradient, W_4 - - - overlaid with baseline —.

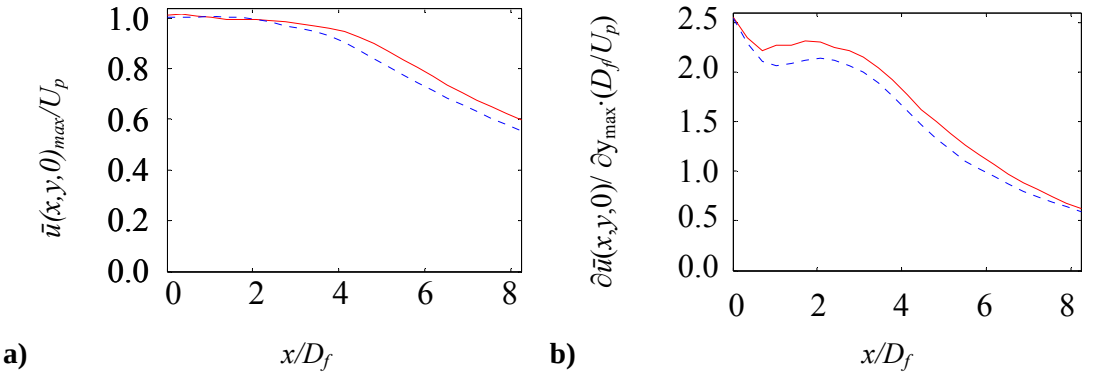

Figure 6.37. Axial distributions of a) maximum mean velocity and b) maximum radial velocity gradient, W_2 + Cap 1 - - - overlaid with baseline —.

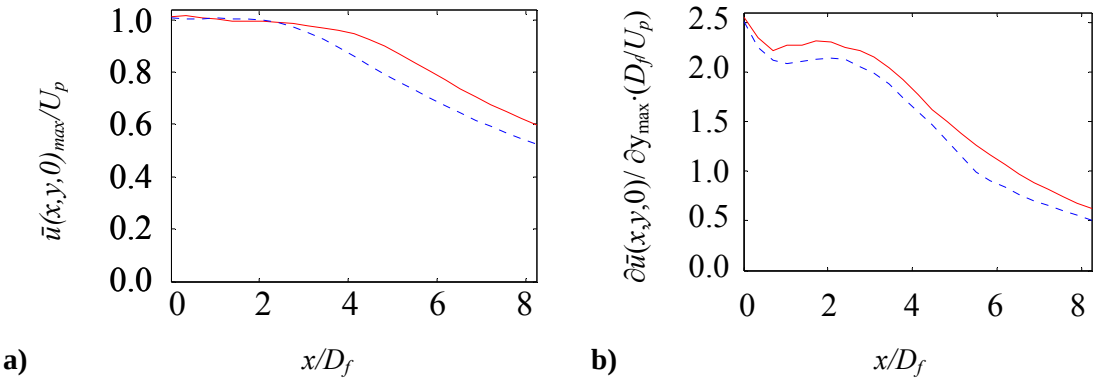

Figure 6.38. Axial distributions of a) maximum mean velocity and b) maximum radial velocity gradient, W_2 + Cap 2 - - - overlaid with baseline —.

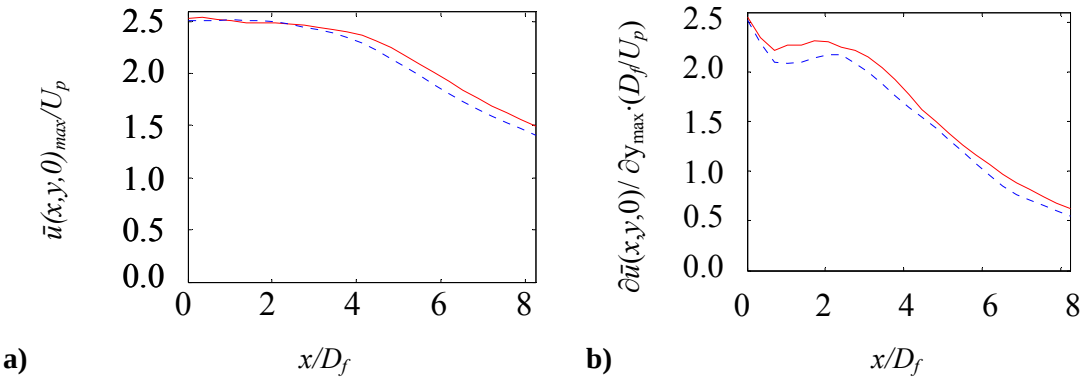

Figure 6.39. Axial distributions of a) maximum mean velocity and b) maximum radial velocity gradient, W_2 + Cap 3 - - - overlaid with baseline —.

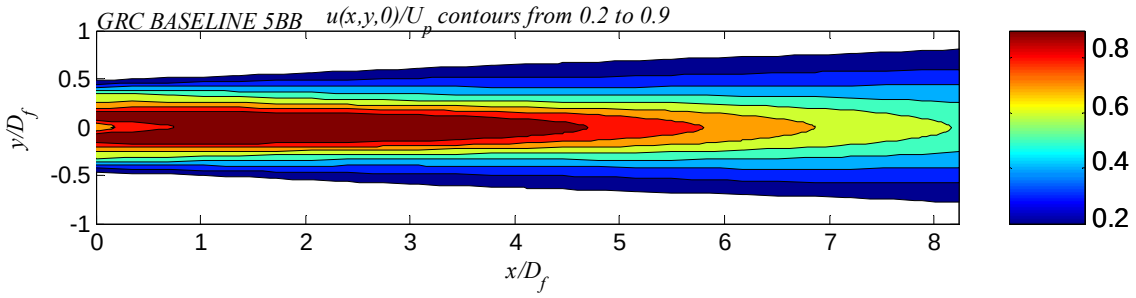

Figure 6.40. Mean axial velocity isocontours, $u(x,y,0)/U_p$ for the baseline jet.

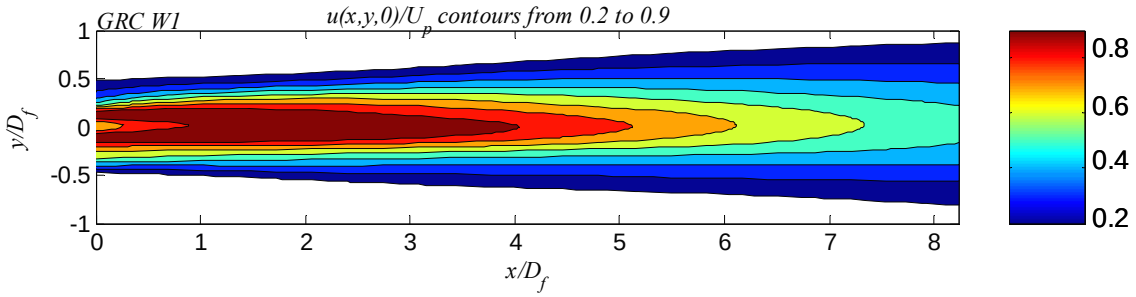

Figure 6.41. Mean axial velocity isocontours, $u(x,y,0)/U_p$ for W_1.

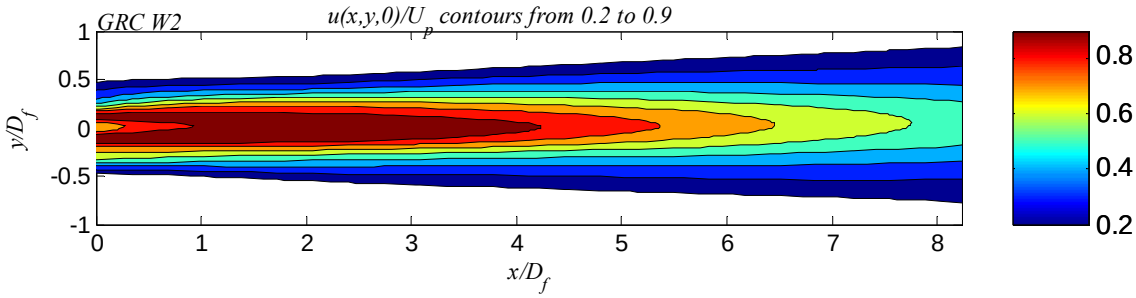

Figure 6.42. Mean axial velocity isocontours, $u(x,y,0)/U_p$ for W_2.

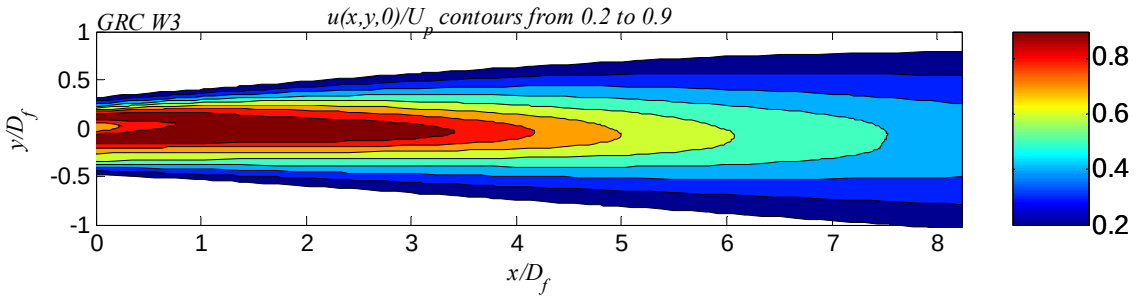

Figure 6.43. Mean axial velocity isocontours, $u(x,y,0)/U_p$ for W_3.

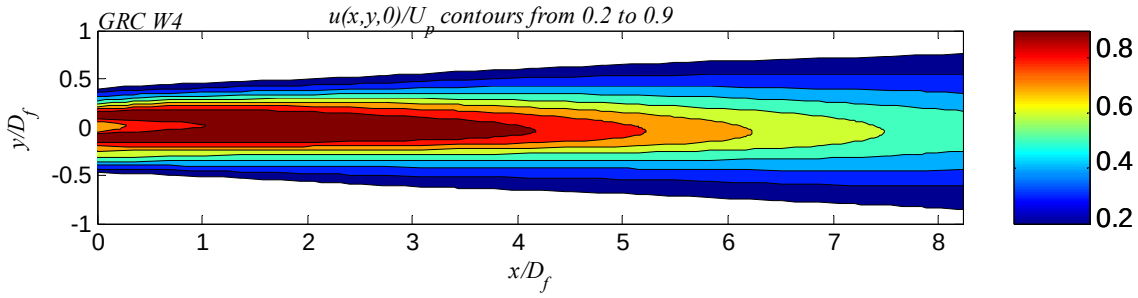

Figure 6.44. Mean axial velocity isocontours, $u(x,y,0)/U_p$ for W_4.

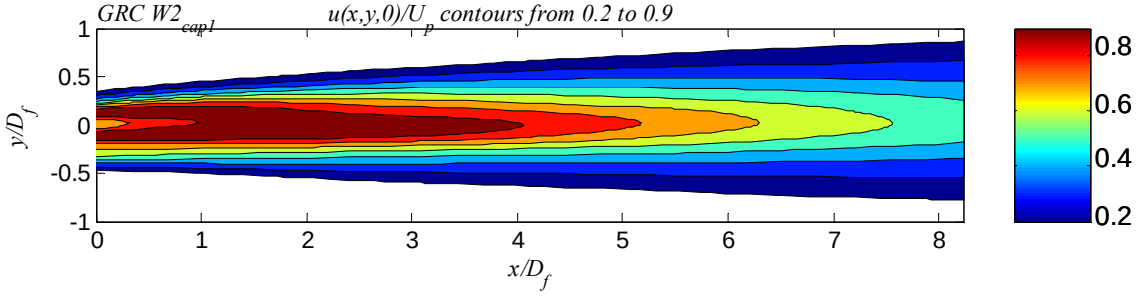

Figure 6.45. Mean axial velocity isocontours, $u(x,y,0)/U_p$ for W_2 + Cap 1.

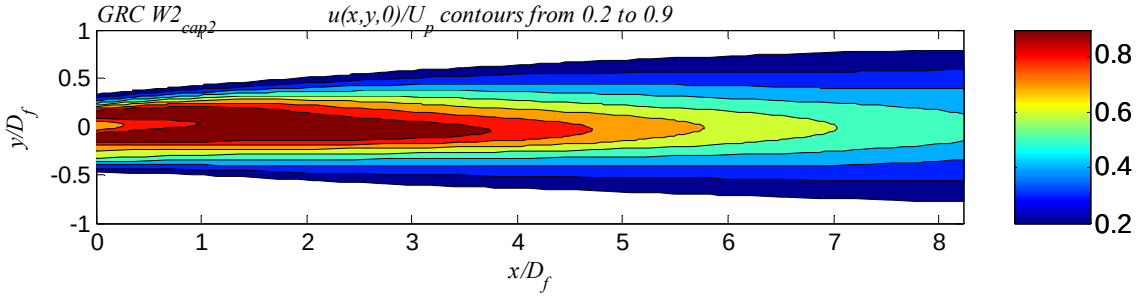

Figure 6.46. Mean axial velocity isocontours, $u(x,y,0)/U_p$ for W_2 + Cap 2.

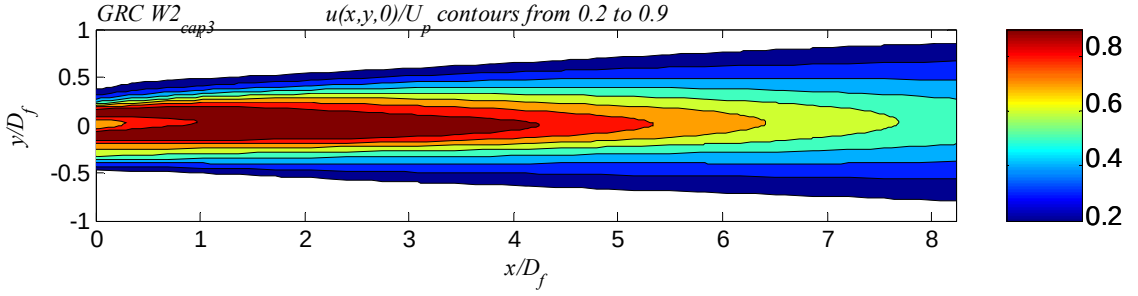

Figure 6.47. Mean axial velocity isocontours, $u(x,y,0)/U_p$ for W_2 + Cap 3.

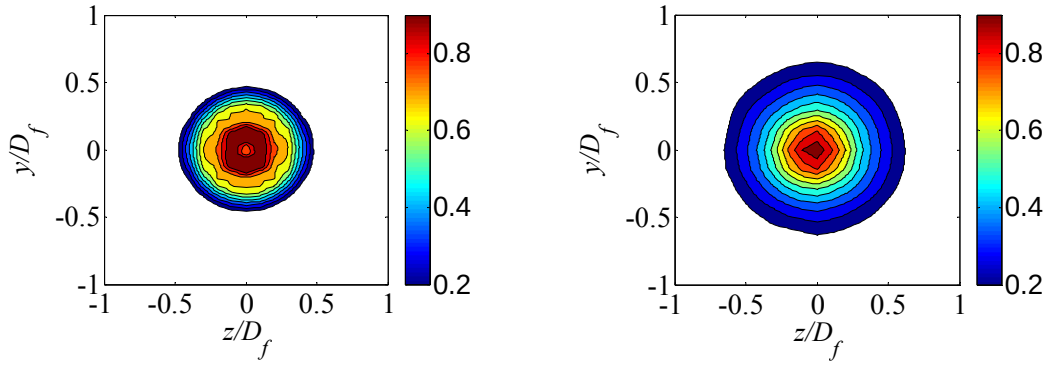

Figure 6.48. Mean axial velocity isocontours, $u(x,y,0)/U_p$ for the baseline jet at a) $x/D_f = 0$ and at b) $x/D_f = 4$.

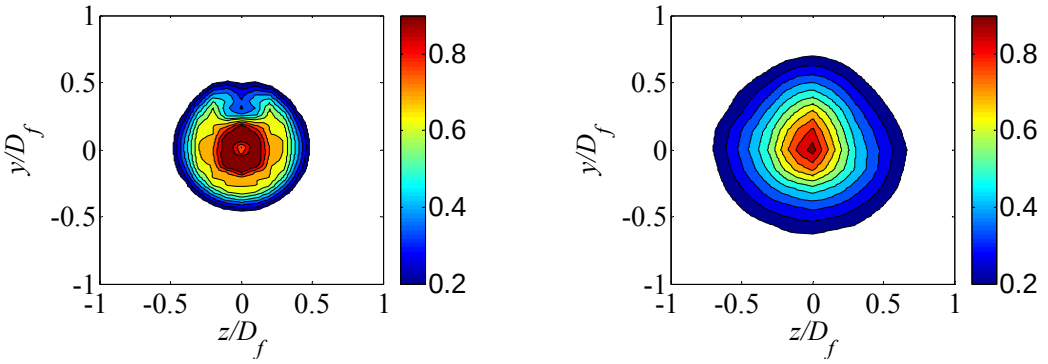

Figure 6.49. Mean axial velocity isocontours, $u(x,y,0)/U_p$ for W_1 at a) $x/D_f = 0$ and b) $x/D_f = 4$.

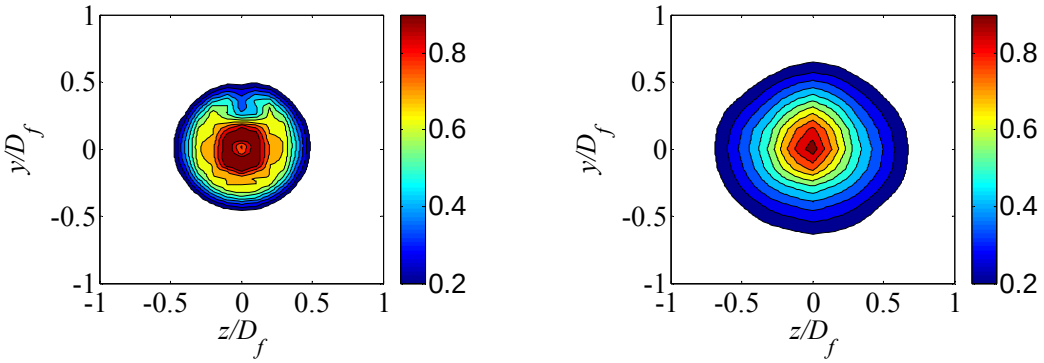

Figure 6.50. Mean axial velocity isocontours, $u(x,y,0)/U_p$ for W_2 at a) $x/D_f = 0$ and b) $x/D_f = 4$.

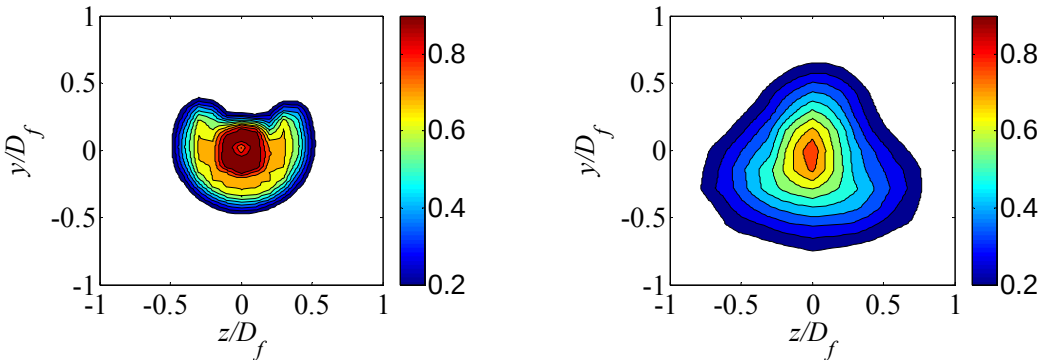

Figure 6.51. Mean axial velocity isocontours, $u(x,y,0)/U_p$ for W_3 at a) $x/D_f = 0$ and b) $x/D_f = 4$.

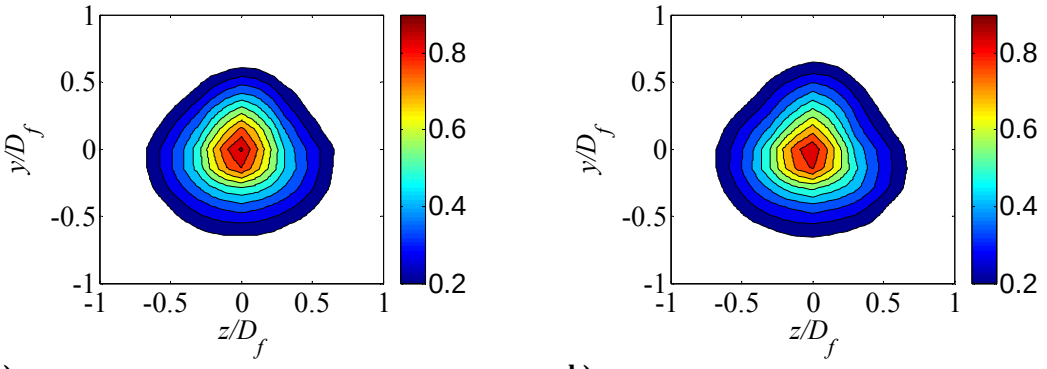

a) b)

Figure 6.52. Mean axial velocity isocontours, $u(x,y,0)/U_p$ for a) W_4 and b) W_4+Pylon at $x/D_f = 4$.

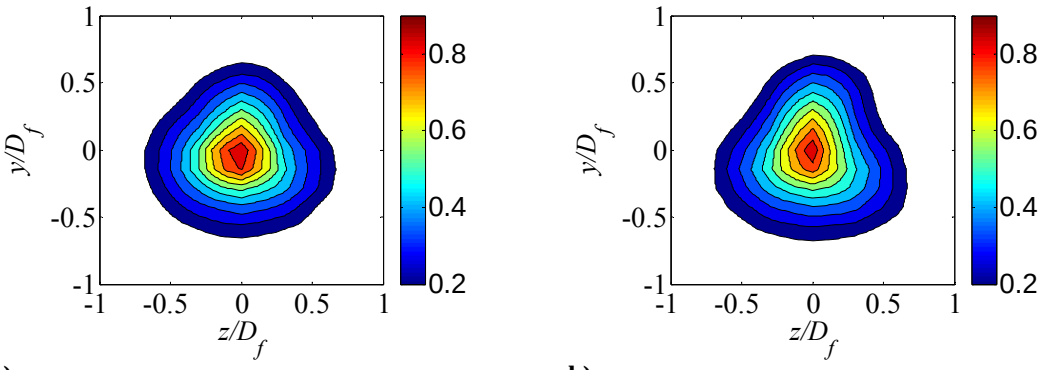

a) b)

Figure 6.53. Mean axial velocity isocontours, $u(x,y,0)/U_p$ for a) W_4 + Pylon and b) W_4+Pylon+Flaps at $x/D_f = 4$.

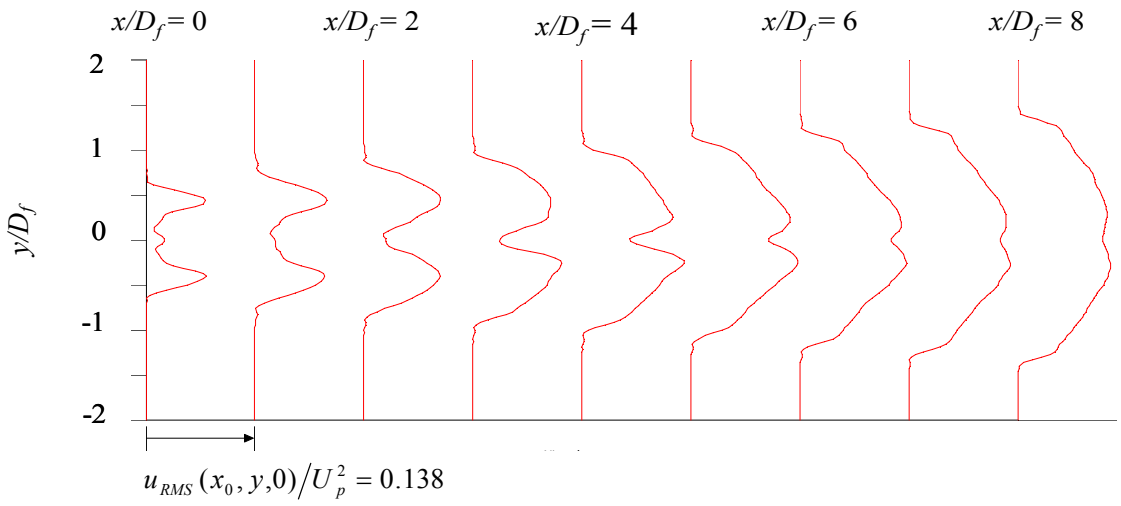

Figure 6.54. Evolution of the horizontal RMS velocity profiles. Baseline jet.

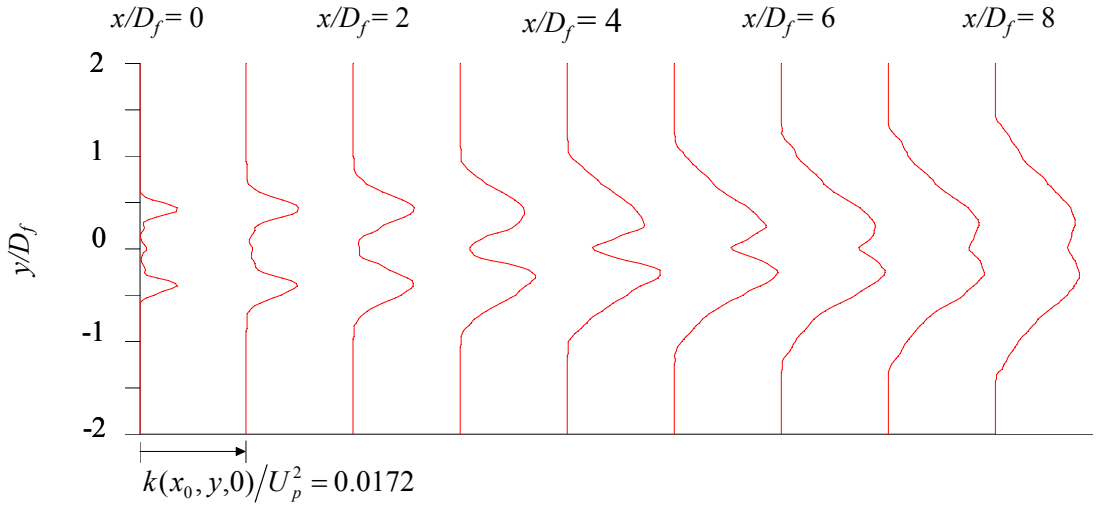

Figure 6.55. Evolution of turbulent kinetic energy transverse profiles. Baseline jet.

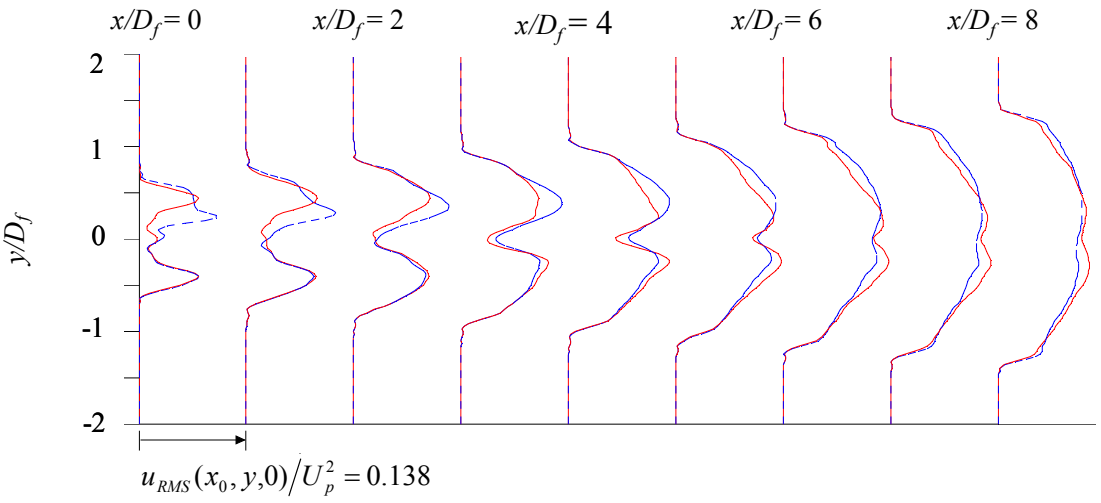

Figure 6.56. Evolution of RMS axial velocity profiles. W_1 - - - overlaid with baseline —.

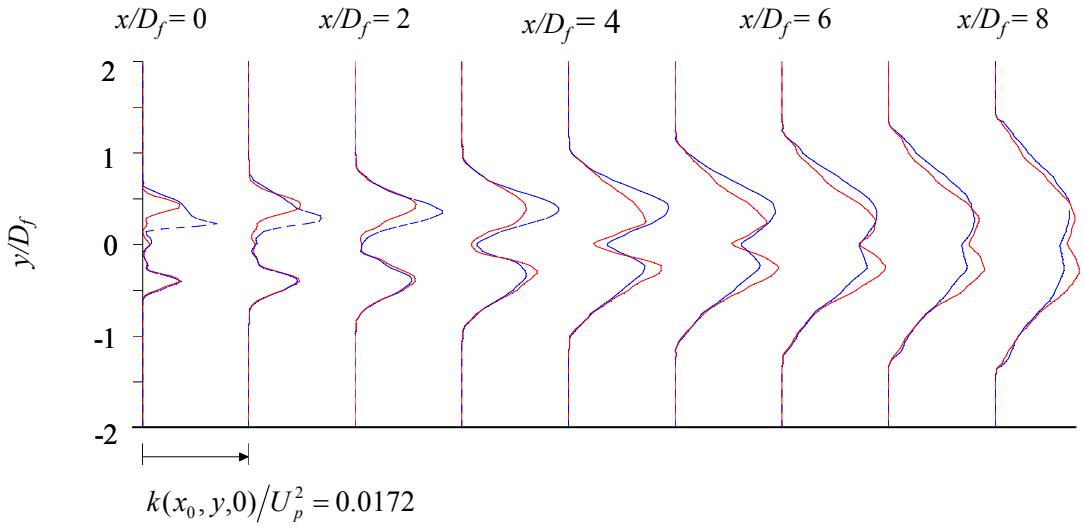

Figure 6.57. Evolution of turbulent kinetic energy transverse profiles. W_1 - - - overlaid with baseline —.

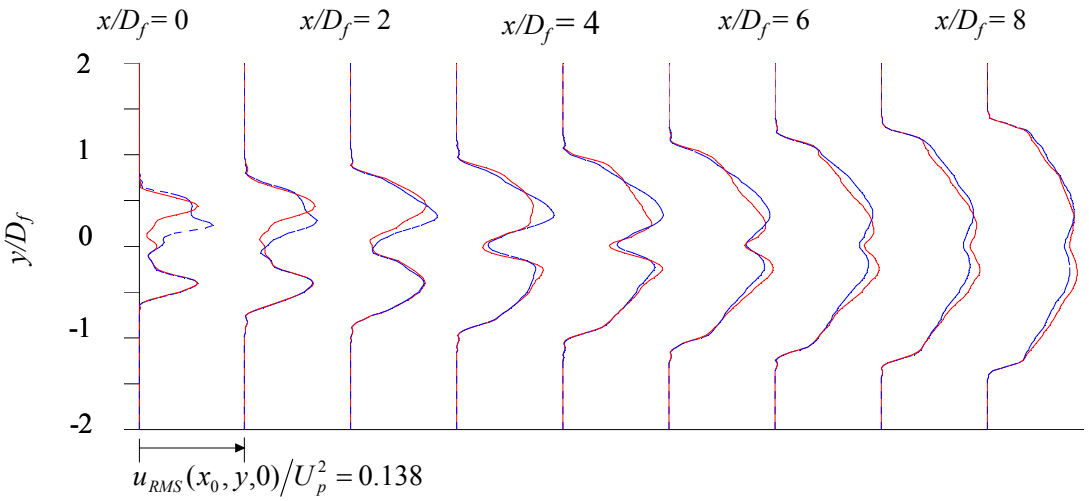

Figure 6.58. Evolution of RMS axial velocity profiles. W_2 - - - overlaid with baseline —.

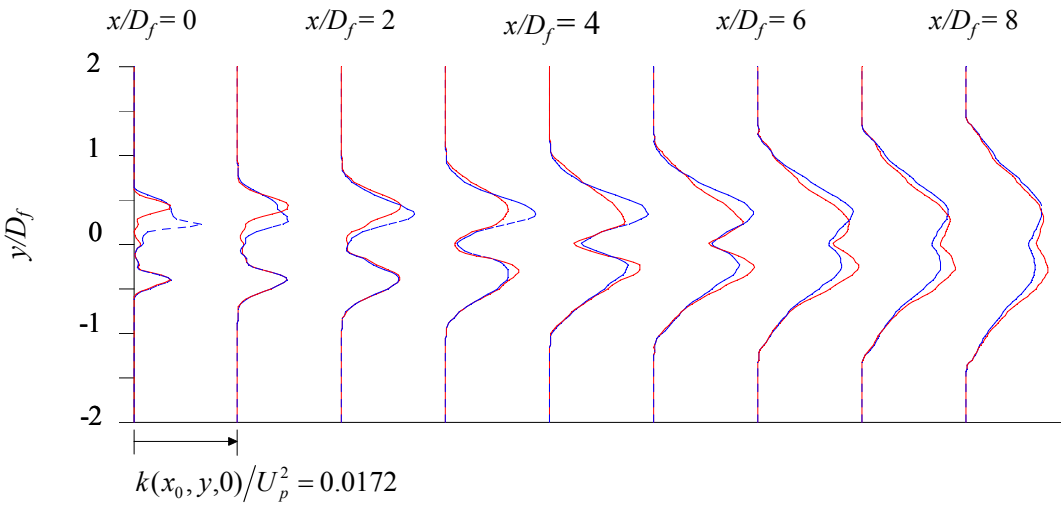

Figure 6.59. Evolution of turbulent kinetic energy transverse profiles. W_2 - - - overlaid with baseline —.

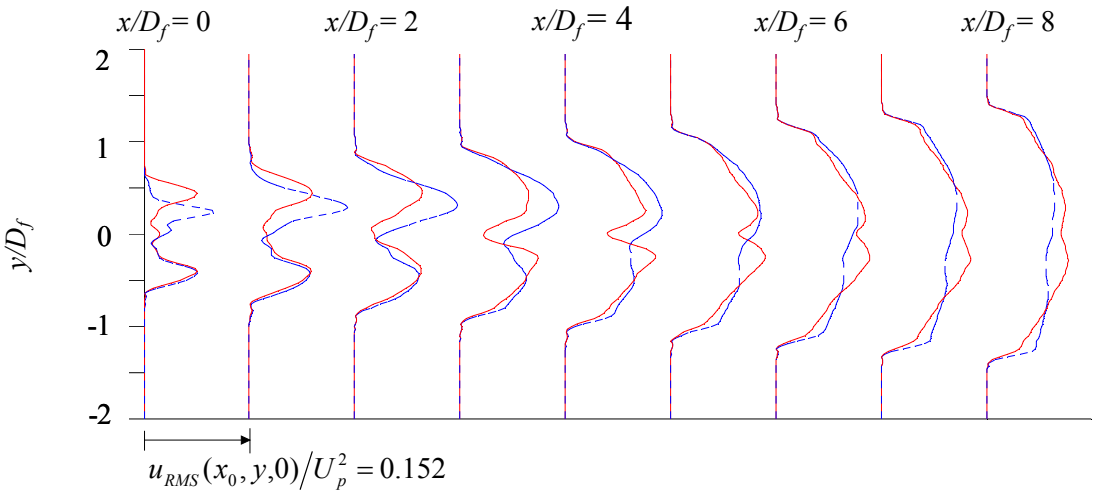

Figure 6.60. Evolution of RMS axial velocity profiles. W_3 - - - overlaid with baseline —.

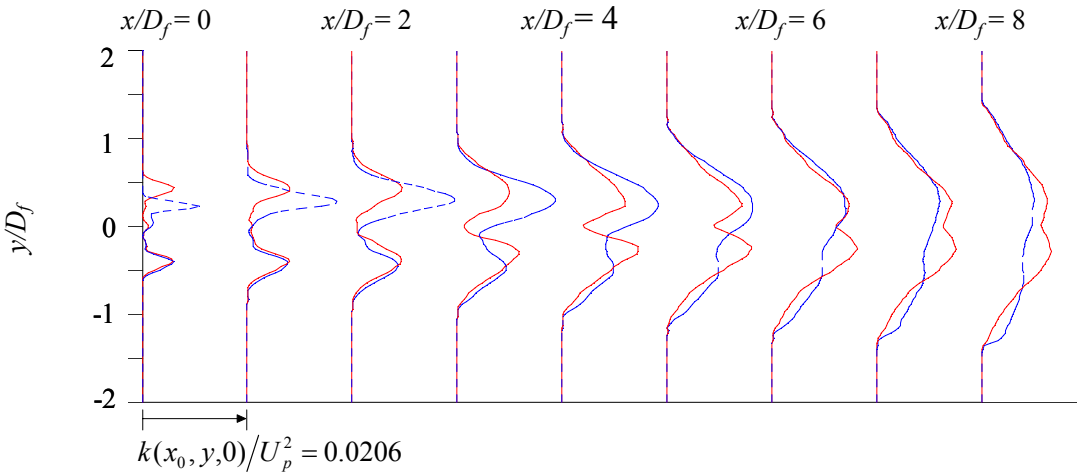

Figure 6.61. Evolution of turbulent kinetic energy transverse profiles. W_3 - - - overlaid with baseline —.

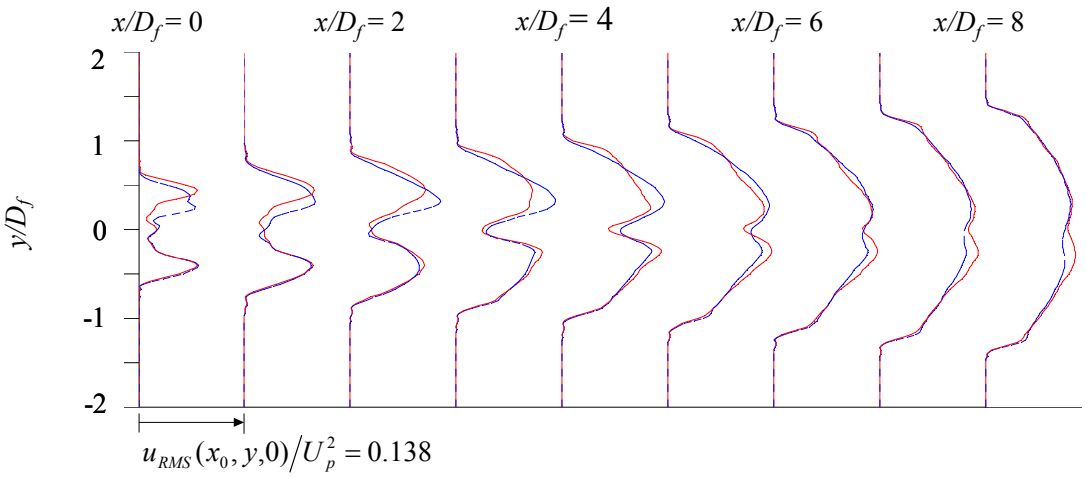

Figure 6.62. Evolution of RMS axial velocity profiles. W_4 - - - overlaid with baseline —.

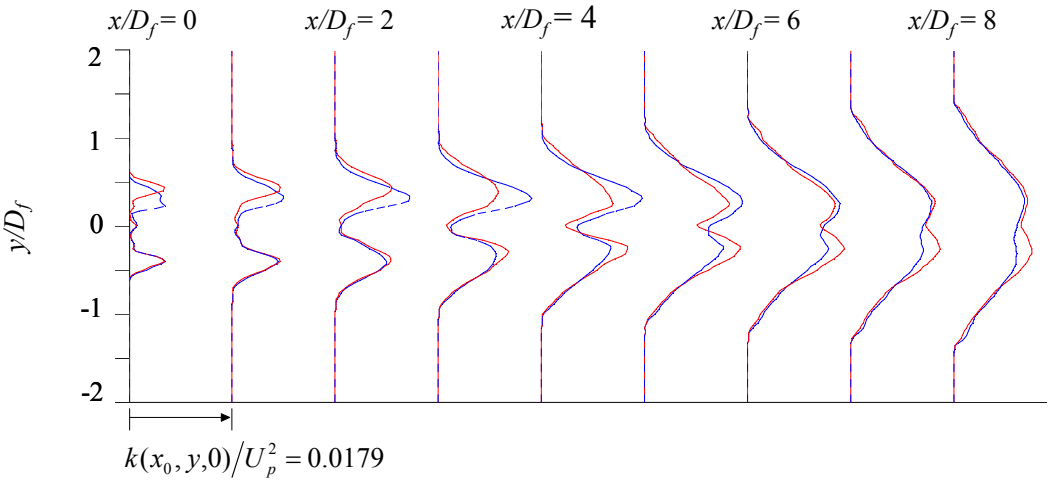

Figure 6.63. Evolution of turbulent kinetic energy transverse profiles, $k(x,y,0)/U_p^2$. W_4 - - - overlaid with baseline —.

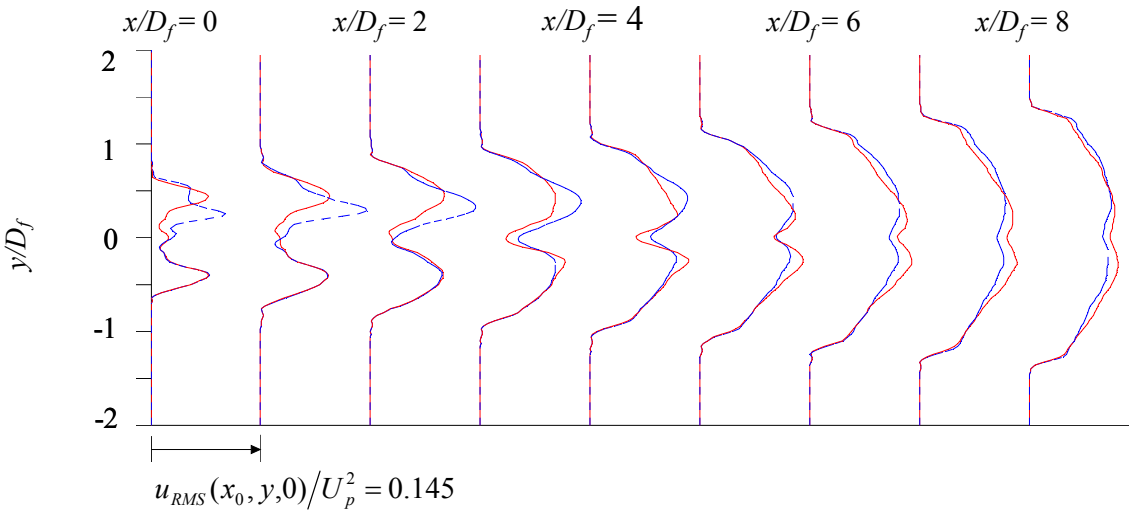

Figure 6.64. Evolution of RMS axial velocity profiles. W_2 +Cap 1 - - -overlaid with baseline —.

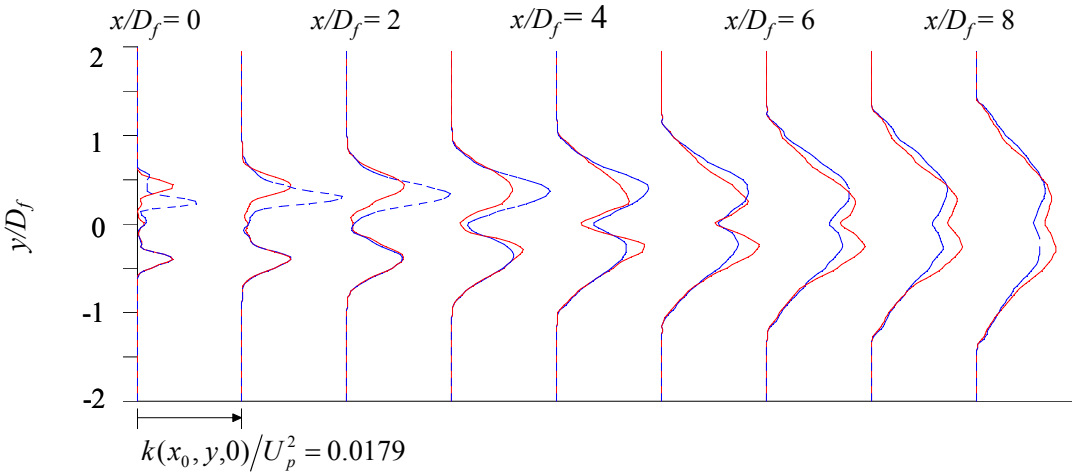

Figure 6.65. Evolution of turbulent kinetic energy transverse profiles. W_2 +Cap 1 - - - overlaid with baseline —.

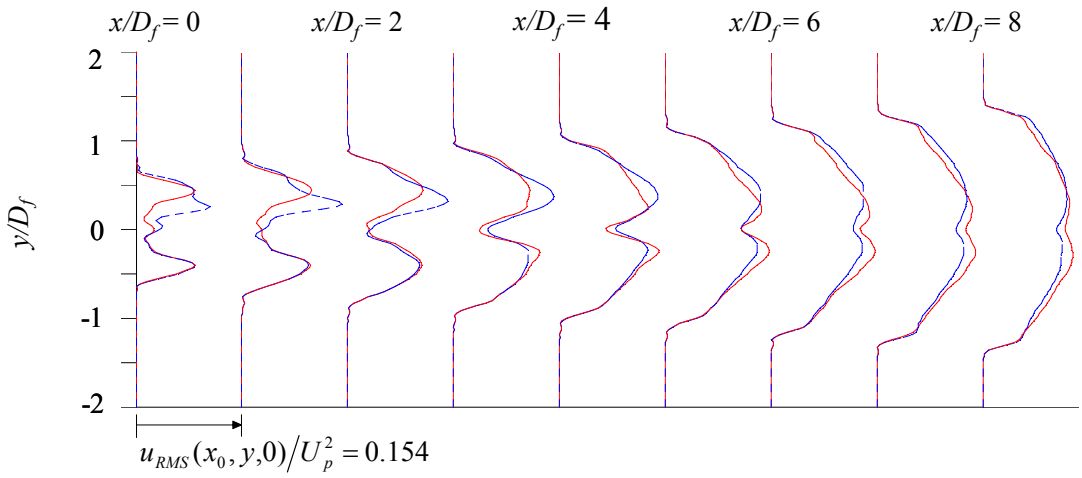

Figure 6.66. Evolution of RMS axial velocity transverse profiles. W_2 + Cap 2 - - - overlaid with baseline —.

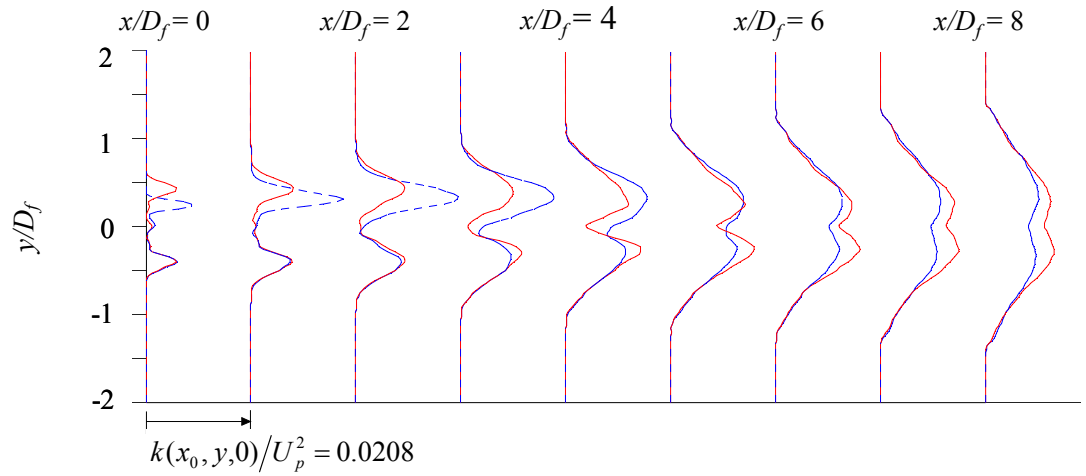

Figure 6.67. Evolution of turbulent kinetic energy transverse profiles. W_2 + Cap 2 - - - overlaid with baseline —.

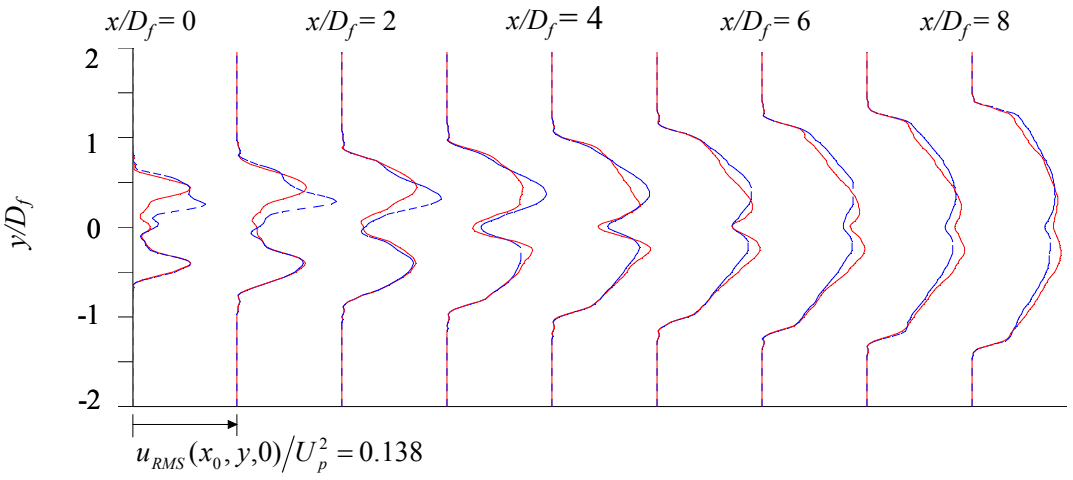

Figure 6.68. Evolution of RMS axial velocity profiles. W_2 + Cap 3 - - - overlaid with baseline —.

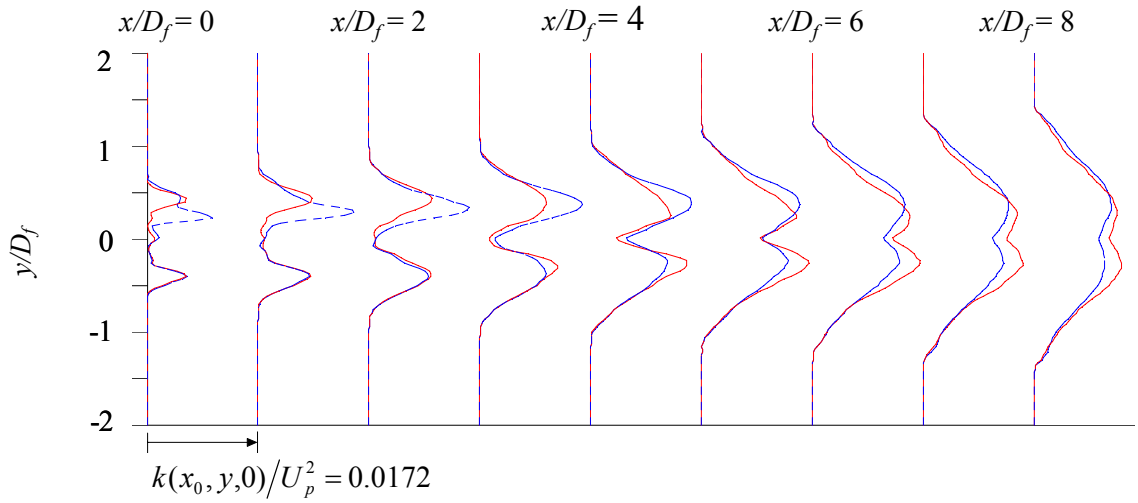

Figure 6.69. Evolution of turbulent kinetic energy transverse profiles. W_2 +Cap 3 - - - overlaid with baseline —.

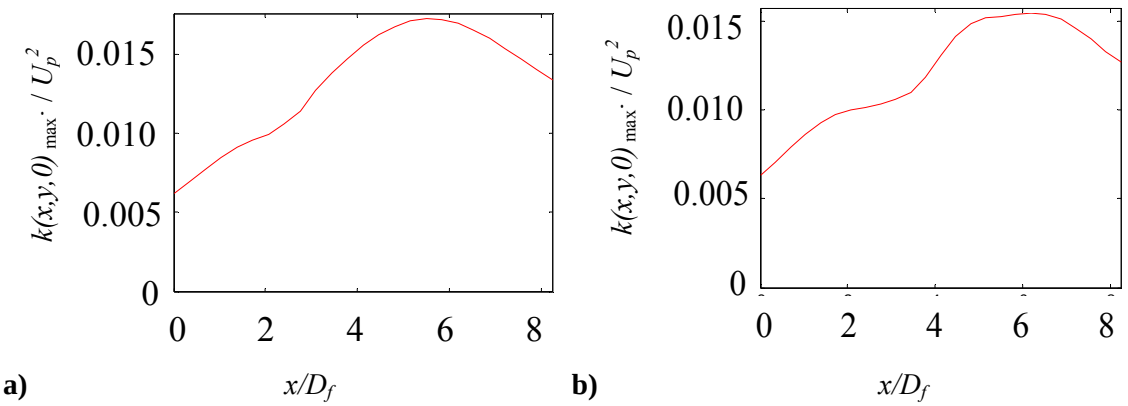

Figure 6.70. Baseline jet axial distribution of maximum turbulent kinetic energy a) below and b) above the jet centerline.

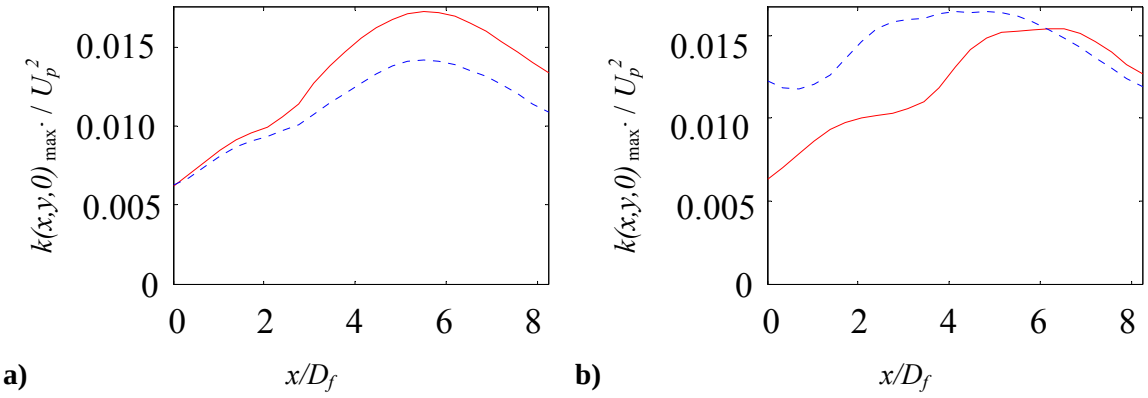

Figure 6.71. Axial distribution of maximum turbulent kinetic energy a) below and b) above the jet centerline. W_1 - - - overlaid with baseline —.

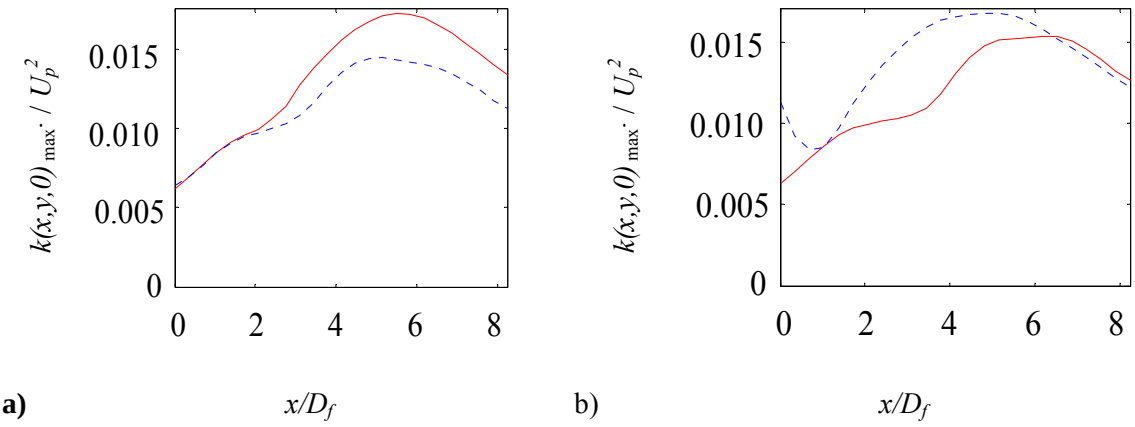

Figure 6.72. Axial distribution of maximum turbulent kinetic energy a) below and b) above the jet centerline. W_2 - - - overlaid with baseline —.

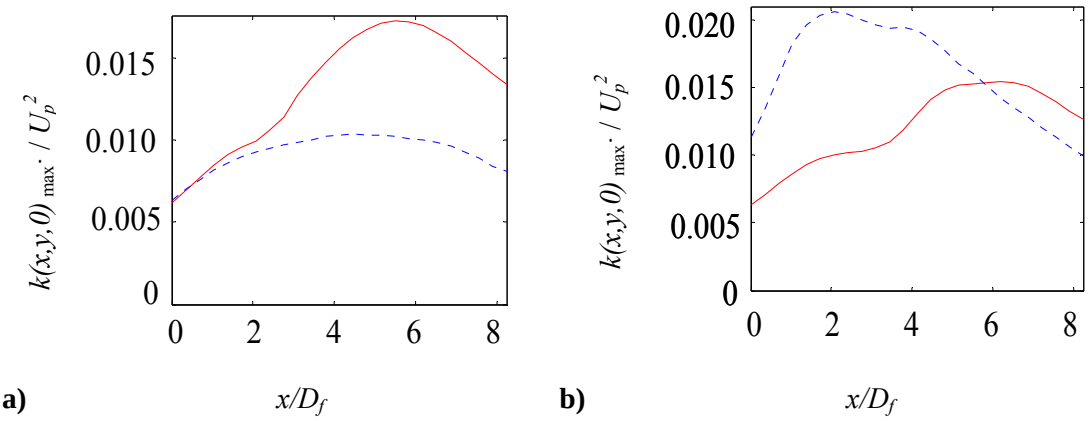

Figure 6.73. Axial distribution of maximum turbulent kinetic energy a) below and b) above the jet centerline. W_3 - - - overlaid with baseline —.

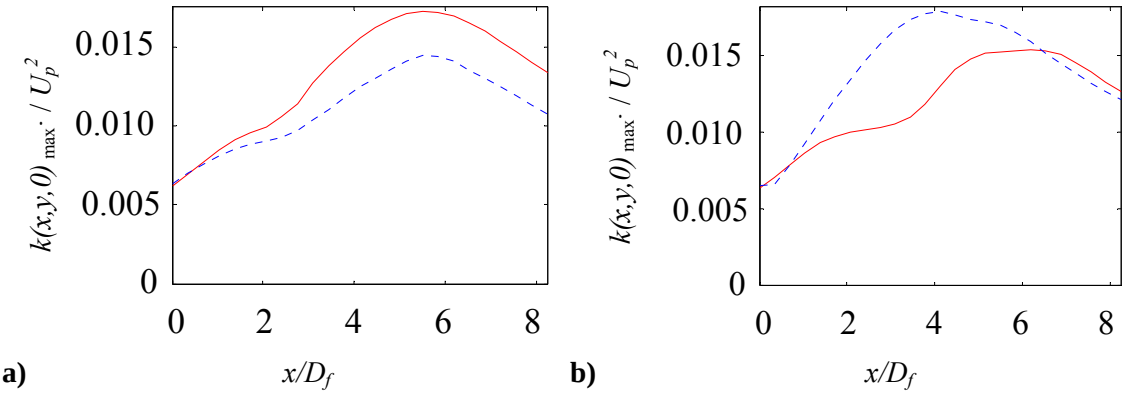

Figure 6.74. Axial distribution of maximum turbulent kinetic energy a) below and b) above the jet centerline. W_4 - - - overlaid with baseline —.

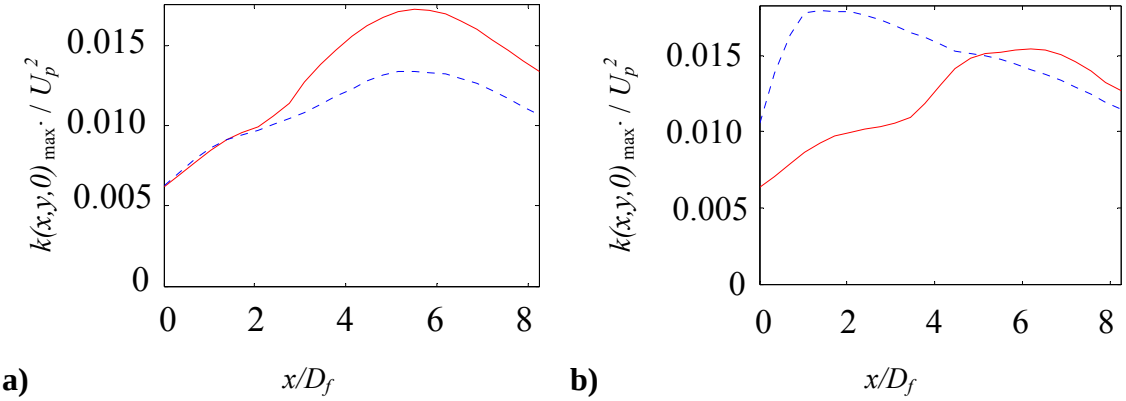

Figure 6.75. Axial distribution of maximum turbulent kinetic energy a) below and b) above the jet centerline. W_2+Cap1 - - - overlaid with baseline —.

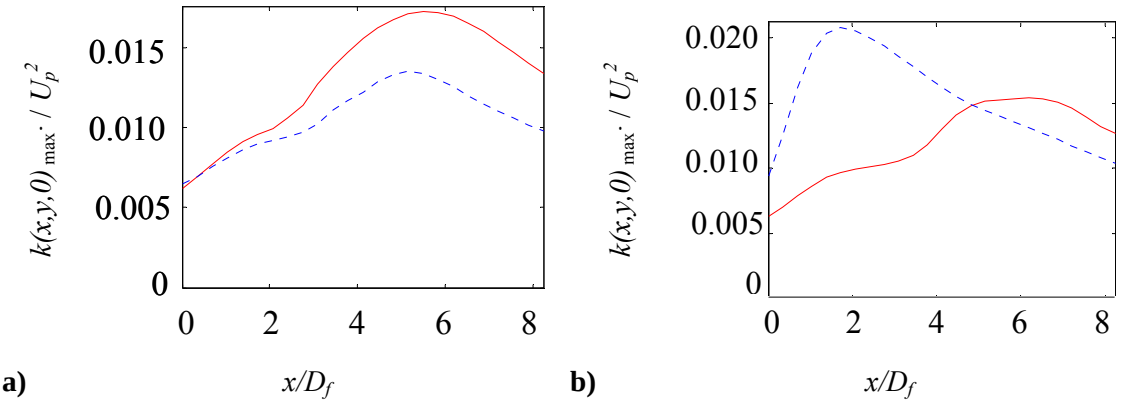

Figure 6.76. Axial distribution of maximum turbulent kinetic energy a) below and b) above the jet centerline. W_2 +Cap 2 - - - overlaid with baseline —.

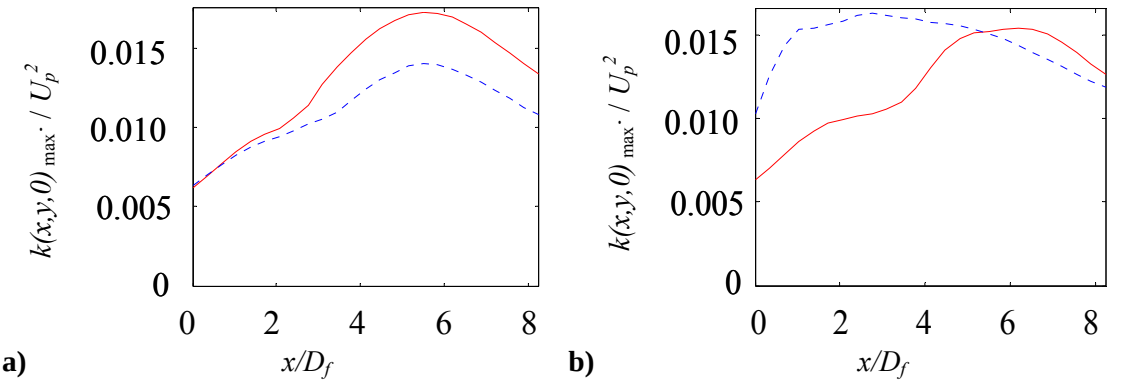

Figure 6.77. Axial distribution of maximum turbulent kinetic energy a) below and b) above the jet centerline. W_2 + Cap 3 - - - overlaid with baseline —.

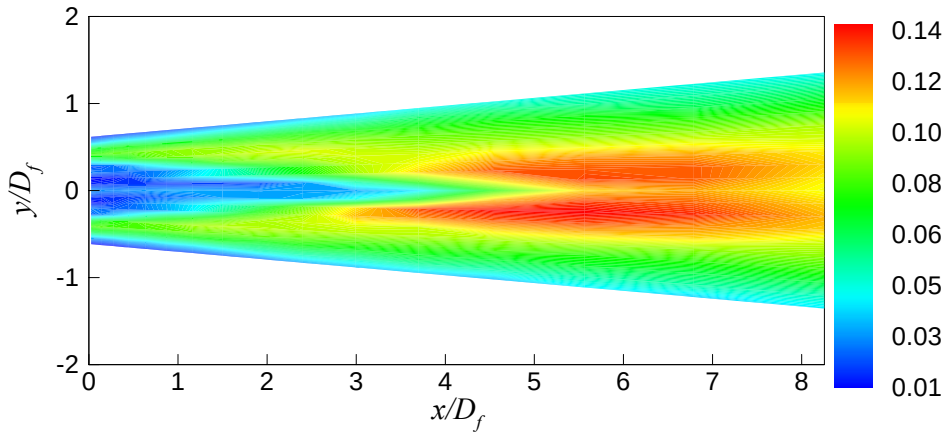

Figure 6.78. Axial RMS velocity distribution, $u_{RMS}(x,y,0)/U_p$ for the baseline jet.

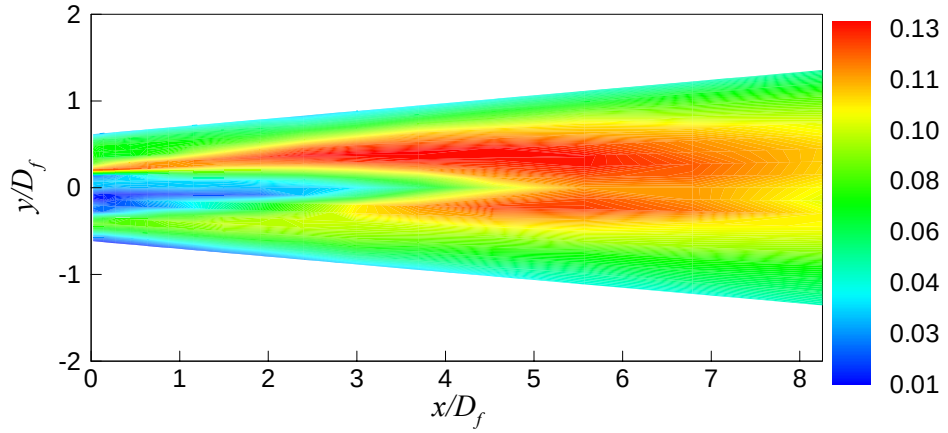

Figure 6.79. Axial RMS velocity distribution, $u_{RMS}(x,y,0)/U_p$ for W_1.

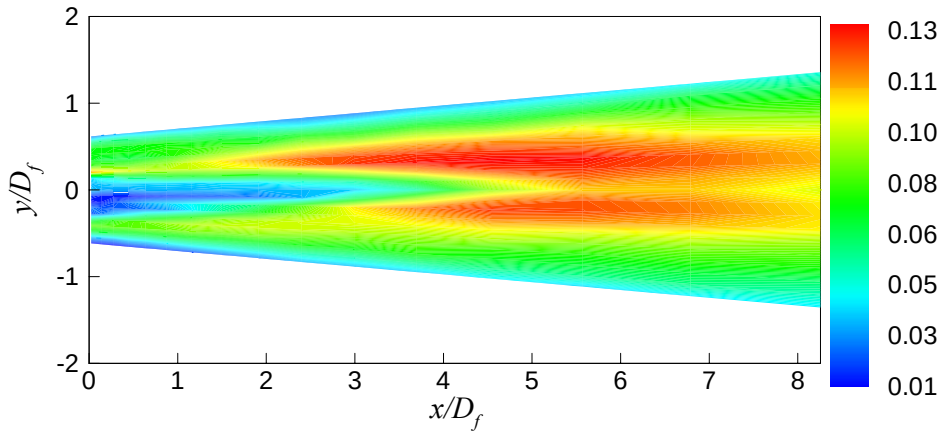

Figure 6.80. Axial RMS velocity distribution, $u_{RMS}(x,y,0)/U_p$ for W_2.

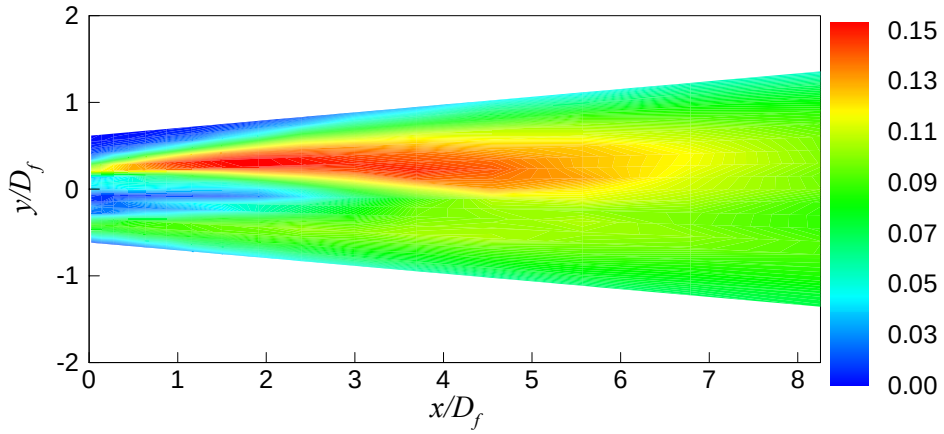

Figure 6.81. Axial RMS velocity distribution, $u_{RMS}(x,y,0)/U_p$ for W_3.

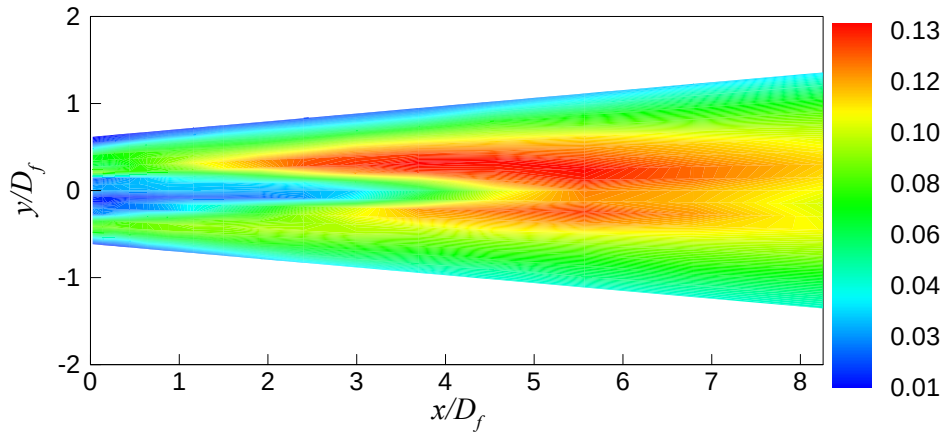

Figure 6.82. Axial RMS velocity distribution, $u_{RMS}(x,y,0)/U_p$ for W_4.

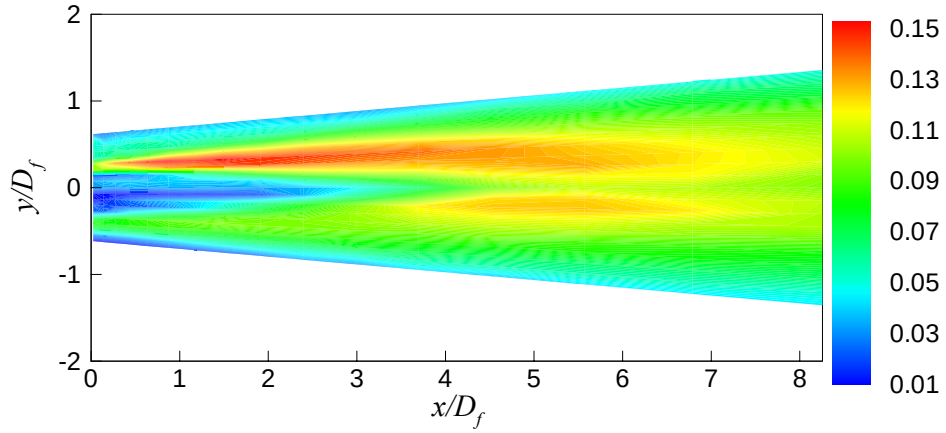

Figure 6.83. Axial RMS velocity distribution, $u_{RMS}(x,y,0)/U_p$ for W_2 + Cap 1.

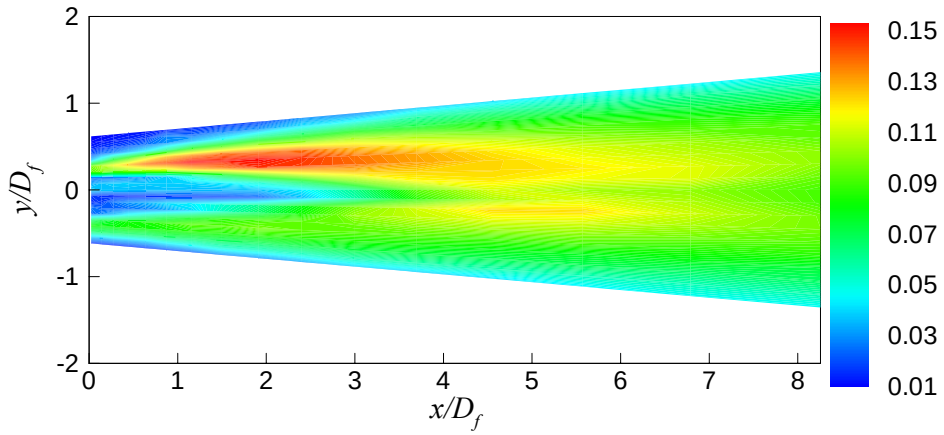

Figure 6.84. Axial RMS velocity distribution, $u_{RMS}(x,y,0)/U_p$ for W_2 + Cap 2.

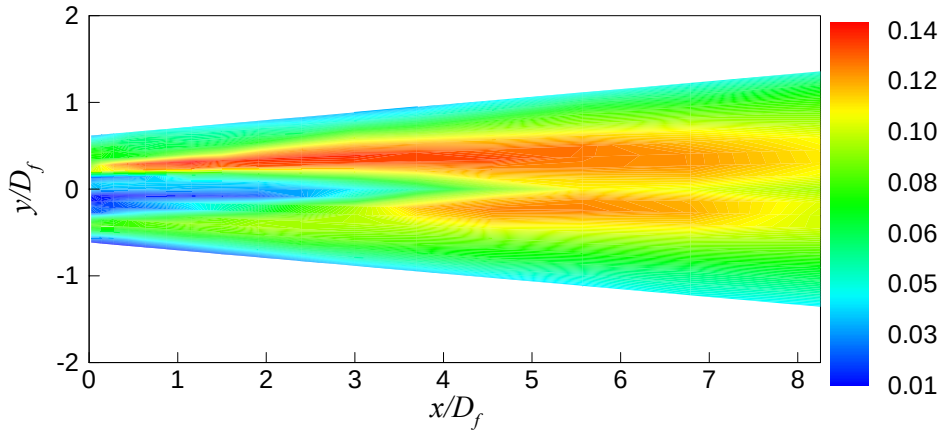

Figure 6.85. Axial RMS velocity distribution, $u_{RMS}(x,y,0)/U_p$ for W_2 + Cap 3.

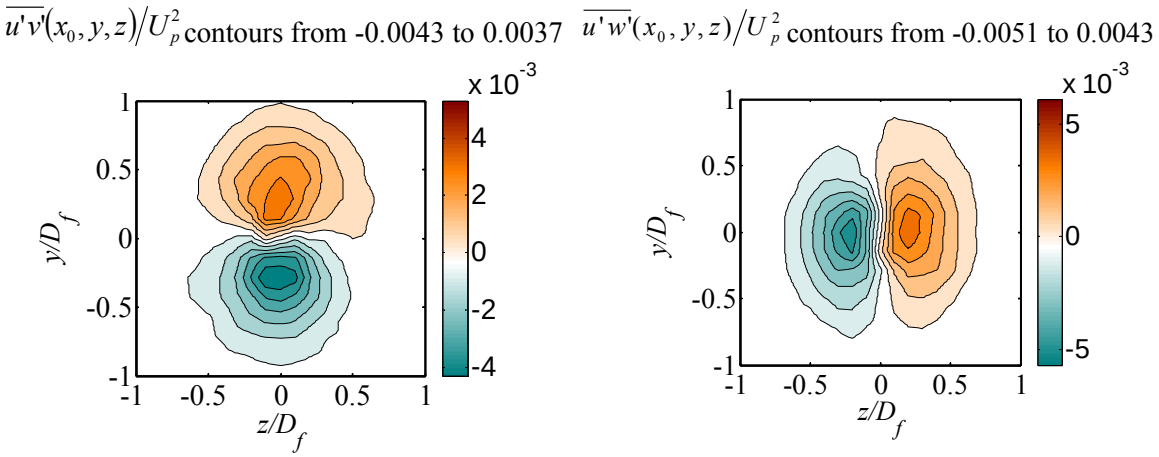

Figure 6.86. Reynolds stresses for baseline jet at $x/D_f = 4$.

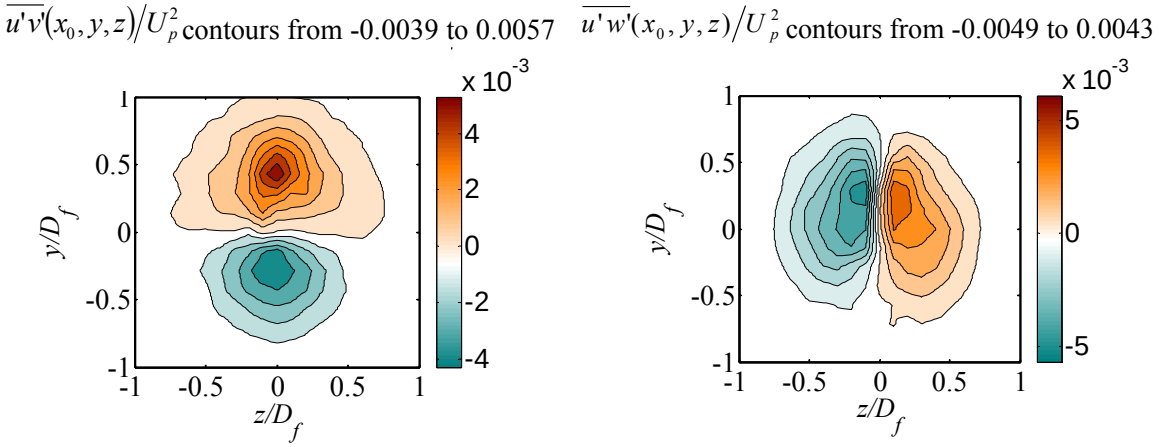

Figure 6.87. Reynolds stresses for W_1 at $x/D_f = 4$.

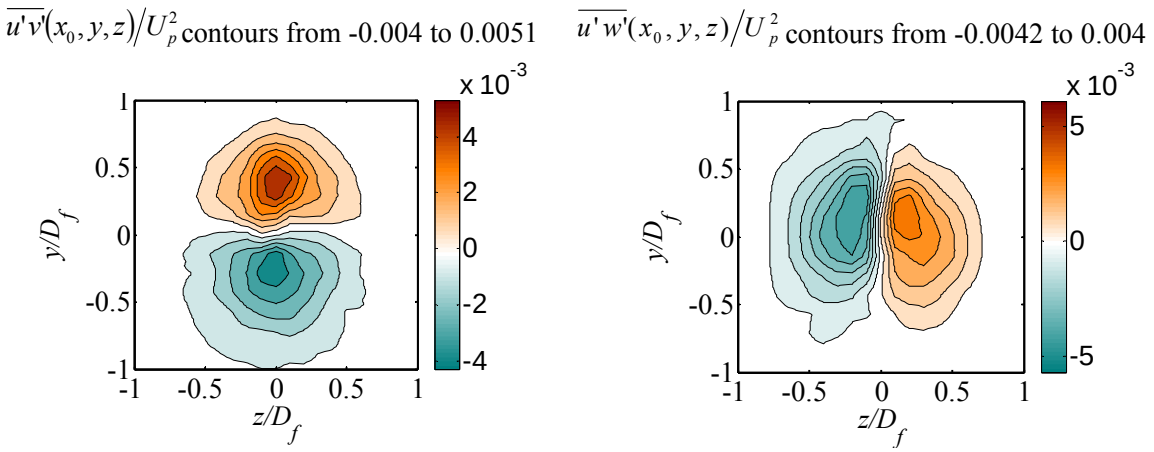

Figure 6.88. Reynolds stresses for W_2 at $x/D_f = 4$.

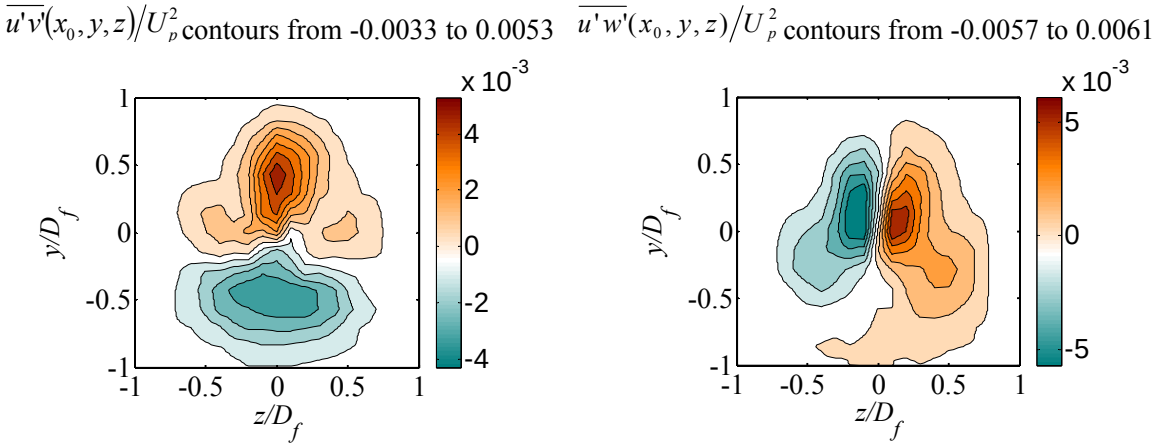

Figure 6.89. Reynolds stresses for W_3 at $x/D_f = 4$.

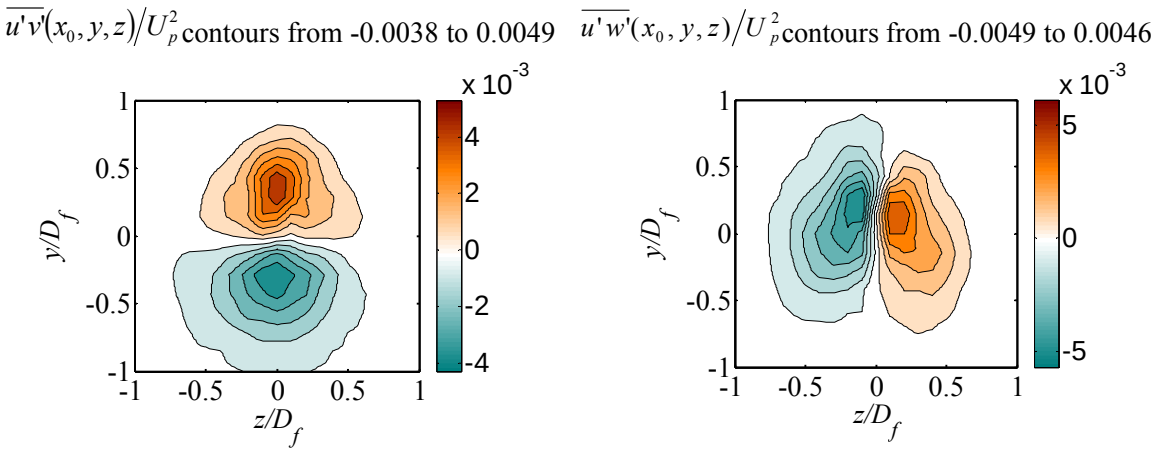

Figure 6.90. Reynolds stresses for W_4 at $x/D_f = 4$.

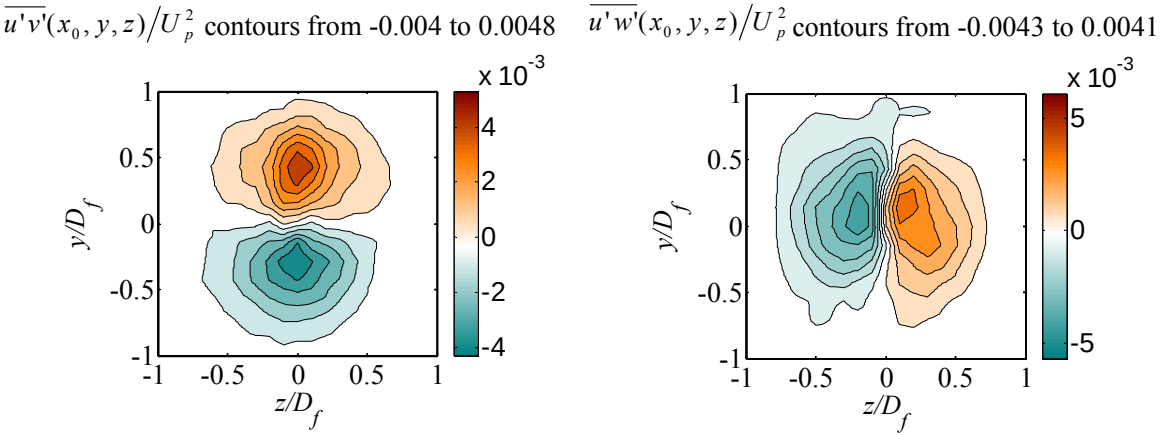

Figure 6.91. Reynolds stresses for W_2 +Cap 1 at $x/D_f = 4$.

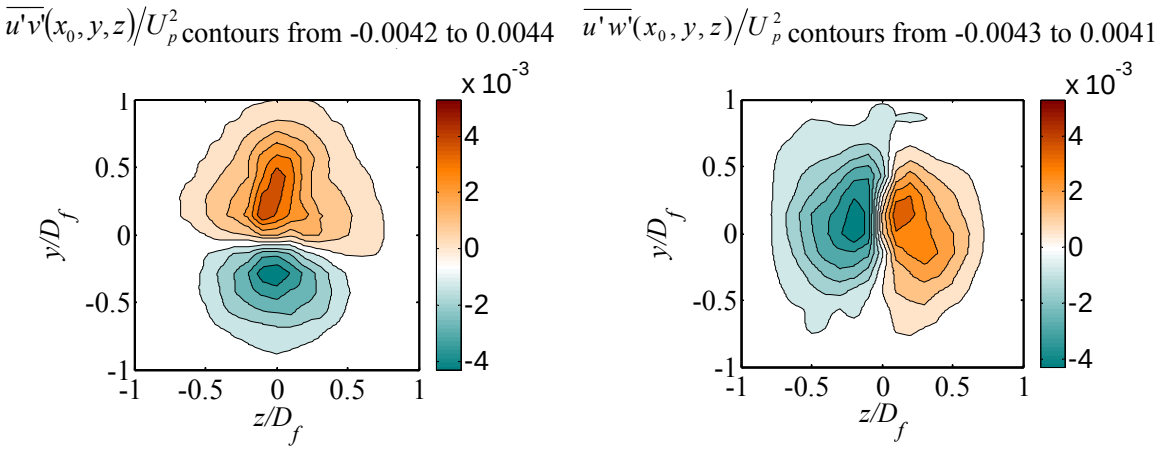

Figure 6.92. Reynolds stresses for W_4 + Pylon at x/D_f = 4.

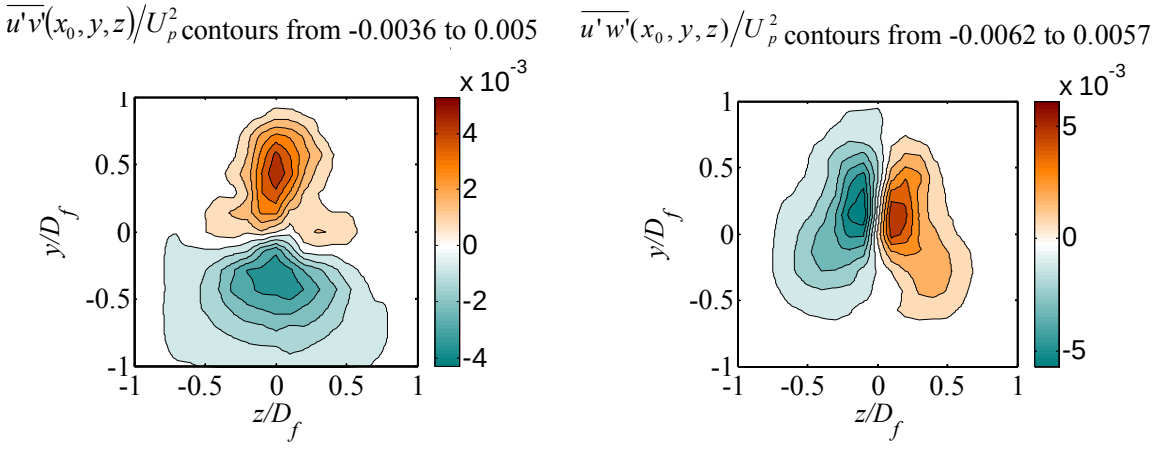

Figure 6.93. Reynolds stresses for W_4 +Pylon+Flaps at x/D_f = 4.

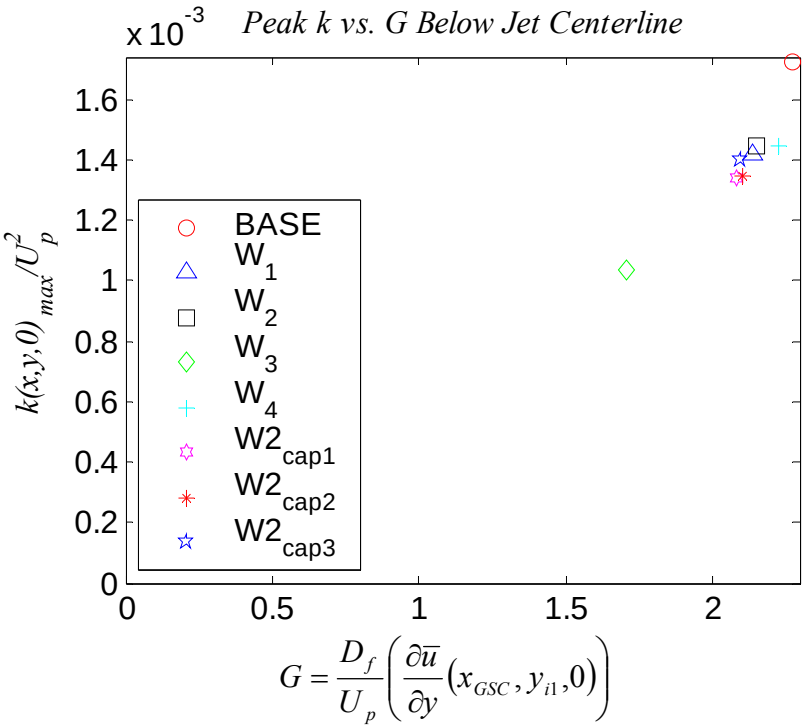

a)

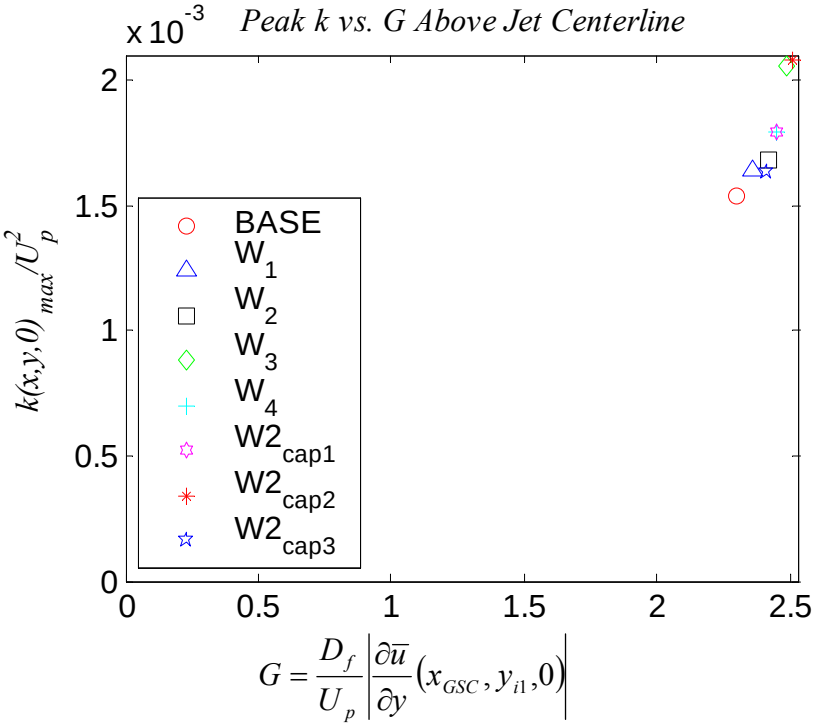

b)

Figure 6.94. Peak *k* vs. *G* a) below and b) above jet centerline. *G* is calculated at x_{GSC}, and it is nondimensionalized using D_f.

a)

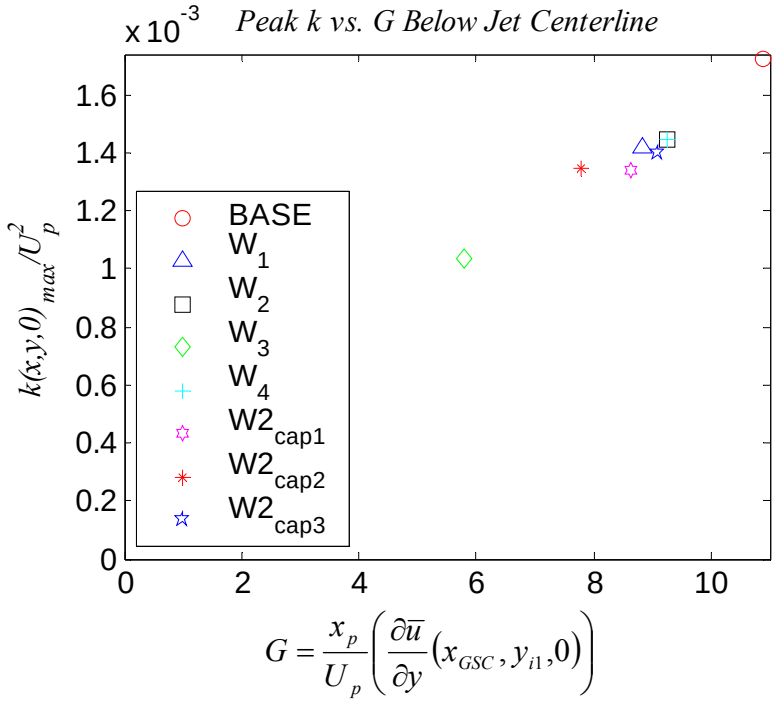

b)

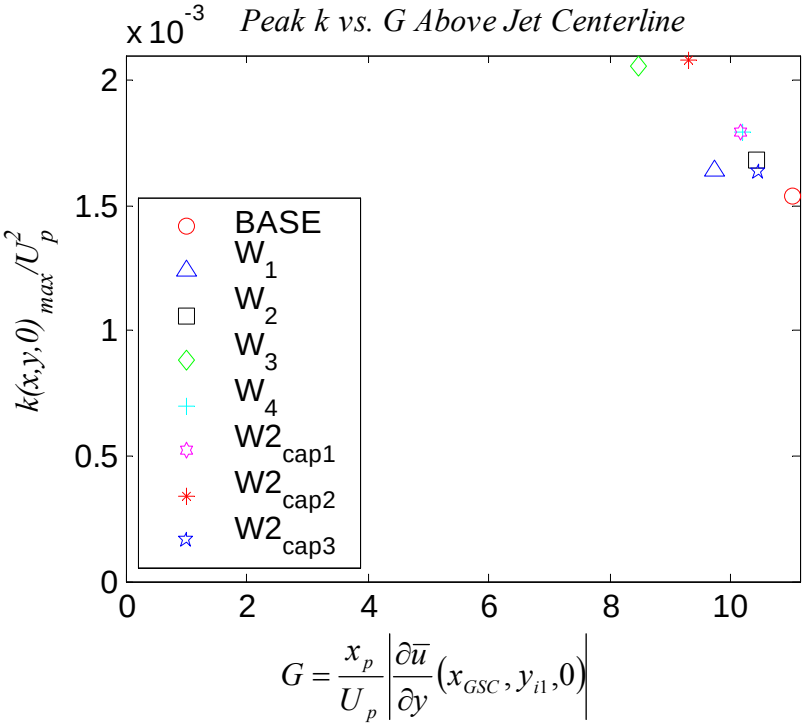

Figure 6.95. Peak *k* vs. *G* a) below and b) above jet centerline. *G* is calculated at x_{GSC}, and it is nondimensionalized using x_p.

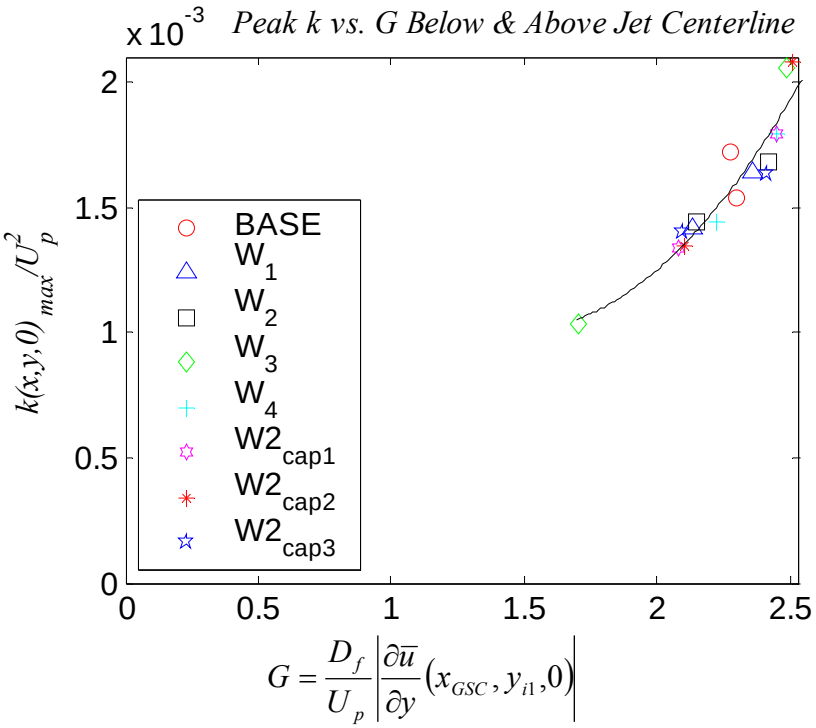

Figure 6.96. Peak *k* vs. G both below and above jet centerline. *G* is calculated at x_{GSC}, and it is non-dimensionalized using D_f. A second order polynomial fit is also plotted.

Chapter 7

Reynolds-Averaged Navier-Stokes (RANS) Investigations

In addition to the experimental program outlined in Chapter 3, computational resources were made available at NASA Glenn Research Center as part of the "offset-stream" technology research program. Comparisons between Reynolds-Averaged Navier-Stokes (RANS) solutions and experimental data are presented here. Computational solutions were obtained using Wind-US 1.0, a Reynolds-Averaged Navier-Stokes (RANS) solver. Wind-US is a product of the NPARC Alliance, a partnership between the NASA Glenn Research Center (GRC) and the Arnold Engineering Development Center (AEDC). The Shear Stress Transport (SST) turbulence model, which is a hybrid between the k-ε and k-ω models, was used. The reader is referred to Ref. 58 for details of the SST model. Currently, acoustics models are not reliable. Here, only the flow field is investigated. The objectives are two-fold: to look at the accuracy of the RANS predictions of mean and turbulent flow field parameters compared with experimental measurements and to look at the effects of forward flight and realistic exhaust Mach number.

Wind is a structured, multi-zone, compressible flow solver with flexible chemistry and turbulence models. The equations in Wind are written using a node-centered finite-volume approach. All boundary conditions can be imposed explicitly, and surface boundary conditions can be imposed implicitly. Inflow conditions may be imposed uniformly or may vary across the boundary. In addition to perfect gas simulations, Wind can predict real-gas effects using either finite-rate chemistry or a frozen chemistry approximation. Several standard chemistry databases are provided, or the user may supply a database of species properties and reaction rates, Refs. 55, 56. Many validation cases have been demonstrated and compared against benchmark data using Wind. Computational solutions along with the experimental databases are available at the Wind validation website (http://www.grc.nasa.gov/WWW/wind/valid/validation.html).

For the turbulent flat plate validation case, the experimental data of Wieghardt (1951) as tabulated by Coles (1968) and separately, the data of Patel, Rodi, and Scheuerer (1985), were used for comparison with the computational solutions obtained in Wind using Chien and SST turbulence models. For a $y+$ value of 2, grid independence was demonstrated and the computational solution showed good agreement with the data of Wieghardt. Another important validation case is for incompressible flow over a backward facing step, in which ten grid points were recommended to be placed between a distance of $y+=30$ and the location of the back-side of the step. The experimental data used for validation in this study are those of Driver and Seegmiller (1985). Grid sensitivity studies were performed in addition to benchmarking.

7.1 Governing Equations of Motion

For a fluid, the conservation of mass is commonly expressed in terms of a balance between the rate of change of mass inside a control volume and the rate of convection of mass in and out of the control volume. The conservation of mass can be expressed locally by the continuity equation

$$\frac{\partial \rho}{\partial t} + \nabla \cdot \left(\rho \underset{\sim}{u} \right) = 0 \tag{7.1}$$

For an incompressible flow this simplifies to an expression that says that the time rate of change of the volume of a fluid element per unit volume does not change, but remains fixed: $\nabla \cdot \underset{\sim}{u} = 0$.

The second fundamental law is the conservation of momentum, which for fluid flows is accounted for by the Navier-Stokes equations

$$\rho \frac{\partial \underset{\sim}{u}}{\partial t} + \rho \underset{\sim}{u} \cdot \nabla \underset{\sim}{u} = -\nabla p + \nabla \cdot \underset{=}{\tau}, \tag{7.2}$$

and the constitutive relation for the shear stress tensor is

$$\underset{=}{\tau} = \lambda \nabla \cdot \underset{\sim}{u} \underset{=}{I} + \mu \left(\nabla \underset{\sim}{u} + \nabla \underset{\sim}{u}^{T} \right), \tag{7.3}$$

accounting for rates of strain and rate of rotation due to viscous forces, including both the normal and tangential effects of viscosity. $\underset{=}{I}$ is the identity matrix, μ is the coefficient of viscosity, $\lambda = -2/3\mu$, and superscript '*T*" denotes the transpose.

We define the total local kinetic energy

$$K = \frac{\underset{\sim}{u} \cdot \underset{\sim}{u}}{2}. \tag{7.4}$$

The equation for conservation of mechanical energy is a vector product between velocity and Eq.7.2:

$$\rho \frac{DK}{Dt} = -\underset{\sim}{u} \cdot \nabla p + \underset{\sim}{u} \cdot \nabla \cdot \underline{\underline{\tau}}, \tag{7.5}$$

where $\frac{D(\ )}{Dt} = \frac{\partial}{\partial t} + \underset{\sim}{u} \cdot \nabla(\ )$ is the Lagrangian derivative, following a fluid particle.

For a turbulent flow, the velocity vector $\underset{\sim}{u}$, the density ρ, the pressure p, and the shear stress tensor, $\underline{\underline{\tau}}$ are decomposed into two components, a fluctuating component and a mean component:

$$\underset{\sim}{u} = \underset{\sim}{u}'(t) + \overline{\underset{\sim}{u}} \tag{7.6}$$

$$\rho = \rho'(t) + \overline{\rho}$$

$$p = p'(t) + \overline{p}$$

$$\underline{\underline{\tau}} = \underline{\underline{\tau}}'(t) + \overline{\underline{\underline{\tau}}}$$

$$K = k'(t) + \overline{k}$$

$$e = e'(t) + \overline{e}$$

The addition of fluctuating components introduces a nonlinear Reynolds stress term making an exact analytic closed-form solution for turbulent flows impossible to obtain without modelling via an artificial eddy viscocity. This is popularly referred to as the closure problem of turbulence. The Prantl's mixing length hypothesis is based on the supposition that the eddy viscosity scales with the Prandtl's mixing length. An artificial eddy viscosity is used to model the Reynolds stresses. The model used in the

computations presented here is a hybrid between the k-ε and k-ω models, called the Shear Stress Transport (SST) model. In Ref. 57, details of the SST and several other turbulent Reynolds stress models available using Wind are provided. In addition, the mass, momentum, and energy equations, used to carry out computations in Wind, are presented in a standard, mass-weighted Reynolds-averaged form. They are restated here:

$$\frac{\partial \overline{\rho}}{\partial t} + \frac{\partial \left(\overline{\rho}\hat{u}_i\right)}{\partial t} = 0 \tag{7.7}$$

$$\frac{\partial \left(\overline{\rho}\hat{u}_i\right)}{\partial t} + \frac{\partial \left(\overline{\rho}\hat{u}_i\hat{u}_j\right)}{\partial x_j} + \frac{\partial \overline{p}}{\partial x_i} - \frac{\partial \overline{\tau}_{ij}}{\partial x_j} - \frac{\partial \overline{\tau}_{ij}^{T}}{\partial x_i} = 0$$

$$\frac{\partial \left(\overline{\rho}\hat{e}_t\right)}{\partial t} + \frac{\partial \left(\overline{\rho}\hat{u}_i\hat{e}_t + \hat{u}_i\overline{p}\right)}{\partial x_j} - \frac{\partial \left(\hat{u}_i\overline{\tau}_{ij} + \hat{u}_i\overline{\tau}_{ij}^{\ T}\right)}{\partial x_j} + \frac{\partial \left(\overline{q}_j + q_j^T\right)}{\partial x_j} = 0$$

Indicial notation is used to denote three dimensional vector space, and the mass-weighted averaged values, denoted by a carat, are obtained as follows: $\hat{a}_i = \frac{1}{\overline{\rho}\tau}\int_t^{t+\tau} \rho a_i dt$.

7.2 Computational Grids and Boundary Conditions

Structured grids were generated using Gridgen software by Pointwise Inc, Ref. 59. The computational domain for the axisymmetric (Baseline) case is shown in Fig.7.1. It is a two-dimensional grid that uses six zones and spans $30D_f$ downstream of the plug tip, and $15D_f$ radially outward from the jet centerline. Because the configuration is axisymmetric, that is, its solution depends on axial and radial position in space only, a solution of the whole flow field can be constructed from one quadrant. $0.13\text{x}10^6$ grid points were distributed across 6 zones for the axisymmetric (Baseline) case. Zone 1 (corresponding to the primary jet) consists of 67x41 grid points. Zone 2 (corresponding to

the secondary jet) consists of 67x41 grid points. Zone 3 (corresponding to the external flow around the secondary nozzle) consists of 67x105 grid points. Zone 4 (corresponding to the external flow around the primary nozzle) consists of 73x175 grid points. Zone 5 (corresponding to external flow around the plug) consists of 61x239 grid points. Zone 6 (corresponding to region downstream of plug tip) consists of 145x217 grid points.

The asymmetric case (Wedge case) is three-dimensional because it is dependent upon axial, radial, and azimuthal positions in space, however it is symmetric about the *xy*-plane. This grid used 6.3 x 10^6 points distributed across eight blocks. A block is a composite of several two-dimensional zones. The zones in any given block may fan out azimuthally to fill a block. The grid on the plane of symmetry is shown in Figs.7.2 and 7.3. Figure 7.2 shows seven blocks, including the blocks above and behind the wedge. Figure 7.3 shows the block starting from the wedge sidewall ending underneath the jet. The computational domain for the asymmetric case spanned $30D_f$ downstream of the plug tip and $15D_f$ radially from the jet axis. Because the flow field is symmetric about the *xy*-plane, the nozzle and computational domain is hemi-cylindrical, that is, the azimuthal range spanned 180^o. Block 1 (corresponding to the primary jet) consists of 67x41x91 grid points. Block 2 (corresponding to the secondary jet) consists of 67x41x67 grid points. Block 3 (corresponding to the external flow around the secondary nozzle) consists of 67x105x67 grid points. Block 4 (above the wedge) consists of 49x57x49 grid points. Block 5 (at the base of the wedge) consists of 25x49x175 grid points. Block 6 (corresponding to the external flow around the primary nozzle) consists of 73x175x67 grid points. Block 7 (corresponding to external flow around the plug) consists of 61x239x91 grid points. Block 8 (corresponding to region downstream of plug tip)

consists of 145x217x91 grid points. Grid sequencing was used to obtain faster convergence. The first grid used ¼ of the total grid points and the second grid used ½ of the total grid points. In each step, a finer grid is used along with the solution from the previous grid as the initial guess. The multi-gridding provides an idea of mesh independence, however, independence was not rigorously demonstrated due to convergence problems on the finer mesh for the wedge case. The grid had to be reduced in size before converged results were obtained (by Dr. Jim DeBonis at NASA Glenn Research Center, who is kindly thanked for his help in obtaining the solutions simulating forward flight for both the wedge and the corresponding baseline cases).

Figure 7.4 shows three-dimensional views of the nozzle and wedge used for the computations. Figure 7.5 shows a close up of a sample grid similar to the one used to obtain the results. For both of the axisymmetric grids and for the asymmetric grid, a y^+ value of 3 corresponding to a distance of 0.0003 inches from the wall was used to ensure accurate resolution of the boundary layers. Behind the wedge, it was expected that the boundary layer would not remain attached, and close packing next to the base of the wedge was not used. Although the wedge is quite a different problem from the rearward facing step, as noted in the introductory section of this chapter, grid independence was demonstrated for the incompressible backward facing step using ten grid points next to the wall within a $y+$ value of 30. For future work, grid independence should be demonstrated for the wedge case, simulating takeoff conditions.

Two Mach number settings were tested for the baseline case. One corresponds to the experimental configuration (low Mach number, static jet) and one corresponds to realistic takeoff conditions simulating forward flight, with M_a=0.2. The asymmetric (wedge) case

was only run at the high Mach number setting. Total (stagnation) pressures were specified for the nozzle inlet boundaries corresponding to the exhaust Mach numbers listed in Table 7.1. The Mach number exhaust settings were chosen to correspond to secondary-to-primary stream velocity ratio of 0.7. The jet Reynolds number based on the primary exit velocity and the fan diameter was 1.1×10^6. The exhaust configurations are listed in Table 7.1. The total pressures were calculated using the definition of total pressure

$$p_0 = p\left(1 + \frac{\gamma - 1}{2} M^2\right)^{\frac{\gamma}{\gamma - 1}}, \tag{7.8}$$

and atmospheric static pressure at the nozzle exit because the exhaust conditions are subsonic. Both streams were composed of cold air, and γ=1.4 was used for the specific heat ratio. Atmospheric pressure was 14.4 psi, corresponding to the average pressure reading in the GRC CW-17 lab during the hot-wire experiments. Total (stagnation) temperature was specified at the nozzle inlets equal to ambient temperature because this was the temperature of the air supply (reservoir) initially at rest before being fed to the CW-17 GRC '5BB' nozzle.

It should be noted that there is a minor difference between the area ratios of the experimental and computational nozzle coordinates, owing to the small imperfections in machining of the primary nozzle and plug diameters. The experimental nozzle area ratio was 3.84, and the computational nozzle area ratio was 3.88. This results in a difference in bypass ratio of 5%. Figure 3.5 shows the nominal '5BB' nozzle coordinates, used in the computational grids. The computations were not adjusted to match the experiment precisely because the nominal coordinates were readily available, and the because the differences were thought to be minor.

7.3 Computational Results

A second order Roe physical upwind differencing was used. Time stepping was performed using a first order implicit scheme. At the wall, the viscous boundary condition was explicitly set so that both tangential and normal velocity were zero at the wall.

In this section computational results are presented for the mean and turbulent flow fields. The axisymmetric case is compared with the asymmetric case and the flow field is assessed for its potential to reduce noise.

7.3.1 Mean Velocity and Radial Velocity Gradient

In Fig. 7.6, the mean axial velocity isocontours are shown, and a recirculation region behind the wedge is revealed by the negative velocity contours. This is to be expected in forward flight. The wedge is envisioned as being deployed only during takeoff and landing, reducing its impact on aerodynamic performance.

In Fig. 7.7, the surface flow visualization experiment photo is juxtaposed with the computational solution for the wedge. Very good qualitative agreement is observed in the angle of the uppermost flow line. This shows that the physics that govern this flow are the same for both the incompressible (experimental) and the compressible (simulated) jets. That is, the magnitude of the velocity on the free surface of an inviscid jet is constant. Ambient pressure was the same in both the experiment and in the simulation. Since the wedge angle was the same, the deflection angle should be the same. In Ch. 5 an inviscid jet analsysis was performed and conservation of area was used in calculations to plot the upper streakline. In the actual flow, the velocity would not be uniform

throughout, instead the wedge causes the velocity to slow down. This was made evident by the pressure measurements of Ref. 17. This means that the uppermost line plotted in Fig. 5.13, would move outward to preserve mass flow rate as is observed in Fig. 7.7. As noted in Ch. 3, the CW-17 experiments were limited to incompressible flow due to safety permit requirements and facility upgrades that were to be performed.

Figure 7.8 shows the evolution of the mean velocity profiles of the baseline jet. Figure 7.9 shows the evolution of the transverse profiles of radial velocity gradient in the baseline jet. Transverse profiles at 8 axial positions referenced from the plug tip are shown. As mentioned earlier, the free-stream velocity is non-zero in all of the mean velocity profiles (M_a=0.2). The velocity is predicted to be exactly zero at the tip of the plug. This measurement was not observed in the hot-wire experimental results for several reasons. The most practical is that the hot-wire could break if it came too close to the nozzle surface, and so the velocity could not be measured exactly at the plug tip in the experiment. Another is that the finite spacing between the hot-wire probes does not allow the measurement at a precise point, but rather, an average is obtained. Another observation in Fig. 7.9 that contrasts the hot-wire results is the mean flow gradient surrounding the plug. The resolution in the initial region of the jet was not high enough to resolve these steep gradients. The effect of the plug on noise emissions is not part of this study, and this difference is not thought to be important in the analyses herein.

Figure 7.10 shows the evolution of the mean velocity profiles for the asymmetric jet overlaid with the axisymmetric jet profiles. The velocity defect is evident behind the wedge in the initial region of the jet. The asymmetric jet profiles decay faster than the axisymmetric profiles, indicating better overall mixing. Figure 7.11 shows the radial

velocity gradient profiles for just two axial stations, one near the end of the generalized secondary core, and one near the end of the primary potential core. The maximum gradient is reduced both underneath and above the jet centerline.

Figs. 7.12 and 7.13 show the inflectional loci and generalized secondary cores above and below the jet centerline. The GSC is elongated below the jet centerline and shortened above the jet centerline in the asymmetric jet. This is similar to the trends observed in the experiment, and is desirable for noise suppression underneath the jet. The elongated secondary core has been demonstrated to reduce the convective Mach number of primary eddies in the shear layer, hindering their ability to transmit sound to the downward far-field, as mentioned in Chapter 2.

Figs. 7.14 and 7.15 show mean velocity isocontours normalized by the primary jet exit velocity, U_p for the two jet plumes. The potential core length is reduced in the asymmetric jet compared with the axisymmetric jet. The potential core is defined to end where the mean velocity drops to 90% of the primary jet exit velocity. This corresponds to the dark brown contour in Figs. 7.14 and 7.15. Also evident in Fig. 7.15 is the defect in the velocity contours due to the placement of the wedge in the initial region on the top of the jet.

Figs. 7.16 and 7.17 show cross-sectional slices of the mean velocity isocontours at x/D_f=0 and at x/D_f=6.7. Figure 7.16 shows the axisymmetric solution. The contours are circular. At x/D_f=0, the two core streams are made distinct, the primary stream having a dark brown color, and the secondary stream having a light green color, corresponding to the contours near $0.9U_p$ and $0.6U_p$ respectively. Between the core streams are the primary and secondary mixing layers with rapidly changing contours marking the steep gradients

here in the initial region of the jet. Further downstream at x/D_f=6.7, the two streams are well mixed, and the contours are evenly distributed. Figure 7.17 shows the effect of the wedge on the contours. The defect in the initial region of the jet is evident in Fig.7.17a. In Fig.7.17b, the contours are pear-shaped showing the thickening of the low-speed region of fluid underneath the jet. The spacing between the contours is wider underneath the jet than it was in the baseline jet, indicating reduced gradients. Also notable is the pinching of the flow at the top of the jet, yielding the reduced gradients on the upperside of the jet as well. These contours are very important in assessing the ability of a nozzle design to suppress noise. An integration of the radial gradients over the range of interest (generally speaking this will be the downward perimeter of the jet, from $-\pi/2$ to $\pi/2$) will enable a prediction of the ability of an asymmetric nozzle design to reduce noise compared with the baseline nozzle.

Figs. 7.18 and 7.19 show the axial distributions of the maximum mean velocity and of the radial velocity gradient beneath the jet centerline. In Fig. 7.18a, it can be seen that the asymmetric jet decays faster than the axisymmetric jet. Figure 7.18b shows that the maximum gradient is reduced for all axial locations underneath the jet centerline. Figure 7.19a shows the reduction in maximum velocity gradient underneath the jet without considering the sharp spike in the initial region. The maximum shear layer radial gradients are reduced at all axial locations, especially in the region near the end of the primary potential core. Figure 7.19b shows the axial distribution in maximum velocity gradient above the jet centerline without considering the sharp spike in the initial region. It is evident that the gradients are significantly reduced at most axial locations, even above the jet centerline. This was also observed in the hot-wire experiment for the

external wedge configuration. Table 7.3 lists some of the important flow field parameters, such as the lengths of the primary potential cores.

7.3.2 Turbulence Field

With increased Mach number exhaust conditions, the peak turbulent kinetic energy in the baseline jet is lower than it is in the low Mach number exhaust jet. This is to be expected, because for a compressible jet, turbulent mixing is much less than for the corresponding incompressible case. The growth rate in the initial region of a compressible jet (or of a turbulent mixing layer) is much less than its incompressible counterpart. Some background on compressible mixing is provided in Chapter 2.

Figs. 7.20–7.21 show the evolution of the turbulent kinetic energy for the baseline case and for the asymmetric configuration. Transverse profiles at 8 axial positions referenced from the plug tip are shown. Figure 7.20 is for the baseline case. The maximum turbulent kinetic energy occurs just past the end of the primary potential core, and the value is k/U_p^2=0.011. The distributions are much like the experimental distributions reported in Chapter 6 with the low (relative to the peak in the secondary shear layer) regions of turbulence being in the primary shear layer and in the wake due to the plug. Figure 7.21 shows the asymmetric profiles overlaid with the baseline profiles. In the initial region of the jet, measured downstream of the plug tip, the maximum value of the turbulent kinetic energy on the upper side of the jet is increased to k/U_p^2=0.0334. This is in contrast with the experimental measurements of k behind the wedge. While there was an increase in k, it was not as steep. This difference is probably because the experiments were run at low Mach number, while the computational result is for realistic

takeoff conditions. Figure 7.22 shows the axial distributions of turbulent kinetic energy. At all axial locations underneath the jet, the maximum value is decreased, except in the very initial region there is a slight increase. There is significant increase in turbulent kinetic energy in the initial region of the jet above the centerline. The increase in turbulent kinetic energy on the upper side of the jet raises the important question of what is the impact on sideline noise relative to the baseline. Also, a very important consideration is from wing-installation effects. The hope is that the effect of an increase in noise on the upper side of the jet will be benign when the wedge-shaped deflector is installed on an aircraft engine. Figure 1.7 shows that the wedge (on a bypass 5 ratio nozzle) suppresses noise for a range of azimuthal directions, including the groundward direction and the sideline direction. More testing will be needed to understand the effect of the three-dimensional flow field on sideline noise emissions.

Figs. 7.23 and 7.24 show the distributions on the *xy*-plane of the turbulent kinetic energy for the baseline and for the asymmetric jet. The asymmetric design significantly reduces turbulence intensity underneath the jet centerline, relative to the baseline jet, suggesting its potential to reduce downward emitted noise. A potential tradeoff is the increase in turbulence intensity above the jet centerline, especially in the initial region of the jet.

The close agreement between the computational model and the experimental measurement of maximum turbulent kinetic energy was quite surprising. For the axisymmetric jet with exhaust conditions matching the experiment, Fig.7.25 shows the axial distribution of maximum k/U_p^2 both above and beneath the jet centerline compared with the experimental measurement. The peak experimentally determined value was

0.0172 and the peak computational value was 0.0176 below the jet centerline (a difference of about 2%). The values on the upperside of the jet match to within about 10%. The peak experimentally determined value was 0.0154 and the peak computational value was 0.0176 above the jet centerline. This is due to the asymmetry in the experimental baseline nozzle, in which the annular gap is narrower in the direction toward the ground. The values are also listed in Table 7.3.

Figure 7.26 shows the axial distributions of maximum radial velocity gradient neglecting the initial large peak due to the presence of the wake behind the center plug. The trend is very similar between the two, both above and below the jet centerline. There is very good quantitative agreement between the two underneath the jet centerline in the region near the end of the generalized secondary cores.

Figure 7.27 re-plots Fig. 6.94 with the computationally predicted value for maximum k/U_p^2 and G from Eq. 6.2 for the axisymmetric jet with exhaust conditions matching the experiment. The computational value lines up nicely on the experimentally obtained correlation curve both above and below the centerline. The agreement between experimental and computationally predicted values, especially of the important flow field parameters to noise emissions, shows the promise of the RANS solver used with the SST model in developing acoustics models. Computational predictions would enable design optimizations to be performed quickly and efficiently. The prediction would still require empirical data for prediction of ΔOASPL toward the ground and in the sideline directions.

Figure 7.28 shows the predicted values at increased Mach number. The trend is the same. The wedge reduces the gradient parameter G, and the maximum turbulent kinetic

energy underneath the centerline. Above the jet centerline, the values are increased. Although the approach here is non-integrative in obtaining G (it is obtained on the ϕ=0^o plane only), the gradient reduction is quite uniformly distributed underneath the jet issuing from nozzles with convergent geometry. Therefore, it is likely that looking at a single slice of the flow (on the ϕ=0^o plane) will be representative of the entire downward perimeter of the jet. The reduction in G underneath the jet corresponds to a thickening of the low speed fluid in the region of intense noise generation, and the results suggest the potential of the wedge for OASPL reduction. Acoustic tests are still necessary to confirm this in the bypass ratio 8 nozzle.

Table 7.1 ***GRC CFD 5BB Nozzle Exit Conditions***

Quantity	Primary	Secondary
Nozzle diameter (mm)	26.29	53.27
Plug diameter (mm)	18.81	-
Lip thickness (mm)	0.61	-
Protrusion (mm)	23.16	-
Velocity (m/s)[a]	63.1	44.2
Mach number[a]	0.18	0.13
Bypass ratio[a]	-	2.71
Velocity (m/s)[b]	255	195
Mach number[b]	0.80	0.54
Bypass ratio[b]	-	2.55

Table 7.2 ***GRC CW17 5BB Nozzle Exit Conditions***

Quantity	Primary	Secondary
Nozzle diameter (mm)	27.2	53.27
Plug diameter (mm)	20.4	-
Lip thickness (mm)	0.70	-
Protrusion (mm)	25.3	-
Velocity (m/s)	63.1	44.2
Mach number	0.18	0.13
Bypass ratio	-	2.67

Table 7.3 ***Predicted Flow Field Parameters***

Case	Peak k/U_p^2 Below	Peak k/U_p^2 Above	*G Below*	*G* Above	x_{GSC}/D_f Below	x_{GSC}/D_f Above	x_p/D_f
Baseline Exp.	0.0172	0.0154	2.27	2.30	1.22	1.66	4.79
Baseline CFD[a]	0.0176	0.0176	2.270	2.270	2.088	2.088	5.23
W1 CFD[b]	0.00967	0.00967	2.112	2.338	2.607	2.109	6.82
Baseline CFD[b]	0.0110	0.0110	2.197	2.197	2.464	2.464	7.28

[a] matched experimental boundary conditions

[b] simulated takeoff boundary conditions

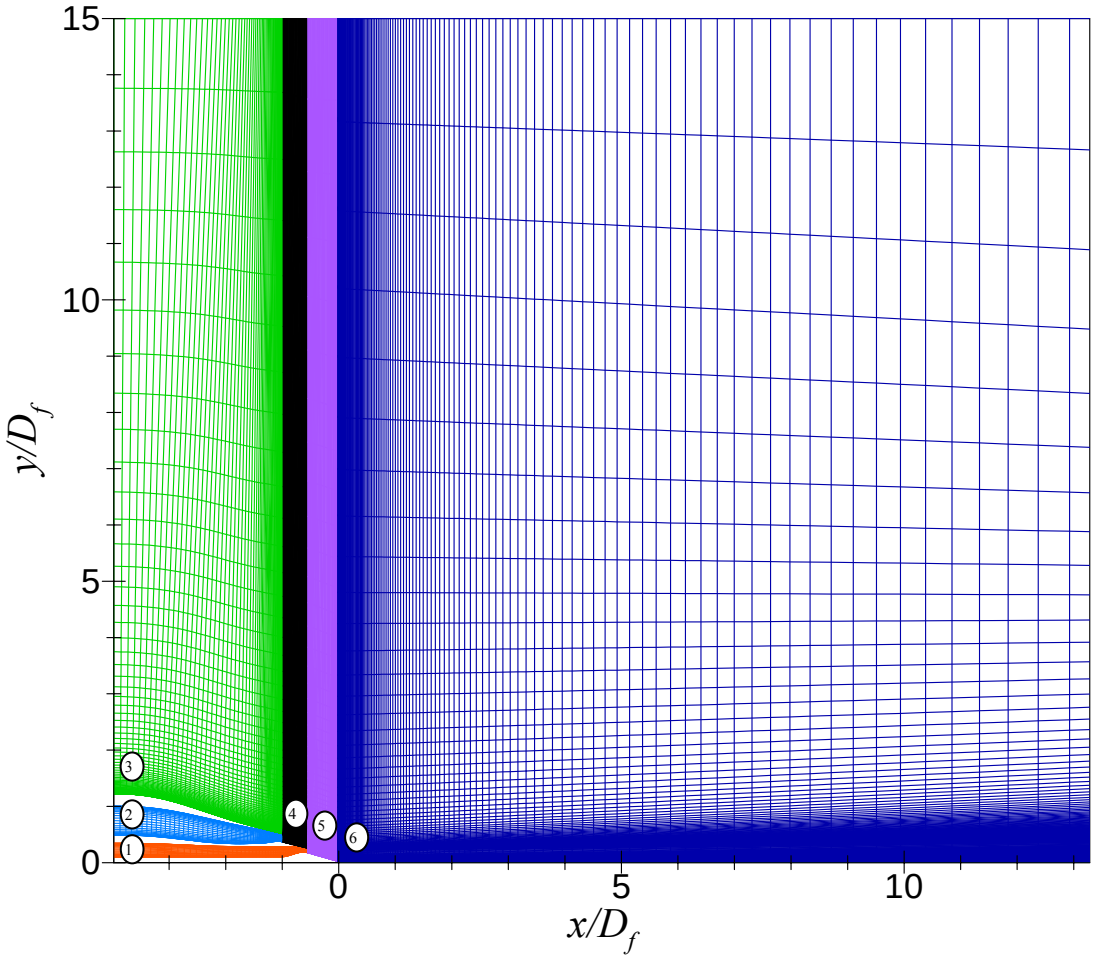

Figure 7.1. Computational grid for the axisymmetric configuration, showing zones 1-6.

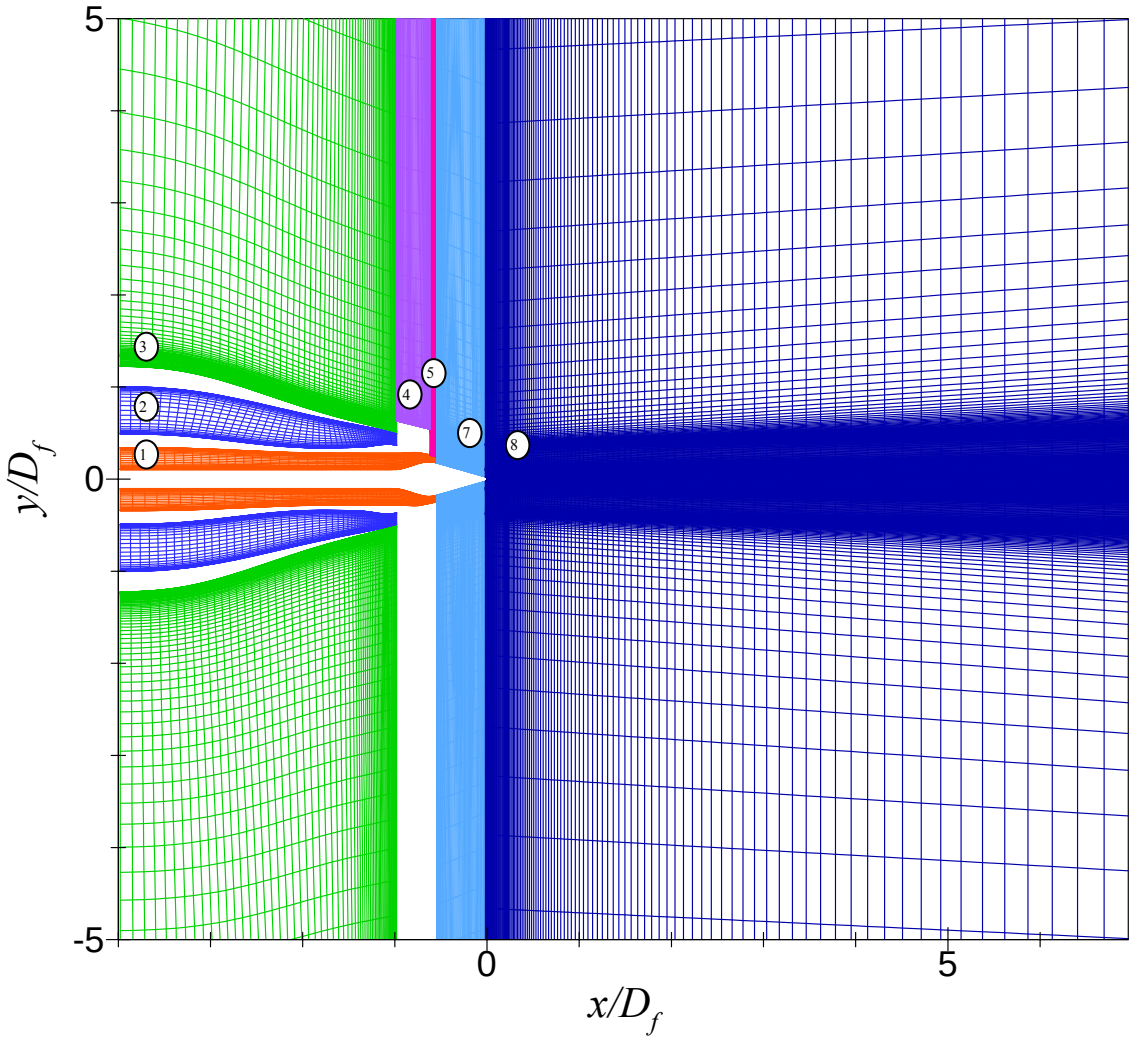

Figure 7.2. Computational grid for the asymmetric configuration, showing blocks 4 and 5, above and behind the wedge, respectively.

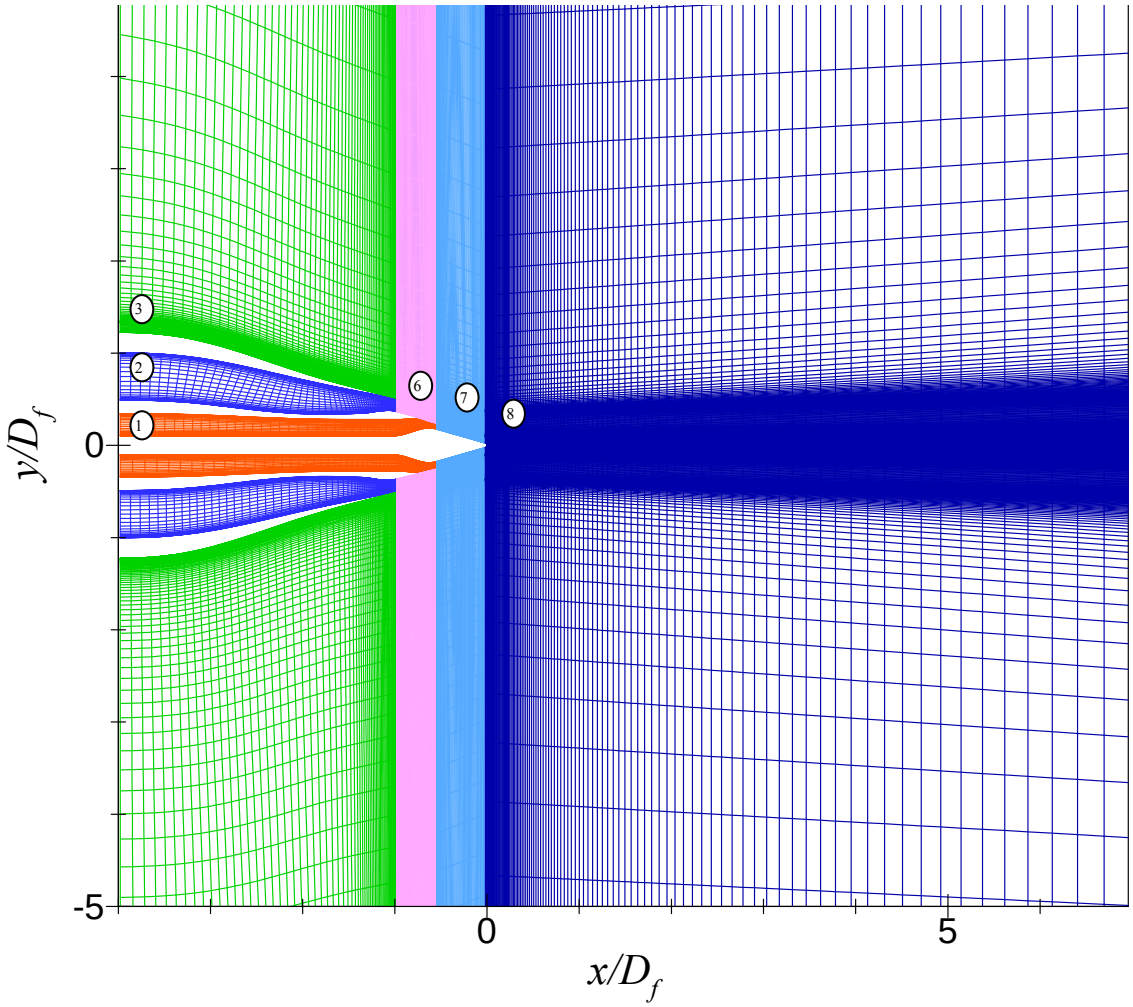

Figure 7.3. Computational grid for the asymmetric configuration, showing blocks 1-3 and 6-8. Block 6 sweeps the region on the side of the wedge.

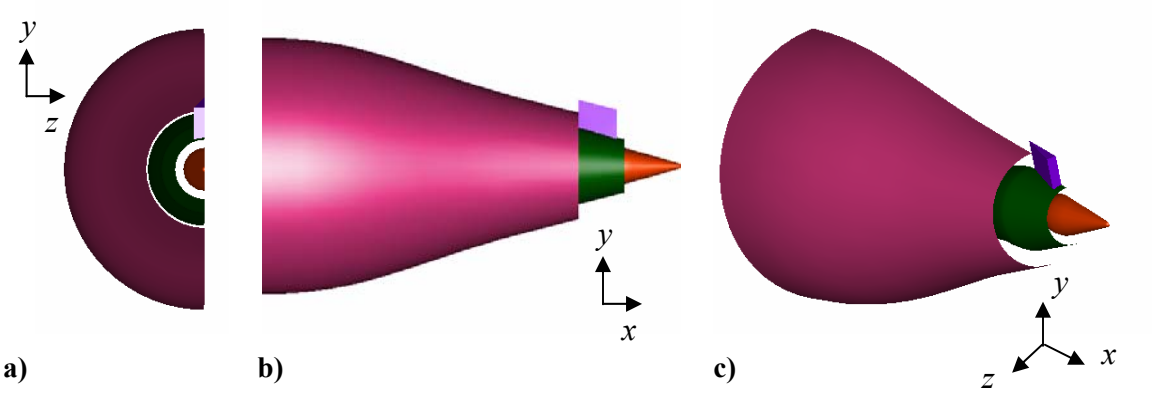

Figure 7.4. 3D views of the '5BB' nozzle and wedge configuration. The flow field is computed from 0^o to 180^o, then the solution may be reflected about the plane of symmetry. The plane of symmetry is clear in a) to be defined by the vertical axis (y-axis) and the nozzle axis (x-axis).

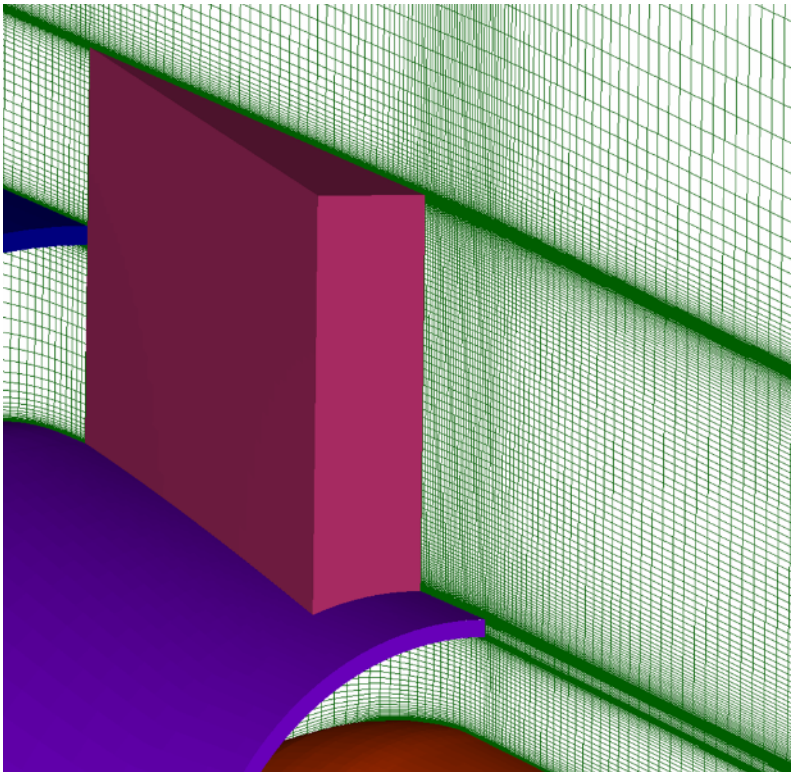

Figure 7.5. Close up of a sample computational grid on plane of symmetry of the wedge.

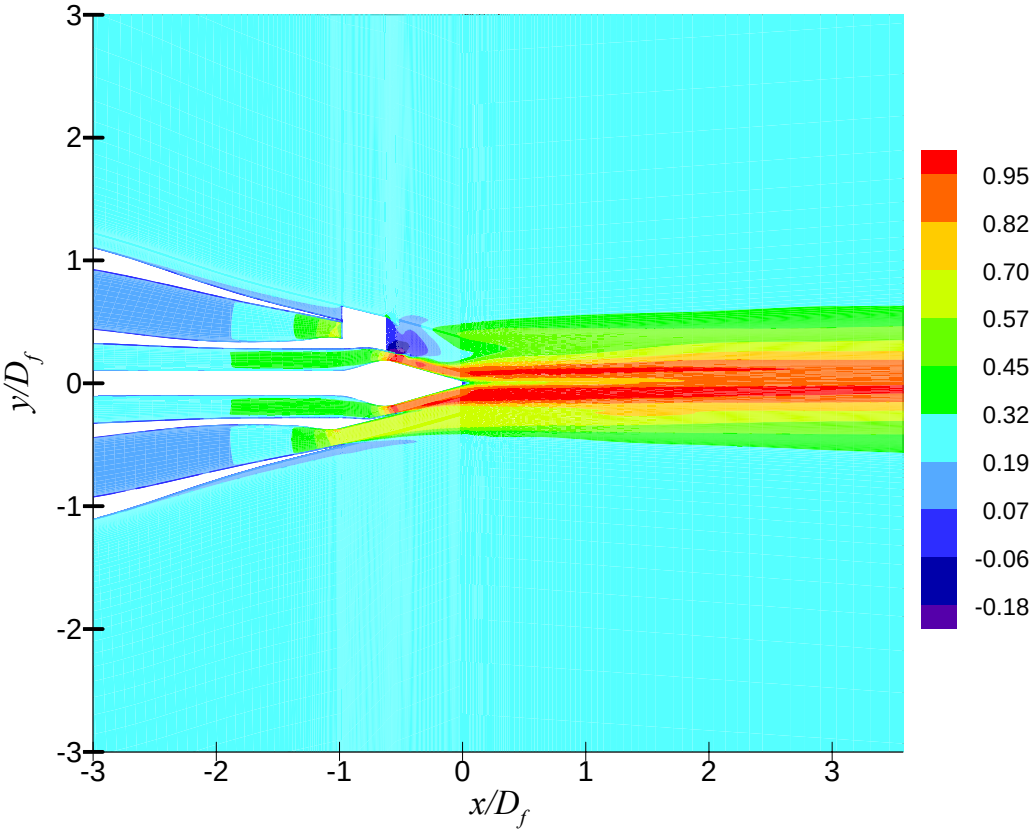

Figure 7.6. Computational solution on the plane of symmetry revealing the wake behind the wedge. Mean axial velocity component, W_1 + '5BB' nozzle.

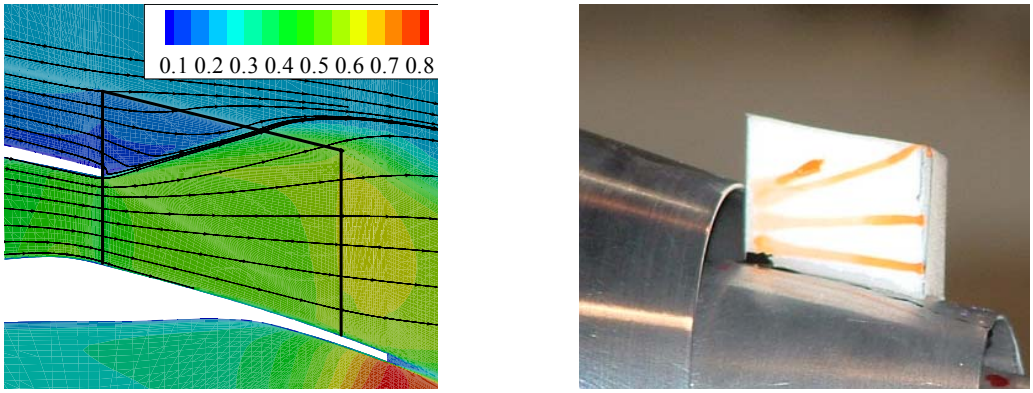

a) **b)**

Figure 7.7. a) Computational solution: tangent lines to mean velocity along wedge sidewall overlaid on Mach number isocontours. M_s=0.54, M_a=0.2. b) Surface flow visualization experiments using watercolor paint M_s=0.13, M_a=0.

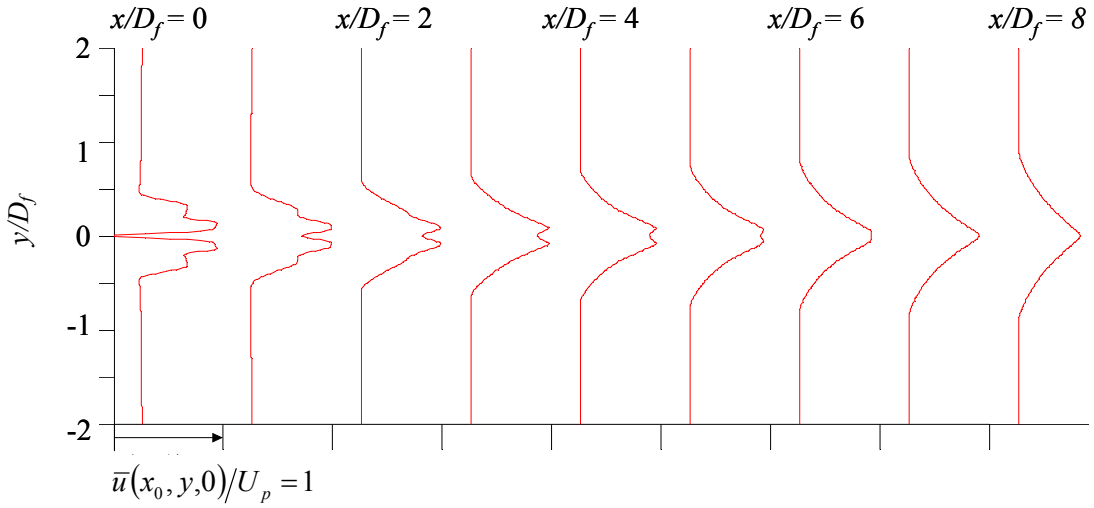

Figure 7.8. Evolution of mean axial velocity profiles. Baseline jet in forward flight.

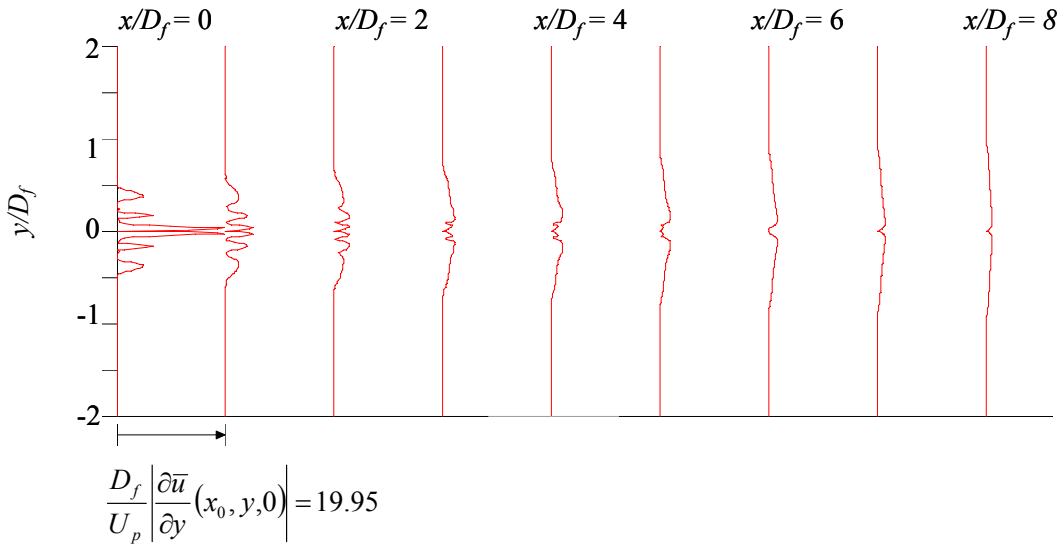

Figure 7.9. Evolution of mean velocity gradient transverse profiles. Baseline jet in forward flight.

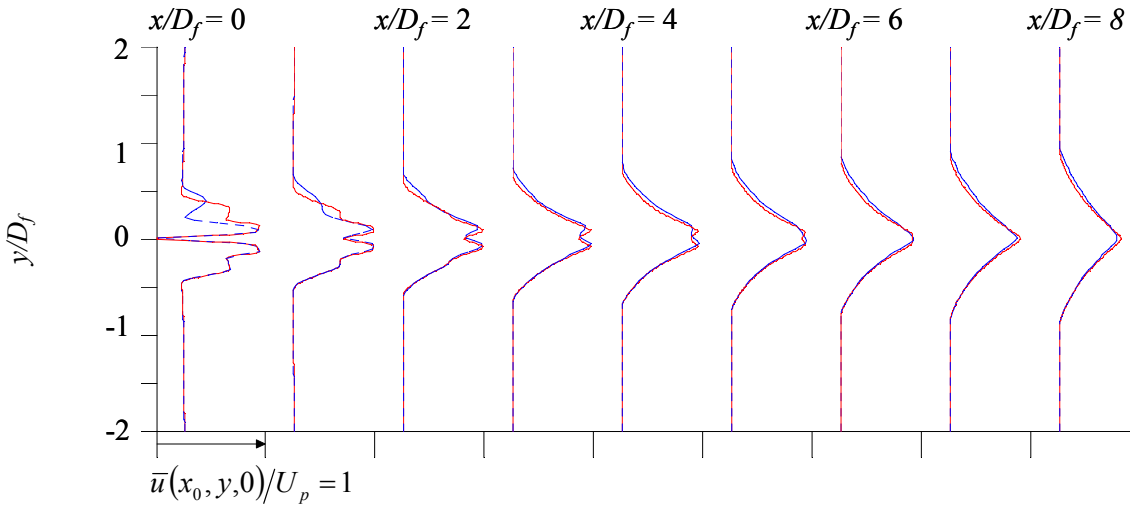

Figure 7.10. Evolution of mean axial velocity profiles. W_1 - - - overlaid with baseline — in forward flight.

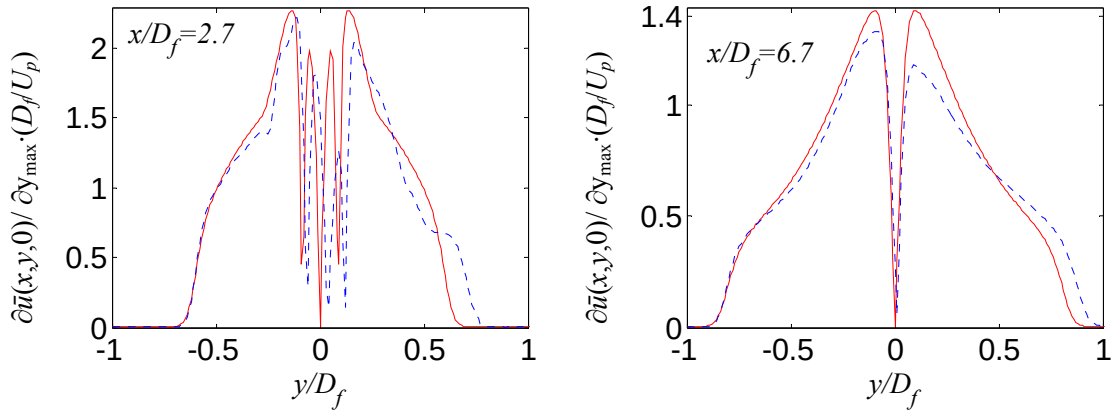

a) **b)**

Figure 7.11. Mean velocity gradient transverse profiles at a) x/D_f=2.7 and b) x/D_f=6.7.
W_1 - - - overlaid with baseline —.

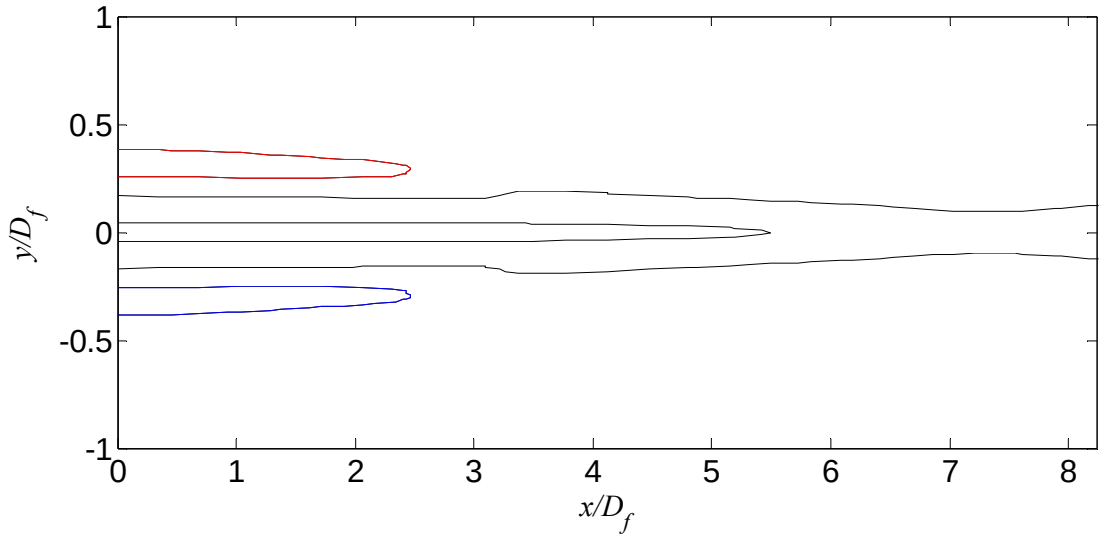

Figure 7.12. Locus of inflection points of $u(x,y,0)/U_p$ for baseline jet in forward flight.

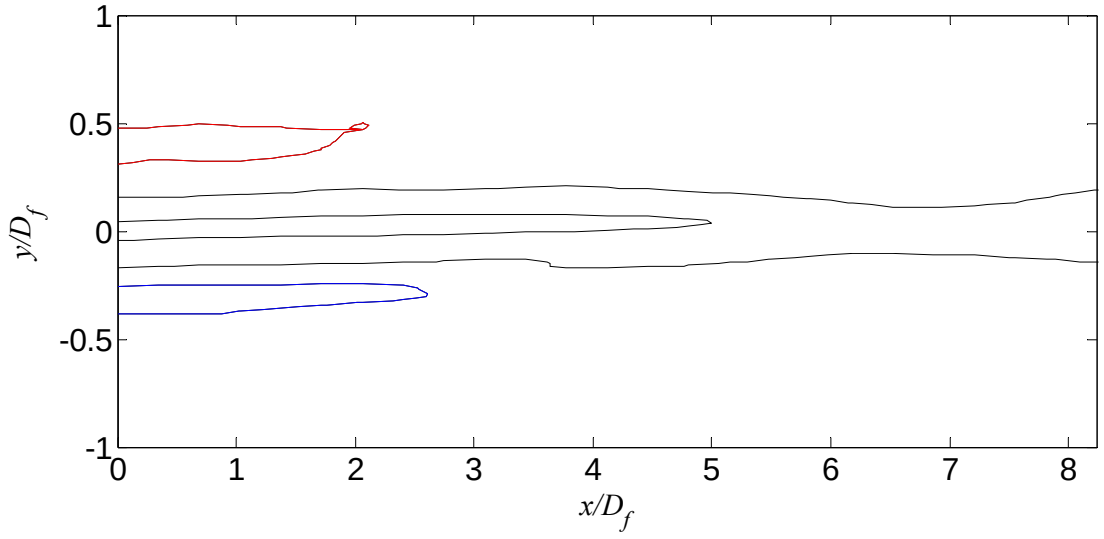

Figure 7.13. Locus of inflection points of $u(x,y,0)/U_p$ for wedge case in forward flight, W_1.

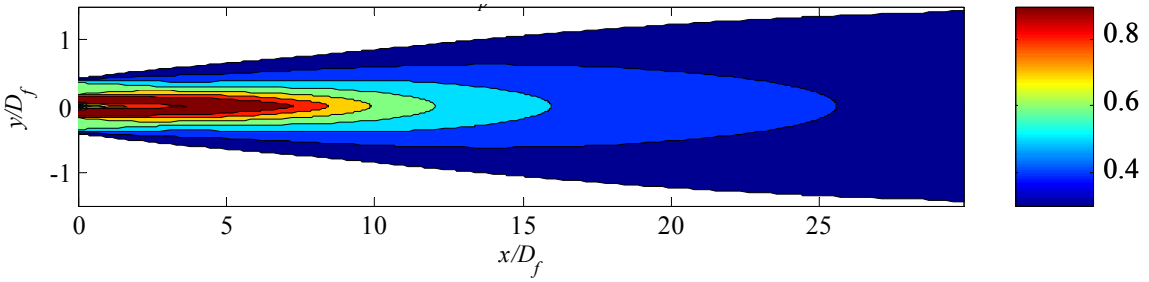

Figure 7.14. Mean axial velocity isocontours, $\bar{u}(x,y,0)/U_p$ for the baseline jet in forward flight.

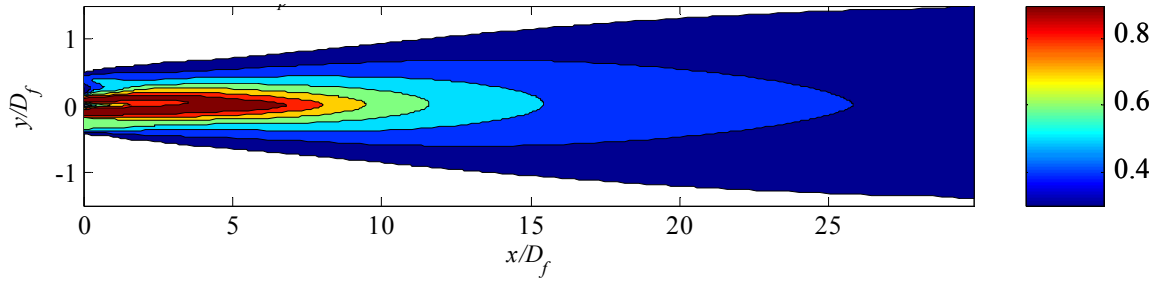

Figure 7.15. Mean axial velocity isocontours, $\bar{u}(x,y,0)/U_p$ for the wedge case, in forward flight W_1.

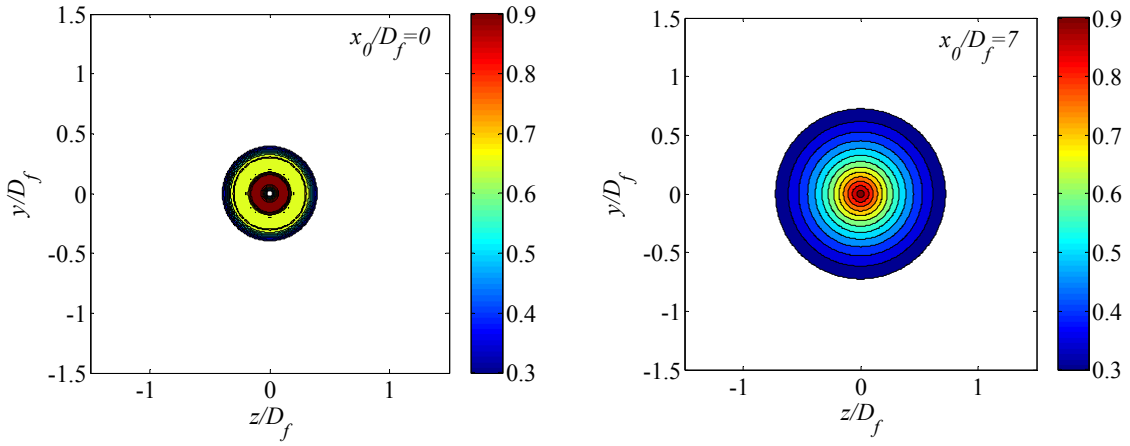

Figure 7.16. Cross-sections of mean axial velocity isocontours, $\bar{u}(x_0,y,z)/U_p$ in the baseline jet plume in forward flight.

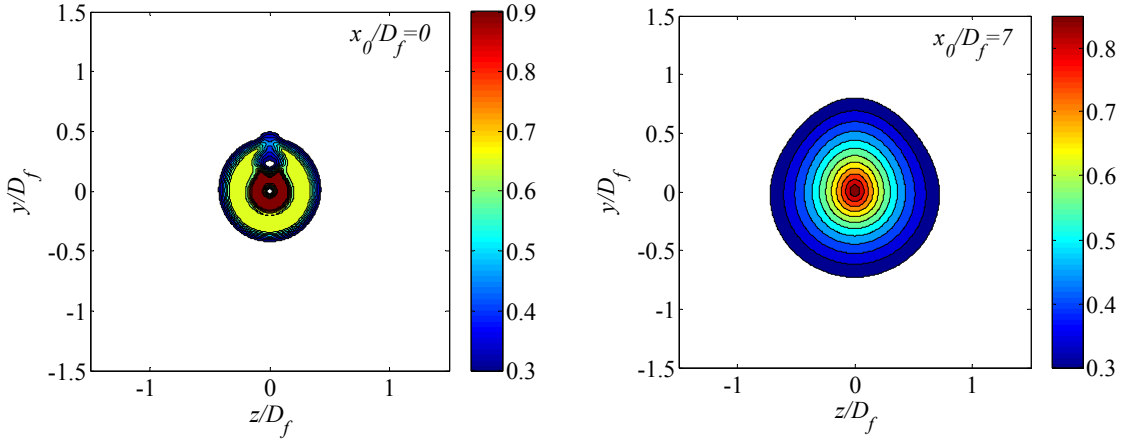

Figure 7.17. Cross-sections of mean axial velocity isocontours in jet plume, $\bar{u}$ $(x_0,y,z)/U_p$ for wedge case in forward flight, W_1.

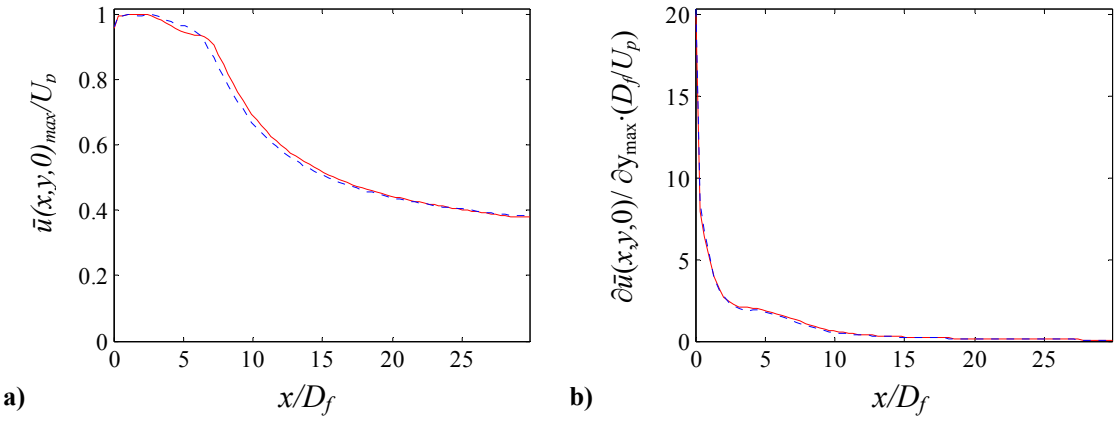

Figure 7.18. Axial distributions of a) maximum mean velocity and b) maximum radial velocity gradient underneath primary jet W_1 - - - overlaid with baseline —.

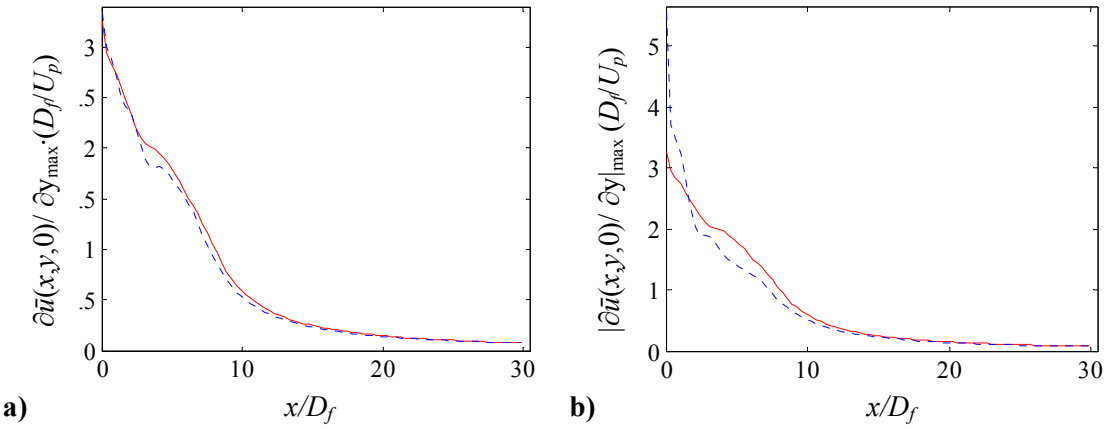

Figure 7.19. Axial distribution of maximum radial velocity gradient not withstanding the large spike in the initial region due to the wake of the plug, a) underneath the primary jet and b) above the primary jet, W_1 - - - overlaid with baseline —.

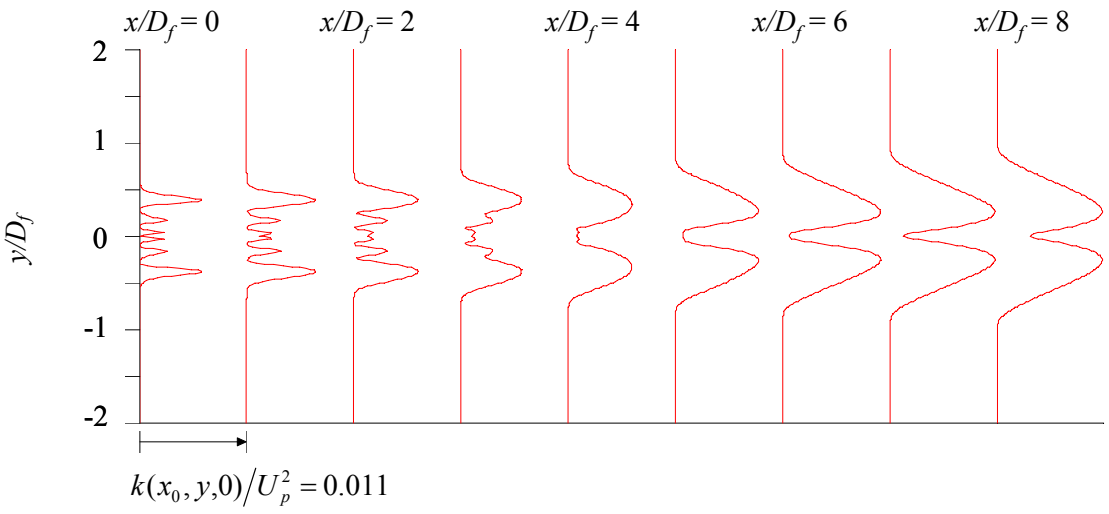

Figure 7.20. Evolution of turbulent kinetic energy profiles. Baseline jet.

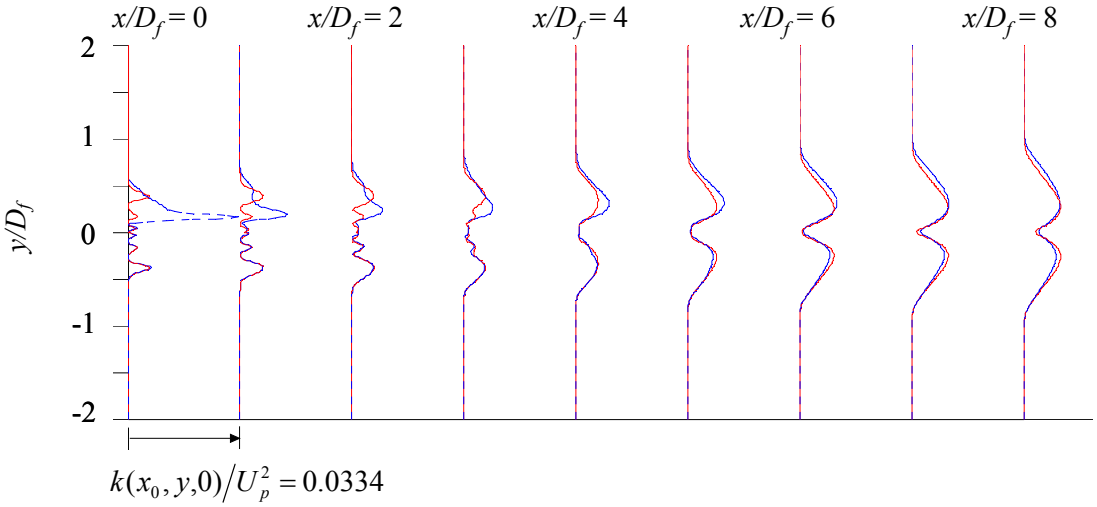

Figure 7.21. Evolution of turbulent kinetic energy, $k(x,y,0)/U_p^2$. W_1 - - - overlaid with baseline —.

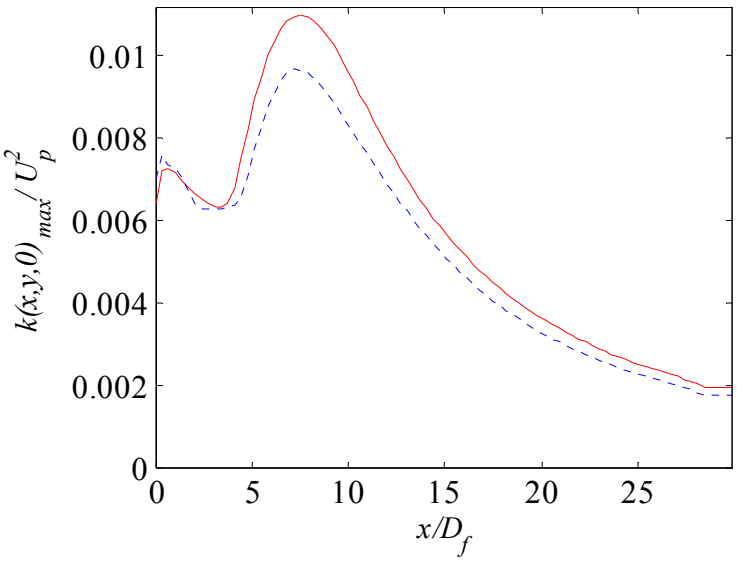

a)

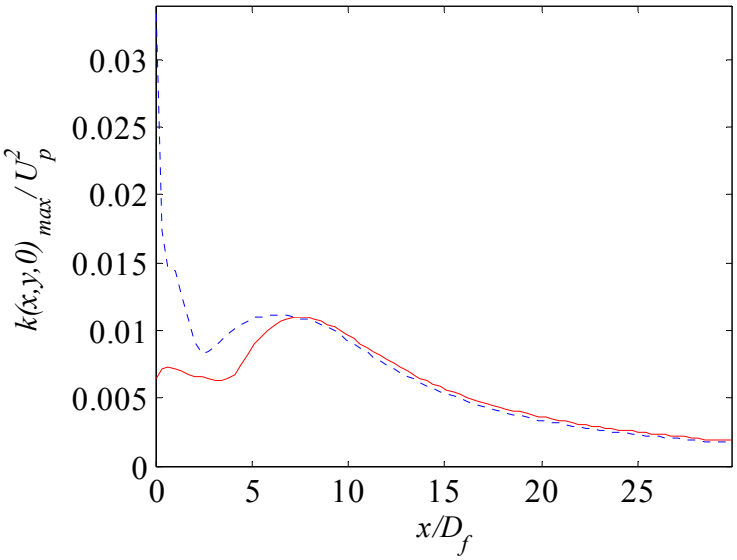

b)

Figure 7.22. Axial distribution of maximum turbulent kinetic energy measured on the z=0 plane a) below and b) above the jet centerplane. W_1 - - - overlaid with baseline —.

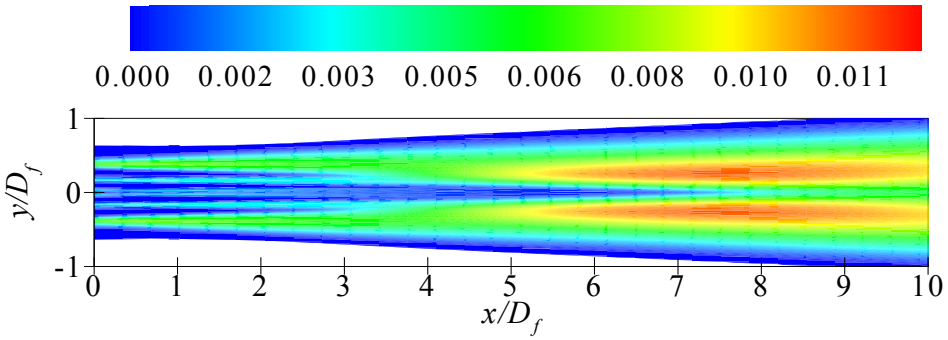

Figure 7.23. Distribution of turbulent kinetic energy $k(x,y,0)/U_p^2$, for the baseline jet in forward flight.

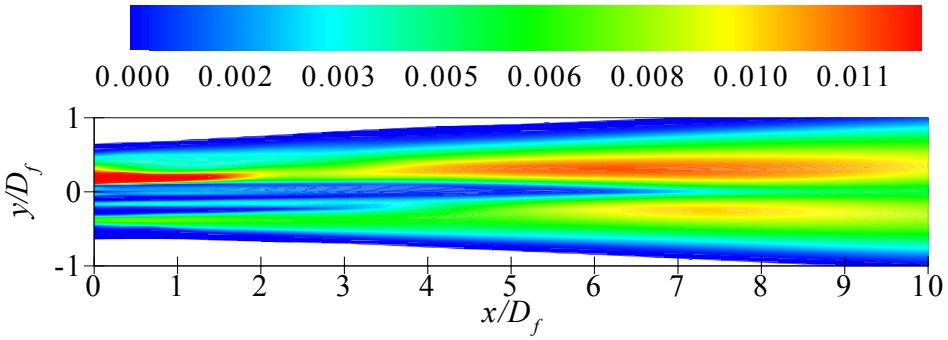

Figure 7.24. Distribution of turbulent kinetic energy $k(x,y,0)/U_p^2$ for wedge case in forward flight, W_1.

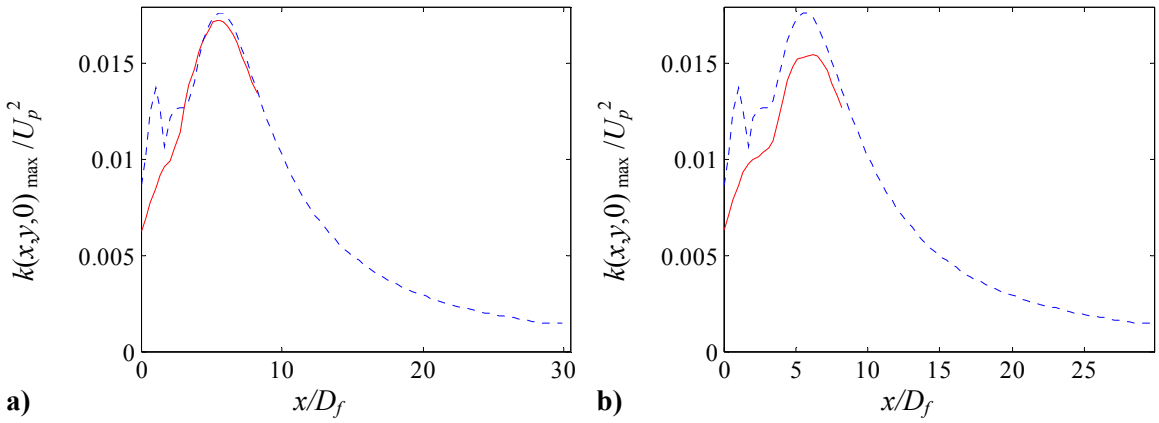

Figure 7.25. Axial distributions of maximum turbulent kinetic energy, a) below and b) above jet centerplane. Experimental — and computational - - - values for the baseline static jet.

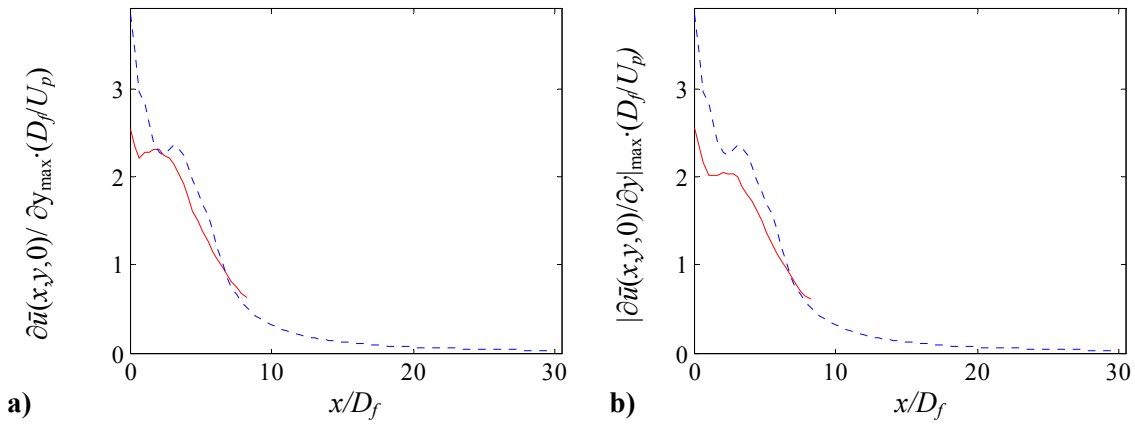

Figure 7.26. Axial distributions of maximum velocity gradient a) below and b) above jet centerplane. Experimental — and computational - - - values for the baseline static jet.

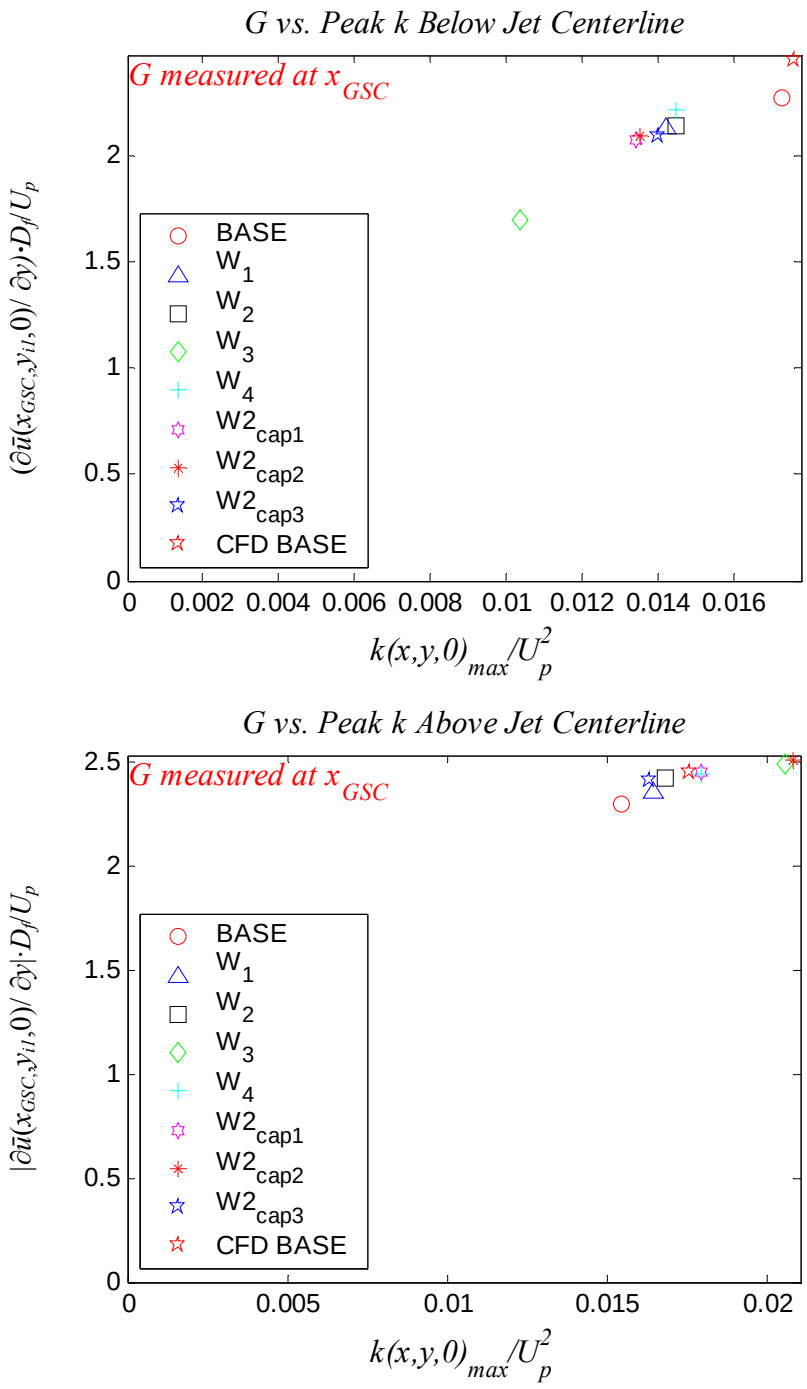

Figure 7.27. *G* vs. Peak *k* a) below and b) above jet centerline. *G* is calculated at x_{GSC}, and it is non-dimensionalized using D_f.

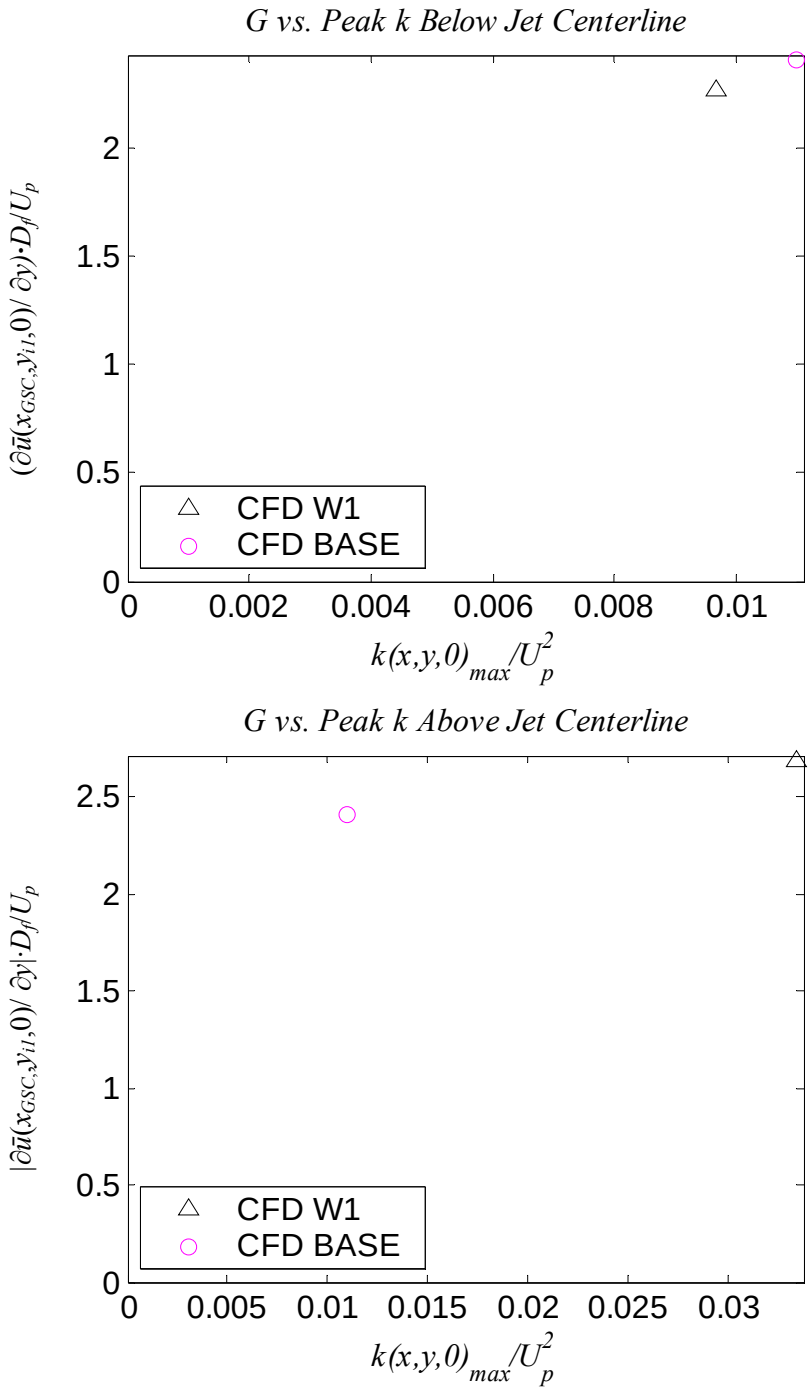

Figure 7.28. *G* vs. Peak *k* a) below and b) above jet centerline. *G* is calculated at x_{GSC}, and it is non-dimensionalized using D_f.

Chapter 8

Conclusions

8.1 Summary

Noise measurements and flow field surveys at the University of California, Irvine, and at NASA Glenn Research Center were conducted in an effort to correlate noise reduction resulting from asymmetry in dual-stream jets with asymmetries in flow field characteristics such as reduced maximum radial velocity gradient, reduced peak turbulent kinetic energy, and reduced peak Reynolds stresses, on the jet plane of symmetry. Pitot-pressure surveys and hot-wire measurements revealed these reductions in the flow fields for several asymmetric dual-stream jet configurations using the Fan Flow Deflection (FFD) noise suppression technology. Additionally, computational investigations predicted similar trends in the flow fields for a baseline and external wedge configuration simulating forward flight conditions. The GRC experiments and computations were instrumental in establishing a link between the asymmetry of the mean velocity field and the reduction in peak turbulent kinetic energy and peak Reynolds stress magnitudes. Based on the GRC data, reduced velocity gradients underneath the jet were correlated with reduced turbulent kinetic energy levels underneath the jet. This correlation is hoped

to help in the development of models connecting noise reduction to the distortion of the mean flow. Through computational flow field predictions, it would enable the selective design of aircraft engine nozzles with directional noise suppression capabilities. The agreement between experimental and computational values for turbulent kinetic energy using the RANS equations and turbulence modeling is encouraging. In an additional related aspect of this work, the UCI experiments illuminated the role of the baseline nozzle geometry on the effectiveness of the FFD technique.

8.2 Recommendations for Future Work

Recommendations include conducting acoustic measurements in the bypass ratio 8 nozzle. Reduction of the radial mean velocity gradient is observed in both the bypass ratio 5 and bypass ratio 8 nozzles, suggesting the potential of the fan flow deflection (FFD) method to reduce noise in high bypass ratio engines. The FFD technique has been demonstrated for noise reduction in the downward and sideline directions. Implementation of this technology can have a direct impact on the health of workers and on small business growth and economy in airport communities around the world. In this line of thinking, it is desirable that the FFD technique be incorporated on next generation turbofan engines for aircraft noise reduction. It is hoped that the correlations presented in this thesis will lead to high-level models for noise reduction, which will then be used in the design of optimized exhaust systems for turbofan engines. In obtaining an optimized jet noise reduction system for a next generation aircraft engine, an integrative approach combining more than one concept may enhance both aerodynamic performance and noise suppression.

References

[1] Papamoschou, D., "Directional Suppression of Noise from a High-Speed Jet," *AIAA Journal*, Vol. 39, No.3, 2001, pp. 380-387.

[2] Papamoschou, D. and Debiasi, M., "Conceptual Development of Quiet Turbofan Engines for Supersonic Aircraft," *AIAA Journal of Propulsion and Power*, Vol. 39, No.3, 2001, pp. 380-387.

[3] Zaman, K.B.M.Q. and Papamoschou, D. "Noise- and Flow-Field of Jets from an Eccentric Coannular Nozzle," *AIAA Paper* 2004-0005, presented at the 42nd AIAA Aerospace Sciences Meeting, January 2004, Reno, NV.

[4] Papamoschou, D., "New Method for Jet Noise Suppression in Turbofan Engines," *AIAA Journal*, Vol. 42, No.11, 2004, pp. 2245-2253.

[5] Papamoschou, D., "Fan Flow Deflection in Simulated Turbofan Exhaust," *AIAA Journal*, Vol. 44, No.12, 2006, pp. 3088-3097.

[6] Papamoschou, D., "Engine Cycle and Exhaust Configuration for Quiet Supersonic Propulsion," *AIAA Journal of Propulsion and Power*, Vol. 20, No.2, 2004, pp. 255-262.

[7] Papamoschou, D., "Mean Flow and Acoustics of Dual-Stream Jets," *AIAA Paper* 2004-0004, presented at the 42nd AIAA Aerospace Sciences Meeting, January 2004, Reno, NV.

[8] Murakami, E. and Papamoschou, D., "Mean Flow Development in Dual-Stream Jets," *AIAA Journal*, Vol.40, No.6, June 2002, pp.1131-1138.

[9] Henderson, B., Norum, T. and Bridges, J. E., "An MDOE Assessment of Nozzle Vanes for High Bypass Ratio Jet Noise Reduction," *AIAA Paper* 2006-2543, presented at the 12th AIAA/CEAS Aeroacoustics Conference, Cambridge, MA, May 8-10, 2006.

[10] Papamoschou, D. and Nishi, K.A., "Turbofan Jet Noise Reduction Via Deflection of the Bypass Stream," *AIAA Paper* 2004-0187, presented at the 42nd AIAA Aerospace Sciences Meeting, January 2004, Reno, NV.

[11] Papamoschou, D. and Shupe, R.S., "Effect of Nozzle Geometry on Jet Noise Reduction using Fan Flow Deflectors," *AIAA Paper* 2006-2707, presented at the 12th AIAA/CEAS Aeroacoustics Conference, Cambridge, MA, May 8-10, 2006.

[12] Papamoschou, D. and Nishi, K.A., "Jet Noise Suppression with Fan Flow Deflectors in Realistic-Shaped Nozzle," *AIAA Paper* 2005-0993, presented at the 43rd AIAA Aerospace Sciences Meeting, January 2005, Reno, NV.

[13] Papamoschou, D., "Parametric Study of Fan Flow Deflectors for Jet Noise Suppression," *AIAA Paper* 2005-2890, presented at the 11th AIAA/CEAS Aeroacoustics Conference, Monterey, CA, May 23-25, 2005.

[14] Zaman, K.B.M.Q. and Papamoschou, D. “Effect of a Wedge on Coannular Jet Noise,” *AIAA Paper* 2006-0007, presented at the 44th AIAA Aerospace Sciences Meeting, January 2006, Reno, NV.

[15] Zaman, K.B.M.Q., Bridges, J. E., and Papamoschou, D., “Offset Stream Technology – Comparison of Results from UCI and GRC Experiments,” *AIAA Paper* 2007-0438, presented at the 45th AIAA Aerospace Sciences Meeting, January 2007, Reno, NV.

[16] Murayama, T., Papamoschou, D., and Liu, F. “Aerodynamics of Fan Flow Deflectors for Jet Noise Suppression,” *AIAA Paper* 2005-0994, presented at the 43rd AIAA Aerospace Sciences Meeting, January 2005, Reno, NV.

[17] Papamoschou, D. Vu, A., and Johnson, A.J., “Aerodynamics of Wedge-Shaped Deflectors for Jet Noise Reduction,” *AIAA Paper* 2006-3655, presented at the 24th AIAA Applied Aerodynamics Conference, June 2006, San Francisco, CA.

[18] Herkes, W.H., Olsen, R.F., and Uellenberg, S., “The Quiet Technology Demonstrator Program: Flight Validation of Airplane Noise-Reduction Concepts,” AIAA Paper 2006-2720, presented at the 12th AIAA/CEAS Aeroacoustics Conference, May 2006, Cambridge, MA.

[19] Saiyed, N.H., Mikkelsen, K.L., and Bridges, J.E., “Acoustics and Thrust of Quiet Separate-Flow High-Bypass-Ratio Nozzles,” *AIAA Journal*, Vol. 41, No.3, 2003, pp. 372-378.

[20] Seiner, J.M., Gilinsky, M.M., “Nozzle Thrust Optimization While Reducing Jet Noise,” *AIAA Journal*, Vol. 35, No.3, 1997, pp. 420-427.

[21] Bogdanoff, D.W., “Compressibility Effects in Turbulent Shear Layers,” *AIAA Journal*, Vol.21, No.6, 1982, pp.926-927.

[22] Papamoschou, D., “Experimental Investigation of Heterogeneous Compressible Shear Layers,” Doctoral Dissertation, California Institute of Technology, 1986.

[23] Papamoschou, D., and Roshko, A., “The Compressible Turbulent Shear Layer: An Experimental Study,” *Journal of Fluid Mechanics*, Vol.197, 1988, pp.453-477.

[24] G. Brown and A. Roshko, “On Density Effects and Large Structure in Turbulent Mixing Layers,” *Journal of Fluid Mechanics*, Vol. 64, part 4, 1974, pp. 775-816.

[25] Zhuang, M., Kubota, T., and Dimotakis, P.E., “Instability Of Inviscid, Compressible Free Shear Layers,” *AIAA Journal*, Vol.28, No.10, October 1990, pp.1728-1733.

[26] Tam, C.K.W. and Hu, F.Q., “On the Three Families of Instability Waves of High-Speed Jets,” *Journal of Fluid Mechanics*, Vol.201, 1989, pp.447-482.

[27] Gropengiesser, H., “Study of the Stability of Boundary Layers in Compressible Fluids,” NASA TT-F-12, 786.

[28] Blumen, W., Drazin, P.G., and Billings, D.F., “Shear Layer Instability of an Inviscid Compressible Fluid,” *Journal of Fluid Mechanics*, Vol.71, Part 2, 1975, pp.305-316.

[29] Jackson, T.L. and Grosch, C.E., "Inviscid Spatial Stability of a Compressible Mixing Layer," *Journal of Fluid Mechanics*, Vol.208, 1989, pp.609-637.

[30] Jackson, T.L. and Grosch, C.E., "Absolute Convective Instabilities and the Convective Mach Number in a Compressible Mixing Layer," *Physics of Fluids A*, Vol.2, No.6, June 1990, pp.949-954.

[31] Kozusko, F. Lasseigne, D.G., Grosch, C.E., and Jackson, T.L., "The Stability of Compressible Mixing Layers in Binary Gases," *Physics of Fluids*, Vol.8, No.7, July 1996, pp.1954-1963.

[32] Day, M.J., Reynolds, W.C., and Mansour, N.N., "The Structure of the Compressible Reacting Mixing Layer: Insights From Linear Stability Analysis," *Physics of Fluids*, Vol.10, No.4, April 1998, pp.993-1007.

[33] Murakami, E. and Papamoschou, D., "Eddy Convection in Supersonic Coaxial Jets," *AIAA Journal*, Vol. 38, No.4, 2000, pp. 628-635.

[34] Ko, N.W.M., and Kwan, A.S.H., "The Initial Region of Subsonic Coaxial Jets," *Journal of Fluid Mechanics*, Vol. 73, part 2, pp. 305-332.

[35] Crow, S.C., and Champagne, F.H., "Orderly Structure in Jet Turbulence," *Journal of Fluid Mechanics*, Vol. 48, part 3, 1971, pp. 547-591.

[36] Guitton, A., Tinney, C.E., Jordan, P., and Delville, J., "Measurements in a Co-Axial Subsonic Jet," *AIAA Paper* 2007-0015, presented at the 45th AIAA Aero-space Sciences Meeting, January 2007, Reno, NV.

[37] Janardan, B.A., Hoff, G.E., Barter, J.W., Martens, S., Gliebe, P.R., Mengle, V., and Dalton, W.N., "AST Critical Propulsion and Noise Reduction Technologies for Future Commercial Subsonic Engines Separate-Flow Exhaust System Noise Reduction Concept Evaluation," NASA CR 2000-210039.

[38] K.B.M.Q. Zaman and D. Papamoschou, "Study of Mixing Enhancement Observed with a Co-Annular Nozzle Configuration", *AIAA Paper* 2000-0094, presented at the 38th AIAA Aerospace Sciences Meeting, January 2000, Reno, NV.

[39] K.B.M.Q. Zaman, "Spreading Characteristics of Compressible Jets," *Journal of Fluid Mechanics*, vol. 383, pp. 197-228, 1999.

[40] Papamoschou, D., "Acoustic Simulation of Hot Coaxial Jets Using Cold Helium-Air Mixture Jets," *AIAA Paper* 2005-0208, presented at the AIAA 43d Aerospace Sciences Meeting, January 2005, Reno, NV. To appear in the *AIAA Journal of Propulsion and Power*.

[41] Doty, M.J. and McLaughlin, D.K., "Acoustic and Mean Flow Measurements of High-Speed, Helium-Air Jets," *International Journal of Aeroacoustics*, Vol. 2, No. 3 & 4, 2003, pp.293-333.

[42] Papamoschou, D. and Dadvar, A., "Localization of Multiple Types of Jet Noise Sources," *AIAA Paper* 2005-0208, presented at the 12th AIAA/CEAS Aeroacoustics Conference, May 2006, Cambridge, MA.

[43] Papamoschou, D., "Small-Aperture Phased Array Study of Noise from Coaxial Jets," *AIAA Paper* 2007-0440, presented at the 45th AIAA Aerospace Sciences Meeting, January 2007, Reno, NV.

[44] Fisher, M.J., Preston, G.A., Bryce, W.D., "A Modeling of the Noise from Simple Coaxial Jets, Part I: with Unheated Primary Flow," *Journal of Sound and Vibration*, Vol. 209, No. 3, 1998, pp. 385-403.

[45] Zaman, K.B.M.Q., and Dahl, M.D., "Noise and Spreading of a Subsonic Coannular Jet – Comparison with Single Equivalent Jet," *AIAA Paper* 2005-0210, presented at the 43rd AIAA Aerospace Sciences Meeting, January 2005, Reno, NV.

[46] Birch, S.F., Khritov, K.M., Maslov, V.P., Mironov, A.K., and Secundov, A.N., "An Experimental Study of Flow Asymmetry in Co-axial Jets," *AIAA Paper* 2005-2845, presented at the 11th AIAA/CEAS Aeroacoustics Conference, May 2005, Monterey, CA.

[47] Birch, S.F., Lyubimov, D.A., Buchshtab, P.A., Secundov, A.N., and Yakubovsky, K. Y., "Jet-Pylon Interaction Effects," *AIAA Paper* 2005-3082, presented at the 11th AIAA/CEAS Aeroacoustics Conference, May 2005, Monterey, CA.

[48] Birch, S.F., "A Review of Axisymmetric Jet Flow Data For Noise Applications," *AIAA Paper* 2006-2602, presented at the 12th AIAA/CEAS Aeroacoustics Conference, May 2006, Cambridge, MA.

[49] Zaman, K.B.M.Q., "Effect of Initial Condition on Subsonic Jet Noise," *AIAA Journal*, Vol. 23, No.9, 1984, pp. 1370-1373.

[50] Georgiadis, N.J. and Papamoschou, D., "Computational Investigations of High-Speed Dual Stream Jets," *AIAA Paper* 2003-3311, presented at the 9th AIAA/CEAS Aeroacoustics Conference, May 2003, Hilton Head, SC.

[51] Georgiadis, N.J. and Papamoschou, D., "Computations of Dual-Stream Jets with Eccentric and Coaxial Bypass Streams," *AIAA Paper* 2004-2981, presented at the 10th AIAA/CEAS Aeroacoustics Conference, May 2004, Manchester, UK.

[52] Georgiadis, N.J, Rumsey, C.L., Yoder, D.A., and Zaman, K.B.M.Q., "Turbulence Modeling Effects on Calculation of Lobed Nozzle Flowfields," *Journal of Propulsion and Power*, Vol.22, No.3, June 2006, pp.567-575.

[53] DalBello, T., Dippold, V., and Georgiadis, N.J., "Computational Study of Separating Flow in a Planar Subsonic Diffuser," NASA TM 2005-213894.

[54] Barber, T.J., Chiappetta, L.M., DeBonis, J.R., Georgiadis, N.J., and Yoder, D.A., "Assessment of Parameters Influencing the Prediction of Shear–Layer Mixing," *Journal of Propulsion and Power*, Vol.15, No.1, 1998, pp.45-53.

[55] Bush, R.H., Power, G.D., and Towne, C.E., "WIND: The Production Flow Solver of the NPARC Alliance," *AIAA Paper*, 1998-0935, Presented at the 36th AIAA Aerospace Sciences Meeting and Exhibit, January 1998, Reno, NV.

[56] Nelson, C.C. and Power, G.D., "CHSSI Project CFD-7: The NPARC Alliance Flow Simulation System," *AIAA Paper*, 2001-0594, Presented at the 39th AIAA Aerospace Sciences Meeting and Exhibit, January 2001, Reno, NV.

[57] Georgiadis, N.J. and DeBonis, J.R., "Navier-Stokes Analysis Methods for Turbulent Jet Flows with Application to Aircraft Exhaust Nozzles," *Progress in Aerospace Sciences*, Vol.42, 2006, pp.377-418.

[58] Menter, F.R., "Two-Equation Eddy-Viscosity Turbulence Models for Engineering Applications," *AIAA Journal*, Vol.32, No.8, 1994, pp.1598-1605.

[59] GRIDGEN, Version 13, User Manual, Pointwise Inc., Bedford, Texas, 1998.

[60] Dahl, M.D. and Papamoschou, D., "Analytical Predictions and Measurements of the Noise Radiated from Supersonic Coaxial Jets," *AIAA Journal*, Vol.38, No.4, April 2000, pp.584-591.

[61] Dahl, M.D. and Morris, P.J., "Noise from Supersonic Coaxial Jets, Part 1: Mean Flow Predictions," *Journal of Sound and Vibration*, Vol.200, No.5, 1997, pp.643-663.

[62] Dahl, M.D. and Morris, P.J., "Noise from Supersonic Coaxial Jets, Part 2: Normal Velocity Profile," *Journal of Sound and Vibration*, Vol.200, No.5, 1997, pp.665-699.

[63] Dahl, M.D. and Morris, P.J., "Noise from Supersonic Coaxial Jets, Part 3: Inverted Velocity Profile," *Journal of Sound and Vibration*, Vol.200, No.5, 1997.

[64] Tam, C.K.W. and Burton, D.E., "Sound Generated by Instability Waves of Supersonic Flows. Part 1. Two-Dimensional Mixing Layers," *Journal of Fluid Mechanics*, Vol.138, 1984, pp.249-271.

[65] Tam, C.K.W. and Burton, D.E., "Sound Generated by Instability Waves of Supersonic Flows. Part 2. Axisymmetric Jets," *Journal of Fluid Mechanics*, Vol.138, 1984, pp.273-295.

[66] McLaughlin, D.K., Morrison, G.D., and Troutt, T.R., "Experiments on the Instability Waves in a Supersonic Jet and their Acoustic Radiation," *Journal of Fluid Mechanics*, Vol.69, No. 11, 1975, pp.73-95.

[67] Savitzky, A., and Golay, M. J. E., "Smoothing and Differentiation of Data by Simplified Least Squares Procedures," Analytical Chemistry, Vol.36, No.8, 1964, p. 1627-1639.

[68] Press, W.H., Flannery, B.P., Teukolsky, S.A., and Vetterling, W.T., *Numerical Recipes in FORTRAN 77: The Art of Scientific Computing*, Cambridge University Press, 1992.

[69] Bruun, H.H., *Hot-Wire Anemometry, Principles and Signal Analysis*, Oxford University Press, New York, 1995.

[70] Bendat, J.S. and Piersol, A.G., *Engineering Applications of Correlation and Spectral Analysis*, *2nd Editio*n, John Wiley & Sons, Inc., New York, 1993.

[71] White, F.M., *Viscous Fluid Flow*, *2nd Edition*, McGraw-Hill, Inc., New York, 1991.

[72] Rossing, T.D., Moore, F.R., and Wheeler, P.A., *The Science of Sound, Third Edition*, Addison Wesley, New York, 2002.

[73] Shevell, R.S., *Fundamentals of Flight*, Prentice Hall, New Jersey, 1989.

[74] Mathieu, J. and Scott, J., *An Introduction to Turbulent Flow*, Cambridge University Press, Cambridge, 2000.

[75] Anderson, J.D., *Modern Compressible Flow, Third Edition*, Mc-Graw Hill, Inc., New York, 2003.

[76] Agrawal, A. and Prasad, A.K., "Integral Solution for the Mean Flow Profiles of Turbulent Jets, Plumes, and Wakes," *Journal of Fluids Engineering*, Vol.125, 2003, pp.813-822.

[77] Liepmann, H.W. and Roshko, A., *Elements of Gasdynamics*, Dover Publications, Inc., New York, 2001.

[78] Papamoschou, D., *Compressible Fluid Dynamics, Lecture Notes*, University of California, Irvine, 2000.

[79] McLaughlin, D.K., Morris, P.J., *Aeroacoustics Seminar, Course Materials*, Pennsylvania State University at University of California Irvine, Winter 2006.